UNIVERSITÀ DEGLI STUDI DI PAVIA

DOTTORATO IN SCIENZE CHIMICHE E FARMACEUTICHE E INNOVAZIONE INDUSTRIALE
(XXXVII Ciclo)

Coordinatore: Chiar.mo Prof. Giorgio Colombo

Novel Materials and Devices For Water Splitting

Tesi di Dottorato di
Costanza Tedesco

AA 2023/2024

Tutor
Chiar.mo Prof. Lorenzo Malavasi

Co-tutor
Dott.ssa Irene Quinzeni

CONTENTS

1. CHAPETER

INTRODUCTION

1.1 GLOBAL ENERGY PROBLEM……...…1

1.1.2 RENEWABLE ENERGY SOURCES……2

1.1.3 ENERGY STORAGE ISSUE……...……2

1.1.4 HYDROGEN AS STORAGE ALTERNATIVE……..……..…3

1.1.5 AMMONIA AS HYDROGEN SOURCE……5

1.2 HYDROGEN PRODUCTION……..……6

2. PHOTOCATALYTIC HYDROGEN AND AMMONIA EVOLUTION…….……....11

2.1 PHOTOCATALYSTS FOR HYDROGEN AND AMMONIA EVOLUTION…….……14

2.2 STRATEGIES TO IMPROVE PHOTOCATALYTIC PERFORMANCE…….……17

3. PEROVSKITE-BASED MATERIALS FOR PHOTOCATALYTIC PURPOSE……..…..23

3.1 METAL HALIDE PEROVSKITE (MHPs) FOR PHOTOCATALYTIC HYDROGEN EVOLUTION……...26

4. AIM OF THE THESIS……30

References……..31

2. CHAPETER

Synthesis of Carbon Nitride Polymorphs by Sacrificial Template Method: Correlation between Physicochemical Properties and Photocatalytic Performance

ABSTRACT…….38

1. INTRODUCTION……...39

2. RESULTS AND DISCUSSION……41

3. CONCLUSION……...57

4. EXPERIMENTAL SECTION……....58
References……..61
Supporting information……..…63

3. CHAPTER

Reaction Mechanism of Hydrogen Generation and Nitrogen Fixation at Carbon Nitride/Double Perovskite Heterojunctions

ToC……...74
ABSTRACT……75
1. INTRODUCTION……...76
2. RESULTS AND DISCUSSION……78
3. CONCLUSIONS……....88
4. EXPERIMENTAL SECTION……....90
References…….....99
Supplementary information…… 102

4. CHAPTER

Compositional and Defect Engineering of Metal Halide Perovskite-based Heterojunctions for Efficient Nitrogen Photofixation

ToC..……....120
ABSTRACT…….. 121
1. INTRODUCTION……122
2. RESULTS AND DISCUSSION……..125
3. CONCLUSIONS……..…...135
References……..…...137
Supporting information……139

5. CHAPTER

Enhancing Visible-Light-Driven Hydrogen Production: Heterojunction Engineering of Graphitic Carbon Nitride and PBDB-T Organic Semiconductor

ABSTRACT…….. 157
1. INTRODUCTION……158
2. RESULTS AND DISCUSSION……..160
3. CONCLUSIONS……..…...176
Supplementary information…… 178
References……...…...187

6. CHAPTER

High Entropy Perovskite Oxides and Graphitic Carbon Nitride Hybrid Heterojunction for Solar Fuel Production

ABSTRACT…….. 193
1. INTRODUCTION……194
2. RESULTS AND DISCUSSION……..197
3. CONCLUSIONS……..... 203
Supplementary information…… 204
References……...…...210

7. CHAPTER

CONCLUSIONS AND OUTLOOKS……...……..211

CHAPTER 1

1. INTRODUCTION

1.1 GLOBAL ENERGY PROBLEM

The constant growing demand for energy and the environmental impact of its production and consumption, together with the unbalanced distribution of energy resources around the world make the global energy problem one of the most urgent challenges of the contemporary era. The energy problem has massive implications in terms of environmental sustainability, economic and politic stability, and social improvement. Since the global population and economies are in continuous expansion, the demand for energy increases at an exponential rate. The economic and social expansion lived by the occidental economies in the post-war owes its boom to the greater reliance on fossil fuels like coal, oil and natural gas that represent immediate and relatively cheap energy sources. Nowadays this massive fossil fuels consumption, especially in emerging economies that are experiencing a delayed economic and social growth, represents on one hand the undiscussed opportunity to power the industrialization and modernization of nations, on the other hand an important environmental problem, since fossil fuels represent the main contributors to greenhouse gas emissions and consequently of the climate change. The environmental effect of the extreme exploitation of energy is related to the release of carbon dioxide (CO_2) as a product of the combustion of fossil fuels.[1] Carbon dioxide is the main responsible of the greenhouse effect leading to global warming, extreme whether manifestation, and the degradation of natural ecosystems as direct consequence. Indirectly, the process of extraction and refinement of fossil fuels cause important environmental irreversible damages where the most worrying are deforestation, water sources contamination and natural habitat destruction. In addition to environmental concerns, dependence on fossil fuels has critical geopolitical implications. [1,2] Facing the global energy crisis requires a multifaceted approach since while some regiones, the developed countries, have stable and affordable energy supplies, billions of people in developing countries suffer

energy poverty. The multifaceted approach includes the gradual but complete transition to renewable and sustainable energy sources.

1.1.2 RENEWABLE ENERGY SOURCES

The primary candidates as alternatives to carbon base fossil fuels are hydroelectric, nuclear and the renewable energy sources. [1–3] Hydroelectric is a clean source of energy but requires building dams to store potential energy in the form of water and nuclear energy has its own challenges in terms of storing waste or cost and historically has generated public discontent, especially in the wake of the recent Fukushima disaster.[1-3] The renewable and primary energy sources have their advantages and disadvantages, but one of the main reasons that has cemented the dominances of the fossil fuels over the last century, besides their low cost, is the ability to provide the necessary energy continuously, 24 hours a day, throughout the entire year. Renewable energy sources offer clean energy indeed, but they are intermittent, whether energy was generated by sun, wind or tides. Paradoxically, during peak operation, renewable sources can generate an overproduction of energy that exceeds the request. These systems would require powerful energy storage units, like batteries or electrochemical capacitors, to smooth the difference between energy supply and demand.[4] Over the years, the issue concerning the storage of energy from intermittent renewable sources has gain a central role in the scientific, political, and economic development, since a zero-impact future is difficult to envision without relying on efficient and cost-effective systems that allow the safe conservation of production surpluses. Energy storage from renewable sources requires to consider both short-term storage (hours or days) and long-term storage (weeks or months).[5] Many technological systems are already widely used with the specific purpose of excess energy storage produced from renewable sources, the most historically famous is the hydroelectric power. This technology relies on the artificial filling of high-altitude reservoirs exploiting pumps powered by surplus energy production. However, this technology is far from sufficient to meet the real energy storage needs that would allow each nation to ensure grid stability and prevent blackouts, especially with a view towards a complete future energy transition.[6].

1.1.3 ENERGY STORAGE ISSUE

Many other technologies are quite advanced beside hydroelectric power and nuclear energy but there is currently no definitive strategy that comprehensively and conclusively addresses the issue of energy storage from renewable sources. Despite that, the most common and immediate answer to the question of energy storage today is probably *"batteries"*. The widespread use of rechargeable lithium-ion batteries in recent years has accustomed our societies to have energy readily available, even when is not available a connection to the electrical grid. Naturally, given their global widespread use, lithium-ion batteries are the focus of current attention in this field. This type of device operates based on the movement of lithium ions (Li^+), which migrate towards one electrode, called cathode, during the discharge phase, while moving on the opposite direction towards the other electrode, called anode, during the charging phase. This technology has become so prevalent not only because it is particularly lightweight and easy to use but also because it can withstand thousands of charge and discharge cycles, offers high energy density, and has high charging efficiency. The versatility of these devices is therefore convenient, with applications ranging from domestic use to the storage of energy from large wind or solar power plants. Nevertheless, lithium batteries have two major problems. The first is their cost, which is still too high to be considered an acceptable solution for global energy storage, also due to the limited amount of lithium, while the second problem is the rare instances of explosions or fires. Although this possibility is remote, the risk must be taken into account, and the systems must be carefully designed to prevent these occurrences. [4,5] The energy production from renewable sources and its storage are two technologies closely intertwined, and energy storage is only advantageous if there are low-cost, intermittent energy sources available. The batteries technologies nowadays are the most commercial-efficient answer to the storage problem, and this explain why they are widely used in electric and hybrid vehicles as well as in portable devices. In light of this, it is reasonable to believe that, regardless the discussed limits, this technology will continue to grow and improve. [4,7]

1.1.4 HYDROGEN AS STORAGE ALTERNATIVE

In the discussion about the energy storage from intermittent renewable sources, beside batteries, hydrogen has played a leading role, especially in recent years. When hydrogen is commonly mentioned, we refer to the colourless and odourless gas composed of two

hydrogen atoms (H_2). Hydrogen was discovered in 1766 by Henry Cavendish and the name ‘hydrogen’, which derives from Greek and means ‘water generator’, was later assigned to the element by Antoine-Laurent Lavoisier. The hydrogen atom is the most widespread element in the universe, and it is also the third most abundant on Earth. However, it is typically found bonded to other elements, such as in water and in hydrocarbon compounds, where hydrogen atoms are bonded to oxygen or carbon atoms. Hydrogen gas, on the other hand, used for energy purposes, does not naturally exist on Earth and therefore cannot be extracted like coal, methane, or oil. Therefore, this gas, which is often highlighted as a key player and starting point for energy transition, must be produced.[7] These days, there are two commercially available sources of hydrogen: the first is fossil fuels, and the second is water. Coal, oil, and natural gas can be decomposed under specific conditions to produce hydrogen and, in most cases, carbon dioxide. A process widely used is, for example, *the reforming* which increases the octane level within a hydrocarbon mixture and has hydrogen gas as a byproduct. This approach, naturally, is of limited interest because it maintains dependence on fossil fuels, which is why hydrogen produced in this way is called grey hydrogen. The process of producing hydrogen form water, on the other hand, is clean but requires an energy source in the form of electricity. If this electricity is generated from clean and renewable sources, the hydrogen produced is called green hydrogen. This process is known as water electrolysis, and its only products are gaseous hydrogen and oxygen. [7,8] Since hydrogen is produced by harnessing other energy sources, it is not a primary energy source but an energy carrier. This characteristic makes it excellent for storing energy from renewable and nuclear sources. Given the intermittent nature of renewable sources, storing the surplus energy in form of hydrogen would allow to have an energy carrier available for use when renewable production decreases. As for nuclear energy, its strength lies in its continuous and constant energy production, but this creates a similar problem to that of renewables sources. Energy demand is not constant and steady throughout the year, so during periods of low demand, the energy produced by the nuclear plant could risk being wasted or sold at very low prices. Hydrogen, as an energy carrier, in this scenario, could be useful to store the excess energy produced and exploiting it during peak demand would also help to keep the price of nuclear energy stable.[4] Concerning the exploitation of hydrogen, this gas is extremely flammable and can be burned like fossil fuels, but with just water as a by-product. However, the most efficient use method involves the fuel cells. Fuel cells are advanced electrochemical devices that generate electricity through a chemical reaction between hydrogen and oxygen, producing only water and heat as byproducts. Unlike

traditional combustion engines, fuel cells operate silently, have high efficiency (about 70-80%), and produce zero emissions at the point of use, making them an attractive option for clean energy applications. They are exploited in several sectors, including transportation, stationary power generation, and portable devices, offering a promising solution for reducing reliance on fossil fuels and mitigating environmental impact. Their versatility and efficiency make them a key technology in the transition to sustainable energy systems, therefore fuel cell technology is at the base of most hydrogen car. Unfortunately, despite its numerous and promising advantages, hydrogen has several issues that limit its applications. Although the energy contained in hydrogen molecule is much higher than that in any fossil fuels, the density of the gas is very low ($d_{H_2\ gas}$= 0.084 $g \cdot L^{-1}$, $d_{H_2\ liquid}$=70,8 $g \cdot L^{-1}$, T=298K, P=1 atm), so its transport and storage involve managing large volumes or high pressure. Below some data that may clarify why the issue of hydrogen as a plausible alternative energy vector to traditional fossil fuels represents a complex problem. The energy per unit mass released by the combustion of hydrogen is about three times that released by gasoline. At the same time, the energy per unit volume released by the combustion of gaseous hydrogen is extremely lower than that released by gasoline (about 1/2650). On the other hand, the energy per unit volume released by combustion of liquid hydrogen is about 1/3.4 times that released by gasoline.[4] Storing or transporting hydrogen under pressure requires additional energy, and converting stored hydrogen into electricity via fuel cells incurs a cost (with a loss of about 20-30%). Considering this, it can be concluded that the energy storage cycle based on hydrogen involves significant losses (about 50% of the initial electrical energy). For this reason, it is crucial to minimize critical steps, such as by planning for local production and use or within short distances, like small home hydrogen production reactors. [4,7] Public transportation, for example, with its fixed daily routes, would require fewer production and refuelling stations, making hydrogen-powered shuttles and buses ideal candidates for the purpose. The same argument can be extended to ships, heavy vehicles, and airplanes, which are unlikely to use batteries in the same way as our cars or scooters do. The future of hydrogen is extremely promising if we menage to overcome these technical issues that have so far limited its widespread adoption.[4]

1.1.5 AMMONIA AS HYDROGEN SOURCE

Most recently, alongside hydrogen itself as potential candidate for storing excess energy produced by intermittent renewable sources, attention has also been turned to ammonia. Ammonia is an organic molecule composed of one nitrogen atom and three hydrogen atoms (NH_3), which is already widely used commercially to produce industrial fertilizers. Ammonia, being an energy carrier as well, could potentially be an ideal candidate for the role because its dual nature. On one hand, it can be used as a fuel, like natural gas, through a combustion process, on the other hand and more conveniently, it can be used as a method of hydrogen storage, which, as previously discussed, requires high pressure or large volume. Ammonia can be conveniently liquefied at ambient temperature and pressure of 0.86 MPa, or at atmospheric pressure with a cooled-down temperature of -33.4°C and can therefore be transported in liquid form much more easily and safely. Moreover, NH_3 with a volumetric energy density of 12.7 MJ L^{-1} highly outperforms liquid hydrogen (8.49 MJ L^{-1}) and compressed gas (4.5 MJ L^{-1} at 69 MPa and 25°C).[9] Only once needed, in situ, ammonia can be exploited to release hydrogen through specific catalyst. Currently, interest in ammonia as a mean of hydrogen storage is still moderate but is expected to grow enormously in the upcoming years. [9,10]

At this point, it is necessary to take a step back. It has been discussed the role of hydrogen and ammonia as ideals candidates for storing energy from renewable sources, but as previously highlighted, molecular hydrogen, when intended for energy purposes, is present on Earth in negligible amounts and ammonia as well. This means they must be produced.

1.2 HYDROGEN PRODUCTION

Green hydrogen refers to hydrogen produced through environmentally friendly processes that do not emit greenhouse gases, and it is considered a key component in the transition to a sustainable and decarbonized society. Several methods are currently being studied and optimized to produce hydrogen from water, each present its advantages and challenges to be overcome. [11,12] The most historically relevant is the electrolysis method. Electrolysis is a chemical process that uses electricity to drive non-spontaneous reaction. The discovery of this phenomenon dates to the early 19th century and it can be tied to the development of modern chemistry. [11,13] The process was first observed in 1800 by British scientists William Nicholson and Anthony Carlisle, who exploited the first chemical battery, a voltaic pile, to

split water into hydrogen and oxygen. This preliminary approach demonstrated the potential of using electricity to drive chemical reactions. Soon after, in 1807 Sir Humphry Davy deepened this work, using electrolysis to separate and study several elements. His pioneering experiments laid the groundwork for understanding the powerful role of electrical energy to isolate elements from their compounds. Later, in 1830s Michael Faraday solidified electrolysis as a fundamental process in both chemistry and industry by formulating the electrolysis low, that quantitatively described the existing relationship between the amount of substance produced at an electrode and the amount of electric charge passed through the electrolyte. These days, electrolysis is the most common and commercially viable method for producing green hydrogen. The process occurs in an electrolyser, where trought the use of electricity the water is splitted into hydrogen at the cathode and oxygen at the anode which are separated by an electrolyte. Several types of electrolysis system have been developed in these recent years; proton exchange membrane (PEM) based system for example use a solid polymer electrolyte to conduct protons from the anode to the cathode of the electrolyser. It operates at high efficiency, and it is largely applied for storage renewable energy sources like wind and solar. Alkaline electrolysis instead, utilizes a liquid alkaline electrolyte (typically potassium hydroxide), is a well-established technology and it is less expensive that PEM technology but has lower efficiency. Solid oxide electrolysis (SOE) system, the last electrolysis technology type, operates at high temperatures (around 700-1000°C) and uses a solid ceramic electrolyte. SOE has the potential for very high efficiencies and can be integrated with high-temperature heat source, but it is still in the early stages of development. The three electrolyser described are outlined in fig.1.[14],[15]

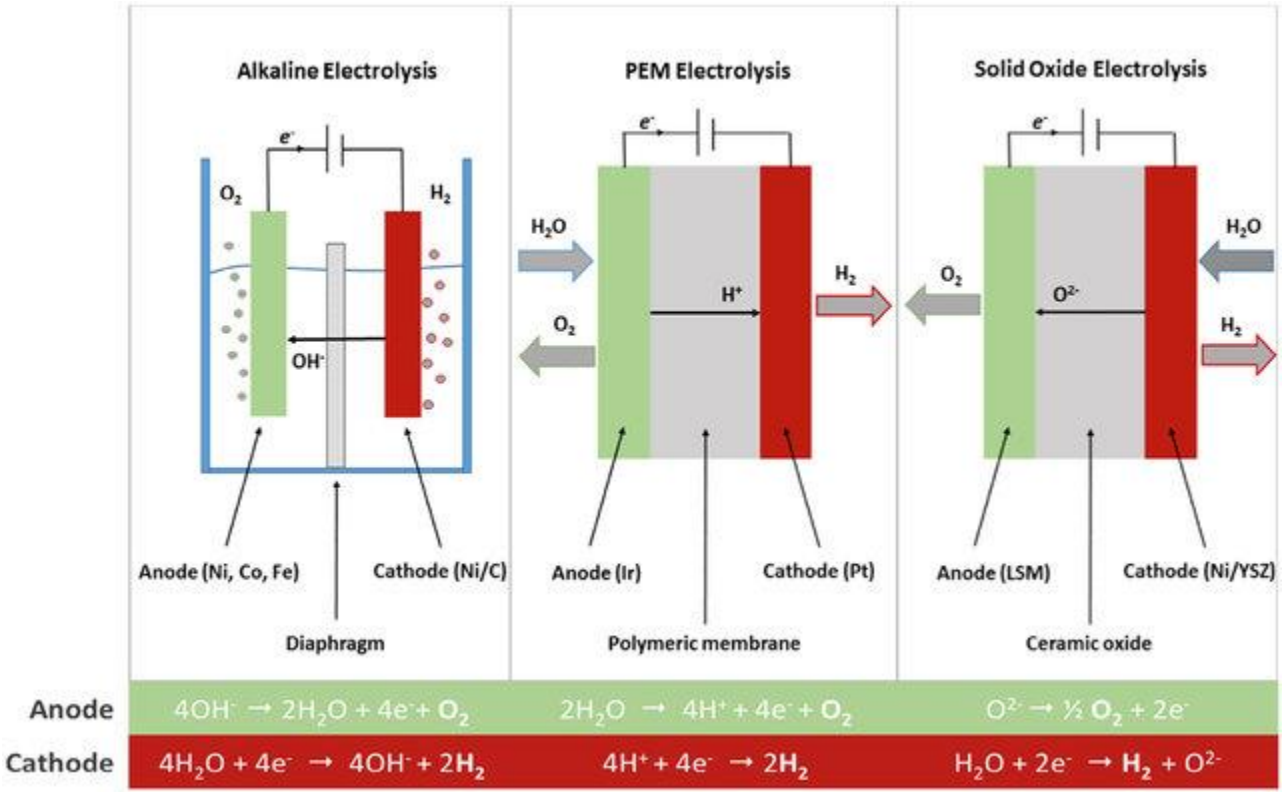

Fig.1. Operational principles of alkaline, PEM (proton-exchange membrane) and solid oxide water electrolysis. The overall reaction is $H_2O \rightarrow H_2 + ½\ O_2$. Oxygen evolution occurs at the anode, hydrogen evolves at the cathode.[14]

The second method of green hydrogen production in terms of exploitation is biomass gasification. Biomass gasification involves the conversion of organic materials, such as agricultural waste, wood chips, or dedicated energy crops, into hydrogen. This process consists in heating the biomass in the presence of a controlled amount of oxygen, producing a mixture of gases, including hydrogen, carbon monoxide, and carbon dioxide. Hydrogen can be separated from this mixture through a process called ‘water-gas shift reaction’. Biomass gasification can be carbon-neutral or even carbon-negative if combined with carbon capture and storage (CCS). However, its widespread use is still limited due to challenges in feedstock collection, processing, and efficiency compared to electrolysis.[16][17] In figure 2 is reported a general scheme representing the biomass gasification process.

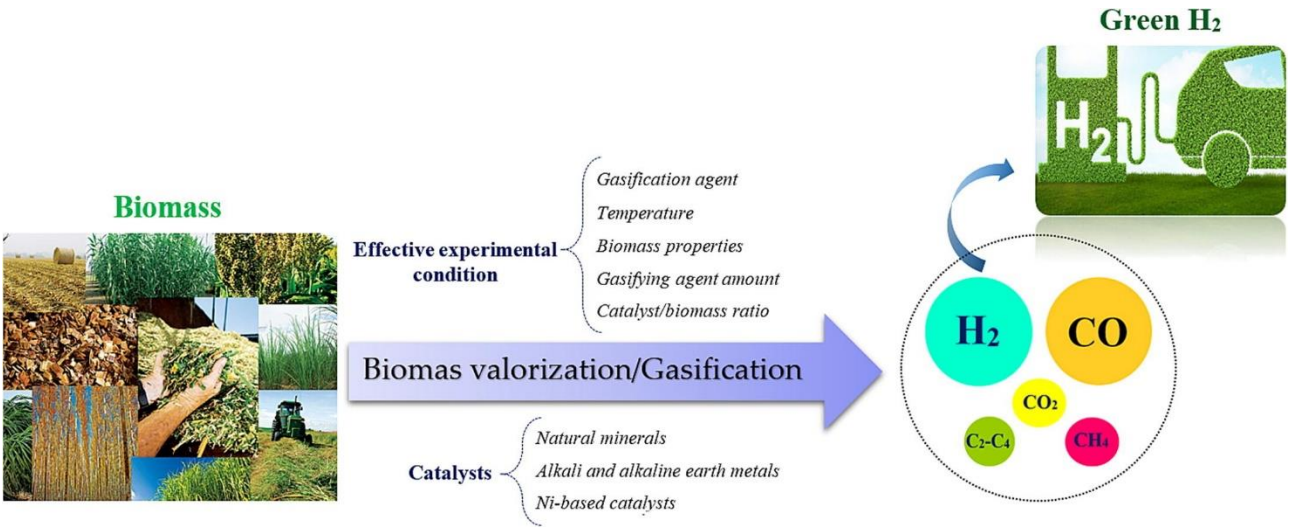

Fig. 2. Schematic representation of Biomass valorisation/gasification process towards green hydrogen production. Reprinted with permission from ref [17]. © *2022 Elsevier Ltd.*

Photocatalytic (PC) and Photoelectrocatalytic (PEC) water splitting for green hydrogen production are still low commercially exploited methods since are both in technological development. Photocatalysis involves the use of sunlight directly to drive the chemical reaction that splits water into hydrogen and oxygen, bypassing the need for electricity, imitating what happens in plats through the mechanism of photosynthesis.[18] The roots of photocatalysis can be traced back to the 19th century, when scientists first observed the effects of light on chemical reactions. One of the earliest notable discoveries occurred in 1839, when Swiss physicist Alexandre Edmond Becquerel observed the "photovoltaic effect", which showed how light could induce electrical currents in certain materials. Though this was not directly related to catalysis, it set the stage for future research into light-driven chemical processes. The formal discovery of photocatalysis occurred in the mid-20th century. In 1938, the German scientist Gerhard Jahn and his colleagues demonstrated that titanium dioxide (TiO_2) could act as a catalyst in photochemical reactions. However, the concept of photocatalysis did not fully take off until decades later when the key discovery was made in the early 1970s. In 1972, Akira Fujishima and Kenichi Honda published a landmark paper demonstrating the "Honda-Fujishima effect." They discovered that titanium dioxide could split water into hydrogen and oxygen under ultraviolet light, a reaction now known as photoelectrochemical water splitting. This groundbreaking discovery highlighted the potential of photocatalysis for hydrogen production, a clean energy source, and catalysed significant interest in the field of solar energy conversion.[19] The photocatalytic water splitting process involves semiconductors materials, preferably nanostructured, that

absorb sunlight and initiate on its surface the water reduction and oxidation reaction, being the photocatalyst thinly dispersed in the aqueous medium. Photocatalysis offers the potential for direct hydrogen evolution with low energy input and costs, making it a highly attractive option for future green hydrogen production. The method currently suffers from low efficiency and the need for more durable and efficient photocatalysts. Research is ongoing to develop materials that can enhance the process and make it viable for large-scale use.[18,20] PEC water splitting involves a more complex system compared to the PC, demanding a photoelectrocatalytic cell, where the semiconductor materials are deposited onto electrodes and immersed in water media, once the circuit cell is closed the recorded photocathodic current corresponds to the amount of hydrogen produced. In figure 3 is reported the general scheme and the configuration of the two systems, (a) outlines a tandem photoelectrochemical cell and (b) a photocatalytic system in suspension set up. The technology is still in the experimental stage, with challenges including the stability of materials, the need for efficient and cost-effective semiconductors, and scaling up for large-scale production.[21]

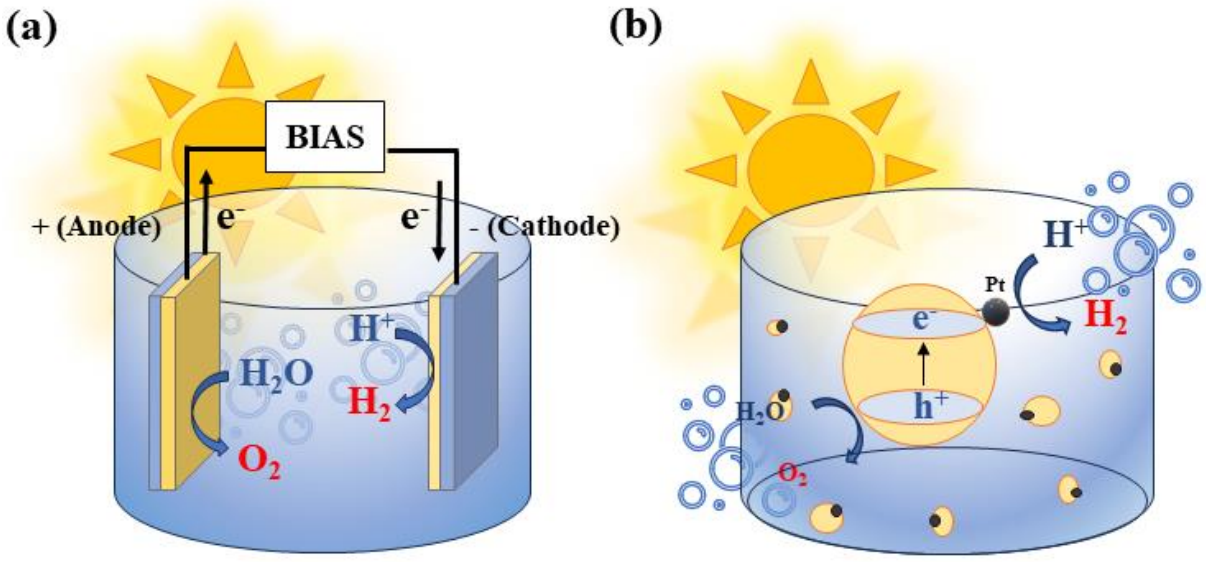

Fig. 3. (a) Proposed mechanism of solar hydrogen production by tandem (both cathode and anode are photoactive) photoelectrochemical devices (PEC); (b) solar hydrogen production by photocatalytic devices (PC).

Thermochemical or thermal water splitting is the less exploited hydrogen production method, still being in a young experimental phase. It is a promising technology for sustainable hydrogen production by breaking down water (H_2O) into its components, hydrogen (H_2) and

oxygen (O_2), using high-temperature heat. This process is typically driven by concentrated solar energy, nuclear energy, or other heat sources, making it a potential key player in future clean energy systems, as reported in the schematic illustration in fig 4.[22] The concept of thermal water splitting leverages heat to overcome the energy barrier required to break the water molecules and it differs from traditional electrolysis, which uses electricity to run the reaction of splitting of water. Instead, here thermochemical cycles are used, where water undergoes multiple chemical reactions involving intermediary compounds.

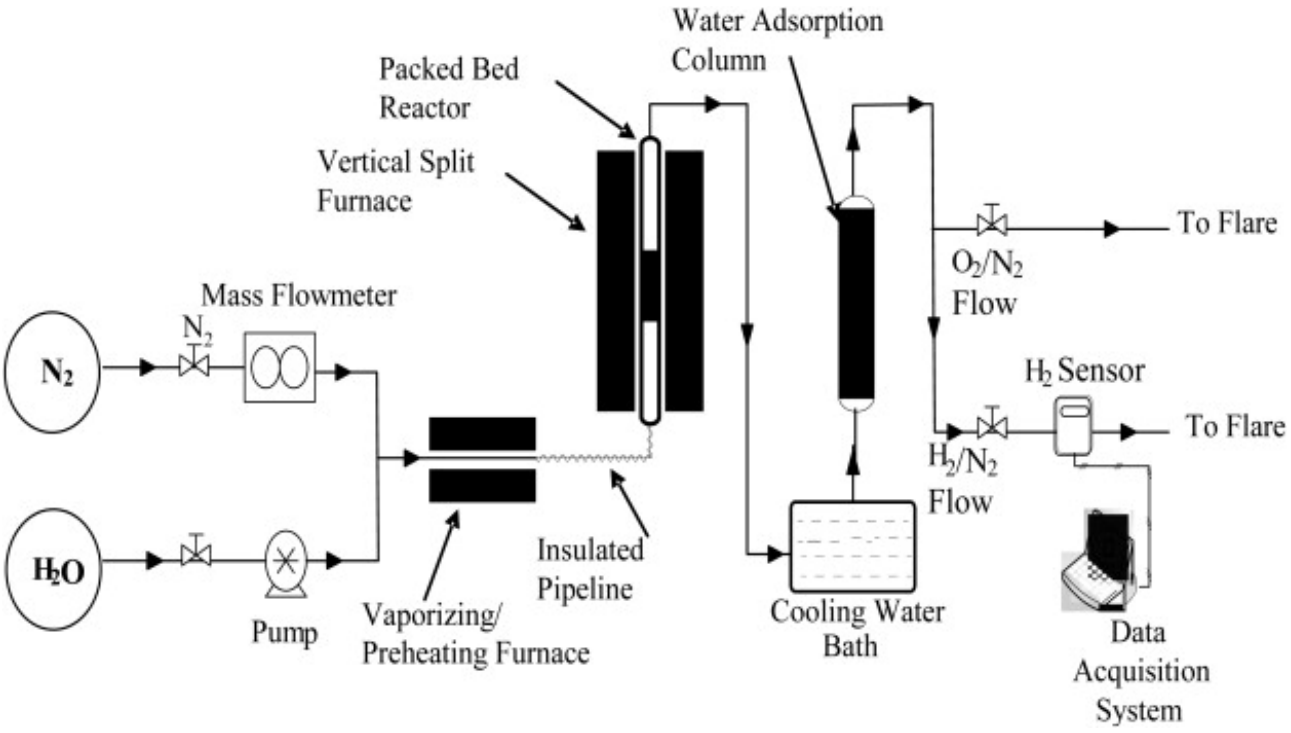

Fig. 4 Thermochemical water-splitting reactor set-up for H_2 generation.[22] Reprinted with permission from ref [21]. *Copyright © 2011 Hydrogen Energy Publications, LLC. Published by Elsevier Ltd.*

Concentrated solar power (CSP) or nuclear reactors are often considered as potential heat sources for thermochemical cycles. The main challenges include the need for very high temperatures (often above 800°C), the development of stable and efficient materials that can withstand these conditions, and the complexity of the chemical cycles involved. While thermochemical water splitting has high theoretical efficiency, it remains in the experimental stage, and significant challenges must be overcome before it can be deployed at a commercial scale. [22–24]

2. PHOTOCATALYTIC HYDROGEN AND AMMONIA EVOLUTION

The focus of the present work has been channelled towards the exploitation of Photocatalytic and Photoelectrocatalytic water media splitting methods for green hydrogen production and Photocatalytic nitrogen fixation towards green ammonia production as hydrogen precursor. As already mentioned, photocatalytic water splitting is fundamentally an artificial photosynthesis process in which a photocatalyst absorbs sunlight and initiates a series of reactions that ultimately produce hydrogen and oxygen from water, outlined in figure 5.[25]

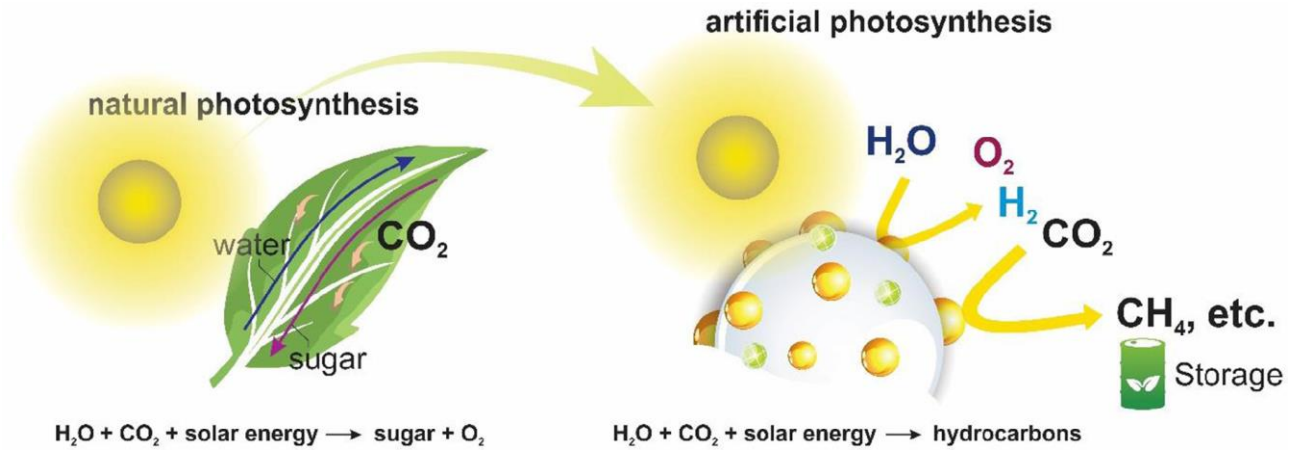

Fig.5. Conversion of solar energy: natural leaf and mimicking photosynthesis in artificial system via photocatalysis.[25] Reprinted with permission from ref [24]. © *2020 Elsevier B.V.*

The ability to harness solar energy through photocatalysis offers the potential for producing renewable hydrogen on a large scale, with water as the sole feedstock and sunlight as the energy input. Despite the significant potential of photocatalytic water splitting, there are numerous challenges that must be addressed to improve its overall efficiency and scalability. Key obstacles include the development of highly efficient photocatalysts capable of utilizing the full spectrum of sunlight, particularly the visible range, minimizing charge recombination rate, and optimizing reaction conditions to facilitate large-scale hydrogen production. Researchers are exploring a variety of materials, including metal oxides, sulphides, and nitrides, as well as co-catalysts and nanostructures, to enhance the photocatalytic performance. [18,26] At the same time, as we already mentioned above, parallelly to the photocatalytic water splitting process for hydrogen production, photocatalytic nitrogen

fixation for ammonia production is gaining attention as practical alternative more convenient way to hydrogen storage. Photocatalytic nitrogen fixation process utilizes nitrogen and water as reagents, with sunlight as the energy source, to produce ammonia, and thus can be considered both an environmentally friendly and energy-saving process. The photocatalytic mechanism starts when N_2 is chemisorbed on the photocatalyst surface, and it is activated. Then the semiconductor is excited by solar light irradiation, resulting in the formation of photogenerated electrons and holes that move, respectively, to the conduction band (CB) and the valence band (VB). Finally, after migrating to the surface of the catalyst, the photogenerated electrons reduce N_2 to NH_3, while the holes oxidize H_2O to O_2, see figure 6 for the simplified mechanism diagram.[27]

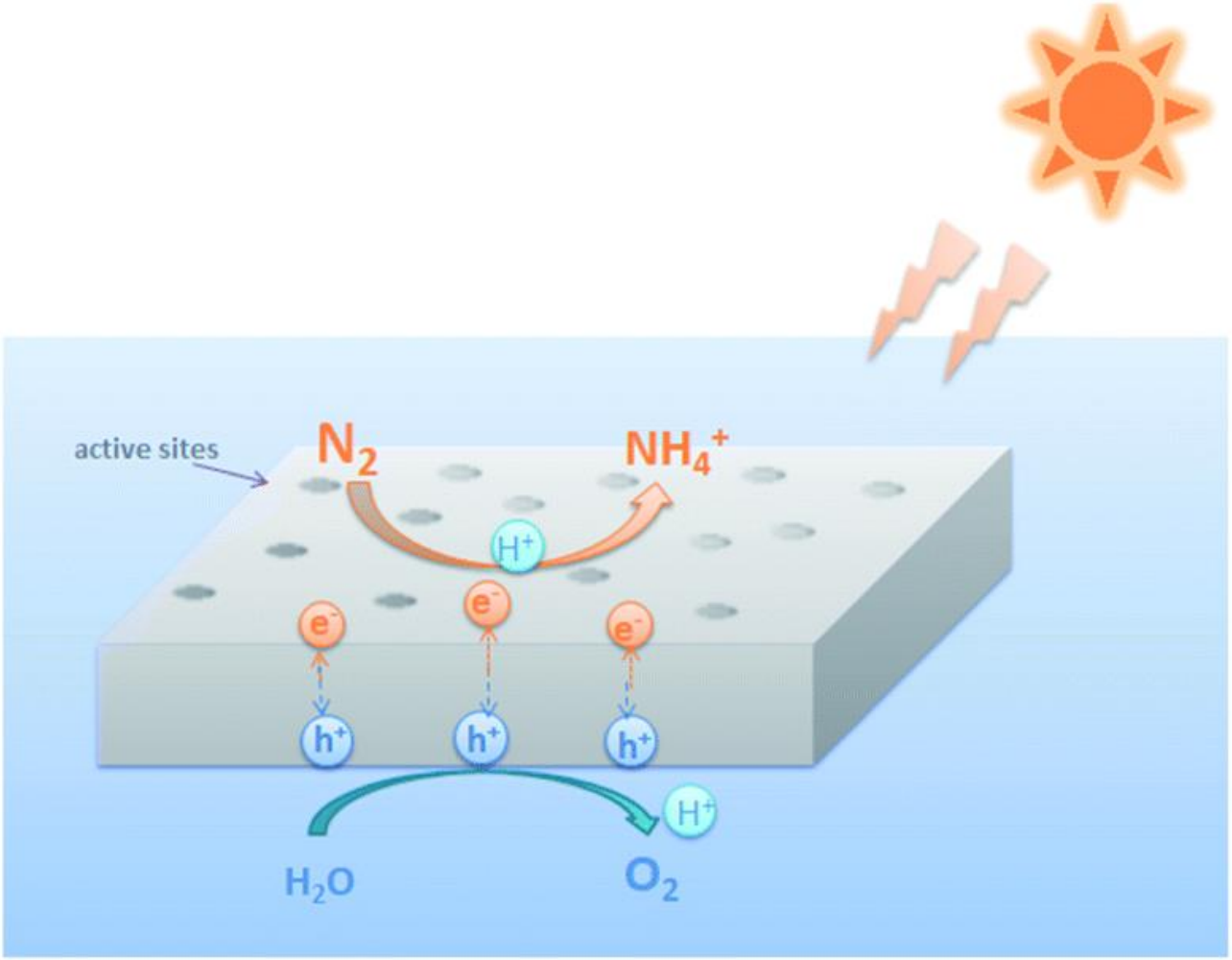

Fig.6 A simple diagram of photocatalytic nitrogen fixation.[27]

The semiconductor's band gap should be narrow enough to utilize a broader range of the solar spectrum, while large enough to have CB energy level more negative than N_2 reduction potential and VB energy level more positive than water oxidation potential to allow both the nitrogen reduction reaction (NRR) and the oxygen evolution reaction (OER). The photocatalyst should also be, ideally, highly selective toward the ammonia synthesis, because, in protic solvents, the hydrogen evolution reaction (HER) is likely to compete with the NRR: this happens because HER requires fewer electrons.[27] In this thesis, we will explore the advancements in photocatalytic materials and processes for efficient hydrogen and ammonia production from aqueous media. Here, the focus will be on understanding the underlying mechanisms governing photocatalytic activity, optimizing material properties, and addressing the main interest into the fundamental research related to the exploration of novel materials and composites slightly exploited before. By advancing our understanding of photocatalytic water splitting and photocatalytic nitrogen fixation, this research aims to contribute to the development of clean, renewable hydrogen energy solutions.

2.1 PHOTOCATALYSTS FOR HYDROGEN AND AMMONIA EVOLUTION

The choice of semiconductor material is crucial in determining the efficiency and feasibility of hydrogen and ammonia evolution reaction, as it directly influences the absorption of light, charge separation, and surface catalytic reactions. Over the past few decades, significant progress has been made in the development and optimization of photocatalytic semiconductor materials, and still several challenges remain. This section discusses the current state of the art in semiconductor materials for hydrogen and ammonia evolution, focusing on their properties, limitations, and recent advancements.[15,26,27] Titanium dioxide (TiO_2) is one of the most extensively studied and widely used photocatalysts for water splitting for green hydrogen evolution due to its chemical stability, low cost, non-toxicity, and abundance.[28] Thanks to the fame gained in the water splitting field, TiO_2 is been recently extensively studied also as semiconductor-base for composites photocatalysts for N_2 fixation.[29–32] TiO_2 operates as an effective photocatalyst under ultraviolet (UV) light, where it absorbs photons and generates electro-hole pairs. However, its wide bandgap (~3.2 eV) limits its activity to only a small portion of the solar spectrum (UV light accounts for only ~4% of sunlight), which severely restricts its efficiency in hydrogen production under visible light conditions. To overcome this limitation, various strategies have been explored to extend the light absorption of TiO_2 into the visible region. These strategies include doping with metals

(e.g., Pt, Au) and non-metals (e.g., nitrogen, carbon, sulphur), coupling with narrower-bandgap semiconductors, and forming TiO_2-based heterojunctions. Despite these modifications, achieving high hydrogen evolution efficiency under visible light remains a challenge, making TiO_2 suitable primarily for UV-driven applications. [26,28] Recent advancements have also explored semiconductor alloys and nanomaterials, such as GaN-ZnO and ZnS-CdS, to optimize the bandgap for visible-light absorption and reduce charge carrier recombination through engineered heterostructures. These nanostructured materials, combined with surface co-catalyst, have demonstrated enhanced efficiency in photocatalytic hydrogen and production, paving the way for future breakthroughs in this field. [18,20] Among these materials, cadmium sulphide (CdS) has shown potential photocatalytic performances due to its narrow bandgap (~2.4 eV), which allows it to absorb visible light more effectively than TiO_2. Under visible light irradiation, CdS can efficiently generate electron-hole pairs and participate in water splitting reaction. However, the use of CdS is hindered by its susceptibility to photo-corrosion and toxicity, which raises environmental concerns and limits its practical applications.[33] To address the stability issues of CdS, researchers have focused on the development of composite materials, coupling CdS with more stable semiconductors or co-catalysts such as noble metals (e.g., Pt, Au) or metal oxides (e.g., TiO_2, ZnO). These hybrid systems can enhance the stability of CdS and improve all the photocatalytic characteristics to higher hydrogen evolution rates. Despite these improvements, the toxicity of cadmium remains a significant barrier to its large-scale application in photocatalysis. [33,34] Also, bismuth vanadate ($BiVO_4$) has gained attention as a visible-light-responsive photocatalyst due to its relatively narrow bandgap (~2.4 eV), which enables it to absorb a substantial portion of the solar spectrum. $BiVO_4$ shows good stability in water splitting, especially for the oxygen evolution reaction (OER), but its performance in hydrogen evolution is limited by poor charge carrier mobility and short charge diffusion lengths.[35] Recent efforts to enhance the hydrogen evolution efficiency of $BiVO_4$ include doping with metals (e.g., W, Mo) to improve charge carrier separation, as well as forming heterojunctions with other semiconductors, such as TiO_2, WO_3, or g-C_3N_4. These modifications have led to enhanced photocatalytic activity and better stability under visible light, although the hydrogen evolution efficiency still requires further optimization.[36] Among the organic photocatalyst, graphitic carbon nitride (g-C_3N_4) is the non-metallic polymeric semiconductor that has attracted the main interest due to its visible light activity, chemical stability, and earth-abundant nature.[37] With a bandgap of approximately 2.7 eV, g-C_3N_4 can absorb visible light and generate electron-hole pairs for hydrogen production. Its layered

structure also provides a high surface area for reactions, making it an attractive candidate for photocatalytic water splitting. [37,38] Moreover, g-C_3N_4 is characterized by the presence of a high density of nitrogen vacancies, V_N, that are well known to be the most suitable active sites for N_2 fixation for NH_3 production, together with oxygen and sulphur vacancies. Tuning the density of these vacancies through several synthetic approaches led g-C_3N_4-based materials to the top of the best performative photocatalyst for green NH_3 production. [39,40] However, the photocatalytic efficiency of g-C_3N_4 is limited by rapid recombination of charge carriers and poor charge transfer kinetics. To overcome these challenges, several strategies have been employed, including surface modification, heterojunction formation with other semiconductors (e.g., TiO_2, ZnO), and doping with metals or non-metals. [38,41,42] These approaches have led to significant improvements in both hydrogen and ammonia evolution efficiency, although further work is needed to achieve practical levels of performance. Interesting and innovative perovskite materials, with the general formula ABX_3, have already largely emerged as highly promising candidates for solar energy applications in photovoltaic systems, and recently also for hydrogen production through water splitting.[43] Their tunable bandgap, excellent light absorption properties, and efficient charge transport characteristics make them highly versatile for several photocatalytic applications. Perovskites can effectively split water into hydrogen and oxygen, degrade pollutants, participate in CO_2 reduction reactions, and recently showed also interesting and unprecedented active role in nitrogen fixation, making them promising materials for energy conversion and environmental remediation. [44–47] Their versatility, along with their ease of fabrication, makes them an exciting focus for research in the field of sustainable energy technologies. Among the various perovskites studied, lead-based halide perovskites (e.g., $CH_3NH_3PbI_3$) have demonstrated impressive hydrogen production capabilities under visible light.[48] Despite their high efficiency, the practical application of perovskite photocatalysts is challenged by their instability in aqueous environments and the toxicity (especially with lead-based perovskites) need to be addressed for practical applications. Researchers are actively exploring new perovskite compositions and surface passivation techniques to improve stability and reduce environmental concerns. Alternatives, such as lead-free perovskites (e.g., tin-based perovskites), are also being investigated, although they typically exhibit lower efficiencies than their lead-based counterparts.[49,50] Metal organic frameworks (MOFs) are another class of materials recently exploited for hydrogen production that combine organic ligands with metal ions to form porous structures with high surface areas.[51] MOFs have shown promise as photocatalysts due to their tunable electronic properties, large surface areas for

catalysis, and ability to incorporate various catalytic sites. Some MOFs have demonstrated visible light activity for hydrogen production, particularly when coupled with metal nanoparticles or semiconductor materials. While MOFs are still in the early stages of development as photocatalysts for hydrogen evolution, their modular structure and versatility offer significant potential for future advancements. Researchers are working to improve the charge transport properties of MOFs and develop more stable and efficient MOF-based photocatalytic systems. [51,52] Organic semiconductors (OSs) are the most recent class of photocatalysts that researcher approached for photocatalytic hydrogen production applications. The OSs materials class are extremely famous thanks to the organic solar cells systems, a specific class of solar cell, that exploits a variety of organic semiconductors, both molecules and polymer, as photoactive material in alternative to the classic inorganic ones. Indeed, in recent years, OSs have received increasing attention in the field of photoelectrocatalysis first and photocatalysis in suspension set up then, thanks to the favourable interaction of OSs with liquid electrolytes compared to inorganic semiconductors. OSs materials showed remarkable results in terms of H_2 production rate when exploited in heterojunction nanoparticles, and as widely demonstrated for photocatalytic application, also for photoelectrodes in PEC the most suitable and performative architecture is the exploitation of electron donor/acceptor organic materials in bulk (BHJ) or layered heterojunction (LHJ). The main difference between BHJ and LHJ lies in the physic contact between the two semiconductor that allows a more effective electron transfer from the electron donor/acceptor and increase the photocatalytic performances when the two photoactive materials are mixed in the bulk phase, proving that this configuration is more efficient most of the time for both PEC and PC hydrogen production. [53–56]

2.2 STRATEGIES TO IMPROVE PHOTOCATALYTIC PERFORMANCE

The heterojunction system realization between two or more semiconductors has emerged as powerful and important approach to enhance photocatalytic performance. As we already explained, photocatalysis is often limited by the intrinsic properties of a single semiconductor.[57] By combining two or more semiconductors, with staggered energy levels, is possible to form heterojunction phase, which can improve charge separation, reduce recombination rates of electron-hole pairs, expand the light absorption range, and tuning the redox properties ultimately boosting the efficiency of photocatalytic systems.[57,58] The

development of heterojunction systems is primarily driven by the inherent limitations of single semiconductor photocatalysts. Historically, photocatalysis research has been dominated by materials like titanium dioxide (TiO_2) due to its stability, low cost, and non-toxicity. However, TiO_2 as we already know has a wide bandgap (~3.2 eV), meaning it can only absorb UV light, which comprises about 4-5% of the solar spectrum. This severely limits its efficiency in utilizing sunlight for photocatalysis. [58,59] In addition to the restricted light absorption, single semiconductors tend to suffer from rapid charge carrier recombination where the photogenerated electron-hole pairs often recombine before participating in redox reactions, reducing the overall photocatalytic efficiency. The limited redox potential is another important obstacle since some reactions, such as water splitting for hydrogen production, N_2 photofixation or CO_2 reduction, require specific redox potentials that single semiconductors cannot achieve due to their fixed energy band positions.[26,57,58] In the light of this, by combining semiconductors with different bandgaps, heterojunctions can utilize a broader spectrum of sunlight, including visible light. Moreover, the staggered energy levels in heterojunctions facilitate the separation of photogenerated electron-hole pairs, reducing recombination and increasing their lifetime. Different materials in a heterojunction can be chosen to achieve desired redox potentials, enabling efficient participation in target photocatalytic reactions. [57,58] Under the theoretical framework, heterojunctions are formed when two semiconductors with different electronic properties are brought into contact. The key concept regarding heterojunction systems is the alignment of their energy bands, the conduction and the valence bands. This alignment dictates how photogenerated charge carriers, electrons and holes, will behave at the interface, which is crucial for enhancing photocatalytic efficiency. The alignment of energy bands between two semiconductors is characterized by their conduction band minima (CBM) and valence band maxima (VBM). [57,60] Depending on the relative positions of these bands, heterojunctions are categorized into four main types: Type I (Straddling Gap), where both the conduction and valence bands of one semiconductor are enclosed by the energy gap of the other semiconductor. This promotes the transfer of both electrons and holes into the same semiconductor, resulting in an efficient charge carrier confinement. The well-aligned energy levels promote efficient charge transfer, leading to improved photocatalytic activity. These junctions are often used when the goal is to confine charge carriers in one material to maximize their interaction with reactants. However, despite better charge separation, Type I junctions may lead to recombination issues unless well-engineered. In the Type II (Staggered Gap) the conduction band of one semiconductor is lower than the other, and the valence band is higher. This

facilitates spatial separation of electrons and holes, electrons are transferred to one semiconductor, and holes to the other. The spatial separation of charge carriers significantly reduces recombination rates, leading to longer carrier lifetimes and enhanced photocatalytic performance. This type is particularly effective for reactions that require extended electron-hole separation, such as water splitting for hydrogen evolution, N_2 fixation for ammonia production or CO_2 reduction to CH_4. This configuration is highly effective in reducing recombination and extending the lifetime of charge carriers, making it ideal for enhanced photocatalysis. While charge separation is improved, this configuration may reduce the redox potential of the system, potentially limiting its ability to drive highly energetic reactions. In the Type III (Broken Gap) the conduction band of one semiconductor is higher than the valence band of the other, creating a large potential difference. This strong driving force for charge separation can further enhance the efficiency of photocatalysis by preventing recombination. The large potential difference can further enhance charge separation and prevent recombination, making it ideal for reactions requiring strong redox potential. This extreme separation may reduce the ability to drive certain reactions and make the design of such systems complex due to the need for well-matched band edges. The p-n heterojunction has gained great interest during these lasts years thanks to their fundamental role in the operation of diodes and transistors, building blocks of modern electronics. This type of systems is formed by the junction of a p-type, hole-dominated, and n-type, electron-dominated semiconductor, where the p-n heterojunctions create an internal electric field at the interface, which aids in the separation of electron-hole pairs. The built-in electric field naturally drives the separation of charge carriers, reducing recombination and enhancing the overall photocatalytic efficiency. The potential mismatch between the two semiconductors can sometimes limit charge mobility, and the redox potential may not be optimal for specific reactions. [58,60] The last heterojunction studied scheme is the Z-Scheme configuration. It is inspired by natural photosynthesis and involves charge transfer across two semiconductors where electrons move from the conduction band of one and recombine themselves with holes in the valence band of the other semiconductor. The remaining high-energy electrons and holes contribute to redox reactions, retaining strong redox potentials. This design retains high redox potentials while improving charge separation, leading to superior photocatalytic activity for processes like again, water splitting, N_2 photofixation and CO_2 reduction. The complex mechanism of charge transfer can be difficult to optimize, and Z-scheme systems typically require careful material selection and design to minimize

recombination and maximize efficiency.[61] The discussed heterojunctions schemes are outlined in figure 7.[60]

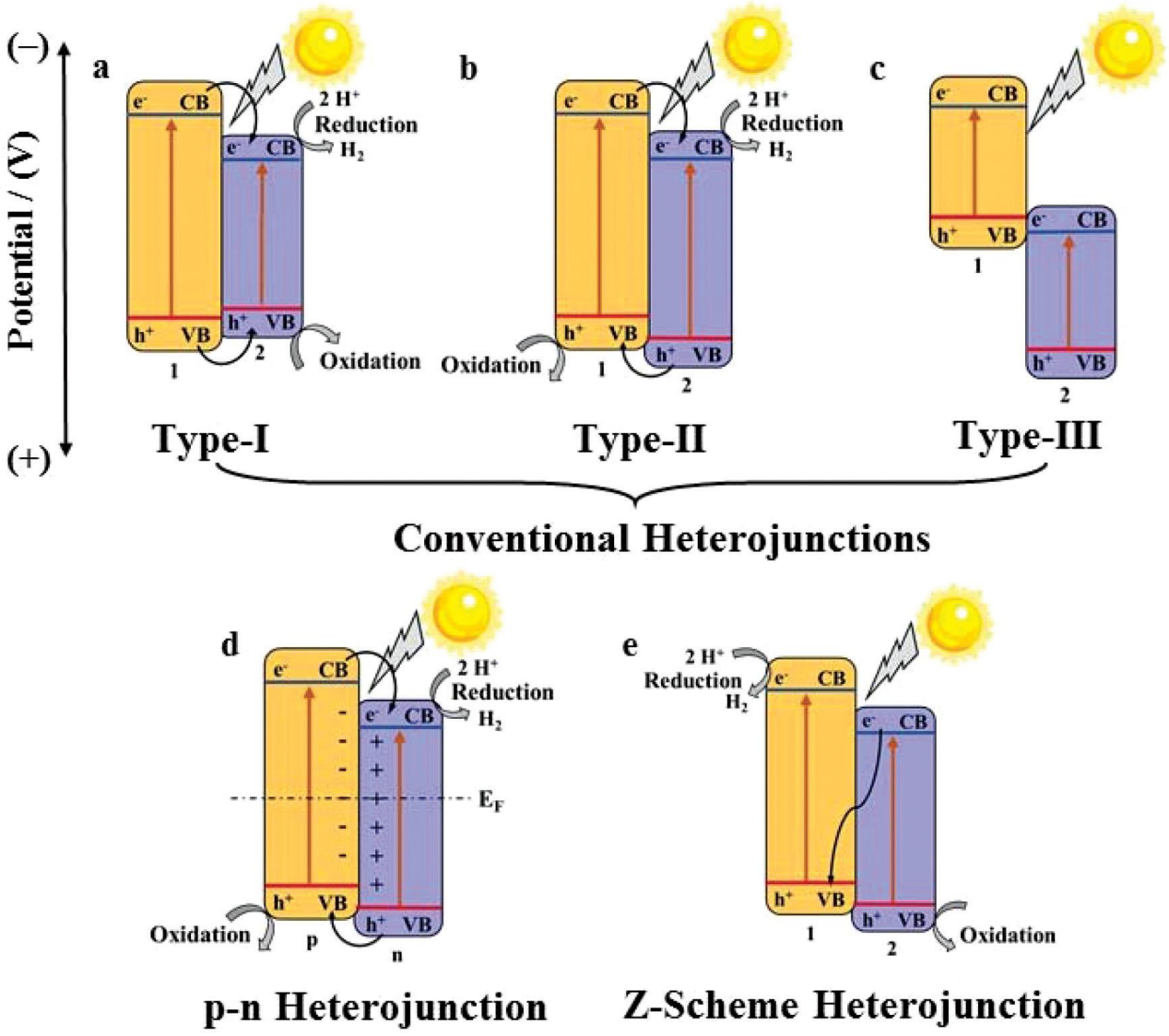

Fig. 7 Diagrams of Type-I (a); Type-II (b); Type-III (c), p–n heterojunction (d), Z-scheme (e) heterojunction. 1, 2, p, and n refer to semiconductor 1, semiconductor 2, p-semiconductor, and n-semiconductor, respectively.[59] Reprinted with permission from [58].

In this perspective, the primary advantage of heterojunctions is the enhancement of electron-hole separation, which is critical for effective photocatalysis. By spatially separating

charge carriers across different materials, the recombination rate is reduced, allowing for longer carrier lifetimes and more efficient participation in redox reactions. Combining semiconductors with different bandgaps can extend the range of light absorption, allowing for the utilization of a broader portion of the solar spectrum and this is particularly beneficial in harvesting visible light, which makes up a large portion of sunlight. Moreover, by carefully selecting materials, heterojunction systems can be designed to provide the desired redox potentials, which are essential for driving specific photocatalytic reactions. [57,58] However, designing heterojunctions requires precise matching of bandgaps, work functions, and electron affinities of the semiconductors involved. Improper material combinations can lead to poor charge transfer efficiency or misalignment of energy levels, which diminishes performance. At the heterojunction interface, defects or mismatches can act as charge carrier traps, which may increase recombination rates or reduce mobility, negatively impacting photocatalytic activity. Some heterojunctions require advanced fabrication techniques to create clean, defect-free interfaces and this can increase the cost and complexity of manufacturing, limiting their scalability for large-scale applications. Future advancements in material science and nanotechnology will likely play a key role in overcoming these hurdles, allowing heterojunction systems to realize their full potential in applications such as water splitting, green ammonia production, pollutant degradation, and CO_2 reduction.[58,60] At the same time, strategies beyond heterojunction formation between multiple semiconductors have been explored to improve the photocatalytic performance of materials.[26,62] Incorporating metal cocatalysts like platinum (Pt), ruthenium (Ru), or nickel (Ni) onto the semiconductor surface improves the photocatalytic performance by facilitating charge separation and lowering the activation energy for the targeted reactions.[62,63] This method is the largest widespread and effective since most of the famous photocatalyst exploited nowadays outperform in presence of Pt as cocatalyst.[65] These metal cocatalysts are particularly useful in reactions like water splitting, where they promote efficient hydrogen or oxygen evolution because the metal presence reduces overpotentials and accelerate redox reactions, boosting overall reaction rate.[64,66] Another important and largely exploited method is the defects creation such as oxygen, nitrogen, and sulphur vacancies or surface defects. These vacancies can tune the electronic structure of semiconductors and introduce mid-gap states that facilitate visible light absorption and increase the number of active sites for catalytic reactions, extremely important in reaction like N_2 or CO_2 fixation where the vacancy plays the active role for the adsorption of N_2 and CO_2 molecules and the consequent reduction to NH_3 and CH_4, respectively. [40] These defects act as electron traps,

reducing recombination and prolonging the lifetime of charge carriers. Moreover, vacancies and defects can enhance charge separation and prolong charge carrier lifetime, increasing catalytic activity. [62,67] A further exploited approach is the introduction of dopants into the semiconductor's crystal lattice that alters the electronic structure, potentially narrowing the bandgap and shifting the absorption spectrum into the visible light region. Metal ions such as Fe^{3+}, Co^{2+}, or Ag^{+}, and non-metals like N, C, or S, can be used.[68] Metal ion doping often introduces shallow impurity levels, reducing electron-hole recombination, while non-metal doping can enhance visible light absorption. The metal ion doping strategy facilitates charge separation and increases surface activity for redox reactions, while, the non-metal doping alters the electronic structure and optical properties, allowing the use of visible light.[69] Also, embedding noble metals like gold (Au), silver (Ag), or copper (Cu) into semiconductors can enhance photocatalytic efficiency through localized surface plasmon resonance (SPR).[70,71] These plasmonic metals can absorb visible light and generate hot electrons, which transfer to the semiconductor, enhancing photocatalytic activity in the visible light spectrum. Plasmonic nanoparticles act as sensitizers and electron reservoirs, improving light absorption and reducing electron-hole recombination.[72] The design and control of semiconductor morphology at the nanoscale, such as nanoparticles, nanorods, nanowires, and nanosheets, can significantly impact surface area, active sites, and light absorption and for these reasons is another largely used approach to increase the photocatalytic performances.[73] High surface area nanostructures provide more active sites for reactions, while tailored geometries can enhance light scattering and absorption.[74] Nanorods, nanotubes, or nanosheets are respectively 1D and 2D structures and promote directional charge transfer and increase active surface areas. At the same time, the hierarchical structures improve light harvesting by enhancing photon capture and scattering within the material.[75] From the photovoltaic materials field, dye sensitization is becoming an interesting approach also for photocatalytic systems to improve the photocatalytic efficiency. It involves coating semiconductor surfaces with organic dyes, such as porphyrins or ruthenium complexes, that absorb visible light and transfer photo-excited electrons to the semiconductor. [56,76] This method effectively extends the light absorption range and increases the photocatalytic performance under visible light. The dye molecules expand the light adsorption spectrum, enhancing activity under lower energy photons, visible light.[76] Dye sensitization has been largely studied in photovoltaic cells but remains mainly unexplored for photocatalytic process like water splitting or CO_2 reduction.[54] Another largely exploited approach is the incorporation of graphene or other carbon-based materials (e.g.,

carbon nanotubes or fullerenes) into photocatalytic systems to enhance performance due to their excellent electrical conductivity, large surface area, and ability to act as electron conductors. These materials improve charge carrier mobility and reduce recombination rates. Graphene-based composites facilitate rapid electron transport and increase the lifetime of photogenerated carriers.[78] Also applying an external electric field or utilizing ferroelectric materials can enhance the separation of photogenerated charge carriers by inducing polarization.[79] This effect reduces electron-hole recombination and increases the efficiency of photocatalytic reactions. The application of an electric field promotes charge separation and prolongs the lifetime of charge carries, improving photocatalytic efficiency.[80] Finally, altering the pH of the reaction environment or functionalizing the surface of photocatalysts with specific chemical groups can further enhance adsorption of reactants and optimize catalytic activity. Tailoring surface properties improves the interaction between the photocatalyst and reactants, leading to higher reaction rates, since surface functionalization increases catalytic activity by optimizing the adsorption of target molecules.[81] In conclusion, it is possible to affirm that enhancing photocatalytic performances requires a multifaceted approach that includes modifying the electronic structure, improving light absorption, and optimizing charge separation. Techniques like doping, nanostructuring, plasmonic enhancement, cocatalyst loading, and defect engineering are complementary strategies that, when combined, can result in significant improvements in photocatalytic activity beyond simple heterojunction formation.

3. PEROVSKITE-BASED MATERIALS FOR PHOTOCATALYTIC PURPOSE

Perovskite materials are named after the Russian mineralogist Lev Perovski by Gustav Rose who first discovered the natural mineral calcium titanate, $CaTiO_3$, in 1839.[82] This mineral opened the research for a broader class of materials with the same crystal structure, referred to as the "perovskite structure." The general formula for perovskites is ABX_3, where A is a larger cation typically an alkaline-earth or rare-earth metal, B is a smaller cation often a transition metal, X is an anion, usually oxygen in oxide perovskites or a halide in halide perovskites.[83] Oxide perovskites first and halide then have been extensively studied due to their wide variety of properties, including ferroelectricity, superconductivity, magnetism, and optoelectronic properties. Their unique crystal structure allows for diverse combinations of elements, resulting in tunable electronic, optical, and catalytic properties. These features make perovskites highly promising candidates for various energy applications, including

photocatalytic water splitting.[83] The first significant application of perovskite materials came in the 1950s in the field of ceramics and capacitors. Barium titanate ($BaTiO_3$), a type of oxide perovskite, was used as a dielectric material in capacitors due to its ferroelectric properties.[84] This application leveraged the high permittivity and tuneable dielectric constant of perovskites, making them ideal for electrical components. The use of perovskites in optoelectronics took off in 2009, when researchers, led by Tsutomu Miyasaka, used methylammonium lead iodide ($CH_3NH_3PbI_3$) as a light-harvesting material in a dye-sensitized solar cell (DSSC).[85] This marked the first use of metal halide perovskites in photovoltaics, achieving a modest power conversion efficiency (PCE) of 3.8%. Despite the initial performance, this study triggered widespread interest due to the material's potential for high efficiency and ease of fabrication.[85] Subsequent developments rapidly improved the efficiency of perovskite solar cells, with PCEs surpassing 25% by the early 2020s, making perovskites a major focus in next-generation solar energy technologies. This period also saw exploration of perovskites in light-emitting diodes (LEDs), photodetectors, and lasers, due to their excellent optoelectronic properties. Meanwhile, the first successful application of oxide perovskites for photocatalytic water splitting dates to 1980s, when Japanese scientist Aitom, H. et al. demonstrated the use of strontium titanate $SrTiO_3$, as a photocatalyst. This pioneering work revealed that $SrTiO_3$ could catalyse the overall water-splitting reaction under ultraviolet (UV) light irradiation. Although the reaction was limited to UV light, which makes up only a small portion of the solar spectrum, this discovery opened new avenues in the development of oxide-based photocatalysts for hydrogen production.[86] Since the initial discovery, significant progress has been made in improving the efficiency, stability, and light absorption capabilities of oxide perovskites for photocatalytic water splitting.[87] Key milestones include the bandgap engineering since early oxide perovskites, such as $SrTiO_3$, suffered from wide bandgaps, typically above 3.0 eV, meaning they could only utilize UV light.[88] In the 1990s and early 2000s, researchers began exploring methods to tune the bandgap of perovskites to absorb visible light (which constitutes over 40% of sunlight). Doping strategies, such as substituting cations at the A or B site (e.g., substituting Sr^{2+} with La^{3+} or Ti^{4+} with Fe^{3+}), were employed to narrow the bandgap and shift light absorption towards the visible spectrum. Researchers discovered that introducing lanthanum (La) into $SrTiO_3$ could narrow its bandgap and improve its activity under visible light. This approach marked a crucial development in making perovskites more practical for solar-driven water splitting. To overcome charge recombination, a major issue in photocatalysis as we already discussed, researchers developed heterostructured

photocatalysts by combining oxide perovskites with other materials like metal oxides or co-catalysts such as Pt, NiO, or RuO_2.[89] These heterostructures improved charge separation and transfer, leading to enhanced photocatalytic performance. In recent years, considerable progress has been made in developing oxide perovskites that are active under visible light. Transition metal-based perovskites, such as $BaFeO_3$, $LaFeO_3$, and $BiFeO_3$, have emerged as promising candidates due to their smaller bandgaps (~2.0-2.5 eV), enabling them to absorb a broader spectrum of sunlight.[88] These materials are now being extensively studied for their potential to improve overall solar-to-hydrogen conversion efficiencies. Surface modification techniques have also been employed to enhance the photocatalytic efficiency of oxide perovskites. Depositing co-catalysts such as Pt, Ru, or Ni on the surface of perovskites can dramatically increase hydrogen evolution rates by providing active sites for the hydrogen evolution reaction (HER). Moreover, surface passivation techniques, such as coating oxide perovskites with protective layers, have improved their stability in aqueous environments, addressing the degradation issues faced by many perovskite photocatalysts.[87] Today, oxide perovskites are recognized as one of the most promising material classes for photocatalytic water splitting due to their stability, tunability, and relatively low cost and while oxide perovskites such as $SrTiO_3$ remain widely studied, there is growing interest in environmentally friendly critical raw materials-free perovskites for photocatalytic water splitting. Materials like $CaTiO_3$, $LaFeO_3$, and $BiFeO_3$ are being explored as sustainable alternatives with improved stability and efficiency.[87] Advances in nanotechnology have enabled the development of nanostructured oxide perovskites with enhanced surface areas and active sites. Nanostructured $SrTiO_3$, for instance, has demonstrated improved light absorption and charge separation, leading to higher hydrogen evolution rates. The use of single-crystal perovskites has shown potential for minimizing defects and grain boundaries, which are major contributors to charge recombination. Single-crystal perovskites offer improved charge carrier mobility and longer carrier lifetimes, making them more efficient for photocatalytic applications. [87,88] There is also increasing interest in bifunctional perovskite-based materials that can perform both hydrogen evolution reaction (HER) and oxygen evolution reaction (OER) efficiently. These materials offer the possibility of a single photocatalyst for overall water splitting, rather than relying on separate catalysts for each half-reaction.[79,88] As research into oxide perovskites for photocatalytic water splitting progresses, several key challenges remain to be addressed, and although oxide perovskites are generally more stable than their halide counterparts, long-term stability in aqueous environments, especially under continuous sunlight, is still an issue. Developing

protective coatings and optimizing material compositions to resist photo-corrosion is a priority. To transition from laboratory-scale research to real-world applications, scaling up the synthesis of perovskite photocatalysts and optimizing their fabrication for large-scale water splitting systems will be crucial. While significant progress has been made in improving the solar-to-hydrogen conversion efficiency of oxide perovskites, the efficiency levels are still far from commercial viability. Further advances in bandgap engineering, co-catalyst integration, and heterostructure design are needed to maximize efficiency.[87] Since their first application in photocatalytic water splitting in 1977, oxide perovskites have evolved significantly, demonstrating great promise as photocatalysts for hydrogen production. Continued innovation in material composition, nanostructuring, and surface modification holds the potential to further improve their efficiency and stability. With ongoing research efforts, oxide perovskites could play a pivotal role in the development of sustainable, solar-driven hydrogen production technologies in the near future.

3.1 METAL HALIDE PEROVSKITE (MHPs) FOR PHOTOCATALYTIC HYDROGEN EVOLUTION

Metal halide perovskites (MHPs) have revolutionized emerging photovoltaic (PV) technologies, quickly becoming one of the strongest competitors to silicon and garnering immense attention due to their unique optoelectronic properties.[90] Additionally, the tunability of their electronic band structure, as anticipated, places MHPs in favourable positions for photocatalytic reactions, such as hydrogen generation, nitrogen fixation, carbon dioxide reduction, and the degradation of organic dyes under visible light irradiation.[43] However, these photocatalytic processes often require water or other polar solvents, which presents a challenge for this class of materials applications. It is well known that MHPs are highly unstable when exposed to moisture or water, making these photocatalytic processes incompatible with most known MHP materials. [44,91] Despite these limitations, several strategies have been developed to overcome this issue, with three main approaches proving particularly successful results. The first approach (Figure 8a) involves encapsulating the active perovskite layer with barriers that prevent water exposure while allowing carrier flow.[44] Field's metals and carbon derivatives have been effectively used for this purpose, enabling MHPs to be included in complete photoelectrochemical (PEC) cells for the first time. Thus far, only lead-based (Pb-based) perovskites have been used in these devices, although no intrinsic obstacles prevent the use of lead-free MHPs in such systems. The

second strategy, first used in 2016, involves leveraging dynamic equilibria between perovskite precursors and perovskite powders dispersed in solution (Figure 8b).[48] To support the continuous formation of suitable perovskite crystalline phases, high concentrations of hydrohalic acids (such as HI or HBr) are needed in the solution. The dissociation of these acids increases halogen concentration, shifting the solubilization equilibrium toward MHP formation. Additionally, hydrohalic acids can provide reagents for hydrogen formation in a mechanism where halide ions act as hole scavengers. The third approach involves the use of water-stable MHPs (Figure 8c).[44]

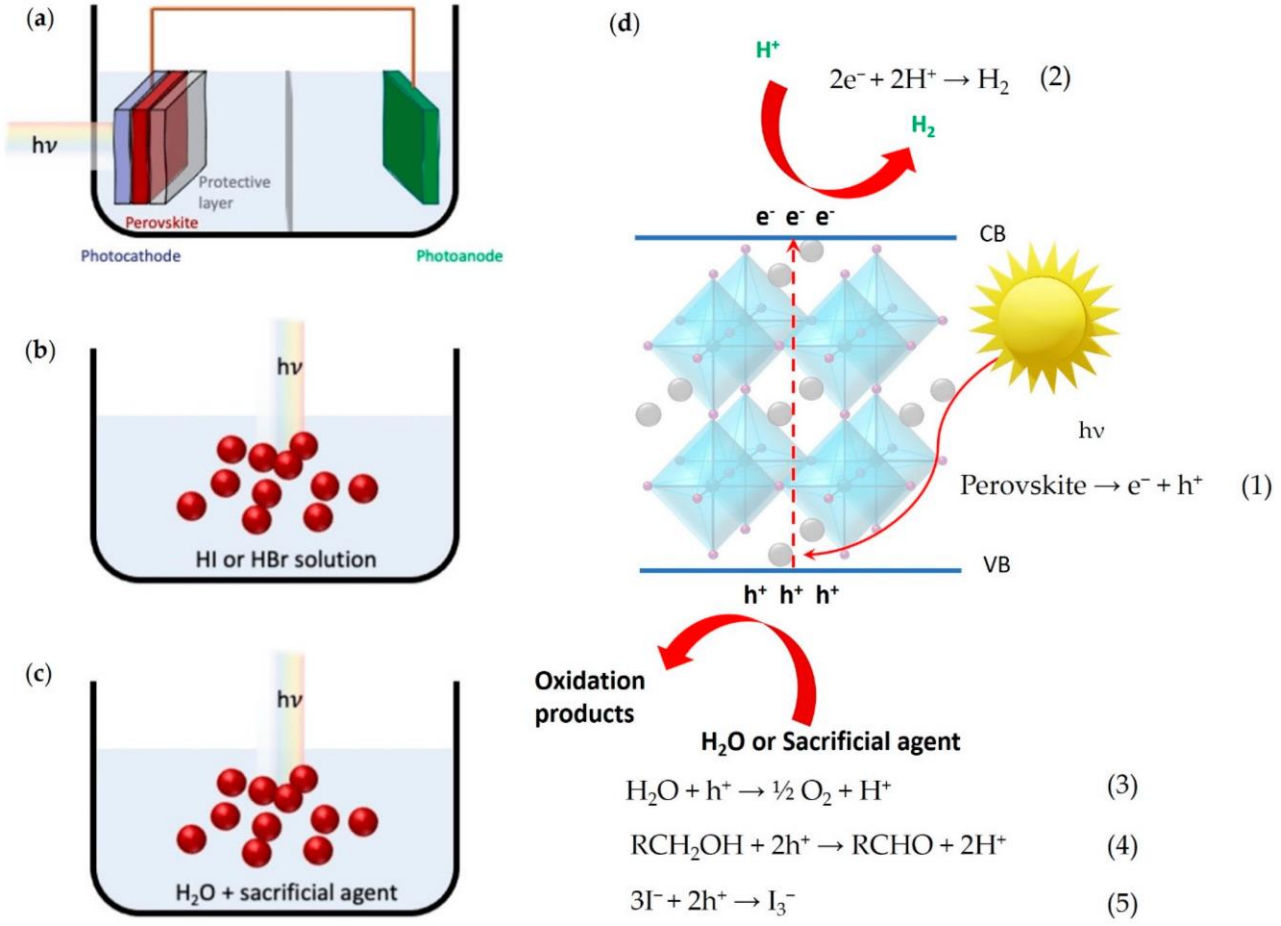

Fig 8. Solar-driven perovskite-based H_2 production systems: (a) photoelectrochemical (PEC) cell; (b) particulate photocatalyst system in dynamic equilibrium; (c) particulate water-stable photocatalyst system. (d) Schematic representation of the processes on the perovskite photocatalyst surface under irradiation and possible reactions involved in the different systems (Equations (1)-(5)).[44]

The recent development of these materials has led to the first successful use of MHPs directly in water for solar-driven hydrogen evolution. [92–94] However, the use of MHPs in aqueous solutions raises concerns about the presence of lead (Pb) in the most efficient materials. Lead atoms in the perovskite structure, particularly due to their outermost $6s^2$ electronic configuration, play a critical role in the material's superior optoelectronic properties, especially those related to charge dynamics. At the same time, the use of lead in material production poses serious environmental and health risks, as lead is a toxic metal that accumulates in vital organs of humans and animals, entering the body through air, water, and food. Lead exposure can cause cumulative poisoning effects, including hematological damage, anemia, kidney dysfunction, and brain damage. Chronic exposure can result in severe damage to the kidneys, liver, lungs, and spleen.[95] This concern is already a major obstacle to large-scale manufacturing of perovskite-based photovoltaic devices, and it is even more pressing for photocatalytic applications, where direct contact between the active material and the reaction medium increases the likelihood of lead leakage into the environment.[44] Given these risks, it should be crucial to prioritize the development and study of lead-free (Pb-free) MHPs for hydrogen evolution in aqueous solutions. Based on that, lead-free based metal halide perovskites are one of the most promising candidates for photocatalytic application.[44,49,50] After the initial success of metal halide perovskites in photovoltaics, reached by Tsutomu Miyasaka and colleagues in 2009,[85] researchers began in the same years, starting from those bases, to explore their potential also for photocatalytic applications, particularly in hydrogen evolution reactions (HER). The key to this transition was the realization that those same properties that made perovskites effective in solar cells like broad light absorption, excellent charge carrier dynamics, and tuneable electronic properties could also be leveraged for photocatalysis. The first notable application of metal halide perovskites in photocatalysis for hydrogen evolution came in 2016 when Park and coauthors used methylammonium lead iodide ($MAPbI_3$) as the photocatalyst.[48] To address the water-induced instability of perovskites, the reaction was conducted in an aqueous solution of hydroiodic acid (HI) and by carefully adjusting the I^- and H^+ concentrations, powdered $MAPbI_3$ underwent continuous dissolution and precipitation under dynamic equilibrium, allowing stable photocatalytic HI splitting and hydrogen evolution (along with I^{3-} formation). $MAPbI_3$ was stable only within specific HI concentration ranges (6.06−2.51 mol L^{-1}). The hydrogen evolution rate, achieved using a solar simulator, was 11.31 μmol h^{-1} g^{-1}, and this was further enhanced by 2 to 2.8 times after thermal annealing of $MAPbI_3$ in a dimethylformamide (DMF) and dimethyl sulfoxide

(DMSO) atmosphere, which improved material crystallinity. The highest hydrogen evolution rate reached about 57 μmol h^{-1} g^{-1} after depositing platinum on the sample, resulting in a solar HI splitting efficiency of 0.81%.[48] Thus, Park at al. demonstrated that lead halide perovskite could be used as photocatalyst for hydrogen production from aqueous solution under sunlight. However, these early attempts faced challenges, including material instability, particularly in aqueous environments, and issues related to the toxicity of lead, as we already largely discussed. From 2016 onward, substantial research has been devoted to overcoming these limitations and improving the performance of metal halide perovskites in photocatalytic hydrogen evolution. Material stability is one of the key areas to be improved since metal halide perovskites are prone to degradation, especially in aqueous and acidic environments as already underlined, which are common in photocatalytic applications. Important work has been done on passivating the perovskite surface with protective layers, such as carbon-based materials, or integrating perovskites with co-catalysts like platinum, to enhance their stability in water splitting reactions.[96,97] To further improve stability and photocatalytic performance, researchers have explored a variety of metal cations (e.g., tin, copper) and halide compositions.[98] Lead-free perovskites, such as tin-based perovskites (e.g., $MASnI_3$), are recently emerging as more stable potential alternatives, also based on all the problems related to the intrinsic instability of the lead-based phases, although lead-free MHPs often exhibit lower efficiencies compared to their lead-based counterparts.[99] Only a few perovskite systems have been reported up to now to possess an intrinsic stability in water and quite promising and unexpected high hydrogen evolution rate, namely $DMASnBr_3$,[92] $DMASnI_3$ [101] and PEA_2SnBr_4,[93] which are extremely favourable for future developments. However, there are some studies that show that Sn is also a harmful chemical, with similar concerns regarding environment and health to Pb at high concentration exposure, so the tin-based alternative became promising and attractive just in terms of stability and durability of the materials and therefore of the general device.[100] Hybrid systems, where perovskites are combined with other materials, such as graphitic carbon nitride (g-C_3N_4), transition metal oxides, or metal-organic frameworks (MOFs), represent an optimal strategy to boost the application of this class of materials.[45,46,102] These hybrid photocatalysts improve charge separation and transfer, thereby enhancing hydrogen evolution rates.[98,103] The integration of metal halide perovskites with traditional semiconductor photocatalysts has shown promise in improving both stability and photocatalytic activity since, as already discussed, one of the main advantages of perovskites is the ability to tune their bandgap by modifying their halide composition. By

adjusting the ratio of iodine, bromine, and chlorine, researchers can tailor the perovskite's light absorption to better match the solar spectrum, enhancing its efficiency for hydrogen evolution under sunlight. Moreover, photocatalytic hydrogen evolution can occur in acidic, neutral, or alkaline conditions, and metal halide perovskites have shown promise in both acidic and aqueous media. [44,48] Their broad absorption spectrum and suitable band alignment for water splitting make them effective photocatalysts under various pH conditions, though their instability in acidic media remains a challenge. Ongoing research aims to develop perovskite-based photocatalysts that are more robust in these harsh environments. Today, metal halide perovskites are recognized as one of the most exciting materials for photocatalytic hydrogen evolution. However, key challenges, particularly in terms of stability and scalability, remain. [43,98] In conclusion, to address these issues, researchers are focusing on the several strategies, where the development of lead-free alternatives that maintain high photocatalytic efficiency while reducing environmental concerns is receiving important attention. Also, engineering perovskite structures or protective layers to withstand harsh reaction conditions, especially in long-term water splitting applications. Exploring advanced reaction systems and hybrid designs that combine perovskites with other materials to improve overall efficiency and stability. As research continues, it is expected that lead-free metal halide perovskites will play a significant role in the development of next-generation photocatalysts for sustainable green hydrogen production, contributing to the broader goal of clean energy generation from solar-driven processes.

4. AIM OF THE THESIS

The aim of this Ph.D. thesis is the study, the application and the characterization of carefully engineered heterojunction systems for photocatalytic green hydrogen and ammonia evolution reactions. During this research four distinct heterostructured systems have been studied, proving how the deliberate design and optimization of suitable semiconductors material interfaces, electron transfer mechanisms, and morphology consistently improve photocatalytic performance. Experimental findings reveal that heterojunction engineering and morphology control not only promote efficient charge carrier separation and transfer but also significantly mitigate the recombination, that as deeply discussed previously, represents a critical bottleneck for most of the main studied photocatalysts. Therefore, the principal focus was the study of the most suitable co-catalyst semiconductor, and the most efficient

heterojunction configuration for graphitic carbon nitride, g-C_3N_4, the primary eco-friendly and non-critical raw material-based photocatalyst studied in this work.

References

[1] K. Calvin, et al. *IPCC, 2023: Climate Change 2023: Synthesis Report. Contribution of Working Groups I, II and III to the Sixth Assessment Report of the Intergovernmental Panel on Climate Change [Core Writing Team, H. Lee and J. Romero (Eds.)]. IPCC, Geneva, Switzerland.*, Intergovernmental Panel On Climate Change (IPCC), 2023.

[2] Statistic Review of World Energy 2022.

[3] D. F. Birol, Key World Energy Statistics 2021.

[4] T. M. Letcher, *Future Energy : Improved, Sustainable and Clean Options for Our Planet*, Elsevier, Amsterdam, Netherlands, 2020.

[5] C. Augustine, N. Blair, *Storage Futures Study: Storage Technology Modeling Input Data Report*, 2021.

[6] International Hydropower Association (IHA), 2020 Hydropower Status Report, 2020.

[7] K. Mongird, V. Viswanathan, J. Alam, C. Vartanian, V. Sprenkle, R. Baxter, 2020.

[8] K. Sadamori, B. Motherway, *Energy Efficiency* 2021.

[9] L. Zhai, S. Liu, Z. Xiang, *Ind. Chem. Mater.* 2023, *1*, 332.

[10] A. Valera-Medina, H. Xiao, M. Owen-Jones, W. I. F. David, P. J. Bowen, *Progress in Energy and Combustion Science* 2018, *69*, 63.

[11] A. O. M. Maka, M. Mehmood, *Clean Energy* 2024, *8*, 1.

[12] M. Jaradat, S. Almashaileh, C. Bendea, A. Juaidi, G. Bendea, T. Bungau, *Energies* 2024, *17*, 3992.

[13] M. Chatenet, B. G. Pollet, D. R. Dekel, F. Dionigi, J. Deseure, P. Millet, R. D. Braatz, M. Z. Bazant, M. Eikerling, I. Staffell, P. Balcombe, Y. Shao-Horn, H. Schäfer, *Chem. Soc. Rev.* 2022, *51*, 4583.

[14] F. M. Sapountzi, J. M. Gracia, C. J. (Kees-J. Weststrate, H. O. A. Fredriksson, J. W. (Hans) Niemantsverdriet, *Progress in Energy and Combustion Science* 2017, *58*, 1.

[15] S. Shiva Kumar, H. Lim, *Energy Reports* 2022, *8*, 13793.

[16] J. A. Okolie, R. Rana, S. Nanda, A. K. Dalai, J. A. Kozinski, *Sustainable Energy Fuels* 2019, *3*, 578.

[17] S. Valizadeh, H. Hakimian, A. Farooq, B.-H. Jeon, W.-H. Chen, S. Hoon Lee, S.-C. Jung, M. Won Seo, Y.-K. Park, *Bioresource Technology* 2022, *365*, 128143.

[18] K. Villa, J. R. Galán-Mascarós, N. López, E. Palomares, *Sustainable Energy Fuels* 2021, *5*, 4560.

[19] A. Fujishima, K. Honda, *Nature* 1972, *238*, 37.

[20] R. Marschall, *Eur J Inorg Chem* 2021, *2021*, 2435.

[21] B. Y. Alfaifi, H. Ullah, S. Alfaifi, A. A. Tahir, T. K. Mallick, *Veruscript Funct. Nanomater.* 2018, *2*, BDJOC3.

[22] R. R. Bhosale, R. V. Shende, J. A. Puszynski, n.d.

[23] H. Ozcan, R. S. El-Emam, B. Amini Horri, *Journal of Cleaner Production* 2023, *382*, 135295.

[24] D. Oudejans, M. Offidani, A. Constantinou, S. Albonetti, N. Dimitratos, A. Bansode, *Energies* 2022, *15*, 3044.

[25] V.-H. Nguyen, B.-S. Nguyen, Z. Jin, M. Shokouhimehr, H. W. Jang, C. Hu, P. Singh, P. Raizada, W. Peng, S. Shiung Lam, C. Xia, C. C. Nguyen, S. Y. Kim, Q. V. Le, *Chemical Engineering Journal* 2020, *402*, 126184.

[26] N. Fajrina, M. Tahir, *International Journal of Hydrogen Energy* 2019, *44*, 540.
[27] R. Huang, X. Li, W. Gao, X. Zhang, S. Liang, M. Luo, *RSC Adv.* 2021, *11*, 14844.
[28] H. Eidsvåg, S. Bentouba, P. Vajeeston, S. Yohi, D. Velauthapillai, *Molecules* 2021, *26*, 1687.
[29] M. Barawi, M. García-Tecedor, M. Gomez-Mendoza, G. Gorni, M. Liras, V. A. De La Peña O'Shea, L. Collado, *ACS Appl. Mater. Interfaces* 2023, *15*, 53382.
[30] K. Pournemati, A. Habibi-Yangjeh, A. Khataee, *Journal of Colloid and Interface Science* 2023, *641*, 1000.
[31] Y. Li, R. Li, Z. Sun, L. Guo, Y. Wang, X. Ma, H. Li, T. Lei, C. Fan, J. Liu, *Journal of Colloid and Interface Science* 2024, *664*, 198.
[32] K. Pournemati, A. Habibi-Yangjeh, A. Khataee, *ACS Appl. Nano Mater.* 2024, *7*, 2200.
[33] C. Prasad, N. Madkhali, J. S. Won, J. E. Lee, S. Sangaraju, H. Y. Choi, *Materials Science and Engineering: B* 2023, *292*, 116413.
[34] K. Sharma, V. Hasija, M. Malhotra, P. K. Verma, A. A. Parwaz Khan, S. Thakur, Q. Van Le, H. H. Phan Quang, V.-H. Nguyen, P. Singh, P. Raizada, *International Journal of Hydrogen Energy* 2024, *52*, 804.
[35] C. Martinez Suarez, S. Hernández, N. Russo, *Applied Catalysis A: General* 2015, *504*, 158.
[36] Z. Wang, X. Huang, X. Wang, *Catalysis Today* 2019, *335*, 31.
[37] S. J. Mun, S.-J. Park, *Catalysts* 2019, *9*, 805.
[38] D. Zhao, X. Guan, S. Shen, *Environ Chem Lett* 2022, *20*, 3505.
[39] G. Dong, W. Ho, C. Wang, *J. Mater. Chem. A* 2015, *3*, 23435.
[40] M. Cheng, C. Xiao, Y. Xie, *J. Mater. Chem. A* 2019, *7*, 19616.
[41] J. Liang, X. Yang, Y. Wang, P. He, H. Fu, Y. Zhao, Q. Zou, X. An, *J. Mater. Chem. A* 2021, *9*, 12898.
[42] X. Xu, X. Feng, W. Wang, K. Song, D. Ma, Y. Zhou, J.-W. Shi, *Journal of Colloid and Interface Science* 2023, *651*, 669.
[43] L. Romani, L. Malavasi, *ACS Omega* 2020, *5*, 25511.
[44] V., Armenise, S., Colella, F., Fracassi & A., Listorti, Nanomaterials 11, 433, 2021
[45] J. Luo, W. Zhang, H. Yang, Q. Fan, F. Xiong, S. Liu, D. Li, B. Liu, *EcoMat* 2021, *3*, e12079.
[46] C. Tedesco, L. Gregori, A. Simbula, F. Pitzalis, A. Speltini, F. Merlo, S. Colella, A. Listorti, E. Mosconi, A. A. Alothman, W. Kaiser, M. Saba, A. Profumo, F. De Angelis, L. Malavasi, *Adv Energy and Sustain Res* 2024, 2400040.
[47] C. Tedesco, A. Simbula, R. Pau, F. Merlo, A. Speltini, V. Armenise, A. Listorti, L. Gregori, A. A. Alothman, E. Mosconi, M. Saba, A. Profumo, L. Malavasi, *SolarRRL* 2025, 202400778
[48] S. Park, W. J. Chang, C. W. Lee, S. Park, H.-Y. Ahn, K. T. Nam, *Nat Energy* 2016, *2*, 16185.
[49] C. Tedesco, L. Malavasi, *Molecules* 2023, *28*, 339.
[50] J. Li, J. Duan, X. Yang, Y. Duan, P. Yang, Q. Tang, *Nano Energy* 2021, *80*, 105526.
[51] W. Wang, X. Xu, W. Zhou, Z. Shao, *Advanced Science* 2017, *4*, 1600371.
[52] R. Jaryal, R. Kumar, S. Khullar, *Coordination Chemistry Reviews* 2022, *464*, 214542.
[53] K. Fukuda, K. Yu, T. Someya, *Adv. Energy Mater.* 2020.

[54] K. Sivula, *ACS Energy Lett.* 2020, *5*, 1970.
[55] D. Zhang, H.-H. Cho, J.-H. Yum, M. Mensi, K. Sivula, *Adv. Energy Mater.* 2022.
[56] Y. Bai, K. Hippalgaonkar, R. S. Sprick, *J. Mater. Chem. A* 2021, *9*, 16222.
[57] J. Low, J. Yu, M. Jaroniec, S. Wageh, A. A. Al-Ghamdi, *Advanced Materials* 2017, *29*, 1601694.
[58] H. Li, Y. Zhou, W. Tu, J. Ye, Z. Zou, *Adv Funct Materials* 2015, *25*, 998.
[59] W. Wang, S. Mei, H. Jiang, L. Wang, H. Tang, Q. Liu, *Chinese Journal of Catalysis* 2023, *55*, 137.
[60] L. Lu, B. Wu, W. Shi, P. Cheng, *Inorg. Chem. Front.* 2019, *6*, 3456.
[61] J. Low, C. Jiang, B. Cheng, S. Wageh, A. A. Al-Ghamdi, J. Yu, *Small Methods* 2017, *1*, 1700080.
[62] S. Li, J. Sun, J. Guan, *Chinese Journal of Catalysis* 2021, *42*, 511.
[63] N. Singh, J. Prakash, R. K. Gupta, *Mol. Syst. Des. Eng.* 2017, *2*, 422.
[64] C. C. L. McCrory, S. Jung, I. M. Ferrer, S. M. Chatman, J. C. Peters, T. F. Jaramillo, *J. Am. Chem. Soc.* 2015, *137*, 4347.
[65] N. Cheng, S. Stambula, D. Wang, M. N. Banis, J. Liu, A. Riese, B. Xiao, R. Li, T.-K. Sham, L.-M. Liu, G. A. Botton, X. Sun, *Nat Commun* 2016, *7*, 13638.
[66] Y. Liu, Z. Sun, Y. H. Hu, *Chemical Engineering Journal* 2021, *409*, 128250.
[67] Y. Ding, S. Maitra, C. Wang, S. Halder, R. Zheng, T. Barakat, S. Roy, L. Chen, B. Su, *Interdisciplinary Materials* 2022, *1*, 213.
[68] A. Joy, M. R. Viswanathan, B. K. Vijayan, C. G. Silva, I. Basheer, S. Sugathan, P. A. Mohamed, A. Solaiappan, A. Shereef, *RSC Adv.* 2024, *14*, 21655.
[69] A. Kudo, R. Niishiro, A. Iwase, H. Kato, *Chemical Physics* 2007, *339*, 104.
[70] Y.-C. Chen, Y.-S. Huang, H. Huang, P.-J. Su, T.-P. Perng, L.-J. Chen, *Nano Energy* 2020, *67*, 104225.
[71] J. Wang, P. Fazil, M. I. Ali Shah, A. Zada, N. Anwar, G. G. Zain, W. Khan, F. Jan, T. Lei, M. Ateeq, *International Journal of Hydrogen Energy* 2023, *48*, 21674.
[72] Z. Li, J. Zi, X. Luan, Y. Zhong, M. Qu, Y. Wang, Z. Lian, *Adv Funct Materials* 2023, *33*, 2303069.
[73] A. Das, N. S.K., R. G. Nair, *Nano-Structures & Nano-Objects* 2019, *19*, 100353.
[74] B. Arkhurst, R. Guo, D. Gunawan, L. Oppong-Antwi, A. N. Ashong, X. Fan, G. B. Rokh, S. L. I. Chan, *International Journal of Hydrogen Energy* 2024, *87*, 321.
[75] Z. He, J. Zhang, X. Li, S. Guan, M. Dai, S. Wang, *Small* 2020, *16*, 2005051.
[76] Y. Yang, D. Li, P. Wang, X. Zhang, H. Zhang, B. Du, C. Guo, T. Wang, D. Liu, *Polymer* 2022, *244*, 124667.
[77] J. Kosco, M. Bidwell, H. Cha, T. Martin, C. T. Howells, M. Sachs, D. H. Anjum, S. Gonzalez Lopez, L. Zou, A. Wadsworth, W. Zhang, L. Zhang, J. Tellam, R. Sougrat, F. Laquai, D. M. DeLongchamp, J. R. Durrant, I. McCulloch, *Nat. Mater.* 2020, *19*, 559.
[78] M. S. Reza, N. B. H. Ahmad, S. Afroze, J. Taweekun, M. Sharifpur, A. K. Azad, *Chem Eng & Technol* 2023, *46*, 420.
[79] G. Wan, L. Yin, X. Chen, X. Xu, J. Huang, C. Zhen, H. Zhu, B. Huang, W. Hu, Z. Ren, H. Tian, L. Wang, G. Liu, H.-M. Cheng, *J. Am. Chem. Soc.* 2022, *144*, 20342.
[80] T. Clarkson, *Materials Science and Technology* 2022, *38*, 1332.

[81] A. Mehta, A. Mishra, S. Basu, N. P. Shetti, K. R. Reddy, T. A. Saleh, T. M. Aminabhavi, *Journal of Environmental Management* 2019, *250*, 109486.
[82] G. Rose, *Annalen der Physik* 1839, *124*, 551.
[83] Y. Zhou, *Matter* 2021, *4*, 3802.
[84] Tanaka, Tetsuro. *Bulletien of the Institute dor Chemical Research*, Kyoto University 32.2 (1954) 43-53.
[85] A. Kojima, K. Teshima, Y. Shirai, T. Miyasaka, *J. Am. Chem. Soc.* 2009, *131*, 6050.
[86] H. Aitom, n.d.
[87] P. Pattanayak, P. Singh, N. K. Bansal, M. Paul, H. Dixit, S. Porwal, S. Mishra, T. Singh, *Journal of Environmental Chemical Engineering* 2022, *10*, 108429.
[88] C. Avcıoğlu, S. Avcıoğlu, M. F. Bekheet, A. Gurlo, *ACS Appl. Energy Mater.* 2023, *6*, 1134.
[89] H. Mai, D. Chen, Y. Tachibana, H. Suzuki, R. Abe, R. A. Caruso, *Chem. Soc. Rev.* 2021, *50*, 13692.
[90] P. Gao, M. Grätzel, M. K. Nazeeruddin, *Energy Environ. Sci.* 2014, *7*, 2448.
[91] B.-M. Bresolin, Y. Park, D. W. Bahnemann, *Catalysts* 2020, *10*, 709.
[92] L. Romani, A. Speltini, F. Ambrosio, E. Mosconi, A. Profumo, M. Marelli, S. Margadonna, A. Milella, F. Fracassi, A. Listorti, F. De Angelis, L. Malavasi, *Angew Chem Int Ed* 2021, *60*, 3611.
[93] L. Romani, A. Bala, V. Kumar, A. Speltini, A. Milella, F. Fracassi, A. Listorti, A. Profumo, L. Malavasi, *J. Mater. Chem. C* 2020, *8*, 9189.
[94] L. Romani, A. Speltini, R. Chiara, M. Morana, C. Coccia, C. Tedesco, V. Armenise, S. Colella, A. Milella, A. Listorti, A. Profumo, F. Ambrosio, E. Mosconi, R. Pau, F. Pitzalis, A. Simbula, D. Ricciarelli, M. Saba, M. Medina-Llamas, F. De Angelis, L. Malavasi, *Cell Reports Physical Science* 2023, *4*, 101214.
[95] A. L. Wani, A. Ara, J. A. Usmani, *Interdisciplinary Toxicology* 2015, *8*, 55.
[96] Y. Wu, P. Wang, X. Zhu, Q. Zhang, Z. Wang, Y. Liu, G. Zou, Y. Dai, M. Whangbo, B. Huang, *Advanced Materials* 2018, *30*, 1704342.
[97] Y. Wu, Q. Wu, Q. Zhang, Z. Lou, K. Liu, Y. Ma, Z. Wang, Z. Zheng, H. Cheng, Y. Liu, Y. Dai, B. Huang, P. Wang, *Energy Environ. Sci.* 2022, *15*, 1271.
[98] S. Tasleem, M. Tahir, *Renewable and Sustainable Energy Reviews* 2020, *132*, 110073.
[99] D. Ricciarelli, W. Kaiser, E. Mosconi, J. Wiktor, M. W. Ashraf, L. Malavasi, F. Ambrosio, F. De Angelis, *ACS Energy Lett.* 2022, *7*, 1308.
[100] H.-J. Lehmler, M. Gadogbe, B. Liu, W. Bao, *Environmental Pollution* **2018**, *240*, 599.
[101] D. Ju, X. Zheng, J. Liu, Y. Chen, J. Zhang, B. Cao, H. Xiao, O. F. Mohammed, O. M. Bakr, X. Tao, *Angewandte Chemie* 2018, *130*, 15084.
[102] T. Wang, C. Zhou, D. Li, J. Gao, C. Fan, W. Tang, *Catal Lett* 2024, *154*, 4134.
[103] S. Purohit, K. L. Yadav, S. Satapathi, *Adv Materials Inter* 2022, *9*, 2200058.

CHAPTER 2

Synthesis of Carbon Nitride Polymorphs by Sacrificial Template Method: Correlation between Physicochemical Properties and Photocatalytic Performance

María Medina-Llamas,[a,b]* Eleonora Bianchi,[c] Maria Cristina Mozzati,[d] Costanza Tedesco,[b] Chiara Milanese,[b] Andrea Speltini,[b] Antonella Profumo,[b] Vincenza Armenise,[e] Antonella Milella,[e] Andrea Listorti [e]* and Lorenzo Malavasi [a]*

[a] Unidad Académica Preparatoria, Plantel II.

Universidad Autónoma de Zacatecas

Avenida Preparatoria 98068, Zacatecas, México

[b] University of Pavia

Via Taramelli 12, 27100 Pavia, Italy.

[c] Eleonora Bianchi

Department of Drug Science

University of Pavia

Via Taramelli 12, 27100 Pavia, Italy.

[d] Maria Cristina Mozzati

Department of Physics and CNISM

University of Pavia

Via Taramelli 12, 27100 Pavia, Italy.

[e] Vincenza Armenise, Antonella Milella and Andrea Listorti

Department of Chemistry
University of Bari Aldo Moro
Vía Orabona 4,70126, Bari, Italy

ABSTRACT

Carbon nitride compounds (CNCs) in the form of graphitic carbon nitride (g-C_3N_4) and poly(heptazine imide) were synthesized using different metal chloride salts (MCl_x), i.e., NaCl, KCl and $CaCl_2$, as sacrificial templates and by varying the MCl_x to melamine molar ratios. A systematic study of their photocatalytic activity for H_2 production in relation to the physicochemical, morphological, and optical properties was carried out. Each sample was tested achieving the highest hydrogen evolution rates of about 7660 μmol g^{-1} h^{-1}, 5380 μmol g^{-1} h^{-1} and 3140 μmol g^{-1} h^{-1} using $CaCl_2$, KCl, and NaCl, respectively. This work demonstrates how the synthesis of CNCs with different MCl_x leads to the production of high-performance photocatalysts due to a combination of factors as the formation of vacancies or cyano groups, a shift in the optical threshold and tuning of micro(nano)structure. The results demonstrate that, when $CaCl_2$ is used as a sacrificial template, porous and exfoliated g-C_3N_4 nanosheets are formed leading to hydrogen productions which outperform most of the previously reported g-C_3N_4 prepared using a single synthetic step.

1. INTRODUCTION

Over the last years, polymeric carbon nitride compounds (CNCs) have emerged as promising candidates for a variety of appealing applications spanning from H_2 production,[1] CO_2 reduction,[2] sensing,[3] to nitrogen photo fixation.[4] This is due to their suitable optical properties, such as a band gap close to 2.7 eV which makes CNCs active in the visible solar spectrum, coupled to an extraordinary chemical and thermal stability.[5] As a matter of fact, CNCs have a basic two-dimensional arrangement formed by triazine rings (C_3N_3) and tri-*s*-triazine rings (C_6N_7).[6] CNCs are synthesized from the thermal polycondensation of inexpensive precursors that contain nitrogen and carbon atoms such as: dicyanamide (DCD), melamine (MLM), urea and thiourea. The most common CNC is graphitic carbon nitride (g-C_3N_4), which is characterized by a bulk and disordered structure. g-C_3N_4 has two main drawbacks, namely high recombination rate of the electron-hole pairs, due to the presence of defects deriving from an incomplete delamination during the thermal condensation process, and a low surface area.[7] Poly (heptazine imide), or PHI, is another carbon nitride polymorph that shows an optical response like that of g-C_3N_4. However, it has a higher degree of crystallinity, and therefore exhibits enhanced photoactivity compared to bulk g-C_3N_4.[8] Both CNCs can be prepared by different approaches such as molecular self-assembly,[9] microwave synthesis,[10] and sacrificial template methods.[11] Among the various procedures, sacrificial template methods are simple, inexpensive, and efficient strategies to obtain high photocatalytic active materials.[12] Under this approach, CNCs precursors, *i.e.* MLM, DCD, urea or thiourea, are mixed with water soluble salts, followed by the thermal polycondensation reaction. For example, salts such as $NaHCO_3$, $MgCO_3$ or NH_4Cl, commonly referred to as sacrificial gas templates, decompose in a mixture of gases during the thermal polymerization of g-C_3N_4, producing a thermal gas-flow shock that leads to the formation of a porous g-C_3N_4. Wu et *al.* (2020) fabricated porous g-C_3N_4 nanosheets (NSs) using DCD and $NaHCO_3$ for hydrogen gas evolution reaction. Their results showed the production of a porous g-C_3N_4 due to the formation of CO_2 from the thermal decomposition of $NaHCO_3$.[11c] A similar procedure was reported by Yan et *al*. (2017) obtaining porous g-C_3N_4 NSs using MLM and $MgCO_3$ as the gas template,[13] while Li et *al*. (2020) used DCD and NH_4Cl.[14] Beyond this method, solid or eutectic salts templates can be used for the g-C_3N_4 and PHI preparation. For example, Xiong et *al*. (2016) synthesized a K^+ doped g-C_3N_4 by mixing KBr and thiourea and investigated its performance for the photocatalytic removal of NO.[15] They demonstrated that K^+ incorporation increases the visible-light absorption and improves the oxidation ability of g-C_3N_4, leading to an enhanced photocatalytic performance.

Eutectic salts such as KCl:LiCl, NaCl:KCl were as well reported for the synthesis of PHI.[15-16] Focusing on H_2 production by CNCs using sacrificial templates, it should be noted that, despite the intensive research recently reported in the literature, significant differences in terms of crystal structure, surface area, morphology etc. have been evidenced, even when the same precursor and/or similar preparation and synthesis conditions were chosen. These differences have a strong influence on the CNCs final characteristics and in turn on the photocatalytic hydrogen production efficiency. In fact, regarding the use of NaCl as sacrificial template, Yang et *al.* (2019) reported the preparation of a porous g-C_3N_4 by dissolving DCD in ethanol and mixing it with a saturated aqueous solution of NaCl; a rotary evaporation treatment allowed the subsequent formation of a powder, which was thermally treated at 550°C.[17] The best sample achieved a hydrogen evolution rate (HER) of 459 µmol/g/h with a 10:1 NaCl:DCD molar ratio.[17] More recently, Teixeira et *al.* (2022) synthesized a sodium doped PHI by subjecting a finely ground mixture of 10:1 NaCl:MLM (weight ratio) to a thermal treatment in N_2 atmosphere at 600°C, and the material achieved a value of 2400 µmol/g/h.[18] A similar material was reported by Tang et *al.* (2020), in which porous g-C_3N_4 is obtained by using a 30:1 NaCl:MLM mixture (weight ratio) treated at 550°C; however the obtained photocatalyst was evaluated for the degradation of tetracyclines only.[19] In the current literature the utilization of KCl as sacrificial salt is as well reported. Indeed, Zhang et *al*. synthesized a K^+-doped g-C_3N_4 by mixing KCl with bulk g-C_3N_4 followed by heating in N_2 atmosphere (550°C).[20] This two-step synthesis allowed a H_2 production of 5235.8 µmol/g/h, which was almost 22 times higher than that provided by the bulk material. On the same line, Yuan et *al.* reported the synthesis of g-C_3N_4 with cyanamide defects, obtained by dissolving thiourea with a KCl aqueous solution.[21] The solution was freeze-dried and then thermally treated at 600°C. The resulting material was able to produce 4000 µmol/g/h of H_2, which it was 5 times higher compared to the bulk material.[21] Another work reports the use of a mixture MLM/Urea/KCl to produce a high performing material for the degradation of tetracycline.[22] The high photocatalytic performance of CNCs synthesized using metal halide templates indicate that there is space to further improve the H_2 production by a single and inexpensive synthetic route and to scale up its production. Indeed, as previously highlighted, such an approach has been applied by different authors to a single metal halide template, with a limited evaluation of the experimental conditions (e.g., CNC precursor to halide salt molar ratios), and by carrying out the synthesis with different thermal treatment protocols which are known to have a huge impact on the final catalytic activity of the CNCs. In addition, most of the studies today have been focused on monovalent metal halides while it would be

of interest to further enlarge the plethora of possible templates. Therefore, to rationalize the role of metal halide templates on the CNCs physico-chemical properties and on their catalytic properties, i.e. H_2 production, we report here a systematic and comprehensive study of CNCs obtained using three metal halide salts, namely NaCl, KCl, and $CaCl_2$. All materials have been prepared according to a common synthetic protocol to provide reliable correlations with structural, optical, and catalytic activity. We highlight that, among these inexpensive metal halide templates, only KCl and NaCl have been previously reported in the literature.

2. RESULTS AND DISCUSSION

Polymeric CNCs were synthesized by the polycondensation of MLM at 550°C using either NaCl, KCl or $CaCl_2$ as sacrificial templates (see Experimental Section). A set of reactions was carried out at different molar ratios of MCl_x:MLM, namely 0:1, 5:1, 10:1, 15:1, 20:1, and 30:1. The amount of g-C_3N_4 NSs obtained was quantified drying the samples after the removal of the MCl_x. The g-C_3N_4 NSs to MLM mass ratio was used to express the reaction yield, reported as mass percentage (%) in Figure 1. The results show a clear decrease in the synthesis yield as the amount of MCl_x increases. Similar yields were obtained using NaCl and $CaCl_2$ across all the molar ratios. However, significantly lower yields were obtained when KCl was used as a sacrificial template.

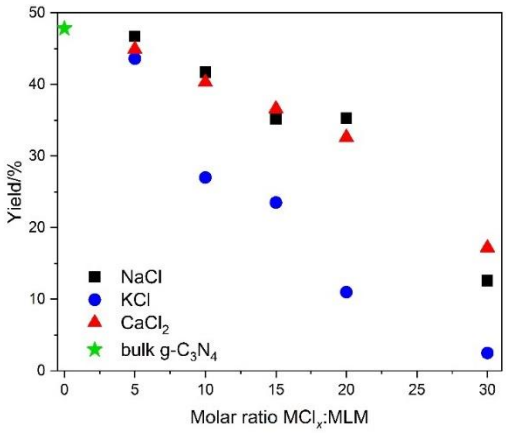

Figure 1. Reaction yields for the bulk g-C_3N_4 and the CNCs synthesized using NaCl, KCl or $CaCl_2$ as sacrificial templates at different MCl_x:MLM molar ratios.

Figure 2 reports the XRD patterns of all CNCs prepared using NaCl (a), $CaCl_2$ (b), and KCl (c). The thermal polycondensation of MLM in the presence of NaCl and $CaCl_2$ lead to the production of g-C_3N_4 NSs. The pattern of bulk g-C_3N_4 is shown as a reference at the bottom of the figures (green pattern) followed by the XRD patterns of the g-C_3N_4 NSs at increasing molar ratios (MCl_x:MLM). Bulk g-C_3N_4 shows the typical pattern characterized by two peculiar peaks at 13.0° and 27.5° ascribed to the (100) and the (002) planes.[22] The first reflection indicates the tris-s-triazine repeating units within a single g-C_3N_4 sheet, while the second one represents the interlayer-stacking reflection.[1] From a visual inspection of Figure 2a and Figure 2b, it is possible to observe some trends as a function of increasing molar ratio MCl_x:MLM. For example, when NaCl is added as sacrificial template (Figure 2a), the peak at 27.5° becomes progressively less intense and broader and the peak at 13° is no longer visible. These observations suggest a strong reduction of the intra-layer order and a significant distribution of (shorter) inter-layer distances, again associated to an increase of the disorder. A similar pattern was reported when g-C_3N_4 NSs were produced by a thermal exfoliation of bulk g-C_3N_4.[23] The incorporation of $CaCl_2$ during the thermal polymerization of MLM lead to the production of g-C_3N_4 NSs and the formation of small amounts of $CaCO_3$, as will be discussed later; the as-prepared g-C_3N_4 containing $CaCl_2$ as sacrificial agent was subjected to a washing process with DI water, despite the low solubility of $CaCO_3$, as it was done when KCl and NaCl were used, followed by filtration and drying. The XRD patterns of this set of samples are shown in Figure S1a. In all the XRD patterns we observe the presence of several sharp peaks, which can be attributed to the formation of $CaCO_3$. Figure S1b compares the XRD pattern of the 15:1 $CaCl_2$:MLM sample with the reference pattern of $CaCO_3$. To obtain the XRD pattern of the g-C_3N_4, $CaCO_3$ was dissolved using 100 mL of 0.1 M HCl solution. The suspension was sonicated for 20 min, filtered, rinsed with water, and finally dried. The XRD patterns of this set of samples were recorded and are shown in Figure 2b. The results show the characteristic peaks of g-C_3N_4, and both peaks become broader and less pronounced indicating a decrease in size in both directions (*i.e.*, parallel and perpendicular to the carbon nitride layers). Figure 2c shows the set of samples synthesized using KCl as sacrificial template. The obtained material is poly (heptazine imide), PHI. The reference pattern of PHI is shown at the bottom of the figure. The production of PHI using KCl, agrees with previous reports in the literature when KCl is used during the thermal polymerization of MLM.[24] The patterns of the samples exhibit several intense and sharp peaks, indicating an increased crystallinity of the sample. The strongest peak is at 28.2°, corresponding to the (001) crystal plane. Figure 2c shows that as the KCl:MLM molar ratio

increases, there is a gradual shift of the (001) to higher 2θ values, suggesting a reduction of the interlayer distance. To better highlight this effect Figure S2 shows a close-up of the (001) plane.

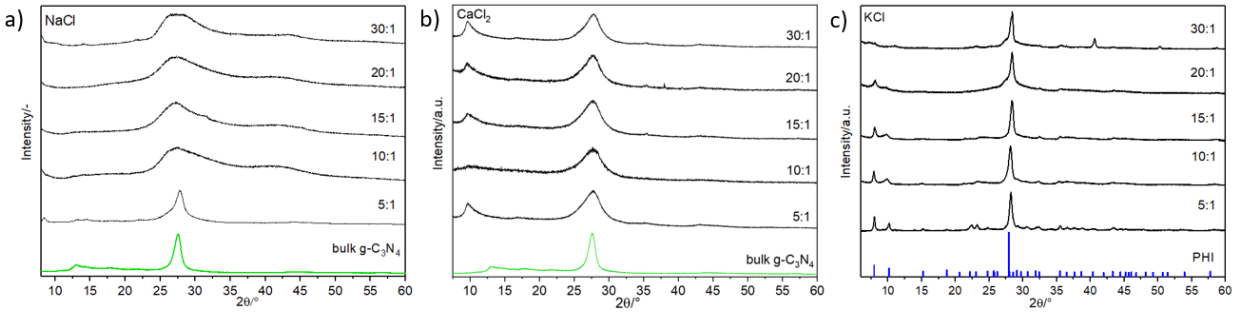

Figure 2. XRD patterns of the samples synthesized using a) NaCl, b) $CaCl_2$ and c) KCl as sacrificial templates at different MCl_x:MLM molar ratios.

The morphology and microstructure of all the CNCs was investigated by SEM and TEM. Figure 3 shows, by way of example, the micrographs for the CNC NSs obtained using the highest molar ratio, i.e. 30:1 MCl_x:MLM for each sacrificial template. The SEM and TEM micrographs for all the synthesized samples can be found in the SI from Figure S3 to S6. As apparent from Figure 3, the bulk g-C_3N_4 is characterized by a non-porous and layered morphology. Firstly, we would like to highlight that it is possible to observe a modulation of the nanostructure of the g-C_3N_4 produced by changing the sacrificial template (MCl_x). For instance, when NaCl was added we observed the formation of exfoliated sheets and small g-C_3N_4 particles within the 2D sheets. The TEM micrographs show that the addition of NaCl produces thinner nanosheets as the MCl_x:MLM molar ratio increases (Figure S3). We also observe a minority fraction of g-C_3N_4 nanotubes (Figure S4). However, the obtained g-C_3N_4 does not have a very porous morphology as reported by Tang Niu et *al*. (2020) even though, both synthesis methods are similar.[18] The morphology is more similar to the g-C_3N_4 NSs reported by Teixeira et *al.* (2022), nevertheless they only synthesized a single sample using 10 NaCl:MLM (weight ratio) and they reported the formation of a sodium doped PHI.[17] Figure S5 reports the set of SEM and TEM micrographs of PHI obtained when KCl is used as sacrificial agent. The obtained materials consist mainly of small particles in the nanometre scale, with sizes ranging from 30 to 70 nm. In the TEM analysis, we also observe the formation of exfoliated layers. It is worth mentioning that a similar morphology was previously reported.[19] The authors synthesized a K^+-doped g-C_3N_4 by mixing KCl with bulk g-C_3N_4 and performing a heat treatment at 600° C to achieve a controlled diffusion of the K^+

ions towards the surface of the bulk g-C_3N_4.[19] The CNC NSs produced using $CaCl_2$ as sacrificial template (Figure S6) show a porous surface. The micrographs show that there is a positive correlation between the porosity of the sample and the amount of $CaCl_2$ incorporated during the synthesis, being the sample with the 30:1 $CaCl_2$:MLM molar ratio, the one with the highest porosity. We would like to highlight that the SEM and TEM micrographs demonstrate the incorporation of $CaCl_2$ during the synthesis of CNC produces a more exfoliated material compared to the use of NaCl or KCl.

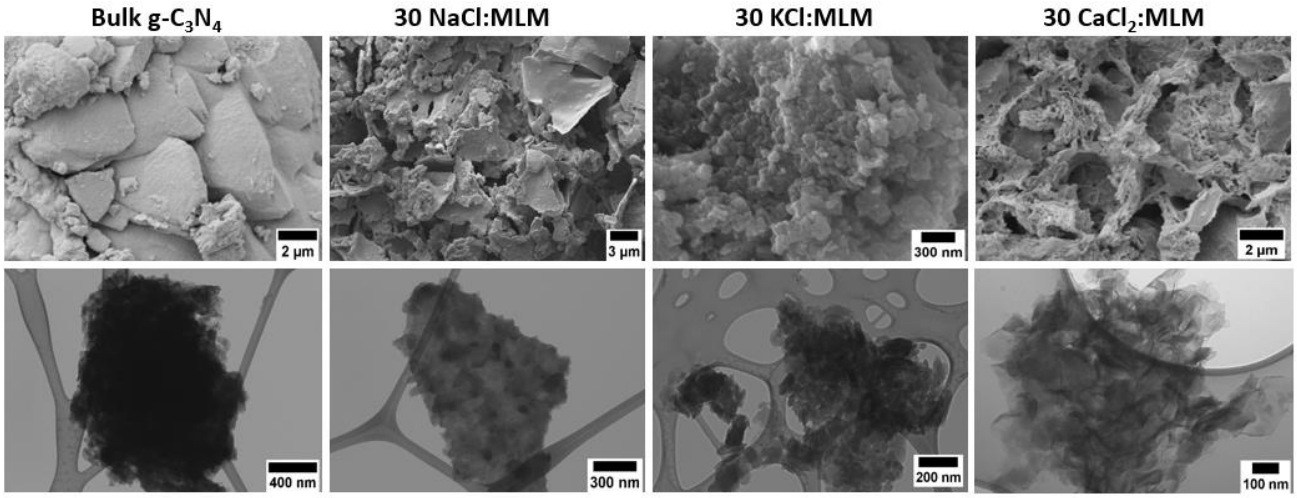

Figure 3. SEM and TEM micrographs of the bulk g-C_3N_4 and the CNCs synthesized using 30:1 MCl_x:MLM.

The specific surface area (SSA) of all the sample was measured and the results are reported in Table 1. The SSA of the bulk g-C_3N_4 is 18.3 m^2/g. The incorporation of salts with MLM during the synthesis causes a clear change in the SSA. In general, when KCl and NaCl are used, the SSA remains below to the one of bulk g-C_3N_4 except for the higher molar ratios of metal halide. On the other hand, there is a clear trend that indicates that higher SSA values are obtained when $CaCl_2$ is used, which can be nicely correlated to the microscopic investigation shown in the micrographs of Figure S6.

Table 1. Specific surface area of the bulk g-C_3N_4 and the CNCs obtained using different sacrificial agents.

	Specific surface area (m^2/g)		
Bulk g-C_3N_4 (from MLM)	18.3		
MCl_x:MLM	NaCl	KCl	$CaCl_2$
5:1	4.0 ± 0.1	10.1 ± 1.1	14.9 ± 1.9
10:1	4.3 ± 0.1	7.0 ± 1.5	18.1 ± 2.2
15:1	7.1 ± 0.2	7.8 ± 0.3	28.4 ± 0.7
20:1	10.6 ± 1.4	15.0 ± 1.7	28.4 ± 1.3
30:1	21.0 ± 2.4	14.8 ± 2.5	36.1 ± 0.6

The optical properties for all the samples were determined by UV–Vis absorption and photoluminescence spectroscopy (Figure 4). The Tauc plots of the bulk g-C_3N_4 and all the CNCs obtained using NaCl, KCl and $CaCl_2$ can be found in Figure 4a, 4c and 4e, respectively. Table 2 repots the estimated band gap value for each sample, while Figure S7 show the UV–Vis absorption spectra for all the samples. First, the bulk g-C_3N_4 has a band gap value of 2.71 eV, which corresponds to an adsorption edge about 457 nm, in good agreement with the value reported in the literature.[25] Interestingly, the incorporation of NaCl, KCl or $CaCl_2$ has a different effect on the optical properties of g-C_3N_4. For instance, when NaCl is used as a sacrificial agent, a shift towards lower energy values is observed which is scarcely affected by the NaCl:MLM ratio (cfr. Table 2 and Figure 4a). In addition, a broad absorption tail in the visible spectrum is observed for all the NaCl:MLM molar ratios (Figure S7a), which can be attributed to the presence of cyano group and Na ion doping, as will be discussed later considering the FTIR analysis. These results indicate the improvement of the light absorption of g-C_3N_4 when NaCl is used to dope the g-C_3N_4 sheets. As a comparision, Yang F. et *al.* (2019) reported a smilar red shift for the synthesis of porou s g-C_3N_4 NSs from different molar ratios of NaCl:DCD (1, 3, 5, 10 and 15).[16] However, only an absorption tail was reported for the g-C_3N_4 prepared using the highest molar ratio. The use of KCl as a sacrificial template, only produces a minimal shift towards lower energy values, compared to the bulk g-C_3N_4, without a correlation with the increasing KCl:MLM molar ratio (Figure 4c).

Table 2. Band gap of the bulk g-C_3N_4 and the CNCs NSs produced at various MCl_x:MLM molar ratios

	Band gap/eV				
Bulk g-C_3N_4	2.71				
Molar ratio MCl_x:MLM	**5:1**	**10:1**	**15:1**	**20:1**	**30:1**
NaCl	2.66	2.68	2.65	2.65	2.66
KCl	2.68	2.69	2.70	2.68	2.71
$CaCl_2$	2.88	2.86	2.86	2.89	2.87

Only a small tail is observed for the 20:1 KCl:MLM sample, since the samples with the highest molar ratio resulted in the formation of cyano groups, as will be discussed later. For the set of CNC NSs synthesized using $CaCl_2$, a shift towards higher energies is observed (cfr. Table 2 and Figure 4e). This change indicates a decrease of the light absorption in the visible range, which is consistent with the changes of colour from yellow for the bulk g-C_3N_4 to white/yellowish of the g-C_3N_4:$CaCl_2$ samples. The photoluminescence of the g-C_3N_4 NSs synthesized using NaCl (Figure 4b), KCl (Figure 4d) and $CaCl_2$ (Figure 4f) was measured from 1.8 eV to 3.4 eV and it was compared to PL spectra of the bulk g-C_3N_4. In the Figure 4b and 4d are presented the normalized intensity curves of NaCl and KCl related samples, these, in comparison to the reference, do not show any shift of the emission peak but only a sharpening of it. This agrees with the absorption measurements which also show for these two salts dopants almost no shift in the band edge, Table 2. Conversely, as can be noticed in Figure 4f the optical behaviour of Ca doped g-C_3N_4 is peculiar, showing a 0.20 eV blue-shift of the emission peak with respect to the reference. This can be related to the altered potential of VB and CB of g-C_3N_4 due to the orbital hybridization between C, N and dopant atoms which in turn affect the photocatalytic properties of the system.[21, 26] The time resolved PL spectra were recorded to monitor the decay process of all the samples. The measurements are reported in Figure S8, where they are compared with the bulk g-C_3N_4. For all the samples, the decay process is clearly faster than the bulk g-C_3N_4, indicating that the recombination of electron-hole pairs was efficiently suppressed upon doping, which can induce a remarkable enhancement of the photocatalytic activity, in line with what was previously observed for metal doped g-C_3N_4 samples.[26]

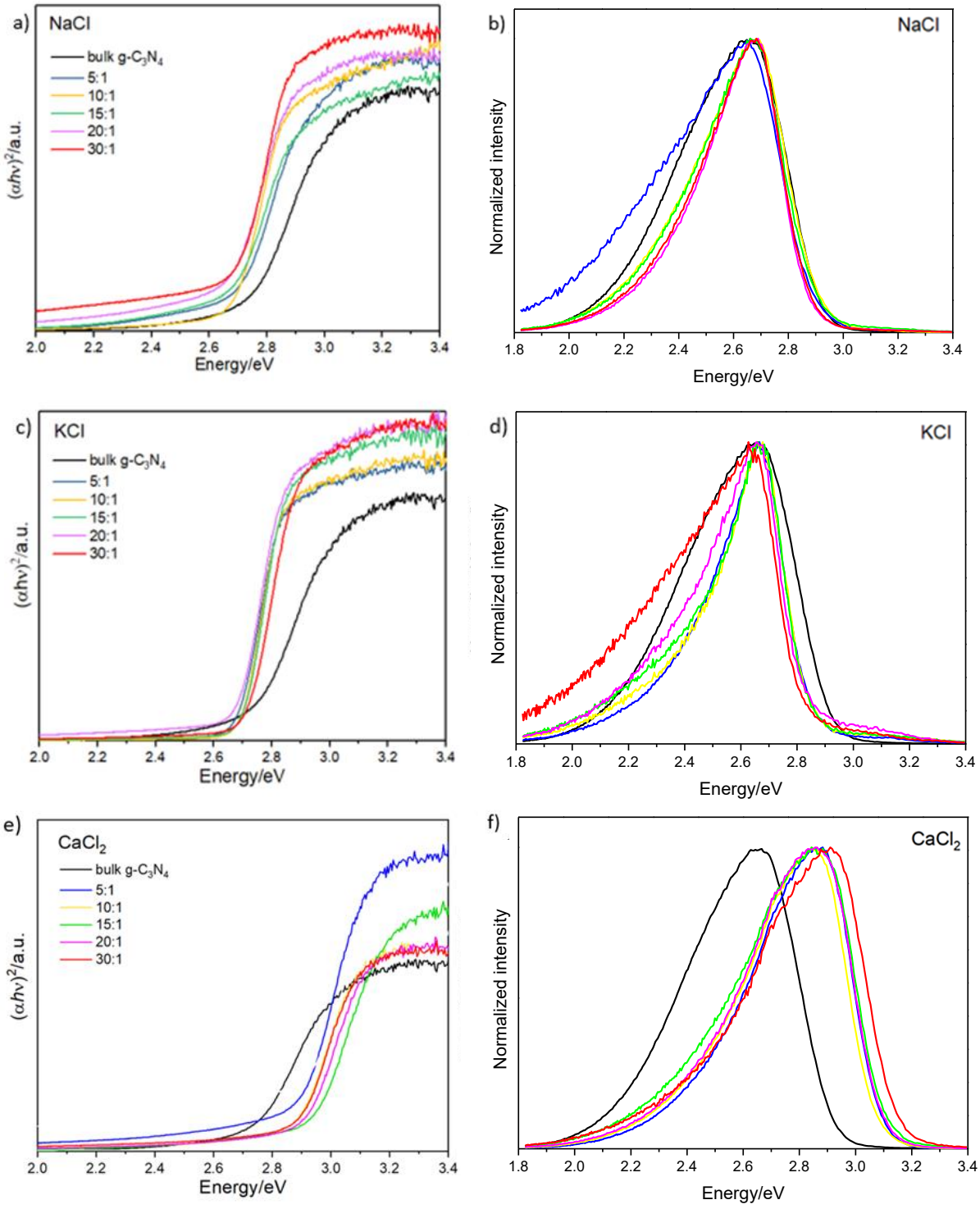

Figure 4. Tauc plot and normalised emission photoluminescence spectra of the bulk g-C_3N_4 and the CNCs using NaCl, KCl and $CaCl_2$ as sacrificial templates.

Further structural information was acquired by FTIR spectroscopy and shown in Figure 5. All the samples are characterized by a number of distinctive peaks. For instance, the peak

at 807 cm^{-1} which can be assigned to the out of the plane bending mode of the heptazine rings.[27] The peak at 890 cm^{-1} corresponds to the vibration of the N-H bonds, the shoulder peak at 1240 cm^{-1} and the bands at 1312, 1400, 1454, and 1574 cm^{-1} are assigned to the aromatic C–N stretching.[27-28] The peak at 1628 cm^{-1} attributed to the C=N stretching vibration modes of heptazine.[17] The broad bands in the range between 3000 to 3 700 cm^{-1} are due to the N-H stretching from residual amino groups and the O-H bonds band from adsorbed H_2O molecules.[29]

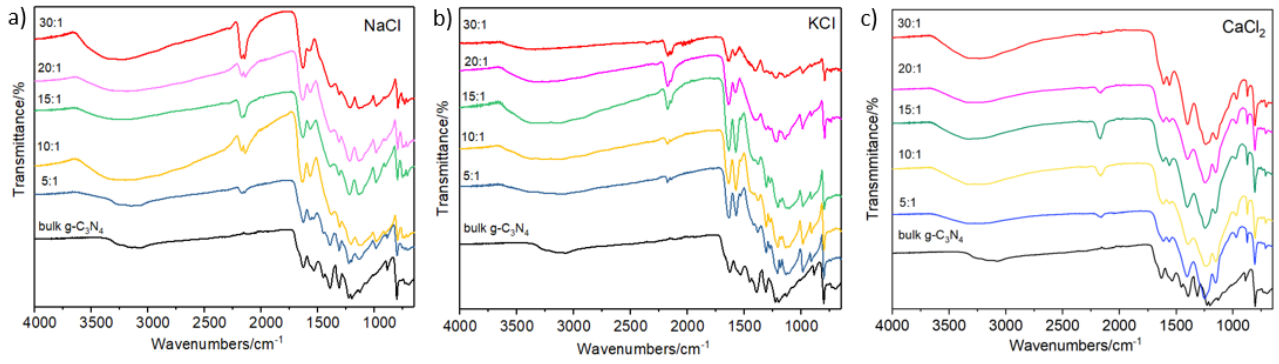

Figure 5. FTIR of the bulk g-C_3N_4 and the CNCs synthesized using a) NaCl, b) KCl and c) $CaCl_2$ as sacrificial templates.

However, the samples containing sacrificial templates show several additional peaks. For instance, the first peak at 2168 cm^{-1} indicates the formation of cyano groups (C≡N), whose intensity in general increases with the increase of the MCl_x:MLM ratio, except for the highest molar ratios when using $CaCl_2$. As reported in the literature, the presence of salts induced an incomplete polymerization and/or partial decomposition of tri-s-triazine units, resulting in the generation of cyano groups within the g-C_3N_4 framework.[30] It is suggested that such groups have a positive effect on the photocatalytic activity of g-C_3N_4.[31] The second peak at 968 cm^{-1} is assigned to the bending vibrations and the symmetric vibrations of the triazine rings, respectively.[32] The third peak at 2140 cm^{-1} is ascribed to the presence of C=O or C-O bonds in the structure, which agrees with the elemental composition values obtained by XPS (see later).[30] The presence of the former peaks demonstrates the reduction of the in-plane periodicity of the heptazine rings thus indicating the presence of defects. Moreover, Figure 5c show a small peak at 710 cm^{-1} that indicates the formation of $CaCO_3$ when $CaCl_2$ is used as sacrificial template.[33] All samples synthesized with a sacrificial template have peaks at 968 cm^{-1} and 1147 cm^{-1} denoting the presence of hydroxyl groups (-OH). However,

the bulk g-C_3N_4 does not show these peaks. XPS analysis was used to investigate surface chemical composition and structures of bulk g-C_3N_4 and the g-C_3N_4 CNSs using NaCl, KCl and $CaCl_2$ as sacrificial templates. Atomic composition is reported in Table S1 while representative core-level spectra of the sample prepared using $CaCl_2$ as template (10:1 molar ration), is reported in Figure 6.

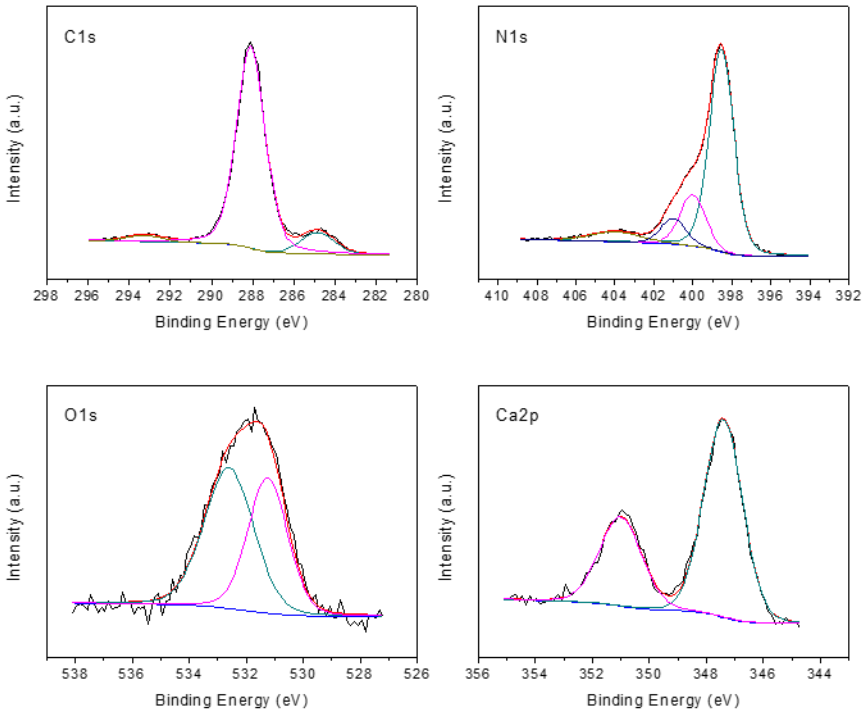

Figure 6. XPS high-resolution spectra for the sample g-C_3N_4 NSs using 10 $CaCl_2$:MLM.

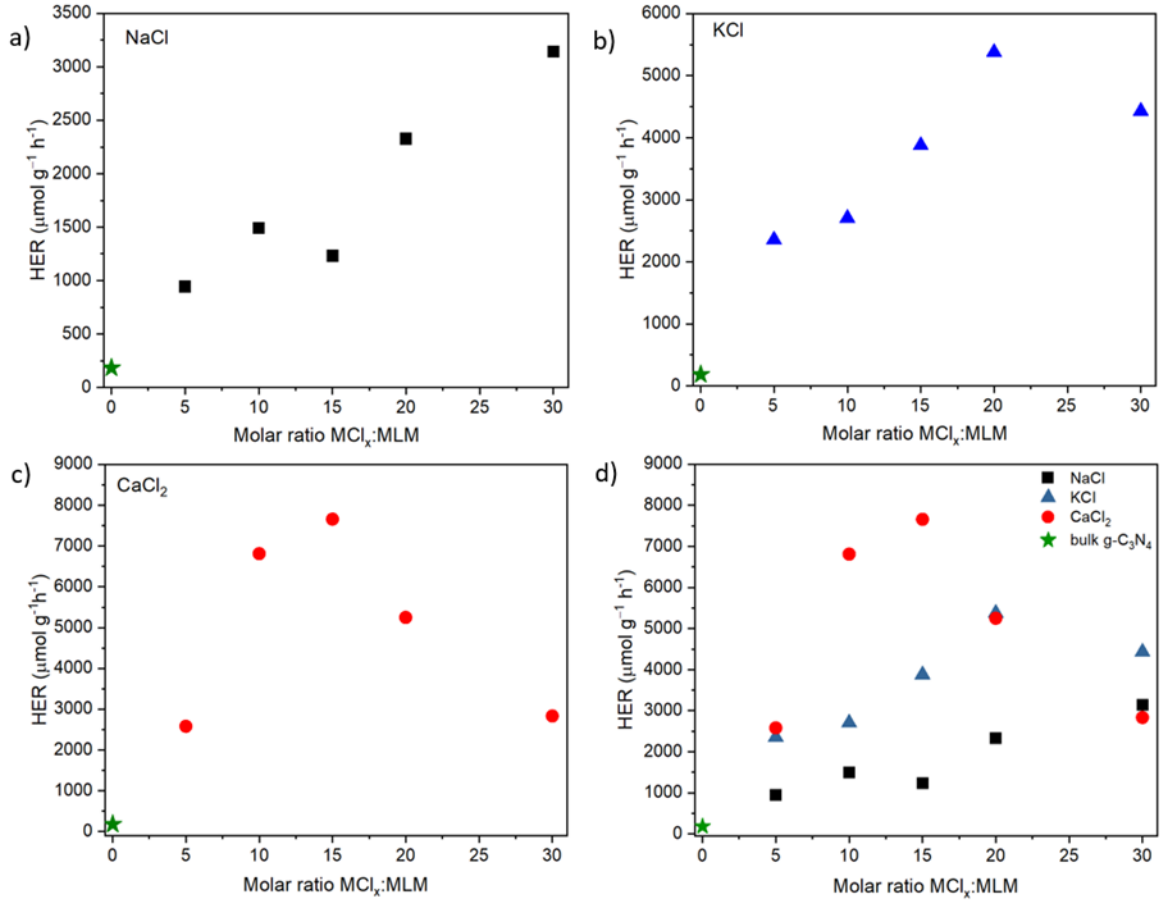

Figure 7. Hydrogen evolution of the bulk g-C_3N_4 and the CNCs synthesized using a) NaCl, b) KCl and c) $CaCl_2$ and d) all the previous data together. The green star represents the H_2 production of the bulk g-C_3N_4; RSD < 20% (*n=4*).

All spectra were best-fitted and assignments were made based on the work reported by D. Morgan (2021).[34] The C1s spectrum consists of three components set at 284.8 eV, 288.1 eV and 293.3 eV, assigned to sp^3-carbon, C in C-N-C and to satellite structure, respectively.[35] The N1s spectrum is characterized by four components: the one at 398.5 eV is ascribed to sp^2-bonded nitrogen in C-N=C, the following peak at 399.5 eV corresponds to the N in tertiary group N-$(C)_3$, while at 400.8 eV is due to amino-functional groups with H atoms.[36] Finally, the broader peak cantered at 404.5 eV is the satellite structure. Oxygen is present in the sample as contamination, and the core-level spectrum could be best-fitted with two peaks, placed at 531.5 eV which is typical of metal hydroxide and a second component at 532.9 eV, assigned to hydroxyl groups. Finally, the Ca2p spectrum consists of a doublet with the main component ($Ca2p_{3/2}$) peaked at 347.6 eV. The solar-driven efficiency of all prepared samples was determined in terms of HER under standard test conditions, *viz.* 10% *v/v* TEOA aqueous solution, as a sacrificial agent and 3 *wt*. % platinum

as co-catalyst. Figure 7 shows the HER results as a function of the MCl_x:MLM molar ratio while Table S2 reports the tabulated values of H_2 production for each sample. It was observed that the incorporation of MCl_x salts during the polymerization of MLM resulted in a general increase of the H_2 production as the MCl_x:MLM molar ratio increases, regardless of the metal halide used. However, significant differences were observed for each salt relative to the peak of highest production. For example, when NaCl is used there is a linear increase of the H_2 production as the molar ratio increases, with the highest H_2 production at around 3144 μmol g^{-1} h^{-1}, for the 30:1 NaCl:MLM ratio, which represents a 17-fold increase in the H_2 production compared to bulk g-C_3N_4 (183 μmol g^{-1} h^{-1}). The favorable H_2 production along the increasing MCl_x:MLM molar ratio reasonably results from the combination of several factors, namely the stronger absorption in the visible range (for the NaCl and KCl preparations), the formation of cyano groups, vacancies and cation doping, as well as an increase of surface area, especially for the catalysts prepared using NaCl and $CaCl_2$. As a matter of fact, Cao S. et *al*. (2017) performed DFT calculations of pristine g-C_3N_4 and Na–P co-doped g-C_3N_4 showing that interstitial sodium doping can change the electron density in the g-C_3N_4 plane by favoring the electron release from the surface of the g-C_3N_4 thus improving the H_2 production.[37] Reports in the literature using NaCl as sacrificial template found optimal H_2 production values in the range 460-2800 μmol/g/h.[16-17, 38] Table 3 summarizes the H_2 production rates reported in the current literature when using different salts as sacrificial templates, including NaCl and KCl. Figure 7b shows the H_2 evolution values when KCl is used as sacrificial template. The results show a linear increase in the H_2 photoproduction up to 5376 μmol g^{-1} h^{-1} for the 20:1 KCl:MLM molar ratio, which corresponds to a 29-fold increase in H_2 production compared to bulk g-C_3N_4. Reported values in the literature for photocatalytic H_2 evolution carried out by mixing KCl and bulk g-C_3N_4, at a mass ratio of 15:1 KCl:bulk g-C_3N_4, lead to a production of 5238 μmol g^{-1} h^{-1}.[19] In another report HER of around 4000 μmol g^{-1} h^{-1} was achieved by using a small amount of KCl mixed with thiourea to create cyanamide defects in the CN sheets.[20] DFT calculations performed by Xiong et *al*. (2016) for K^+ and Na^+ ions doping on g-C_3N_4 demonstrated that K^+ are intercalated into the space between layers and could decrease the electronic localization and extend the π conjugated system, while Na^+ tends to enter the caves of the CN planes.[39] Consequently, the presence of K^+ intercalated into the CNCs sheets improves the charge carrier transfer between adjacent layers while Na^+ doping increased the in-planar electron density.[39] The incorporation of $CaCl_2$ during the synthesis of g-C_3N_4 leads to a completely different behavior in the H_2 production as the MCl_x:MLM

molar ratio increases (Figure 7c). The results indicate an increase in the H_2 production up to 6813 µmol g^{-1} h^{-1} when the $CaCl_2$:MLM molar ratio is 10:1 and up to 7657 µmol g^{-1} h^{-1} when the molar ratio is 15:1. Higher molar ratios lead to a decrease in the HER, for instance 5249 µmol g^{-1} h^{-1} and 2835 µmol g^{-1} h^{-1} are measured when the molar ratios $CaCl_2$:MLM are 20:1 and 30:1, respectively. The reason for this peaked behavior is not fully understood and will be subject of future computational and advanced characterization investigations.

Table 3. Hydrogen evolution rate (HER) of CNCs synthesized using different sacrificial templates.

Template	Precursor	HER (μmol g^{-1} h^{-1})	Experimental conditions	Ref.
$NaHCO_3$	DCD	1 010	Synthesis: 2 g DCD + 0.1 g $NaHCO_3$ (550°C/4 h/3°C min^{-1}). Photocatalysis: 1 % *wt* Pt, 0.63 $g_{Catalyst}$/L, 25°C, 50 W/m^2.	[11c]
NaCl	MLM	2 400	Synthesis:10:1 NaCl/MLM *wt.* ratio (600°C/4 h/2.3°C min^{-1}). Photocatalysis: 3 % *wt*. Pt, 1.3 $g_{Catalyst}$/L, 10 % *v/v* TEOA, 25°C, 50 W/m^2.	[17]
NaCl	DCD	2 801	Synthesis: 30:1 NaCl/DCD *wt*. ratio (550°C/4 h/2.3°C min^{-1}). Photocatalysis: 3 % *wt*. Pt, 1.1 $g_{Catalyst}$/L, 10 % *v/v* TEOA, 25°C, 300 W Xenon lamp.	[38]
NaCl	DCD	459	Synthesis: 10:1 NaCl/DCD molar ratio (600°C/4 h/2.3°C min^{-1}). Photocatalysis: 3 % *wt*. Pt, 0.2 $g_{Catalyst}$/L, 10 % *v/v* lactic acid, 25°C, 300 W Xenon lamp.	[16]
KCl	MLM	5 238	Synthesis: 1.5 g bulk g-C_3N_4 + 10 g KCl (600°C/2 h/10°C min^{-1}). Photocatalysis: 3 % *wt*. Pt, 1 $g_{Catalyst}$/L, 20 % *v/v* TEOA, 15°C, 300 W Xenon lamp.	[19]
KCl	Thiourea	4 000	Synthesis: 10 g thiourea + 0.03 g KCl (600°C/2h/2.5 °C min^{-1}). Photocatalysis: 3 % *wt*. Pt, 0.63 $g_{Catalyst}$/L, 15 % *v/v* TEOA, 1200 W/m^2.	[20]
NaCl	MLM	3 144	Synthesis: 30:1 NaCl/MLM molar ratio (550°C/4 h/4°C min^{-1}). Photocatalysis: 3 % *wt.* Pt, 1 $g_{Catalyst}$/L, 10 % *v/v* TEOA, 1500W Xenon lamp, 500 W/m^2.	**This work**
KCl	MLM	5 376	Synthesis: 20:1 KCl/MLM molar ratio (550°C/4 h/4°C min^{-1}). Photocatalysis: 3 % *wt.* Pt, 1 $g_{Catalyst}$/L, 10 % *v/v* TEOA, 1500W Xenon lamp, 500 W/m^2.	**This work**

$CaCl_2$	MLM	7 657	Synthesis: 15:1 $CaCl_2$/MLM molar ratio (550°C/4 h/4°C min^{-1}). Photocatalysis: 3 % *wt.* Pt, 1 $g_{Catalyst}$/L, 10 % *v/v* TEOA, 1500W Xenon lamp, 500 W/m^2.	**This work**

Dicyandiamine (DCD), melamine (MLM), hydrogen evolution rate (HER), triethanolamine (TEOA).

A previous work conducted by Teixeira ***et al***. using g-C_3N_4 for photocatalytic H_2 evolution in the presence of alkali chlorides found a positive correlation between the H_2 production and the hydration energy of the cations.[17] The authors suggest that the presence of cations in the solution pulls the oxygen atoms from the water molecule making the hydrogen protons more mobile which, in turn, promotes the proton migration to the surface of Pt according to the Volmer step, forming the intermediate adsorbed hydrogen species, according to the following reaction:

$$2H_2O + Pt + 2e^- \rightleftharpoons 2Pt - H_{ads} + 2OH^- \quad (1)$$

As a consecutive step, molecular H_2 is being produced, showed by the Heyrovsky and Tafel steps, respectively:

$$H_2O + 2Pt - H_{ads} + e^- \rightleftharpoons Pt + H_2 + OH^- \quad (2)$$

$$2Pt - H_{ads} \rightleftharpoons Pt + H_2 \quad (3)$$

The authors proposed that the presence of cations in photocatalytic hydrogen evolution, in addition, favours the equilibrium of the Heyrovsky step to the products by stabilizing the OH^- ions. EPR spectroscopy has recently found wide applications in the field of polymer science[37] and, in particular, in the g-C_3N_4 framework.[38] EPR measurements were performed on our samples at room temperature to investigate the presence of nitrogen vacancies and possibly to relate them to the efficiency of the H_2 production. Indeed, they are generally considered to be one of the main factors responsible for the increase H_2 production by increasing the MClx:MLM ratio. Figure 8 shows, as representative case for each sacrificial template, the EPR spectrum obtained for the NSs displaying the highest H_2 production, *i.e.* 30:1 NaCl:MLM, 20 KCl:MLM and 15:1 $CaCl_2$:MLM. These three signals are centered at the same g-value (2.0034 ± 0.0001). A unique signal with linewidth of about 4 G is observed in the case of NaCl and KCl incorporation while the superposition of at least two differently wide signals is evident in the case of $CaCl_2$ incorporation. The spectrum of bulk

g-C_3N_4 synthesized from MLM is also reported as a reference signal because this material should be characterized by a low degree of vacancies. Only negligible deviations from a diamagnetic response can be observed in this last case. The results for all the investigated NSs, synthesized adding the three different sacrificial agents, are reported in Figure S9, together with the spectrum obtained for bulk g-C_3N_4, shown as reference signal. A low intensity EPR signal centered at a g-value between 2.003 and 2.005 was observed for all the NSs. As shown in Figure 8 and in Figure S9, the incorporation of either NaCl, KCl or $CaCl_2$ had a different effect on the EPR spectrum features. In most cases a narrow, nearly isotropic signal is recorded. This type of signal obtained for these materials has already been attributed to localized unpaired electrons hosted in the *p* orbital belonging to a sp^2 hybridized C atom and has been finally correlated to the formation of nitrogen vacancies.[40] When NaCl is used as a sacrificial template, a trend of the signal intensity with respect to the NaCl:MLM ratio is difficult to be outlined, due to the spread in the EPR linewidth values, in addition to the low intensity of the signals. As a result, a relationship between the degree of nitrogen vacancies and H_2 production can be hardly defined in this case. However, undoubtedly the most intense signal comes from the g-C_3N_4 synthesized at a molar ratio of 30 NaCl:MLM, *i.e.* the one corresponding to the highest H_2 production within the NaCl series. Opposite, when KCl is used as sacrificial template most of the signals shows very similar line shape and linewidth and a positive correlation between signal intensity - then the degree of vacancies - and the molar ratio KCl:MLM occurs. For this set of samples, characterized by the highest degree of crystallinity, the highest amount of vacancies comes from the 20:1 and 30:1 KCl:MLM, which also had the highest H_2 production values within this series (5376 and 4429 μmol/g/h, respectively). When $CaCl_2$ was used as sacrificial template, all the EPR spectra showed a more complex and wider lineshape, generally due to the superposition of different contributions. This is possibly consistent with a generally “disordered” environment. This material displays higher porosity and is more exfoliated with respect to those obtained with the use of NaCl or KCl as sacrificial templates and it shows the highest SSA values, too (see Table 1). Besides, small quantities of $CaCO_3$ are present as impurity phases. However, it is worth noticing that the series obtained with $CaCl_2$ shows the lowest N/C ratio (Table S1) among the investigated series of samples so it would logically present higher density of nitrogen vacancies. This could be consistent with the generally higher EPR signal intensity, related to the EPR linewidth markedly broader with respect to those observed for NaCl and KCl series. Only for 15:1 $CaCl_2$:MLM a narrow signal, similar to the nearly isotropic signals typically recorded for NaCl and KCl series, is observed superimposed to broader lines. We

recall here that this is just the case showing the highest H_2 production. Finally, measurements on the available EPR standard, carried out under the same experimental conditions used for the NSs, allowed us to estimate, by comparison of signal intensities, that the average amount of paramagnetic centres with spin s=1/2 responsible for the observed EPR signals is of the order of parts per million. The electrons from the localized π-conjugated structure cannot move freely in the whole 2D g-C_3N_4 plane, as they only move freely within the heptazine ring. This behaviour endows g-C_3N_4 a poor electrical and thermal conductivity, but good semiconducting properties such as visible light response and a much negative VB potential.[40a] In a photocatalytic experiment, when the g-C_3N_4 is irradiated, the electrons move from the σ-type bonds to the π-type bonds, which corresponds to the fact that electrons move from the VB (composed of 2*s* and 2*p* orbits of carbon and nitride atoms) to the CB (composed of approximate half 2*p* orbits of carbon atoms and nitride atoms).[40b]

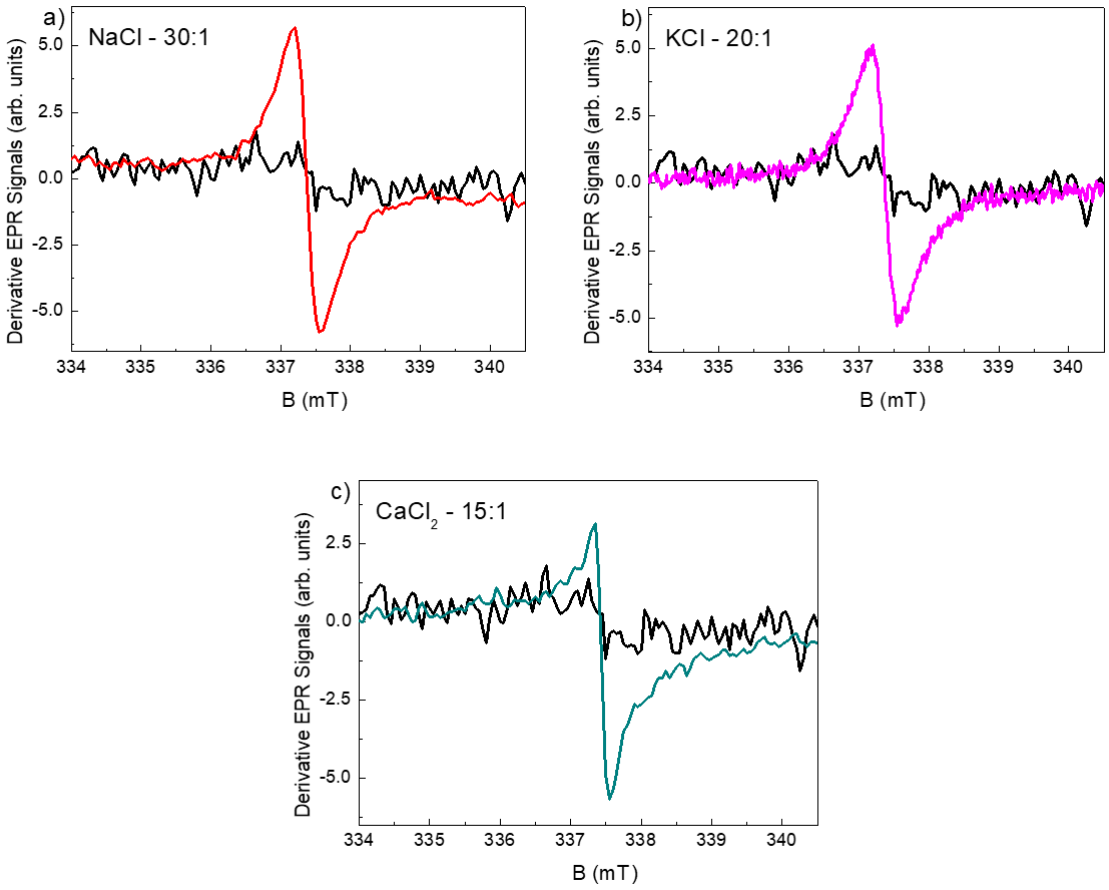

Figure 8. EPR spectrum of the CNC NSs with MCl_x:MLM molar ratio corresponding to the highest H_2 production for each sacrificial template: a) NaCl, b) KCl and c) $CaCl_2$. The spectrum of the bulk g-C_3N_4 is reported in each figure as reference signal (black line).

3. CONCLUSION

Different carbon nitride compounds (CNCs) were synthesized using MLM and different molar ratios of NaCl, KCl and $CaCl_2$ as sacrificial templates. The incorporation of each salt (MCl_x) had a different effect on the morphological, optical and structural properties of the CNCs and consequently in the performance of the photocatalyst for H_2 production. The use of NaCl and $CaCl_2$ as sacrificial templates led to the production of exfoliated g-C_3N_4, whereas KCl induced the formation of poly(heptazine imide). SEM and TEM micrographs showed an evident change in the morphology by changing the template. Nevertheless, all the samples show a higher exfoliation degree by increasing the MCl_x:MLM molar ratio. A shift of the optical absorption threshold was observed with respect to the bulk g-C_3N_4, with the addition of NaCl and KCl producing a very small red shift, while $CaCl_2$ led to a reasonably small blue shift. A reduction of photoluminescence decay was also observed for all samples. EPR and FTIR experiments indicated the formation of vacancies or cyano groups, which play a crucial role in the performance of the CNCs for H_2 production. The highest H_2 evolution rates observed were about 5380 μmol g^{-1} h^{-1} using KCl and 3140 μmol g^{-1} h^{-1} using NaCl, with a significative improvement achieved using $CaCl_2$ as the template (7657 μmol g^{-1} h^{-1}), most probably related to the superior porosity and surface area of these specimens. This work has provided further evidence for r the synthesis of inexpensive, safe and highly performance photocatalysts for H_2 production under solar radiation. Further work will be addressed to their application for green H_2 production under sustainable conditions.

4.EXPERIMENTAL SECTION

Synthesis of bulk CNCs and CNC nanosheets

CNC NSs were synthesized by the thermal polymerization of MLM (Sigma Aldrich, 99 %) in the presence of a metal halide salts, namely NaCl (Sigma Aldrich, 99 %), KCl (Sigma Aldrich, 99 %) or $CaCl_2•2H_2O$ (AlfaAesar, 99 %). Before use, the salts were dehydrated in a furnace at 120°C for 24 h. Different molar ratios of the metal chloride (MCl_x) to melamine, MCl_x:MLM, (5:1, 10:1, 15:1, 20:1 and 30:1) were tested. The MCl_x and the MLM were finely ground and mixed using a pestle and a mortar and placed in an alumina crucible. Thermal polymerization was carried out under N_2 atmosphere at 550° C, 4° C min^{-1}, 4 h dwell and allowed to cool down. The g-C_3N_4 was added to 80 mL of DI water and sonicated for 20 minutes to dissolve the salts. The suspension was filtered and rinsed thoroughly using DI water. All samples were dried at 65° C for 6 hours and finely ground in a mortar. As a reference material, bulk g-C_3N_4 was synthesized by polymerization of MLM using the same thermal treatment without the incorporation of MCl_x during the synthesis.

Characterization

The crystal structure of the samples was acquired at room temperature Cu-radiation X-ray diffraction (XRD) using a Bruker D2 diffractometer. Diffuse reflectance spectroscopy spectra were obtained in the wavelength range 250-850 nm using a Jasco V-750 spectrophotometer, equipped with an integrating sphere (Jasco ISV-922). Microstructural characterization of the samples was achieved via a high-resolution scanning electron microscope (SEM, TESCAN Mira 3) operated at 20 kV. Specific surface area was determined out via Brunauer, Emmett and Teller (BET) single point method (Flowsorb II 2300, Micromeritics, US). Each sample was weighed (~ 300 mg) were degassed at 120 °C for 2 hours under a continuous stream of a N_2 : He 30 : 70 mixture. Gas adsorption was then achieved by placing the sample in liquid nitrogen, followed by gas desorption by placing the sample in water. Three replicates were made for each sample. Transmission electron microscopy (TEM) micrographs of the CNCs were taken by a JEOL JEM-1200 EX II microscope operating at 100 kV, equipped with a tungsten filament as electron source. Fourier Transform Infrared (FTIR) analyses were conducted using a Nicolet FTIR iS10 spectrometer (Nicolet, Madison, WI, USA) equipped with Smart iTR with diamond plate. The analysis was conducted by collecting 32 scans from 4 000 to 600 cm^{-1} and 4 cm^{-1} of resolution. The photoluminescence (PL) spectra were recorded by means of a Fluorolog®-3 spectrofluorometer (HORIBA Jobin-Yvon), equipped with a 450 W xenon lamp as exciting source and double grating excitation and

emission monochromators. All the optical measurements were performed at room temperature on powder dispersed samples as obtained from the synthesis without any size sorting treatment. The PL emission spectra were recorded by using an excitation wavelength of 350 nm. Time-Resolved PL (TRPL) measurements were carried out by Time Correlated Single Photon Counting (TCSPC) technique, with a FluoroHub (HORIBA Jobin-Yvon). CDs solutions were excited using 80 ps laser diode sources at 375 nm (NanoLED 375L). Time resolution was ~300 ps for all the measurements. Surface chemical composition was investigated by X-ray photoelectron spectroscopy (XPS) analyses with a PHI 5000 Versa Probe II spectrometer (Physical Electronics) equipped with a monochromatic Al Kα X-ray source (1486.6 eV), operated at 15 kV and 24.8 W, with a spot size of 100 μm. Survey (0–1400 eV) and high-resolution spectra were recorded in FAT (Fixed Analyser Transmission) mode at a pass energy of 117.40 and 29.35 eV, respectively. Surface charging was compensated using a dual beam charge neutralization system. The hydrocarbon component of C1s spectrum was used as internal standard for charging correction and it was fixed at 284.8 eV. Spectra were processed with MultiPak software (Physical Electronics). Electron paramagnetic resonance (EPR) experiments were conducted at room temperature by using a Bruker spectrometer in the X-band (about 9.46 GHz), with microwave power of 62 mW and a peak-to-peak modulation field of 0.05 mT. Particular care was taken in positioning the samples in the resonator and in determining the sample mass, which was kept around ten milligrams for each sample. A suitable standard (Varian Pitch, g=2.0028) was used both for the instrumental calibration and to estimate the number of paramagnetic centers by comparison of signal intensities.

Photocatalytic hydrogen experiments

Hydrogen evolution experiments took place in Pyrex glass containers (28 mL) containing 24 mL of an aqueous solution 10 % (v/v) triethanolamine (TEOA, Aldrich, ≥ 99%) and 24 mg of the photocatalyst (1 g catalyst/L solution). Oxygen was removed by argon bubbling for 20 min, then 42 μL of a 0.08 M H_2PtCl_6 solution (hexachloroplatinic acid hydrate, 38 % Pt basis, Sigma Aldrich) as the Pt co-catalyst precursor (*in situ* photodeposited on the catalyst during irradiation) was added to the suspension, and the photoreactors were sealed using sleeve stopper septa. Irradiation was performed under simulated solar light (1500 W Xenon lamp, 300-800 nm) using a Solar Box 1500e (CO.FO.ME.GRA S.r.l.) at 500 W/m^2 for 6 hours. Four independent experiments were performed on all samples. The headspace evolved gas was

quantified by gas chromatography coupled to thermal conductivity detection (GC-TCD). The H_2 evolution is expressed as μmol *per* gram of catalyst *per* hour of irradiation (μmol g^{-1} h^{-1}).

Supporting Information

The authors added in the supporting information additional details: XRD patterns of the CNCs synthetized using $CaCl_2$:MLM; SEM and TEM micrographs of the CNCs at different molar ratios MCl_x:MLM; Absorbance spectra for the CNCs; atomic percentage obtained by XPS of the CNCs; Hydrogen evolution rate for the CNCs; PL decay of the CNCs and EPR spectra of the CNCs.

Acknowledgements

L.M. and A.L. acknowledge support from the Italian Ministry of University and Research through PRIN 2022 Grant No. P20223HSWX with title A bio-inspired chemical approach for agro-industrial waste valorization (BEAGLE) funded by European Union – Next Generation EU. A.L. acknowledge the financial support from the University of Bari "Aldo Moro", within the Horizon Europe Seeds programme, Project S13 - "CARBON-ALT, CUP H91I21001600006

The co-author Costanza Tedesco, author of the present Ph.D. work, carried out all the revision of the experimental part of the paper and part of the synthesis and characterization of the photocatalytic materials.

References

[1] M. Medina-Llamas, A. Speltini, A. Profumo, F. Panzarea, A. Milella, F. Fracassi, A. Listorti, L. Malavasi, *Nanomaterials* 2023, *13*, 263.

[2] M. Aggarwal, S. Basu, N. P. Shetti, M. N. Nadagouda, E. E. Kwon, Y.-K. Park, T. M. Aminabhavi, *Chem. Eng. J.* 2021, *425*, 131402.

[3] A. Alaghmandfard, K. Ghandi, *Nanomaterials* 2022, *12*, 294.

[4] E. Vesali-Kermani, A. Habibi-Yangjeh, S. Ghosh, *J. Ind. Eng. Chem.* 2020, *84*, 185-195.

[5] J. Wen, J. Xie, X. Chen, X. Li, *Appl. Surf. Sci.* 2017, *391*, 72-123.

[6] B. Jürgens, E. Irran, J. Senker, P. Kroll, H. Müller, W. Schnick, *J. Am. Chem. Soc.* 2003, *125*, 10288-10300.

[7] L. Romani, A. Speltini, R. Chiara, M. Morana, C. Coccia, C. Tedesco, V. Armenise, S. Colella, A. Milella, A. Listorti, A. Profumo, F. Ambrosio, E. Mosconi, R. Pau, F. Pitzalis, A. Simbula, D. Ricciarelli, M. Saba, M. Medina-Llamas, F. De Angelis, L. Malavasi, *Cell Reports Physical Science* 2023, *4*.

[8] K. Schwinghammer, B. Tuffy, M. B. Mesch, E. Wirnhier, C. Martineau, F. Taulelle, W. Schnick, J. Senker, B. V. Lotsch, *Angew. Chem. Int. Ed.* 2013, *52*, 2435-2439.

[9] M. Shalom, S. Inal, C. Fettkenhauer, D. Neher, M. Antonietti, *J. Am. Chem. Soc.* 2013, *135*, 7118-7121.

[10] L. Lin, P. Ye, C. Cao, Q. Jin, G.-S. Xu, Y.-H. Shen, Y.-P. Yuan, *Journal of Materials Chemistry A* 2015, *3*, 10205-10208.

[11] aJ. Zhao, L. Ma, H. Wang, Y. Zhao, J. Zhang, S. Hu, *Appl. Surf. Sci.* 2015, *332*, 625-630; bX. Qu, S. Hu, J. Bai, P. Li, G. Lu, X. Kang, *Journal of materials science & technology* 2018, *34*, 1932-1938; cX. Wu, H. Ma, W. Zhong, J. Fan, H. Yu, *Applied Catalysis B: Environmental* 2020, *271*, 118899.

[12] J. Yan, X. Han, X. Zheng, J. Qian, J. Liu, X. Dong, F. Xi, *Mater. Res. Bull.* 2017, *94*, 423-427.

[13] J. Li, M. Zahid, W. Sun, X. Tian, Y. Zhu, *Appl. Surf. Sci.* 2020, *528*, 146983.

[14] A. Jin, X. Liu, M. Li, Y. Jia, C. Chen, X. Chen, *ACS Sustainable Chemistry & Engineering* 2019, *7*, 5122-5133.

[15] aM. J. Bojdys, J. O. Müller, M. Antonietti, A. Thomas, *Chemistry–A European Journal* 2008, *14*, 8177-8182; bM. Chang, Z. Pan, D. Zheng, S. Wang, G. Zhang, M. Anpo, X. Wang, *ChemSusChem* 2023, e202202255.

[16] F. Yang, D. Liu, Y. Li, L. Cheng, J. Ye, *Applied Catalysis B: Environmental* 2019, *240*, 64-71.

[17] I. F. Teixeira, N. V. Tarakina, I. F. Silva, N. López-Salas, A. Savateev, M. Antonietti, *Advanced Sustainable Systems* 2022, 2100429.

[18] Q. Tang, R. Niu, J. Gong, *New J. Chem.* 2020, *44*, 17405-17412.

[19] G. Zhang, Y. Xu, D. Yan, C. He, Y. Li, X. Ren, P. Zhang, H. Mi, *ACS Catalysis* 2021, *11*, 6995-7005.

[20] J. Yuan, X. Liu, Y. Tang, Y. Zeng, L. Wang, S. Zhang, T. Cai, Y. Liu, S. Luo, Y. Pei, *Applied Catalysis B: Environmental* 2018, *237*, 24-31.

[21] C. Hu, Z.-T. Liu, K.-Y. A. Lin, W.-H. Wei, K.-H. Wang, *J. Ind. Eng. Chem.* 2022, *107*, 118-125.

[22] aC. Xu, X. Liu, D. Li, Z. Chen, J. Yang, J. Huang, H. Pan, *ACS Applied Materials & Interfaces* 2021, *13*, 20114-20124; bM. Sturini, A. Speltini, F. Maraschi, G. Vinci, A. Profumo, L. Pretali, A. Albini, L. Malavasi, *Environmental Science and Pollution Research* 2017, *24*, 4153-4161.
[23] L. Yang, X. Liu, Z. Liu, C. Wang, G. Liu, Q. Li, X. Feng, *Ceram. Int.* 2018, *44*, 20613-20619.
[24] aH. Schlomberg, J. Kröger, G. k. Savasci, M. W. Terban, S. Bette, I. Moudrakovski, V. Duppel, F. Podjaski, R. Siegel, J. r. Senker, *Chem. Mater.* 2019, *31*, 7478-7486; bL. Lin, C. Wang, W. Ren, H. Ou, Y. Zhang, X. Wang, *Chemical Science* 2017, *8*, 5506-5511.
[25] Z. Zhao, Z. Shu, J. Zhou, W. Wang, T. Li, J. Chen, *Mater. Res. Bull.* 2022, *145*, 111565.
[26] J. Shi, Z. Liu, Y. Luo, C. Guo, Y. Li, T. Yang, C. Ju, H. Wang, X. Li, Z. Fan, *Colloids Surf. Physicochem. Eng. Aspects* 2021, *623*, 126758.
[27] X. Du, G. Zou, Z. Wang, X. Wang, *Nanoscale* 2015, *7*, 8701-8706.
[28] I. Khan, N. Baig, A. Qurashi, *ACS Applied Energy Materials* 2018, *2*, 607-615.
[29] I. Papailias, T. Giannakopoulou, N. Todorova, D. Demotikali, T. Vaimakis, C. Trapalis, *Appl. Surf. Sci.* 2015, *358*, 278-286.
[30] Y. Xu, Y. Gong, H. Ren, W. Liu, L. Niu, C. Li, X. Liu, *RSC advances* 2017, *7*, 32592-32600.
[31] aG. Liu, S. Yan, L. Shi, L. Yao, *Frontiers in Chemistry* 2019, *7*, 639; bH. Gao, J. Xu, J. Zhou, S. Zhang, R. Zhou, *J. Colloid Interface Sci.* 2020, *570*, 125-134.
[32] J. Fu, C. Bie, B. Cheng, C. Jiang, J. Yu, *Acs Sustainable Chemistry & Engineering* 2018, *6*, 2767-2779.
[33] N. Vagenas, A. Gatsouli, C. Kontoyannis, *Talanta* 2003, *59*, 831-836.
[34] D. J. Morgan, *Surface Science Spectra* 2021, *28*.
[35] M. Medina-Llamas, D. Mattia, *Appl. Surf. Sci.* 2019, *463*, 504-512.
[36] M. Medina-Llamas, C. M. Taylor, J. Ji, J. Wenk, D. Mattia, *Ind. Eng. Chem. Res.* 2020, *59*, 9085-9094.
[37] S. Cao, Q. Huang, B. Zhu, J. Yu, *J. Power Sources* 2017, *351*, 151-159.
[38] Z. Shu, Y. Wang, W. Wang, J. Zhou, T. Li, X. Liu, Y. Tan, Z. Zhao, *Int. J. Hydrogen Energy* 2019, *44*, 748-756.
[39] T. Xiong, W. Cen, Y. Zhang, F. Dong, *Acs Catalysis* 2016, *6*, 2462-2472.
[40] aD. Wei, Y. Liu, Y. Wang, H. Zhang, L. Huang, G. Yu, *Nano Lett.* 2009, *9*, 1752-1758; bP. Xia, B. Cheng, J. Jiang, H. Tang, *Appl. Surf. Sci.* 2019, *487*, 335-342.

Supporting information

SYNTHESIS OF CARBON NITRIDE POLYMORPHS BY SACRIFICAL TEMPLATE METHOD: CORRELATION BETWEEN PHYSICO-CHEMICAL PROPOERTIES AND PHOTOCATALYTIC PERFORMANCE

María Medina-Llamas,[a,b*] Eleonora Bianchi,[c] Maria Cristina Mozzati,[d] Costanza Tedesco,[b] Chiara Milanese,[b] Andrea Speltini,[b] Antonella Profumo,[b] Vincenza Armenise,[e] Antonella Milella,[e] Andrea Listorti[e*] and Lorenzo Malavasi[a*]

---

[a] Unidad Académica Preparatoria, Plantel II.

Universidad Autónoma de Zacatecas

Avenida Preparatoria 98068, Zacatecas, México

[b] María Medina-Llamas, Constanza Tedesco, Chiara Milanese, Andrea Speltini, Antonella Profumo and Lorenzo Malavasi.

Department of Chemistry

University of Pavia

Via Taramelli 12, 27100 Pavia, Italy.

Email: lorenzo.malavasi@unipv.it

[c] Eleonora Bianchi

Department of Drug Science

University of Pavia

Via Taramelli 12, 27100 Pavia, Italy.

[a] Maria Cristina Mozzati

Department of Physics and CNISM

University of Pavia

Via Taramelli 12, 27100 Pavia, Italy.

[e] Vincenza Armenise, Antonella Milella and Andrea Listorti

Department of Chemistry

University of Bari Aldo Moro

Vía Orabona 4,70126, Bari, Italy

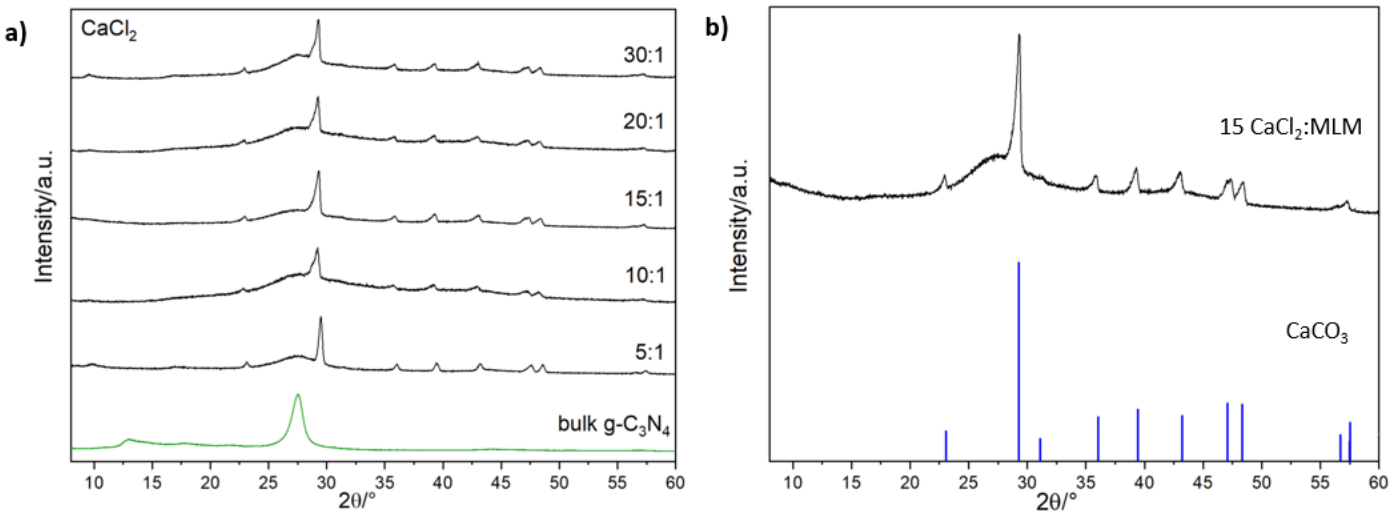

Figure S1. XRD pattern of the a) g-C_3N_4 NSs synthesized using different molar ratios $CaCl_2$:MLM and b) XRD pattern of the g-C_3N_4 NSs obtained using a 15:1 $CaCl_2$:MLM molar ratio and the reference pattern of $CaCO_3$.

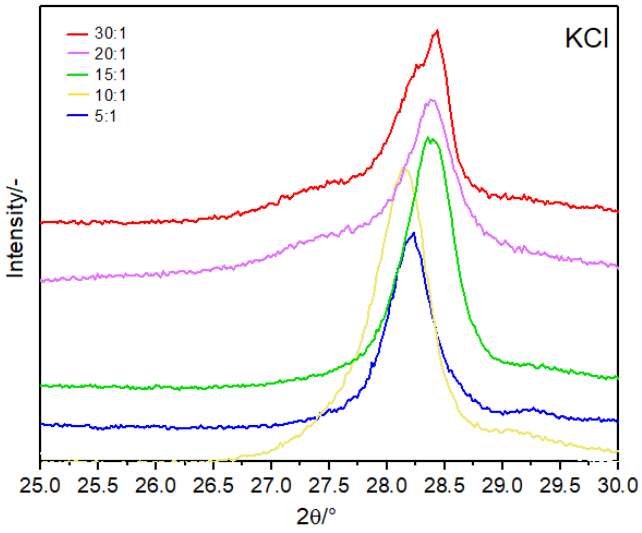

Figure S2. Close up to the (001) plane of the poly(heptazine imide) synthetized using different molar ratios of KCl:MLM.

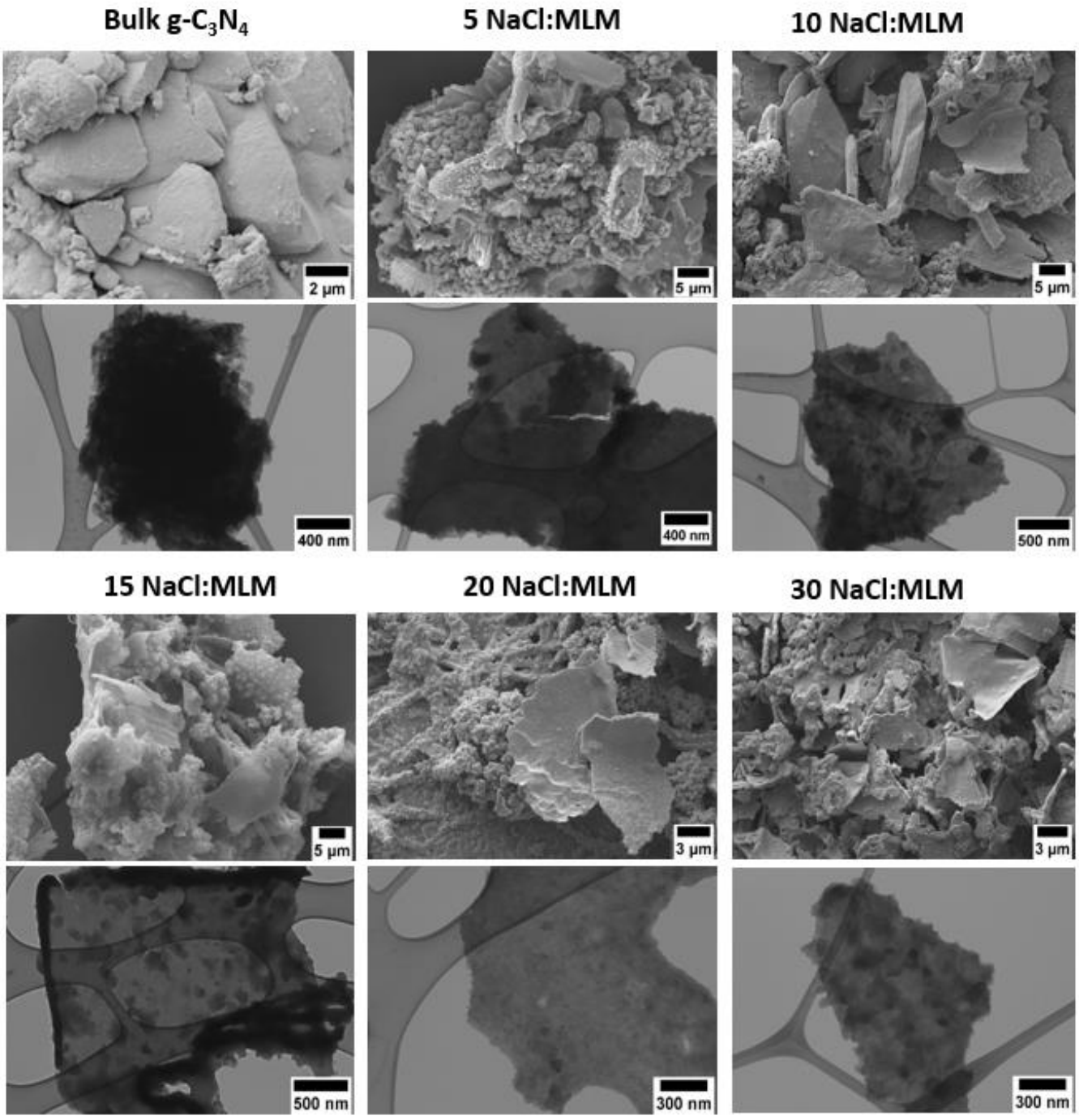

Figure S3. SEM and TEM micrographs of the bulk g-C_3N_4 and the g-C_3N_4 NSs synthetized using different molar ratios NaCl/MLM.

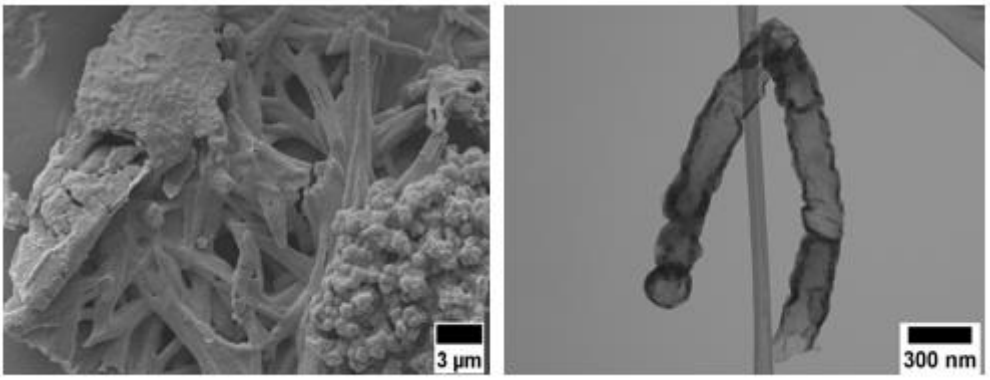

Figure S4. a) SEM and b) TEM micrographs showing different morphologies obtained using NaCl as sacrificial template.

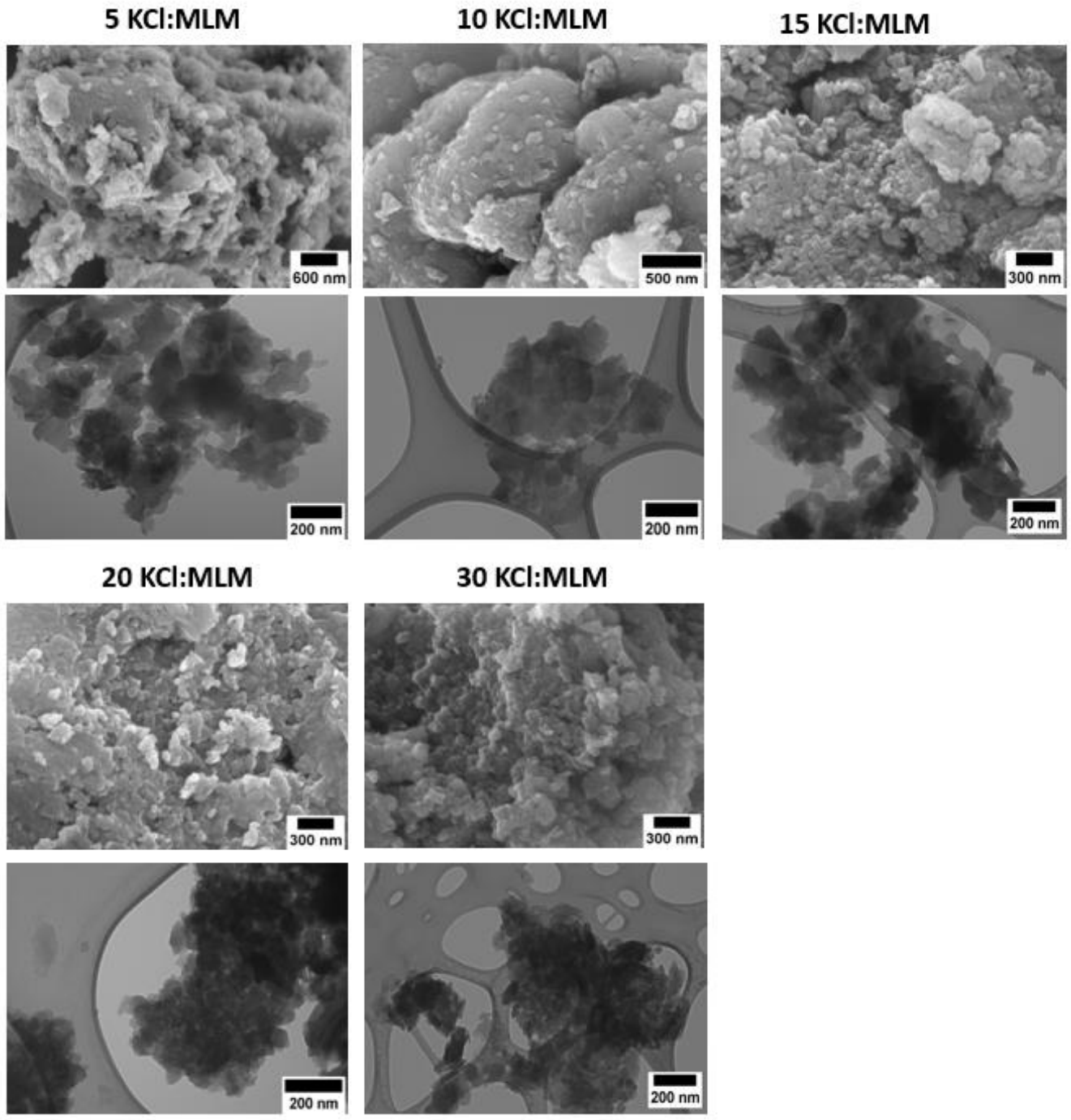

Figure S5. SEM and TEM micrographs of the poly(heptazine imide) synthetized using different molar ratios KCl:MLM

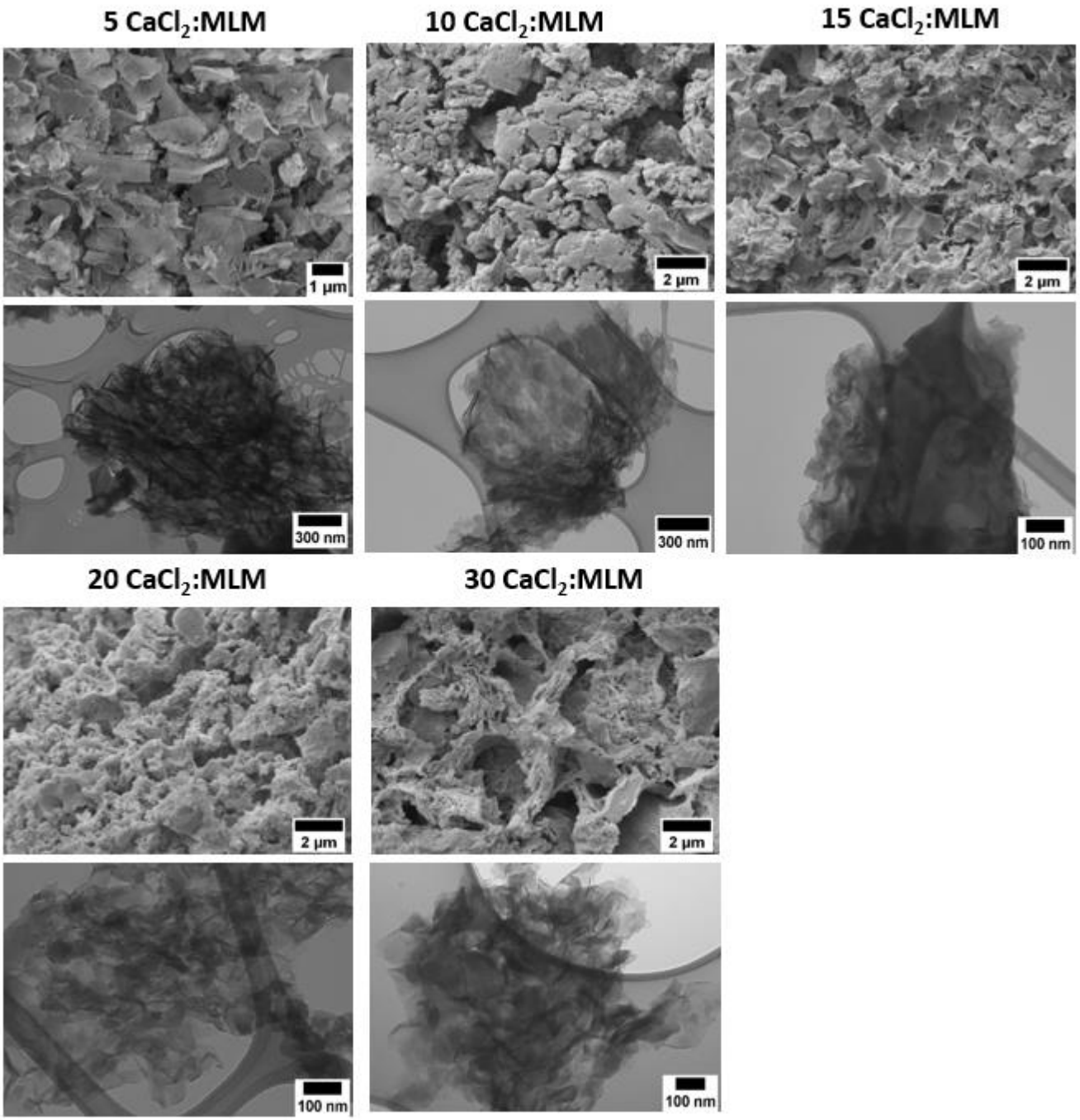

Figure S6. SEM and TEM micrographs of the g-C_3N_4 NSs synthetized using different molar ratios of $CaCl_2$:MLM

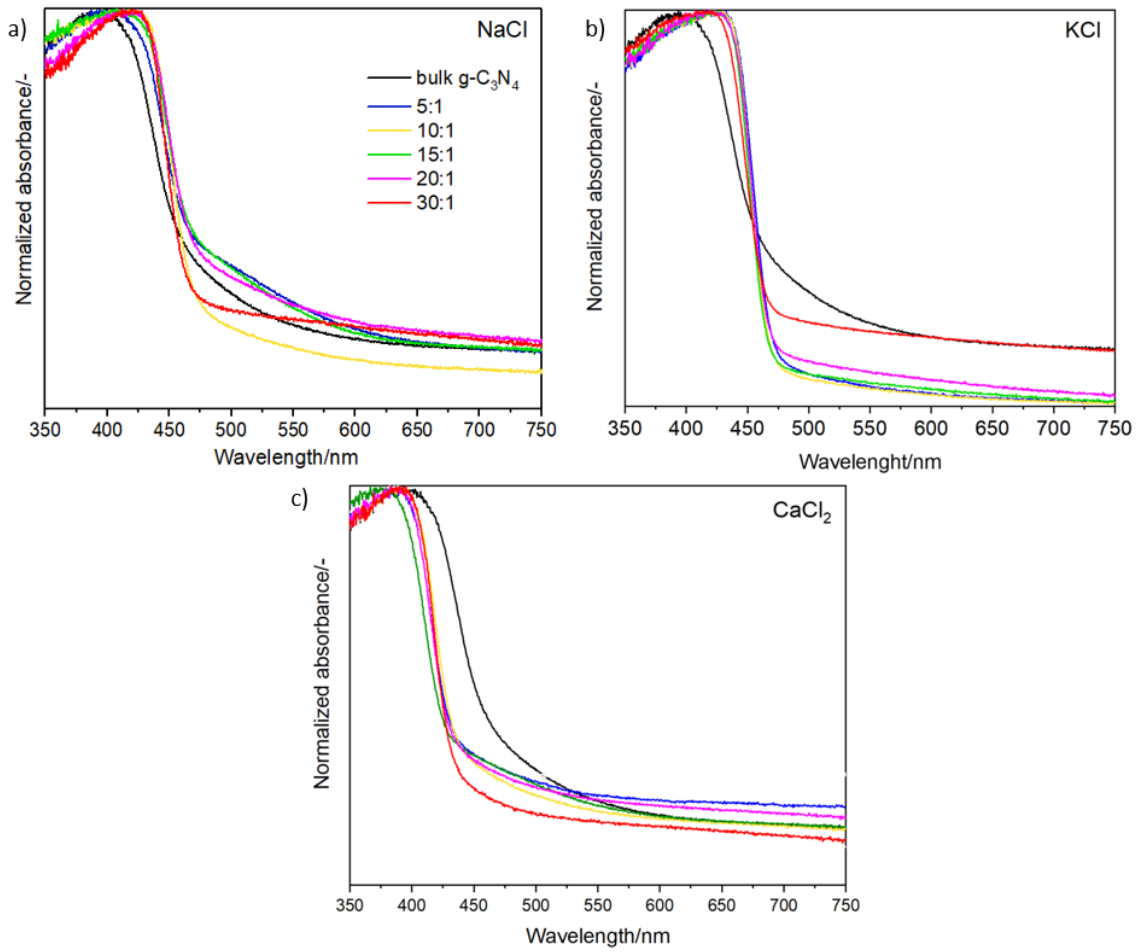

Figure S7. Absorbance spectra versus wavelength of the bulk g-C_3N_4 and the CNCs obtained using NaCl, KCl and $CaCl_2$ as sacrificial templates.

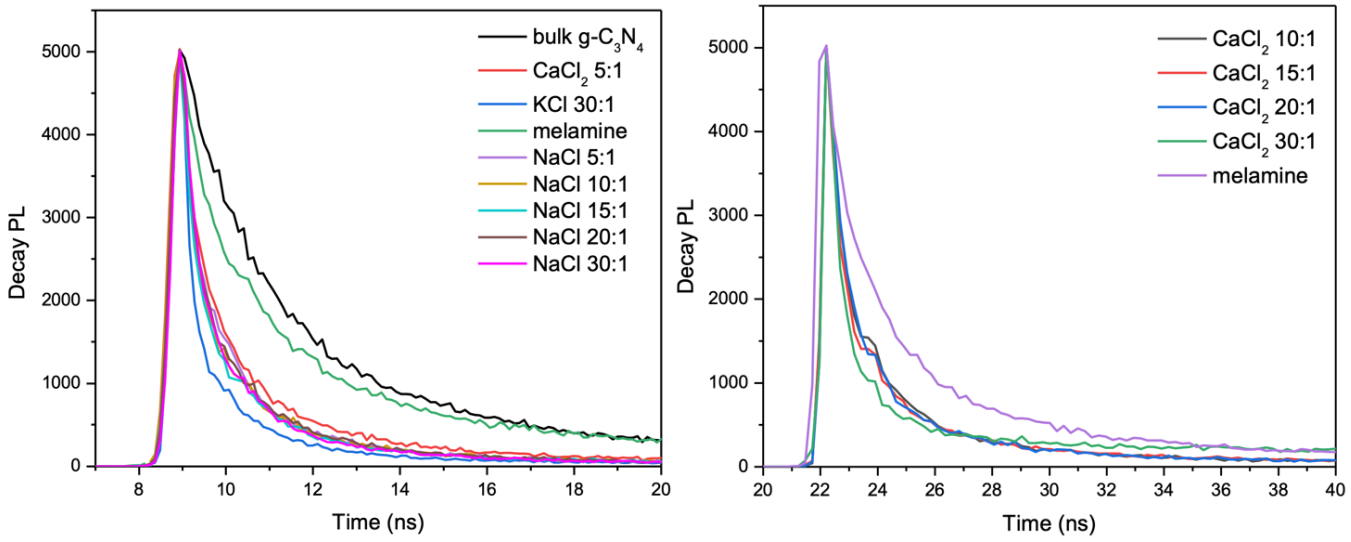

Figure S8. Photoluminescence decays of the bulk g-C_3N_4 and the CNCs obtained using NaCl, KCl and $CaCl_2$ as sacrificial templates.

Table S1. Atomic percentages of the bulk g-C_3N_4 and the CNCs synthesized using NaCl, KCl and $CaCl_2$ as sacrificial templates.

Atomic ratios	% C	% N	% O	% Na	% K	% Ca	% Cl	N/C
Bulk g-C_3N_4	38.4	60.9	0.7	-	-	-	-	1.59
NaCl:MLM								
5:1	43.4	45.6	6.7	4.3	-	-	ND	1.05
10:1	42.1	46.1	6.8	4.9	-	-	0.1	1.10
15:1	42.0	42.6	8.6	6.6	-	-	0.1	1.01
20:1	42.3	43.5	7.9	6.3	-	-	<0.1	1.03
30:1	44.7	40.2	8.4	6.4	-	-	0.3	0.90
KCl:MLM								
5:1	47.4	41.0	5.4	-	5.8	-	0.5	0.86
10:1	40.4	50.4	3.2	-	5.9	-	0.1	1.25
15:1	42.3	47.8	3.8	-	6.0	-	0.1	1.13
20:1	49.2	38.3	5.8	-	6.3	-	0.4	0.79
30:1	45.5	39.5	6.5	-	7.6	-	0.9	0.87
$CaCl_2$:MLM								
5:1	44.2	41.0	11.5			3.3	ND	0.93
10:1	40.9	45.4	9.7	-	-	3.8	0.2	1.11
15:1	49.4	38.7	9.1	-	-	2.8	0.1	0.78
20:1	52.8	34.0	9.30	-	-	3.8	0.1	0.64
30:1	37.4	11.2	28.2	-	-	11.9	11.3	0.30

Table S2. Hydrogen evolution rate (HER) of the bulk g-C_3N_4 and the CNCs synthetized using NaCl, KCl and $CaCl_2$.

	HER (μmol g^{-1} h^{-1}), *n = 4*		
Bulk g-C_3N_4	183		
Molar ratio (MCl_x:MLM)	**NaCl**	**KCl**	**$CaCl_2$**
5	944	2355	2581
10	1492	2703	6813
15	1231	3878	7657
20	2327	5376	5249
30	3144	4429	2835

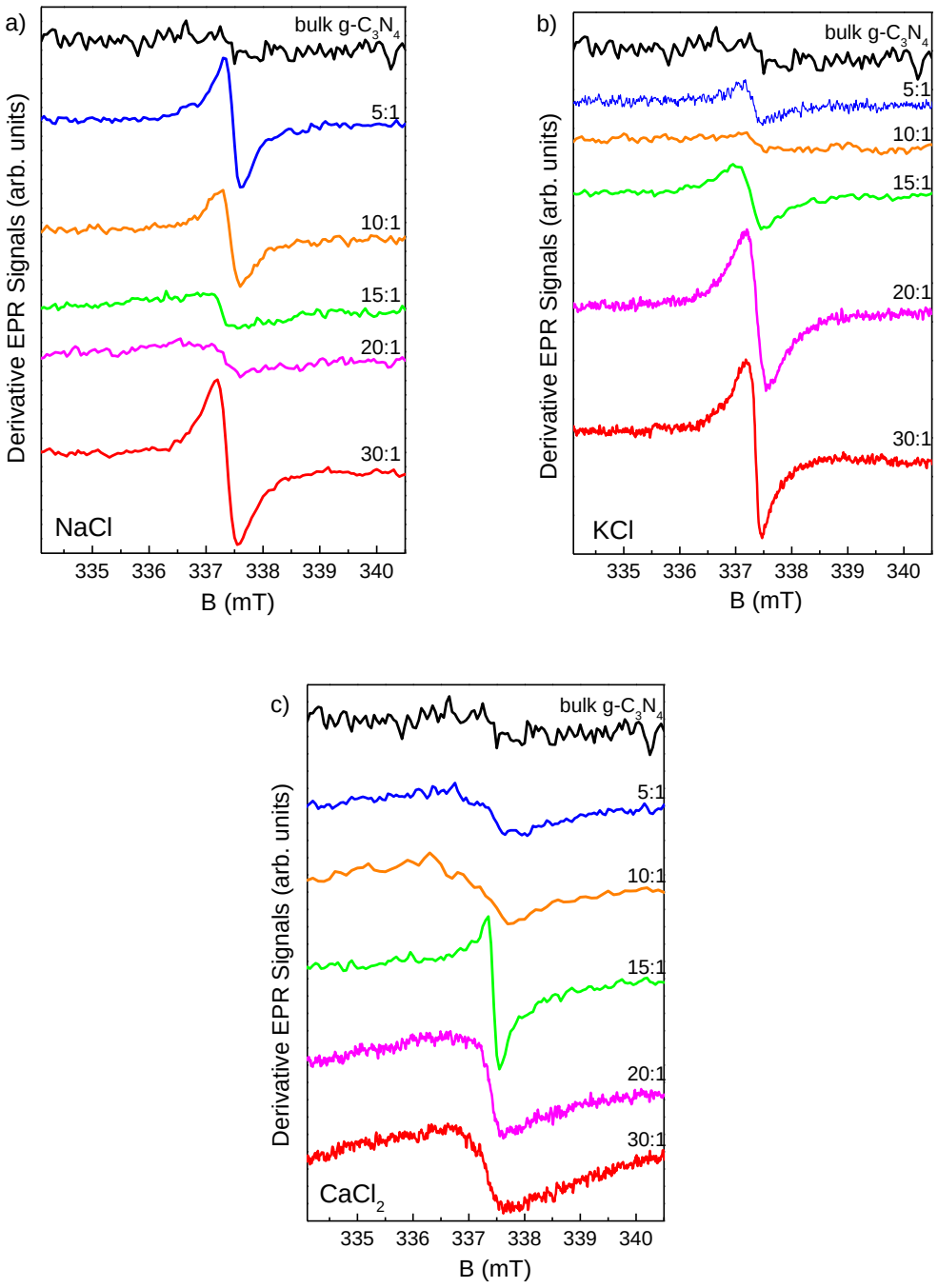

Figure S9. EPR spectra of the bulk g-C_3N_4 and the CNCs obtained using a) NaCl, b) KCl and c) $CaCl_2$ as sacrificial templates at different molar ratios of MCl_x:MLM.

This is an open access article distributed under the terms of the Creative Commons CC BY license, which permits unrestricted use, distribution, and reproduction in any medium, provided the original work is properly cited.

© 2024 The Authors. ChemSusChem published by Wiley-VCH GmbH

CHAPTER 3

Reaction Mechanism of Hydrogen Generation and Nitrogen Fixation at Carbon Nitride/Double Perovskite Heterojunctions

Costanza Tedesco,[a§] Luca Gregori,[b§] Angelica Simbula,[c] Federico Pitzalis,[c] Andrea Speltini,[a] Francesca Merlo,[a] Silvia Colella,[d] Andrea Listorti,[e] Edoardo Mosconi,[f,g] Asma A. Alothman,[g] Waldemar Kaiser,[f] Michele Saba,[c] Antonella Profumo,[a] Filippo De Angelis,[b,f,g,h] Lorenzo Malavasi[a,*]*

[a]Department of Chemistry and INSTM, University of Pavia,Via Taramelli 16, Pavia, 27100, Italy

[b]Department of Chemistry, Biology and Biotechnology, University of Perugia and INSTM, Via Elce di Sotto 8, 06123 Perugia, Italy

[c]Dipartimento di Fisica, Università di Cagliari, 09042 Monserrato, Italy

[d]CNR NANOTEC - c/o Dipartimento di Chimica, Università di Bari, Via Orabona 4, 70126 Bari, Italy

[e]Department of Chemistry, University of Bari “Aldo Moro”, via Orabona 4, 70126, Bari, Italy

[f]Computational Laboratory for Hybrid/Organic Photovoltaics (CLHYO), Istituto CNR di Scienze e Tecnologie Chimiche “Giulio Natta” (CNR-SCITEC), Via Elce di Sotto 8, 06123 Perugia, Italy

[g]Chemistry Department, College of Science, King Saud University, Riyadh 11451, Kingdom of Saudi Arabia

[h]SKKU Institute of Energy Science and Technology (SIEST) Sungkyunkwan University, Suwon, Korea 440-746

Corresponding Authors

Edoardo Mosconi, email: edoardo@thch.unipg.it

Lorenzo Malavasi, email: lorenzo.malavasi@unipv.it

§ CT and LG should be considered joint first author: CT has carried out experimental part while LG has performed computational simulations.

Keywords: Perovskite; hydrogen production; nitrogen fixation; photocatalysis; DFT calculations

Table of Contents (ToC)

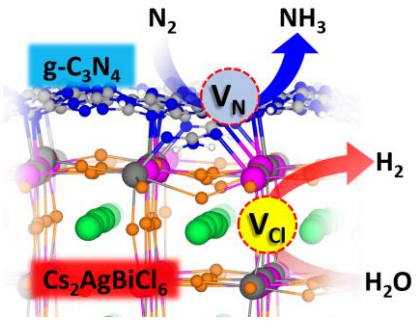

Perovskite halide vacancies are the primary reactive sites for hydrogen generation, withstanding a positive contribution of low loaded g-C_3N_4, in reducing carrier recombination. For nitrogen reduction, instead, the active sites are g-C_3N_4 nitrogen vacancies, and the heterojunction best performs at low perovskites loadings, as the composites maximizes light absorption and reduced carrier losses.

ABSTRACT

Photocatalytically active heterojunctions based on metal halide perovskites (MHPs) are drawing significant interest for their chameleon ability to foster several redox reactions. The lack of mechanistic insights into their performance, however, limits the ability of engineering novel and optimized materials. Herein, we report on a composite system including a double perovskite, $Cs_2AgBiCl_6$/g-C_3N_4, used in parallel for solar-driven hydrogen generation and nitrogen reduction, quantified by a rigorous analytical approach. The composite efficiently promotes the two reactions, but its activity strongly depends on the perovskite/carbon nitride relative amounts. Through advanced spectroscopic investigation and density function theory modelling we studied the H_2 and NH_3 production reaction mechanisms, finding perovskite halide vacancies as the primary reactive sites for hydrogen generation, withstanding a positive contribution of low loaded g-C_3N_4, in reducing carrier recombination. For nitrogen reduction, instead, the active sites are g-C_3N_4 nitrogen vacancies, and the heterojunction best performs at low perovskites loadings, as the composites maximizes light absorption and reduced carrier losses. We believe these insights are important add-ons towards universal exploitation of MHPs in contemporary photocatalysis.

1. INTRODUCTION

Photocatalytic reactions mediated by metal halide perovskites (MHPs) have become a topic of current interest because of the promise of improved low-cost devices for solar fuel production.[1–8] Thanks to their excellent optoelectronic properties, namely tunable band gap, high absorption coefficient, low exciton binding energy, and high carrier mobility, MHPs were successfully applied to a wide range of photocatalytic reactions. Furthermore, a suitable band alignment of MHPs with the most common redox half-reactions allows to run both reduction and oxidation reactions,[1] as confirmed by the recent experimental demonstrations of the two most representative examples, namely hydrogen photogeneration and CO_2 reduction.[1–3,9–15]

With respect to traditional metal oxides photocatalysts, MHPs present a large chemical and structural variety, which allows the design and tailoring the material composition for the envisaged solar-drive reaction. In this respect, both lead-based and lead-free systems have been explored, ranging from 3D to 2D perovskites, perovskite derivatives of general formula $A_3B_2X_9$, and $A_2(BB')X_6$ double perovskites.[16–25]

The general strategy to realize a spatial separation of photo-excited electron-hole pairs in MHPs-based photocatalysts is to design suitable heterojunctions by coupling two semiconductors.[26,27] In addition, the second semiconductor can also act as co-catalyst to improve surface reaction.[28] Again, the high tunability of MHPs allows the design of materials with suitable conduction band (CB) and valence band (VB) offsets to achieve the heterojunction and to provide enough overpotential to drive the target photoreaction.

In recent years, several type II and Z-scheme heterojunction including MHPs have been reported for a range of photocatalytic reactions. The partner semiconductor of choice, in most cases, has been graphitic carbon nitride (g-C_3N_4).[16–18,29–35] g-C_3N_4 is one of the most appealing and performing metal-free photocatalysts having a good absorption in the visible spectrum (band gap of about 2.7 eV), ease of preparation from cheap precursors, it is atoxic, and is stable in both acidic and basic media.[36] In MHPs/g-C_3N_4 heterojunctions, photogenerated electrons tend to migrate and accumulate in g-C_3N_4, where active sites for the photocatalytic reaction are present, while holes from graphitic carbon nitride migrate to the MHP. On the other hand, the perovskite itself can efficiently photogenerate hydrogen by hydrohalic acid splitting, as demonstrated in $MAPbI_3$ (MA=methylammonium) and then in

other systems such as $CsPbBr_3$.[20,37] Moving away from toxic lead, Bi-based perovskite derivatives were also successfully employed in heterojunctions for hydrogen photogeneration.[18,31,35] More recently, significant interest has been triggered by Bi-based double perovskites for their potential use in different photocatalytic reactions, thanks to their superior stability, wide compositional tunability, and good optical properties. $Cs_2AgBiBr_6$ has been investigated for photocatalytic CO_2 reduction, where it has been found that the surface of the perovskites acts as reaction site in the reduction process.[23,33] Fewer reports refer to the hydrogen generation mediated by this double perovskites, with the NiCoP/$Cs_2AgBiBr_6$ heterojunction representing the best report to date with about 400 μmol g^{-1} h^{-1} of evolved hydrogen under 300 W illumination at $\lambda \geq 420$ nm.[38] The proposed mechanism in this system considers an effective transfer of electrons from $Cs_2AgBiBr_6$ to the CB of NiCoP on which the H_2 generation reaction occurs.[38]

While there is an increasing amount of evidence about the effective role of MHPs and MHP-based heterojunctions in running various photocatalytic processes, a detailed description of the reaction mechanism(s) is still lacking. For this reason, herein, we report a combined experimental and computational study on $Cs_2AgBiCl_6$/g-C_3N_4 heterojunctions which has been applied to run two different photocatalytic reactions: hydrogen generation and nitrogen reduction to ammonia, to the best of our knowledge. This last reaction has never been explored before in any MHP-based system. $Cs_2AgBiCl_6$ has been selected based on its optimal moisture stability, suitable band alignment and because it is a lead-free compound. The $Cs_2AgBiCl_6$/g-C_3N_4 composite system has been investigated in the whole weight ratio between perovskite and g-C_3N_4. We found that MHP-rich compositions perform better in the H_2 photogeneration, while g-C_3N_4-rich systems are more effective in the nitrogen photofixation reaction. As reported above, due to the limited microscopic details about the photocatalytic activity of MHP-based heterojunctions, key aim of this work is to provide a comprehensive description of the mechanism underpinning the solar-light mediated reactions in terms of charge carrier dynamics and reaction active sites. This has been achieved through a detailed photophysical and computational modelling study on the prepared systems and for the two photocatalytic reactions investigated providing solid clues about reaction mechanisms. While the application of MHPs-based heterojunction for hydrogen photogeneration is now quite well established, the present work clarifies the suitability of such composite systems to run nitrogen reduction reaction, exploring a new avenue in the photocatalytic application of MHPs.

2. RESULTS AND DISCUSSION

The $Cs_2AgBiCl_6$/g-C_3N_4 systems have been synthesized according to the experimental procedure reported in the Supplementary Information (SI). Weight ratios investigated between $Cs_2AgBiCl_6$ and g-C_3N_4 nanosheets are (wt% of perovskite) 100, 99, 97.5, 95, 90, 85, 82.5, 80, 70, 50, 25, 10, 2.5, and 0. Figure 1a reports the room temperature X-ray diffraction patterns of some selected compositions investigated (corresponding to the best performances, see later in the text).

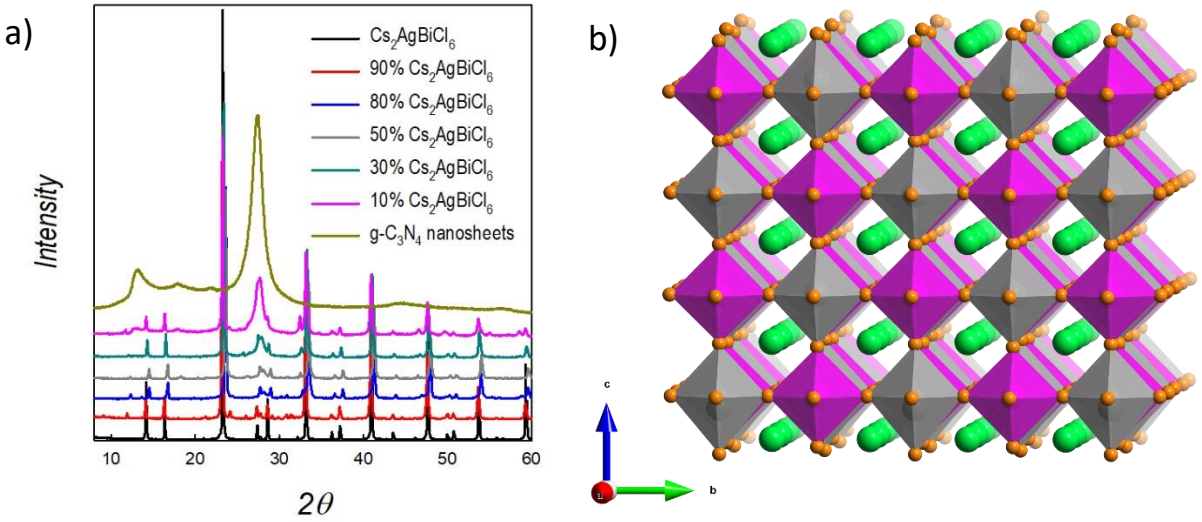

c)

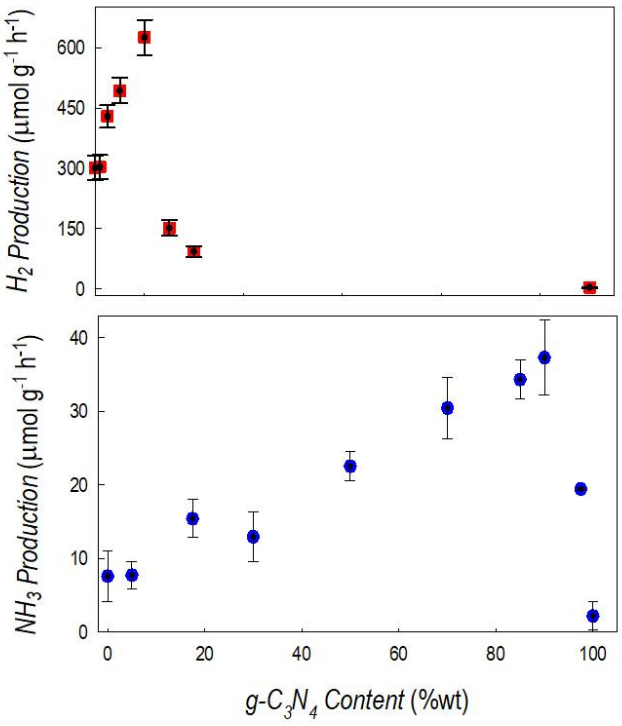

Figure 1. a) XRD pattern of selected $Cs_2AgBiCl_6$/g-C_3N_4 composites; b) sketch of $Cs_2AgBiCl_6$ crystal structure where Cs^+ ions are shown as green spheres, the chloride ions as orange spheres, while the Ag and Bi octahedra are shown as silver and purple polyhedra, respectively; c) hydrogen and ammonia productions as a function of g-C_3N_4 wt% in the composites. (*n*=*3*, simulated solar light, 500 W m^{-2}).

In the bottom part of Figure 1a, the pattern of $Cs_2AgBiCl_6$ double perovskite is reported (with a sketch of its crystal structure in Figure 1b), displaying a cubic symmetry with *Fm3̄m* space group (#225) and a lattice parameter of 10.7761(2) Å, in agreement with previous results.[39] Figure S1 shows a comparison between experimental and calculated pattern for $Cs_2AgBiCl_6$. At the top of Figure 1a, the X-ray pattern of pure g-C_3N_4 nanosheets is reported showing the typical broad peaks around 13° and 28° corresponding to the (100) and (002) reflections.[40] The patterns of the composites (cfr. Figure 1b) are dominated by perovskite reflections at high wt% of $Cs_2AgBiCl_6$ and the reflections of g-C_3N_4 start to be evident around 50 wt%. Also, at 10 wt% of perovskite its pattern is still clearly detectable, due to its high scattering power with respect to g-C_3N_4. Morphological inspection of $Cs_2AgBiCl_6$, g-C_3N_4, and selected composites has been carried out by Scanning Electron Microscopy (SEM) and the results are reported in Figure S2. g-C_3N_4 nanosheets have been also characterized by Transmission Electron Microscopy (TEM) and representative images showing their

nanostructure are shown in Figure S3. Finally, elemental mapping through energy-dispersive (EDS) x-ray spectroscopy has been carried out for the composite with 10wt% of $Cs_2AgBiCl_6$ as an illustrative example and is reported in Figure S4, further confirming the formation of a composite between the two semiconductors.

Figure 1c reports the results in terms of hydrogen and ammonia evolution rates (top and bottom graphs, respectively), expressed as μmol g^{-1} h^{-1}, obtained by photocatalytic experiments under simulated solar light (for details see Experimental section). The two production rates follow opposite trends as a function of composition, with perovskite-rich samples performing better for the hydrogen generation and perovskite-poor ones running the nitrogen reduction more efficiently. The trend of hydrogen evolution rate (HER), deriving from HCl splitting, steeply increases from pure $Cs_2AgBiCl_6$ to the composite including 10wt% of g-C_3N_4, reaching a value of 625 μmol g^{-1} h^{-1} which is more than double with respect to pure perovskite. Note that pure g-C_3N_4, under these reaction conditions, provide an HER of 4 μmol g^{-1} h^{-1}. The reported data confirm a synergistic effect of the composite in enhancing the photocatalytic HCl splitting ability of $Cs_2AgBiCl_6$, thanks to the formation of an effective heterojunction (see later in the text). The present results, while being the first related to the hydrogen generation by $Cs_2AgBiCl_6$, can be compared to analogous sytems involving double perovskites. To date, only the HBr splitting by $Cs_2AgBiBr_6$ has been explored in heterojunctions with reduced graphene oxide, NiCoP or nitrogen-doped carbon.[38,41,42] The best HER has been reported for the $Cs_2AgBiBr_6$/2.5%RGO system providing around 490 μmol g^{-1} h^{-1} of hydrogen under solar illumination in HBr employing a 300 W illumination and with an apparent quantum efficiency (AQE) of 0.16%.[41] The present $Cs_2AgBiCl_6$/10% g-C_3N_4 composite, with an AQE of 2.3% (under 500 W illumination), lead to a high hydrogen photogeneration of about 625 μmol g^{-1} h^{-1} indicating an effective HCl splitting by a lead free double perovskite which is comparable to the data reported for HBr or HI reported so far but, clearly, is more appealing from an applicative point of view being the hydrogen evolved in HCl.[9]

The reduction of nitrogen to ammonia, as mentioned, follows a different trend with respect to the composition (Figure 1c), with a gradual increase of the NH_3 generation rate starting from pure $Cs_2AgBiCl_6$ up to the $Cs_2AgBiCl_6$/90% g-C_3N_4 composite, reaching a maximum value of about 40 μmol g^{-1} h^{-1}. Pure g-C_3N_4 nanosheets or lower amounts of perovskite in the composite (see the point at 5wt%) perform significantly less effectively. Also in this case, by looking at the nitrogen fixation results of the pure compounds, it is possible to unveil an

effective synergy between the two semiconductors. As mentioned, there are no previous reports about nitrogen reduction by an MHP-based heterojunction. However, g-C_3N_4 has been reported as a suitable material for this reaction, in particular thanks to the presence of nitrogen vacancies.[43,44] Therefore, g-C_3N_4 nanosheets used to prepare the present samples have been synthesized to promote the presence of such defects (see Experimental Section), as determined by Electron Paramagnetic Resonance (EPR) experiments (see Figure S5). The presence of nitrogen vacancies result in the appearance of an EPR signal related to the number of unpaired electron directly correlated to the defect formation.[44] The presence of nitrogen vacancies was further confirmed by x-ray photoelectron spectroscopy (XPS) carried out on a bulk sample of g-C_3N_4 and on the present nanosheets. The N/C ratio decreased from 1.59 to 1.15 further confirming the formation of nitrogen vacancies.[45]

From a quantitative point of view, previously reported NH_3 production rates of pure g-C_3N_4 or of heterojunctions including g-C_3N_4, are higher than those obtained here. However, it is important to stress a delicate point related to the method employed to measure the photogenerated NH_3. Currently, most of the reports about ammonia production by nitrogen fixation make use of colorimetric methods which are known to be possibly affected by several interfering compounds, in particular in presence of a sacrificial agent (which should be removed according to ref. 46 before the analysis) and when employing catalysts containing nitrogen.[46,47] In the present paper, we devised and optimized an analytical method based on ammonia ion selective electrode (ISE, for the details see the Experimental Section) to determine the produced ammonia, thus the efficiency of the nitrogen reduction reaction. The ammonia ISE method was preferred to the colorimetric ones (Nessler's reagent method and indophenol blue method) as it is highly sensitive and selective in controlled experimental conditions (temperature, stirring rate, pH, ionic strength, equilibration time) and not affected by the sacrificial agents and/or by-products.

The results reported above demonstrate the suitability of the novel $Cs_2AgBiCl_6$/g-C_3N_4 system for the photocatalytic hydrogen and ammonia production, also showing a different trend in the production rates as a function of composition. To understand the mechanisms underpinning the two reactions and the charge carrier dynamics, we afforded a detailed spectroscopic and computational modelling work.

The UV-Vis absorption spectra and the Tauc plots for the samples of the novel $Cs_2AgBiCl_6$/g-C_3N_4 composite are shown in Figure S6. The band gap of $Cs_2AgBiCl_6$ is 2.67 eV while that of g-C_3N_4 2.78 eV, in agreement with previous reports.[39,40] According to the relative weight

ratio in the composite, the gap lies closer to that of the perovskite or the carbon nitride, without significant variations between the values of the two pure compounds.

The normalized photoluminescence spectra of the $Cs_2AgBiCl_6$/g-C_3N_4 systems are reported in Figure 2. The emission is dominated by the broad and intense features of graphitic carbon nitride, even at very high perovskite loading. Such broad spectra, that completely covers the weak perovskite emission, derive from the superimposition of multiple electronic transitions.[48] In particular, three transitions have been modeled in pristine g-C_3N_4: a high energy one, centered at around 444 nm, which derives from the relaxation of δ* electrons to the LP state, and two low energy transitions centered at 455 and 505 nm. To access these low energy transitions a non-radiative mechanism to populate the π* state is required, thus the structure of the broadband spectrum depends on the efficiency of this process. In previous works, the interplay between the density of defects and the non-radiative population of π* state have been studied and related to the photocatalytic properties of g-C_3N_4.[48] Composites with lead-free perovskite have also been investigated, with particular focus on population of non-radiative states and its impact on photocatalytic efficiency.[18]

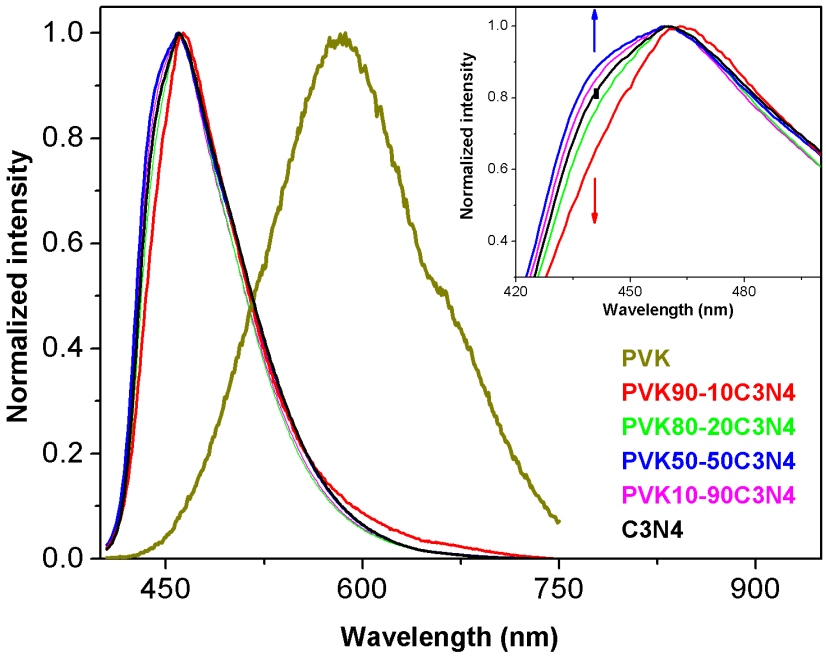

Figure 2. Emission spectra of $Cs_2AgBiCl_6$/g-C_3N_4 composites powders at different percentages of perovskite loading (wt%). g-C_3N_4 and $Cs_2AgBiCl_6$ refer to pristine materials. λ_{ex} = 375 nm. Inset: zoom on an interesting spectral zone. PVK stays for $Cs_2AgBiCl_6$.

Despite the dominative behavior of the graphitic carbon nitride emission, a close inspection of the spectral region around the emission band peak (inset of Figure 2), shows that for low loading of perovskite in the composites there was a reduction of low-lying sub-band population, as the emission displays a stronger contribution from the high energy transition. Conversely, by increasing the perovskite content, the low energy transitions became more and more pronounced. In Figure 2 we reported only representative samples, but the composite 90-10 $Cs_2AgBiCl_6$-g-C_3N_4 with the best HER performance was also the sample with the weaker contribution to the broad band by the δ* → LP state transition. These observation points out on the effect of perovskite inclusion in funneling optical excitations to the sites where they can be exploited in photocatalytic processes. To further deepen the relations between the excited state dynamics and $Cs_2AgBiCl_6$/g-C_3N_4 composition Differential Transmission (DT) measurements were also performed. Optical excitations were injected with 100-femtosecond laser pulses, 360 nm in wavelength and 1kHz in repetition rate. A white light supercontinuum was employed as broadband probe (see Supporting Information for experimental details). DT was directly performed on the solutions, with the same concentration used for photocatalytic studies, *i.e.* 1g/L in the case of H_2 production (Fig. 3a) and 0.5 g/L in the case of NH_3 production (Fig. 3b).

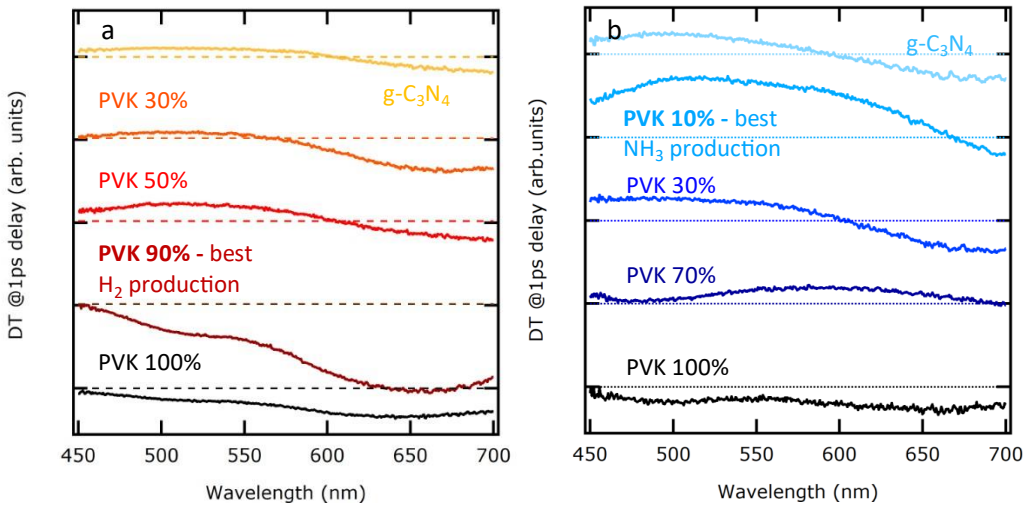

Figure 3. a) Results ranging from 100% $Cs_2AgBiCl_6$ perovskite (black line) to 100% g-C_3N_4 (yellow line), with the 90-10 PVK-gC_3N_4 case corresponding to the best HER. B) Results ranging from 100% $Cs_2AgBiCl_6$ perovskite (black line) to 100% g-C_3N_4 (light-blue line) highlighting the one with 10-90 PVK-gC_3N_4, corresponding to the best nitrogen reduction. Spectra are reported on the same scale, with zero offset for better readability, with dashed horizontal lines representing the zero for the spectrum of the same color. PVK stand for $Cs_2AgBiCl_6$.

Full spectrograms obtained from a DT measurement are reported in Figure S7, while relevant DT spectra extracted at 1 ps delay are reported in Fig. 3. The DT spectrum for the pure perovskite sample is characterized by a broadband photoinduced absorption feature, due to absorption from excited states. The 90-10 $Cs_2AgBiCl_6$-g-C_3N_4 composite optimized for H_2 generation has an enhanced photoinduced signal with respect to the 100% perovskite sample. This suggests that g-C_3N_4 helps in keeping optical excitations in the perovskite and the HER happens at perovskite sites.

On the other hand, in samples optimized for nitrogen reduction, shown in Figure 3b, the signal is maximum in the case 10-90 $Cs_2AgBiCl_6$-g-C_3N_4, which is the one giving the highest NH_3 production rate. Opposite to what inferred from Figure 3a, in this case the response is the analogous to that of g-C_3N_4, but with an enhanced signal. This suggests that ammonia generation happens at graphitic carbon nitride sites, but the concentration of optical excitations in carbon nitride and thus the ammonia generation rate are enhanced by the presence of perovskite with respect to pure g-C_3N_4.

As a general observation, the combination between g-C_3N_4 and the perovskite enhances the DT signal of the component actively involved in the reaction. Measurements were repeated for different compositions, and the maximum value of the DT signal was extracted for the two different features of the spectrum, i.e., the one at 500-520 nm and the one at 630-650 nm, as reported in Figure 4. In the case of composites optimized for HER, the spectrum mainly consists of photoinduced absorption (negative DT, thus positive differential absorption DA=-DT) and evolves on a picosecond timescale, as shown in Figure 4a.

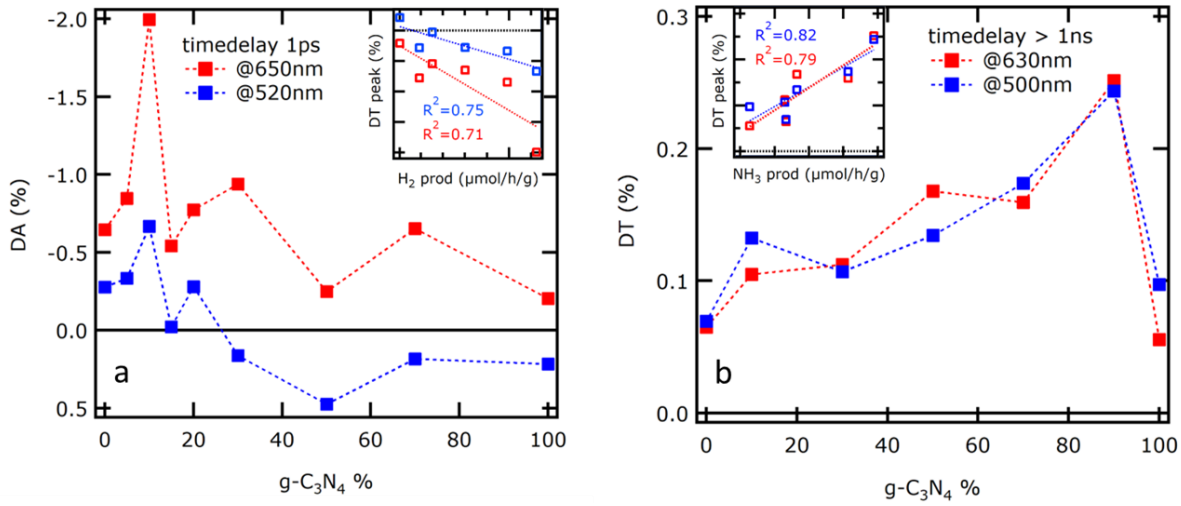

Figure 4. a) Maximum of DA (DT with a minus sign) extracted at 1ps time delay for different composites as a function of g-C_3N_4 amount; b) Maximum of DT extracted at time delay >1ns. The colors of markers are indicating the DA (DT) wavelength ranges 500-520 nm region (blue) and 630-650 nm (red). The insets show the linear correlation between DT peaks amplitude and production rates, with R^2 linear correlation coefficients, with the same color legends as the main plots.

Interestingly, the trend of the DA signal as a function of composition was closely related to the trend of HER efficiency. In the case of composites optimized for ammonia generation, a relevant correspondence was found instead between the NH_3 production efficiency and the peak of DT signal at long time delay (above 1ns), as shown in Figure 4b. This observation confirms that for NH_3 production photoinjected carriers, which are always generated in the perovskite, are transferred to the g-C_3N_4, where the ammonia evolution reaction occurs, within a nanoseconds timescale. Additional relevant data reporting the whole DT decay for different compounds and spectra extracted at longer time delay can be found in Supporting Information (Figures S8 and S9).

We performed density functional theory (DFT) calculations to rationalize the trends in hydrogen and ammonia production rates with varying g-C_3N_4 concentration, Figure 1c. All calculations have been carried out at high level of accuracy using hybrid PBE0 functional for geometry optimization with refined HSE06+SOC calculations for single point energies, as summarized in the Computational Details section. We start with consideration of the pure $Cs_2AgBiCl_6$ phase. Notably, the standalone $Cs_2AgBiCl_6$ generates a substantial amount of hydrogen, Figure 1c. Recent studies have pointed out halide vacancies as potential defects controlling the hydrogen production in the bromide-based analogue $Cs_2AgBiBr_6$.[49,50] Theoretical studies further showed low formation energies of chloride vacancies, V_{Cl}, in

$Cs_2AgBiCl_6$ bulk phases.[51] We modeled chloride vacancies in different charge states at a (001)-surface of $Cs_2AgBiCl_6$ with $(Ag_{0.5}Bi_{0.5})Cl_2$-termination, see Figure S10 and Table S2. Our calculations predict deep (+/-) transition levels for a surface V_{Cl} at 1.7 eV above the valence band maximum, see Figure 5a. V_{Cl} in its negative charge state forms a stable Bi-Ag dimer by trapping 2 electrons, see Figure 5d and Figure S11. These electrons are localized at surface defects and likely are key for the hydrogen evolution, as previously reported for Sn-Sn dimers in tin-halide perovskites.[15] The respective (+/-) transition further matches fairly with the experimental photoinduced signals, Figures 3a and 4a. Furthermore, our DFT calculations predict the formation of self-trapped excitons, see Figure S12 and Table S3, being - together with emission from halide vacancies - responsible for the broad emission features in the pure $Cs_2AgBiCl_6$ phase, Figure 2, in line with previous reports.[52–54]

To rationalize the trend in HER, we study the band alignment of the g-C_3N_4/$Cs_2AgBiCl_6$ heterostructure for the $Cs_2AgBiCl_6$ with and without the g-C_3N_4 monolayer adsorbed, representative for the low and high-wt% of g-C_3N_4 regions, respectively; see Figure 5a and Figure S13 for model setup. The band edges of $Cs_2AgBiCl_6$ at the g-C_3N_4 /$Cs_2AgBiCl_6$ interface appears favorable for charge separation, as the conduction band minimum (CBM) of g-C_3N_4 lies energetically lower (3.27 eV) than the one of g-C_3N_4 /$Cs_2AgBiCl_6$ (2.86 eV), in line with the density of states of the heterostructure model, Figure S13c. This results in electron transfer from the perovskite absorber to g-C_3N_4. Moreover, a large offset in band edges of the g-C_3N_4/$Cs_2AgBiCl_6$ to the $Cs_2AgBiCl_6$ itself is present, suggesting a driving force for electrons from the interface to the $Cs_2AgBiCl_6$ bulk. Increasing the amount of g-C_3N_4 may consequently increase the lifetime of charge carriers due to efficient charge separation, but also suppresses the formation of STEs as seen experimentally, Figure 2, resulting in the increase in HER, Figure 1c.

Our DFT calculations of the g-C_3N_4/$Cs_2AgBiCl_6$ heterostructure shows a strong binding of the g-C_3N_4 on the $(Ag_{0.5}Bi_{0.5})Cl_2$-terminated $Cs_2AgBiCl_6$ surface with a formation energy of -4.22 eV/nm^2, mediated by formation nitrogen-metal bonds with average bond length of 3.09 and 3.23 Å for N-Ag and N-Bi, respectively, see Figure 5b. Consequently, reactive V_{Cl} surface sites are passivated upon increase of g-C_3N_4 and further proton transport to the $Cs_2AgBiCl_6$ surface may be effectively hindered, reducing the evolution of H_2. Note that already a small wt% of g-C_3N_4 may be sufficient to cover the $Cs_2AgBiCl_6$ surface to a large extent, as we estimated from a toy model based on geometrical considerations, see Figure S14. Controlling the wt% of g-C_3N_4 consequently results in an ideal composition that

balances efficient charge separation and carrier lifetime as well as the access to active catalytic sites, thereby maximizing the hydrogen evolution rate.

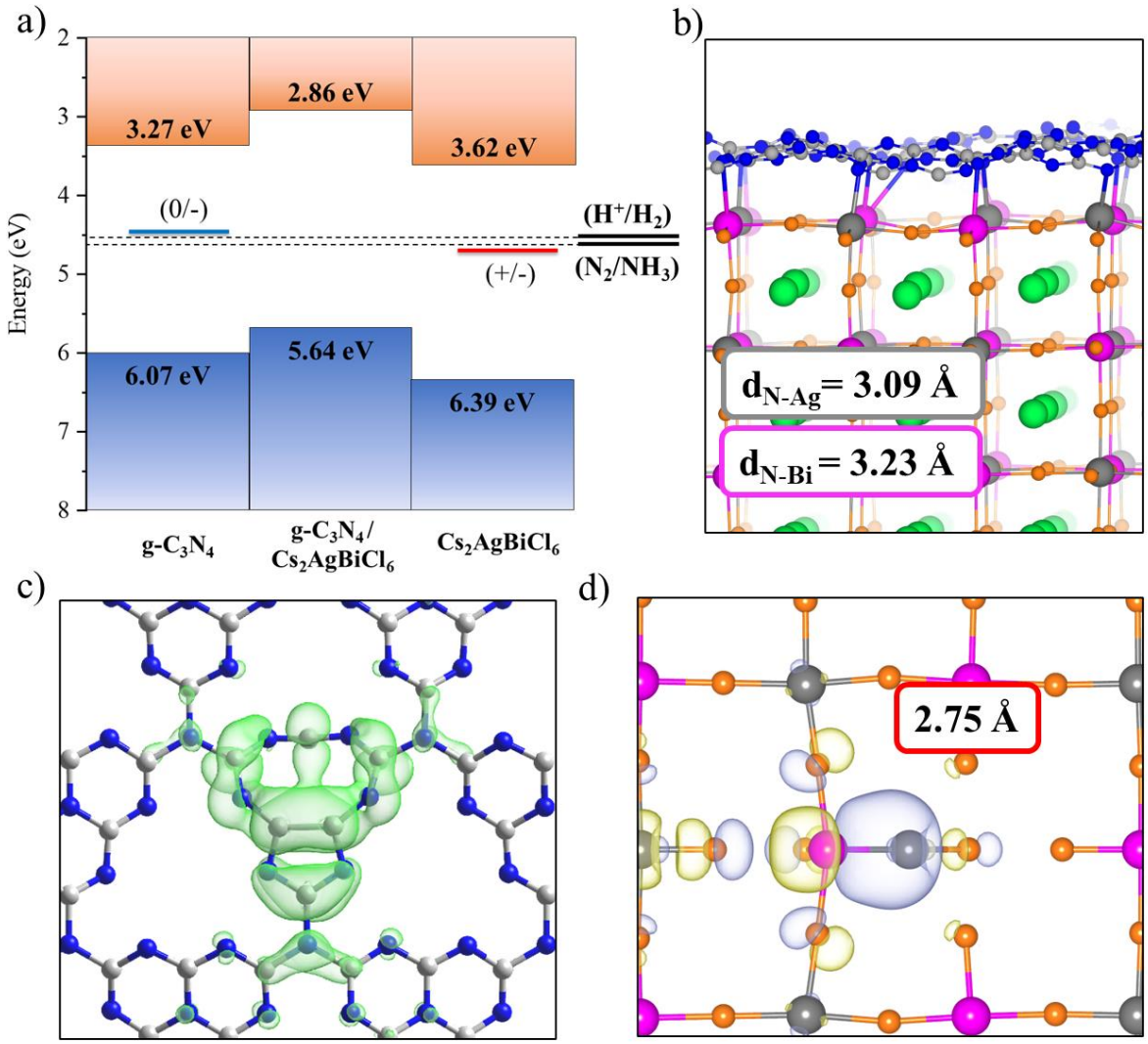

Figure 5. a) Band alignment of g-C_3N_4, $Cs_2AgBiCl_6$ and the g-C_3N_4/$Cs_2AgBiCl_6$ interface. H^+/H_2 and N_2/NH_3 redox levels as well as thermodynamic transition levels for the nitrogen vacancy, V_N, and the chloride vacancy, V_{Cl}, are explicitly visualized in the respective phases. Values are referred to the vacuum level; b) Optimized g-C_3N_4/$Cs_2AgBiCl_6$ interface reporting the average bond lengths for N-Ag and N-Bi; c) Isodensity plot of the unoccupied state of the neutral nitrogen vacancy V_N responsible for electron trapping in the g-C_3N_4; d) Isodensity plot of the localized state related to the negatively charged V_{Cl}^-, resulting in the formation of a Ag-Bi dimer with 2.75 Å bond length.

Considering the rate of NH_3 production, we observe a different trend compared to H_2 production, Figure 1c. Initially, the presence of g-C_3N_4 alone is sufficient to generate few amounts of NH_3. Considering the band alignment, electrons should jump from the $Cs_2AgBiCl_6$ to the g-C_3N_4. As potential active sites, we calculate the formation of nitrogen

vacancy in g-C_3N_4, resulting in V_N^0 formation energies of 3.36 eV, see Table S5, which is in good agreement with previous studies.[55–57] The nitrogen vacancy introduces localized energy levels within the band gap, see Figure S15, and introduces a (0/-) transition at 1.56 eV, see Table S5. Importantly, the (0/-) level of nitrogen vacancies are close to the redox potential for N_2/NH_3 (reported by dashed line), suggesting a plausible way for the initial steps in the photofixation mechanism. Upon addition of $Cs_2AgBiCl_6$, the catalytic activity is enhanced which we may attribute to the superior absorbance of the $Cs_2AgBiCl_6$ perovskite. At highest perovskite concentration, surface defects of the $Cs_2AgBiCl_6$ likely compete with the electron transfer to g-C_3N_4, limiting NH_3 production. This observation highlights the delicate balance required for optimal performance in the heterostructure system, requiring a fine tuning of the heterostructure composition.

3. CONCLUSIONS

$Cs_2AgBiCl_6$/g-C_3N_4 heterojunctions for hydrogen photogeneration and nitrogen reduction to ammonia have been investigated through advanced spectroscopy and computational modelling, aiming at unveiling the mechanism of these reactions. TAS provided detailed information on the charge carried dynamics in the heterojunction indicating that for high perovskite amounts (best performing compositions for H_2 photogeneration) the optical excitations are confined on the $Cs_2AgBiCl_6$, where the reaction occurs. The opposite situation is found for low $Cs_2AgBiCl_6$ (high g-C_3N_4) containing systems (best performing compositions for nitrogen reduction) where the typical DT signal of g-C_3N_4 results to be enchanted. This finding suggests that active sites for ammonia production are confined in the carbon nitride. The trend of DA signal as a function of the composition well follows the trend of the two photocatalytic reactions. DFT calculations show that the active sites for HER are of chloride vacancies, V_{Cl}, and that the coupling to g-C_3N_4, thanks to a favorable band alignment at the interface, increases the lifetime of charge carriers and suppress STE of $Cs_2AgBiCl_6$. The positive effect of the heterojunction formation in promoting hydrogen photogeneration is however progressively lost by increasing the amount of g-C_3N_4 due to a passivating effect of the V_{Cl}. Such mechanistic insight correlates well with the trend of HER of the $Cs_2AgBiCl_6$ /g-C_3N_4 heterojunction and confirms the active role of the perovskite in this reaction. On the other hand, DFT calculations confirm the role of nitrogen vacancies as the active sites for nitrogen reduction. Herein the positive effect of small perovskite amounts

is mostly related to its superior light absorbance, while further increase of $Cs_2AgBiCl_6$amounts progressively reduces the ammonia generation rate promoting the charge funneling towards perovskite active sites, in good agreement with experimental results.

Overall, this study on photoactive heterojunctions including a perovskite and graphitic carbon nitride provides a detailed microscopic insight into the reaction mechanisms, pointing out the key role of the heterostructure composition tuning tailoring different photocatalytic reactions.

4. EXPERIMENTAL SECTION

Sample Synthesis, Structural and Morphological Characterization

Nanosheets g-C_3N_4 has been synthesized from the bulk form (bulk g-C_3N_4) with a polymerization of Dicyandiamine DCD ($NH_2C(=NH)NHCN$, Aldrich, 99%) by the following thermal treatment under N_2 flux: heating (1 °C min^{-1}) to a selected temperature of 550 °C, the isothermal step for 4 hours followed by cooling to room temperature (10 °C min^{-1}). The synthesis was carried out in a partially closed alumina crucible. The thermal exfoliated catalyst (nanosheets) was prepared by heating to a selected temperature of 500 °C with an isothermal step for 2h the bulk g-C_3N_4 in air. The $Cs_2AgBiCl_6$/nanosheets g-C_3N_4 composite has been synthesized dissolving a stoichiometric ratio of the precursor salts AgCl (Aldrich 99%), $BiCl_3$ (Aldrich 99%) and CsCl (Aldrich 99%) in organic solvent *N,N*-dimethylformamide (DMF) and dried under vigorous stilling at 65 °C. This polar solvent can dissolve most organic and inorganic salts and may be suitable for the cations that are insoluble in HCl. The composites series have been realized changing the percentage of the perovskite ($Cs_2AgBiCl_6$) and the nanosheets g-C_3N_4 (g-C_3N_4 ns) in the composites: 100% $Cs_2AgBiCl_6$, 90% $Cs_2AgBiCl_6$ -10% g-C_3N_4, 80% $Cs_2AgBiCl_6$ -20% g-C_3N_4 ns, 50% $Cs_2AgBiCl_6$ -50% g-C_3N_4 ns, 30% $Cs_2AgBiCl_6$ -70% g-C_3N_4 ns, 10% $Cs_2AgBiCl_6$ -90% g-C_3N_4 ns. The crystal structure of the samples has been characterized by room temperature Cu-radiation XRD acquired with Bruker D2 diffractometer. DRS spectra were acquired in the wavelength range 300-800 nm directly on the powders by using a Jasco V-750 spectrophotometer, equipped with an integrating sphere (Jasco ISV-922). Microstructural characterization of the samples was made using a high-resolution scanning electron microscope (SEM, TESCAN Mira 3) operated at 25 kV.

Hydrogen Evolution Experiments

H_2 evolution experiments were conducted in 37% HCl-50% H_3PO_2 (5:1, v/v) solutions (concentrated acids were from Aldrich) irradiated in Pyrex glass containers (36 mL capacity, 24 mL sample). After addition of the catalyst (1 g L^{-1}), the sample was deoxygenated by Ar bubbling (20 min) to obtain anoxic conditions and irradiated under magnetic stirring for 4 hours. Chloroplatinic acid (H_2PtCl_6, 38% Pt basis) was added as precursor for metallic Pt (Aldrich). Since Pt is *in situ* photodeposited on the catalyst surface, after Ar bubbling a small volume from a 14 g L^{-1} H_2PtCl_6 aqueous solution was added by a 10-100 µL micropipette to

the catalyst suspension, corresponding to 3% w/w Pt. Each photoreactor was closed with sleeve stopper septa and irradiated, as described in the following, achieving simultaneous Pt deposition and H_2 production.[58]

Irradiation was performed under simulated solar light (1500 W Xenon lamp, 300-800 nm) using a Solar Box 1500e (CO.FO.ME.GRA S.r.l., Milan, Italy) set at a power factor 500 W m^{-2}, and equipped with UV outdoor filter made of IR-treated soda lime glass. Triplicate photoproduction experiments were done on all samples. The headspace evolved gas was quantified by gas chromatography coupled with thermal conductivity detection (GC-TCD), as detailed in previous work.[59] The results obtained in terms of H_2 evolution rate (HER) are expressed in the paper as µmol of gas *per* gram of catalyst *per* hour (µmole g^{-1} h^{-1}). The kinetics of H_2 formation, studied for the best performing composite through duplicate experiments, is reported in Figure S16. The photon flux, measured as previously reported[60], was 1.53×10^{-7} photons moles s^{-1}. The apparent quantum yield (AQY), calculated as the percent ratio H_2 moles/incident photons moles[59], was 2.3% for the composite giving the highest H_2 evolution.

Nitrogen Photofixation Experiments

N_2 photofixation experiments were conducted in tridistilled water containing 10% (v/v) methanol (Aldrich, ≥99.9%) irradiated in Pyrex glass container (250 mL capacity, 100 mL sample). After addition of the catalyst (0.5 g L^{-1}), the sample suspension was deoxygenated by N_2 bubbling (45 min) to obtain a saturated solution and then irradiated under magnetic stirring for 3 hours maintaining the temperature at 15°C. For the experiments involving use of 1 % w/w Pt co-catalyst, the same Chloroplatinic acid (H_2PtCl_6, 38% Pt basis) was added as precursor for metallic Pt (Aldrich). The quantification was performed with ammonia ion selective electrode, as reported below.

Ammonia Determination

The Thermo Scientific Orion Ammonia Ion Selective Electrode (ISE) was selected as it measures ammonia ions in aqueous solutions quickly, simply, economically, and accurately.

The ammonia ISE uses a hydrophobic gas-permeable membrane which separates the sample solution from the electrode filling solution. Water does not wet the membrane and does not penetrate the holes, whereas the dissolved ammonia in the sample solution

diffuses through the membrane until the partial pressure of ammonia is the same on both sides of the membrane. In any sample the partial pressure of ammonia is proportional to its concentration.

Daily freshly tridistilled water[46], free of volatile amines that can positively interfere with the measurements, was used for all standards and samples. The pH of all standards and samples was adjusted above 11 with a strong base (10 N NaOH) to quantify ammonia in its uncharged form, *viz.* NH_3(aq). Standard solutions and samples had ionic strength < 1 M with about the same level of ions and dissolved species. The ionic species cannot cross the membrane but can change the solubility of ammonia and/or form metal complexes. Most of metals are removed in the form of hydroxide complexes or precipitates in the basic solution.

All measurements were performed in a beaker with minimized surface area/volume ratio, at a uniform and moderate rate, under controlled temperature. Since a change in temperature can cause a change of the slope and potential, a piece of insulating material, e.g., ceramic or cardboard, was placed between the magnetic stirring plate and beaker to prevent measurement errors from transfer of heat to sample.

In details, ISE was immersed in the solution (standard or sample, 1% v/v 10 N NaOH, 10% v/v MeOH) until a stable potential value (mV) was obtained (at least 2 or 3 minutes). For the quantification, a calibration curve was daily constructed plotting the mV value recorded against the Log Concentration, to verify the slope (varying in the range - 54 ÷ -60 mV). The ammonia concentration in the sample was further assessed by two standard additions. Figure S17 reports an example of mean calibration curve (0.25 mg L^{-1} ÷ 10 mg L^{-1} as NH_3). The influence of different parameters was carefully investigated to exclude any possible interferences on the quantification of ammonia in solution. Sample colour and turbidity did not affect the ISE quantification, as experimentally verified by measurements on both filtered and not-filtered samples obtaining not significantly different NH_3 concentrations ($p < 0.05$). Therefore, the final method was applied to not filtered samples. On the contrast, coloured or cloudy solutions lead to an overestimation of the NH_3 concentration in spectrophotometric assays. The effect of methanol, used as sacrificial agent, and its by-products, namely formaldehyde and formic acid, was evaluated by constructing calibration curves. Accordingly, standard solutions were prepared in presence of MeOH in the range 1 ÷ 20 % v/v, HCHO in the range 0.01 mg L^{-1} ÷ 10 mg L^{-1} and formic acid 0.001 ÷ 0.1 % v/v, respectively. The slope of each curve was compared with the one obtained in ultrapure water, achieving not significantly different values ($p < 0.05$). On the contrary, when using the

colorimetric Nessler's reagent method, methanol interferes heavily, resulting in an overestimation of the NH_3 concentration[46], and herein experimentally verified.

Ag and Bi leaching tests

The leaching tests were performed by dispersion of the perovskite powder in distilled water, under magnetic stirring for 4 h. Then the suspension was filtered on 0.2 µm nylon membrane and the amount of Ag and Bi in solution was determined by ICP-OES, after acidification (1% v/v ultrapure nitric acid). The $Cs_2AgBiCl_6$ perovskite resulted stable, with a leaching < 0.1 % for Ag and < 0.05 % for Bi. As silver could interfere by complexing ammonia, leaching tests were also performed on all the g-C_3N_4/$Cs_2AgBiCl_6$ composites, highlighting a negligible Ag release (< 0.9 %) also for the best performing material with negligible complex formation, further confirmed by ISE measurements, in NaOH/EDTA in place of NaOH solution.

Ultrafast spectroscopy measurements

Differential Transmission (DT) measurements were performed on the composite solution in a pump and probe configuration. Ti:Sapphire laser (Libra – Coherent) delivering 100-fs pulses at 800nm with 1kHz repetition rate is sent to a tunable parametric optic amplifier (TOPAS - Light Conversion) to get pulses at the chosen excitation wavelength (360nm). The measurement is performed with two different configurations to explore two different delay range:

- Helios (Ultrafast Systems) with optical delay line (max 8 ns delay), where supercontinuum white probe pulses are derived by focusing the 800nm laser on a Sapphire crystal, thus allowing for sub-ps resolution.
- EOS (ultrafast Systems) with digitally controlled delay (max 1ms delay), with white probe pulses generated by means of a fibre laser.

DT transmitted and reference spectra are collected with two spectrometers coupled to CMOS detectors, in differential configuration. The samples are analysed in form of solution, which is first sonicated for 15 minutes and then poured into a 1-mm thick quartz cuvette. The concentration of the composites is the same used for the photocatalytic measurements, i.e. 1g/L in the case of HER and 0.5g/L in the case of NH_3 photofixation.

Density functional theory calculations

Computational Details

Density functional theory (DFT) calculations have been carried out for the $Cs_2AgBiCl_6$ and g-C_3N_4 phases, the interface, and defect in the supercell approach. Ionic positions were optimized using the CP2K software package using the PBE0 exchange-correlation functional, and by including DFT-D3 dispersion corrections.[61–64] For g-C_3N_4, we employ an orthorhombic 2×2×2 supercell with *a*=7.08 Å, *b*=12.27 Å, *c*=6.97 Å; for $Cs_2AgBiCl_6$, we use the cubic phase with *a*=*b*=*c*=10.77 Å.[17,39] In all cases, geometry optimization was carried out at the Γ-point of the Brillouin zone. We used the Goedecker-Teter-Hutter (GTH) norm-conserving pseudopotentials and MOLOPT double-zeta Gaussian basis sets.[65,66] The auxiliary density matrix method has been used to accelerate calculations with the hybrid PBE0 functional.[67]

To refine the defect formation energies and thermodynamic ionizations levels, single point DFT calculations were carried out using the hybrid HSE06 functional with inclusion of spin orbit coupling (SOC) corrections on the optimized geometries within the Quantum Espresso software package.[68] Screening of the fraction of exact exchange of the $Cs_2AgBiCl_6$ shows best agreement at a value of α=0.31 with the experimental values, as shown in Table S1. All calculations were carried out at the Γ point of the Brillouin zone, using norm conserving full relativistic pseudopotentials with electrons from Cl 5s, 5p; Cs 5s, 5p, 6s; Ag 5s, 5p, 4d; and Bi 6s, 6p, 5d shells explicitly included. Plane-wave basis set cutoffs for the smooth part of the wave functions and the Fock grid of 40 and 80 Ry, respectively, were chosen. Dispersion corrections were accounted for using the D3 scheme.

Defect formation energies (DFEs) and thermodynamic ionization levels (TILs) were calculated within the supercell approach following the expressions:

$$\mathrm{DFE}[\mathrm{X}^q] = E[\mathrm{X}^q] - E[\mathrm{pristine}] - \sum_i n_i\mu_i + q(\varepsilon_{\mathrm{VB}} + \varepsilon_{\mathrm{F}}) \qquad \text{Eq (1)}$$

$$\varepsilon(q/q') = \frac{\mathrm{DFE}(\mathrm{X}^q|E_{\mathrm{F}}=0) - \mathrm{DFE}(\mathrm{X}^{q'}|E_{\mathrm{F}}=0)}{q'-q} \qquad \text{Eq (2)}$$

where $E[X^q]$ is the energy of the supercell with defect X in the charge state q, E(pristine) is the energy of the pristine (non-defective) supercell. n_i and μ_i are the number and the chemical potentials of the species added or subtracted, respectively and ε_{VB} is the valence band energy of the pristine system.[69] The last two terms of Eq (1) represent the energy to the exchange electrons with the Fermi level of the system (ε_F).

Model setup

Firstly, we optimized the pristine structure of g-C_3N_4 using a 3x2 supercell, see Figure S10a. The monolayer was cut along the (001) direction, and an additional 15 Å of vacuum was added perpendicular to the monolayer to prevent interactions with periodic replicas. Similarly, we optimize a slab model of the double perovskite $Cs_2AgBiCl_6$ using a 2×2 in-plane supercell, with (001) direction, and added 15 Å of vacuum to maintain separation from periodic images. Two different surface terminations were investigated for $Cs_2AgBiCl_6$: $(Ag_{0.5}Bi_{0.5})Cl_2$ and CsCl, see Figure S10b.

Chloride Vacancies in CABC

Considering the $Cs_2AgBiCl_6$, we specifically investigate a chloride vacancy on the $(Ag_{0.5}Bi_{0.5})Cl_2$-terminated surface. The vacancy was stable in the positive charge state (+1), and its presence did not significantly alter the lattice structure of $Cs_2AgBiCl_6$. Upon addition of electrons, we observe the formation of an Ag–Bi dimer. In the neutral state, the dimer shows a distance of 2.82 Å, while in the negatively charged state the distance is reduced to 2.75 Å, shown in Figure S11. The thermodynamic ionization levels (TILs) for the (+/0) and (+/–) transitions are 1.76 eV and 1.69 eV above the valence band maximum, respectively, indicating a deep trap state associated with the defect, see Table S2. As highlighted in the main text of our research, this specific defect holds significant implications as an active site for H_2 production.

We further investigate the geometry of the V_{Cl}^- on the $Cs_2AgBiCl_6$ surface upon inclusion of SOC corrections, as SOC could potentially destabilize the formation of metal dimers as known for the lead-halide perovskites.[70] We optimize the structure containing the V_{Cl}^- vacancy using PBE+SOC within the Quantum Espresso software package. Comparison of the PBE0 and PBE+SOC optimized structures suggest the stability of the Ag-Bi dimer, with bond lengths only slightly varying, see Figure S11. Thus, we can confidently trust the PBE0 structural properties despite neglecting SOC.

Self-trapped excitons

We investigate the formation of self-trapped excitons (STEs) upon illumination. Figure S13a summarizes the STE formation mechanism. Optimizing the system in the triplet state, using the PBE0 functional, results in the localization of the exciton, see Figure S13b. The localization of the electron Kohn-Sham orbital is accompanied by an increase in Bi-Cl bond lengths from 2.7 Å to above 3.0 Å, see Figure S13b. Similarly, the hole Kohn-Sham orbital localized within strongly shortened axial Ag-Cl bonds of 2.3 Å, see Figure S13b. The calculated emission signal is of 1.46 eV while the estimated absorption is at 2.8 eV, see Table S3. Note that halide vacancies likely strongly contribute to the emission. Self-trapping of excitons is key to observe broad emission features, while the detailed contribution of STEs or by recombination from halide vacancies is still under debate.[71,72]

Interface Model

Finally, we model the interface between the g-C_3N_4 and $Cs_2AgBiCl_6$ to gain insight into the structural and electronic modifications upon interface formation. The lattice constants of g-C_3N_4 and $Cs_2AgBiCl_6$ nicely match along the a direction, while the b direction shows substantial differences in the lattice constants of 13%. Thus, we cut the g-C_3N_4 layer along the b-direction and passivate undercoordinated N atoms with H atoms, see Figure S13b. This ensures maximal coverage without introducing artificial strain into the g-C_3N_4. Considering the electronic properties, we obtain a band gap of 3.22 eV for the modified g-C_3N_4, which is in excellent agreement with the fully periodic g-C_3N_4 monolayer (3.4 eV). We passivated both surfaces in the perovskite slab with the modified g-C_3N_4 layers. We initially performed single point calculations at different distances between the $Cs_2AgBiCl_6$ and the g-C_3N_4, as well as for different horizontal alignment for g-C_3N_4. Starting from the low energy configuration, geometry optimization was performed, resulting in a strongly bound heterostructure with a binding energy of -4.22 eV/nm^2. Looking closer at the structure shows that each undercoordinated surface metal ion is successfully passivated (see Figure S13a and Figure 5b of the manuscript). The DOS shown in Figure S13c shows a type II band alignment with the VB and CB of g-C_3N_4 below the ones of the perovskite layer.

The large binding energy presents an interesting hypothesis that may explain the observed drop in the H_2 production rate when adding a small weight percentage of g-C_3N_4. To estimate

the surface coverage, we derive a simple toy system relying on pure geometric considerations, shown in Figure S14b. We assume cubic nanocrystals of $Cs_2AgBiCl_6$. The nanocrystal surface area is given by $6L^2$, where L represents the nanocubes dimension. The g-C_3N_4 is modeled as 2D rectangular layers, which may passivate the surfaces of the perovskite nanocubes. The given wt% of g-C_3N_4 allows us to calculate the surface ratio of the $Cs_2AgBiCl_6$ to the g-C_3N_4, as shown in Figure S14a. Our model system indicates that substantial coverage of the nanocrystal surface can already be achieved at low wt%. This suggests that the passivation of the surface may inhibit the catalytic active site of $Cs_2AgBiCl_6$ due to a small amount of g-C_3N_4.

Nitrogen Vacancies in g-C_3N_4

In g-C_3N_4, three nitrogen atoms can be removed to create vacancies: N1, nitrogen being bonded to three carbon atoms connecting three heptazine flakes; N2, nitrogen being bonded to only two C atoms; and N3, nitrogen being removed from inside a heptazine sub-structure. To determine the most stable state, we considered the neutral state of the vacancy and examined the various possible spin states. Our analysis reveals that the N3 vacancy in a doublet spin state is the most stable, as shown in Table S4.

We further determine the thermodynamic ionization level of N2 and N3 vacancies by calculating the negative charge state by adding an electron. DFEs provide insights into the thermodynamic stability and formation abilities of specific defects. On the other hand, TILs represent the redox potential associated with the capture of carriers at defect sites. For both defects considered, the (0/-) transition is found to be deep within the band gap, see Table S5. This implies that the nitrogen vacancies can trap electrons, localized state within the band gap of the monolayer, as shown in Figure S15. For the monolayer, a band gap value of 3.4 eV was calculated, significantly larger than the experimental values of 2.7 eV due to the reduction in dimensionality. To estimate the accuracy of given defects, we calculate the DFEs and TILs of all nitrogen vacancies in a g-C_3N_4 bulk supercell at same level of theory. The obtained bulk band gap value of 2.9 eV closely aligns with the experimental values, shown in Table S5. Defect TILs remain deep in the band gap, while being shifted downwards in energy.

Conflict of Interest

Authors have no conflict of interest.

Acknowledgement

L.M., A.S., A.P. acknowledge support from the Ministero dell'Università e della Ricerca (MUR) and the University of Pavia through the program "Dipartimenti di Eccellenza 2023–2027. L.M., E.M. and A.L. acknowledge support from the Ministero dell'Università e della Ricerca (MUR) through PRIN Project REVOLUTION (2022HRZH7P) and from European Union – Next Generation EU under PRIN PNRR 2022 project "BEAGLE" (P20223HSWX). A. P. acknowledges support from the Ministero dell'Università e della Ricerca (MUR) through PRIN Project PHOTOFIX (2022TWKM4X). E.M. and S.C. acknowledge project Ricerca@Cnr PHOTOCAT (CUP B93C21000060006). E.M. acknowledges funds by the European Union - NextGenerationEU under the POR H2 AdP project, L.A.1.1.35 (CUP B93C22000630006). F.D.A. acknowledges funds by the European Union - NextGenerationEU under the Italian Ministry of University and Research (MUR) National Innovation Ecosystem grant ECS00000041 - VITALITY. S.C. acknowledges support from the Ministero dell'Università e della Ricerca (MUR) through PRIN Project INTERFACE (2022HWWW3S). L.M. and C.T. acknowledge financial support from R.S.E. SpA (Ricerca sul Sistema Energetico). E.M. and A.A.A. wish to thank the Distinguished Scientist Fellowship Program (DSFP) of King Saud University, Riyadh, Kingdom of Saudi Arabia.

The first-author Costanza Tedesco, author of the present Ph.D. work, carried out all the experimental parts: the synthesis and the characterization of all photocatalytic materials and the revision of the experimental part of the paper.

References

[1] H. Huang, B. Pradhan, J. Hofkens, M. B. J. Roeffaers, J. A. Steele, *ACS Energy Lett.* 2020, *5*, 1107.

[2] K. A. Huynh, D. L. T. Nguyen, V.-H. Nguyen, D.-V. N. Vo, Q. T. Trinh, T. P. Nguyen, S. Y. Kim, Q. V. Le, *Journal of Chemical Technology & Biotechnology* 2020, *95*, 2579.

[3] B.-M. Bresolin, Y. Park, D. W. Bahnemann, *Catalysts* 2020, *10*, 709.

[4] M. Corti, S. Bonomi, R. Chiara, L. Romani, P. Quadrelli, L. Malavasi, *Inorganics* 2021, *9*, 56.

[5] J. Yuan, H. Liu, S. Wang, X. Li, *Nanoscale* 2021.

[6] F. Temerov, Y. Baghdadi, E. Rattner, S. Eslava, *ACS Appl. Energy Mater.* 2022, *5*, 14605.

[7] M. Xiao, Y. Zhang, J. You, Z. Wang, J.-H. Yun, M. Konarova, G. Liu, L. Wang, *J. Phys. Energy* 2022, *4*, 042005.

[8] Z.-Y. Chen, N.-Y. Huang, Q. Xu, *Coordination Chemistry Reviews* 2023, *481*, 215031.

[9] L. Romani, L. Malavasi, *ACS Omega* 2020, *5*, 25511.

[10] V. Armenise, S. Colella, F. Fracassi, A. Listorti, *Nanomaterials* 2021, *11*, 433.

[11] J. Wang, Y. Shi, Y. Wang, Z. Li, *ACS Energy Lett.* 2022, *7*, 2043.

[12] M. A. Raza, F. Li, M. Que, L. Zhu, X. Chen, *Mater. Adv.* 2021, *2*, 7187.

[13] X. Wang, J. He, X. Chen, B. Ma, M. Zhu, *Coordination Chemistry Reviews* 2023, *482*, 215076.

[14] C. Tedesco, L. Malavasi, *Molecules* 2023, *28*, 339.

[15] D. Ricciarelli, W. Kaiser, E. Mosconi, J. Wiktor, M. W. Ashraf, L. Malavasi, F. Ambrosio, F. De Angelis, *ACS Energy Lett.* 2022, 1308.

[16] L. Romani, A. Bala, V. Kumar, A. Speltini, A. Milella, F. Fracassi, A. Listorti, A. Profumo, L. Malavasi, *J. Mater. Chem. C* 2020, *8*, 9189.

[17] L. Romani, A. Speltini, F. Ambrosio, E. Mosconi, A. Profumo, M. Marelli, S. Margadonna, A. Milella, F. Fracassi, A. Listorti, F. De Angelis, L. Malavasi, *Angewandte Chemie International Edition* 2021, *60*, 3611.

[18] L. Romani, A. Speltini, C. N. Dibenedetto, A. Listorti, F. Ambrosio, E. Mosconi, A. Simbula, M. Saba, A. Profumo, P. Quadrelli, F. De Angelis, L. Malavasi, *Adv. Funct. Mater.* 2021, *31*, 2104428.

[19] B.-M. Bresolin, C. Günnemann, D. W. Bahnemann, M. Sillanpää, *Nanomaterials* 2020, *10*, 763.

[20] S. Park, W. J. Chang, C. W. Lee, S. Park, H.-Y. Ahn, K. T. Nam, *Nat Energy* 2017, *2*, 16185.

[21] A. Pisanu, A. Speltini, P. Quadrelli, G. Drera, L. Sangaletti, L. Malavasi, *J. Mater. Chem. C* 2019, *7*, 7020.

[22] K. Li, S. Li, W. Zhang, Z. Shi, D. Wu, X. Chen, P. Lin, Y. Tian, X. Li, *Journal of Colloid and Interface Science* 2021, *596*, 376.

[23] L. Zhou, Y.-F. Xu, B.-X. Chen, D.-B. Kuang, C.-Y. Su, *Small* 2018, *14*, 1703762.

[24] Y. Jiang, R. Zhou, Z. Zhang, Z. Dong, J. Xu, *J. Mater. Chem. C* 2023, *11*, 2540.

[25] S. Cheng, X. Chen, M. Wang, G. Li, X. Qi, Y. Tian, M. Jia, Y. Han, D. Wu, X. Li, Z. Shi, *Applied Surface Science* 2023, *621*, 156877.

[26] H. Huang, D. Verhaeghe, B. Weng, B. Ghosh, H. Zhang, J. Hofkens, J. A. Steele, M. B. J. Roeffaers, *Angew Chem Int Ed* 2022, *61*, DOI 10.1002/anie.202203261.
[27] R. Mishra, S. Bera, R. Chatterjee, S. Banerjee, S. Bhattacharya, A. Biswas, S. Mallick, S. Roy, *Applied Surface Science Advances* 2022, *9*, 100241.
[28] J. Yang, D. Wang, H. Han, C. Li, *Acc. Chem. Res.* 2013, *46*, 1900.
[29] T. Paul, D. Das, B. K. Das, S. Sarkar, S. Maiti, K. K. Chattopadhyay, *Journal of Hazardous Materials* 2019, *380*, 120855.
[30] B. Xie, D. Chen, N. Li, Q. Xu, H. Li, J. He, J. Lu, *Chemical Engineering Journal* 2022, *430*, 132968.
[31] Z.-J. Bai, Y. Mao, B.-H. Wang, L. Chen, S. Tian, B. Hu, Y.-J. Li, C.-T. Au, S.-F. Yin, *Nano Res.* 2022, DOI 10.1007/s12274-022-4835-z.
[32] M. Corti, R. Chiara, L. Romani, B. Mannucci, L. Malavasi, P. Quadrelli, *Catal. Sci. Technol.* 2021, *11*, 2292.
[33] Y. Wang, H. Huang, Z. Zhang, C. Wang, Y. Yang, Q. Li, D. Xu, *Applied Catalysis B: Environmental* 2021, *282*, 119570.
[34] M. Zhang, W. Wang, F. Gao, D. Luo, *Catalysts* 2021, *11*, 505.
[35] M. Medina-Llamas, A. Speltini, A. Profumo, F. Panzarea, A. Milella, F. Fracassi, A. Listorti, L. Malavasi, *Nanomaterials* 2023, *13*, 263.
[36] M. Ismael, Y. Wu, *Sustainable Energy Fuels* 2019, *3*, 2907.
[37] Z. Guan, Y. Wu, P. Wang, Q. Zhang, Z. Wang, Z. Zheng, Y. Liu, Y. Dai, M.-H. Whangbo, B. Huang, *Applied Catalysis B: Environmental* 2019, *245*, 522.
[38] Q. Huang, Y. Guo, J. Chen, Y. Lou, Y. Zhao, *New J. Chem.* 2022, *46*, 7395.
[39] E. T. McClure, M. R. Ball, W. Windl, P. M. Woodward, *Chem. Mater.* 2016, *28*, 1348.
[40] X. Wang, K. Maeda, A. Thomas, K. Takanabe, G. Xin, J. M. Carlsson, K. Domen, M. Antonietti, *Nature Mater* 2009, *8*, 76.
[41] T. Wang, D. Yue, X. Li, Y. Zhao, *Applied Catalysis B: Environmental* 2020, *268*, 118399.
[42] Y. Jiang, K. Li, X. Wu, M. Zhu, H. Zhang, K. Zhang, Y. Wang, K. P. Loh, Y. Shi, Q.-H. Xu, *ACS Appl. Mater. Interfaces* 2021, *13*, 10037.
[43] M. Cheng, C. Xiao, Y. Xie, *J. Mater. Chem. A* 2019, *7*, 19616.
[44] G. Dong, W. Ho, C. Wang, *J. Mater. Chem. A* 2015, *3*, 23435.
[45] Y. Li, M. Ti, D. Zhao, Y. Zhang, L. Wu, Y. He, *Journal of Alloys and Compounds* 2021, *870*, 159298.
[46] R. Huang, X. Li, W. Gao, X. Zhang, S. Liang, M. Luo, *RSC Adv.* 2021, *11*, 14844.
[47] Y. Zhao, R. Shi, X. Bian, C. Zhou, Y. Zhao, S. Zhang, F. Wu, G. I. N. Waterhouse, L. Wu, C. Tung, T. Zhang, *Adv. Sci.* 2019, *6*, 1802109.
[48] A. Sharma, M. Varshney, K. H. Chae, S. O. Won, *Current Applied Physics* 2018, *18*, 1458.
[49] S. Zhang, Y. Yuan, J. Gu, X. Huang, P. Li, K. Yin, Z. Xiao, D. Wang, *Applied Surface Science* 2023, *609*, 155446.
[50] Z. He, Q. Tang, X. Liu, X. Yan, K. Li, D. Yue, *Energy Fuels* 2021, *35*, 15005.
[51] J. Xu, J. Liu, B. Liu, J. Wang, B. Huang, *Adv Funct Materials* 2019, *29*, 1805870.
[52] M. Palummo, E. Berrios, D. Varsano, G. Giorgi, *ACS Energy Lett.* 2020, *5*, 457.

[53] J. Luo, X. Wang, S. Li, J. Liu, Y. Guo, G. Niu, L. Yao, Y. Fu, L. Gao, Q. Dong, C. Zhao, M. Leng, F. Ma, W. Liang, L. Wang, S. Jin, J. Han, L. Zhang, J. Etheridge, J. Wang, Y. Yan, E. H. Sargent, J. Tang, *Nature* 2018, *563*, 541.
[54] L. Zhang, Y. Fang, L. Sui, J. Yan, K. Wang, K. Yuan, W. L. Mao, B. Zou, *ACS Energy Lett.* 2019, *4*, 2975.
[55] E. Raciti, S. M. Gali, M. Melchionna, G. Filippini, A. Actis, M. Chiesa, M. Bevilacqua, P. Fornasiero, M. Prato, D. Beljonne, R. Lazzaroni, *Chem. Sci.* 2022, *13*, 9927.
[56] X. Liu, W. Kang, W. Zeng, Y. Zhang, L. Qi, F. Ling, L. Fang, Q. Chen, M. Zhou, *Applied Surface Science* 2020, *499*, 143994.
[57] P. Huang, M. Grzeszczyk, K. Vaklinova, K. Watanabe, T. Taniguchi, K. S. Novoselov, M. Koperski, *Phys. Rev. B* 2022, *106*, 014107.
[58] J. Huang, G. Nie, Y. Ding, *Catalysts* 2019, *10*, 6.
[59] A. Speltini, M. Sturini, D. Dondi, E. Annovazzi, F. Maraschi, V. Caratto, A. Profumo, A. Buttafava, *Photochem Photobiol Sci* 2014, *13*, 1410.
[60] A. Speltini, L. Romani, D. Dondi, L. Malavasi, A. Profumo, *Catalysts* 2020, *10*, 1259.
[61] J. VandeVondele, M. Krack, F. Mohamed, M. Parrinello, T. Chassaing, J. Hutter, *Computer Physics Communications* 2005, *167*, 103.
[62] C. Adamo, V. Barone, *The Journal of Chemical Physics* 1999, *110*, 6158.
[63] J. P. Perdew, M. Ernzerhof, K. Burke, *The Journal of Chemical Physics* 1996, *105*, 9982.
[64] S. Grimme, J. Antony, S. Ehrlich, H. Krieg, *The Journal of Chemical Physics* 2010, *132*, 154104.
[65] S. Goedecker, M. Teter, J. Hutter, *Phys. Rev. B* 1996, *54*, 1703.
[66] J. VandeVondele, J. Hutter, *The Journal of Chemical Physics* 2007, *127*, 114105.
[67] M. Guidon, J. Hutter, J. VandeVondele, *J. Chem. Theory Comput.* 2010, *6*, 2348.
[68] P. Giannozzi, S. Baroni, N. Bonini, M. Calandra, R. Car, C. Cavazzoni, D. Ceresoli, G. L. Chiarotti, M. Cococcioni, I. Dabo, A. D. Corso, S. de Gironcoli, S. Fabris, G. Fratesi, R. Gebauer, U. Gerstmann, C. Gougoussis, A. Kokalj, M. Lazzeri, L. Martin-Samos, N. Marzari, F. Mauri, R. Mazzarello, S. Paolini, A. Pasquarello, L. Paulatto, C. Sbraccia, S. Scandolo, G. Sclauzero, A. P. Seitsonen, A. Smogunov, P. Umari, R. M. Wentzcovitch, *Journal of Physics: Condensed Matter* 2009, *21*, 395502.
[69] C. G. Van De Walle, J. Neugebauer, *Journal of Applied Physics* 2004, *95*, 3851.
[70] D. Meggiolaro, F. De Angelis, *ACS Energy Lett.* 2018, *3*, 2206.
[71] S. Kahmann, D. Meggiolaro, L. Gregori, E. K. Tekelenburg, M. Pitaro, S. D. Stranks, F. De Angelis, M. A. Loi, *ACS Energy Lett.* 2022, *7*, 4232.
[72] M. Morana, W. Kaiser, R. Chiara, B. Albini, D. Meggiolaro, E. Mosconi, P. Galinetto, F. De Angelis, L. Malavasi, *J. Phys. Chem. Lett.* 2023, 7860.

SUPPLEMENTARY INFORMATION

Reaction Mechanism of Hydrogen Generation and Nitrogen Fixation at Carbon Nitride/Double Perovskite Heterojunctions

Costanza Tedesco,[a§] Luca Gregori,[b§] Angelica Simbula,[c] Federico Pitzalis,[c] Andrea Speltini,[a] Francesca Merlo,[a] Silvia Colella,[d] Andrea Listorti,[e] Edoardo Mosconi,[f,g] Asma A. Alothman,[g] Waldemar Kaiser,[f] Michele Saba,[c] Antonella Profumo,[a] Filippo De Angelis,[b,f,g,h] Lorenzo Malavasi [a,*]*

[a]Department of Chemistry and INSTM, University of Pavia,Via Taramelli16, Pavia, 27100, Italy
[b]Department of Chemistry, Biology and Biotechnology, University of Perugia and INSTM, Via Elce di Sotto 8, 06123 Perugia, Italy
[c]Dipartimento di Fisica, Università di Cagliari, 09042 Monserrato, Italy
[d]CNR NANOTEC -c/o Dipartimento di Chimica, Università di Bari, Via Orabona 4, 70126 Bari, Italy
[e]Department of Chemistry, University of Bari "Aldo Moro", via Orabona 4, 70126, Bari, Italy
[f]Computational Laboratory for Hybrid/Organic Photovoltaics (CLHYO), Istituto CNR di Scienze e Tecnologie Chimiche "Giulio Natta" (CNR-SCITEC), Via Elce di Sotto 8, 06123 Perugia, Italy
[g]Chemistry Department, College of Science, King Saud University, Riyadh 11451, Kingdom of Saudi Arabia
[h]SKKU Institute of Energy Science and Technology (SIEST)Sungkyunkwan University, Suwon, Korea 440-746

Corresponding Authors

Edoardo Mosconi, email: edoardo@thch.unipg.it

Lorenzo Malavasi, email: lorenzo.malavasi@unipv.it

a)

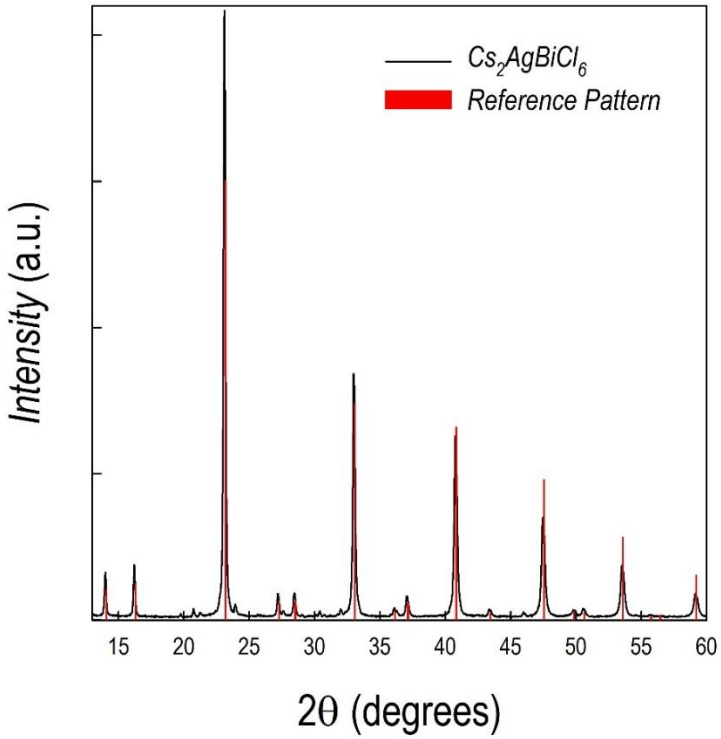
$Cs_2AgBiCl_6$
Reference Pattern
Intensity (a.u.)
15
20
25
30
35
40
45
50
55
60
2θ (degrees)

b)

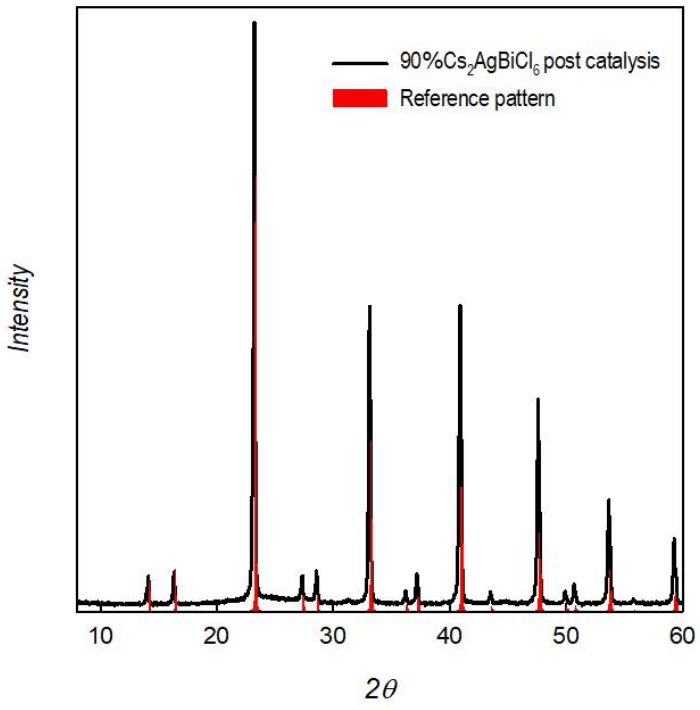
90%$Cs_2AgBiCl_6$ post catalysis
Reference pattern
Intensity
10
20
30
40
50
60
2θ

Figure S1. a) XRD pattern of $Cs_2AgBiCl_6$ against the reference cubic structure.[1] b) XRD pattern of $Cs_2AgBiCl_6$ /10% g-C_3N_4 after the photocatalytic run.

a)

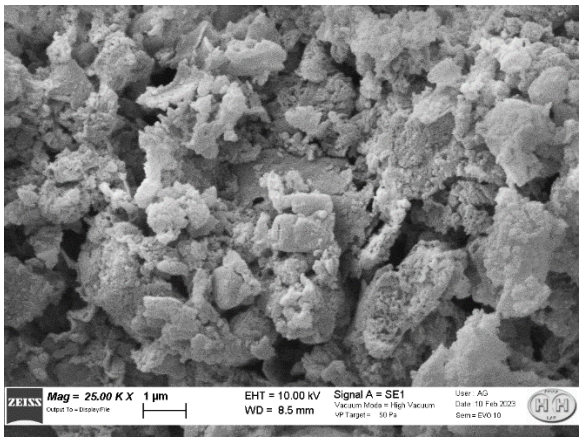

b)

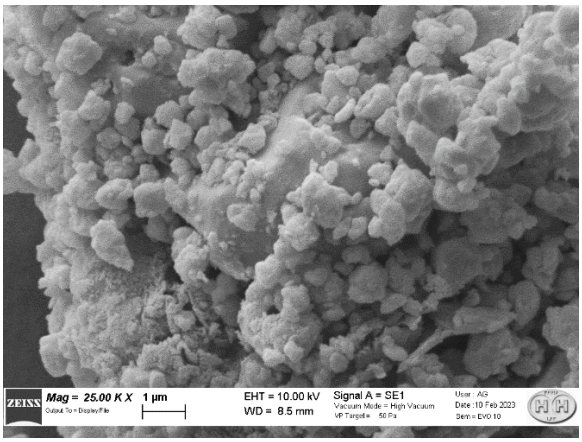

c)

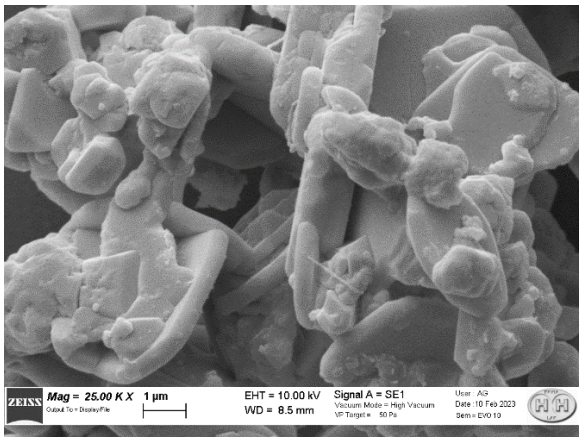

d)

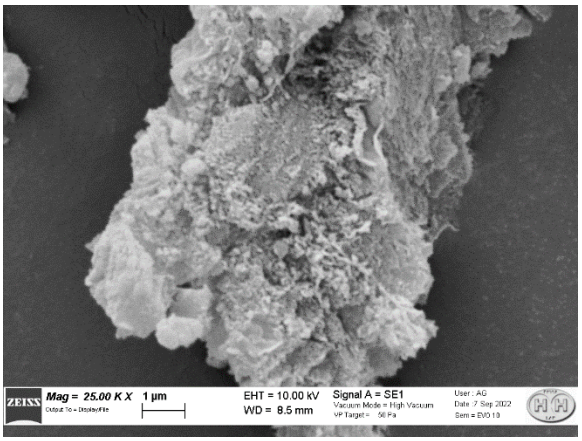

Figure S2. Representative SEM images of $Cs_2AgBiCl_6$/g-C_3N_4 composites. a) $Cs_2AgBiCl_6$ 90%/g-C_3N_4 10% best performing composites for HER. b) $Cs_2AgBiCl_6$ 10%/g-C_3N_4 90% best performing composite for N_2 photo-fixation. c) pure $Cs_2AgBiCl_6$ d) nanosheets g-C_3N_4.

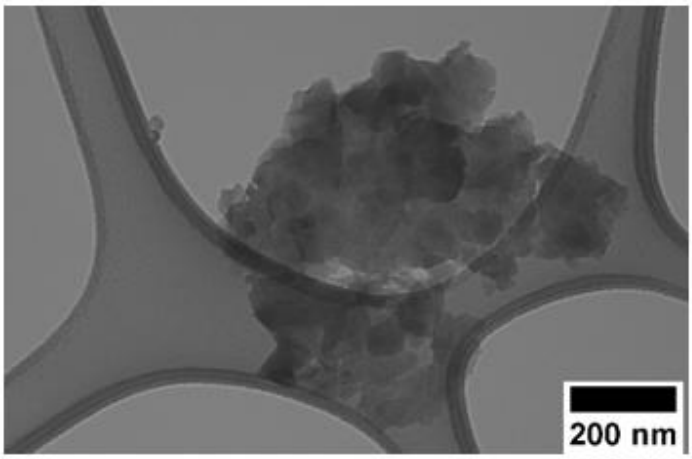

Figure S3. TEM image of g-C_3N_4 nanosheets.

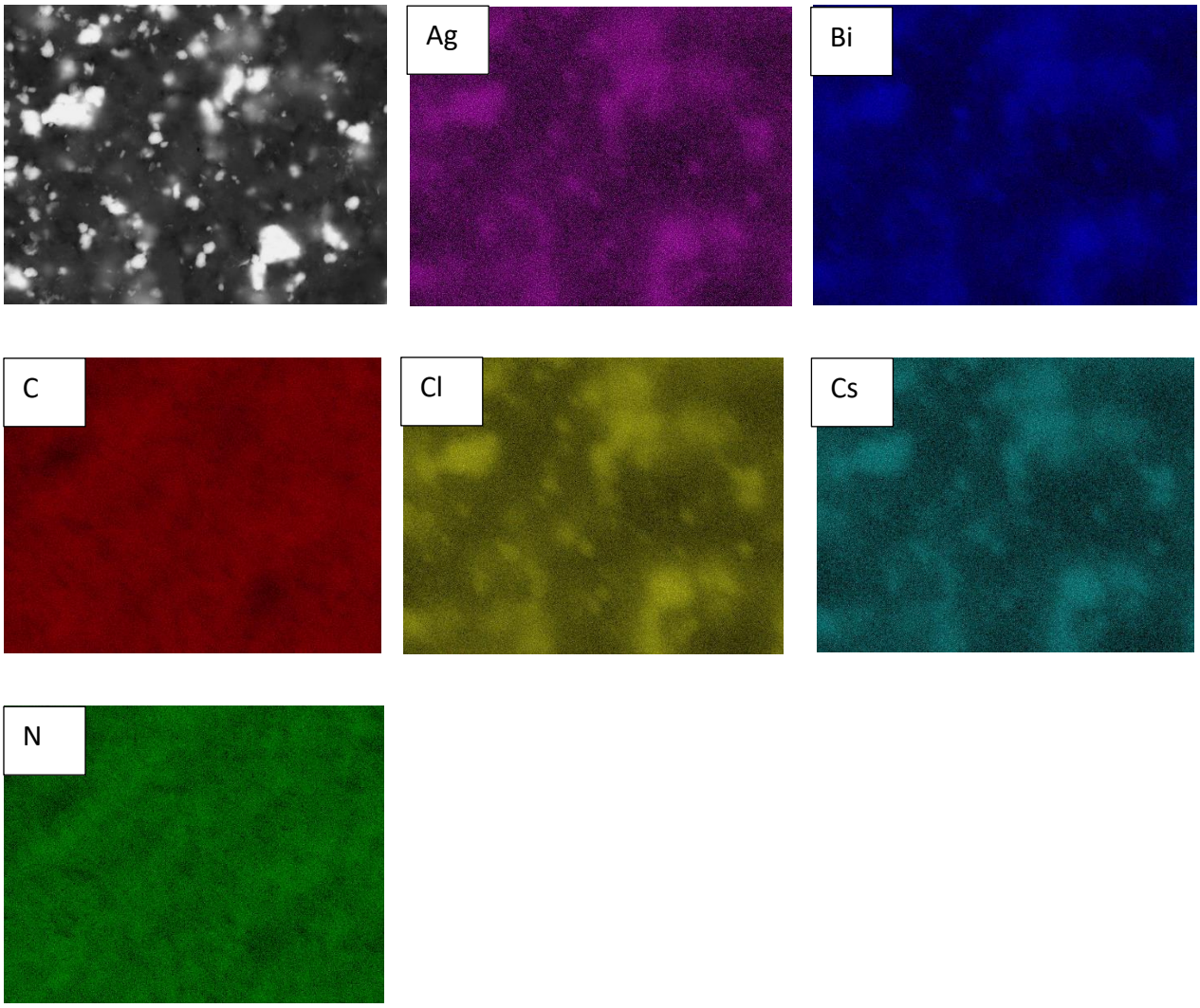

Figure S4. EDS elemental mapping for $Cs_2AgBiCl_6$ 10%g-C_3N_4 composite.

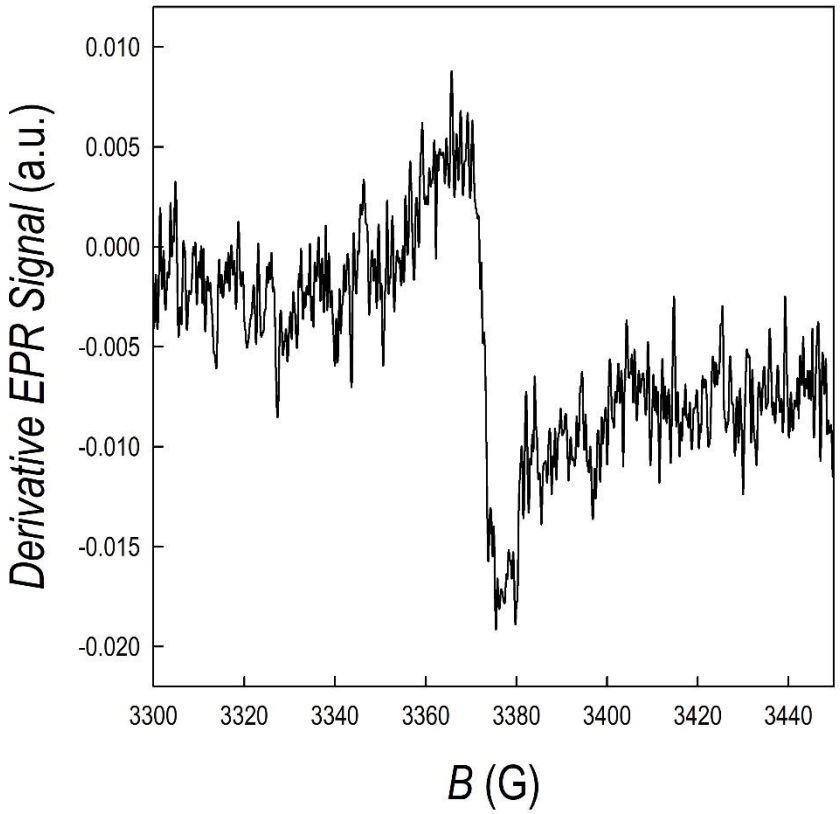

Figure S5. EPR data for g-C_3N_4 nanosheets.

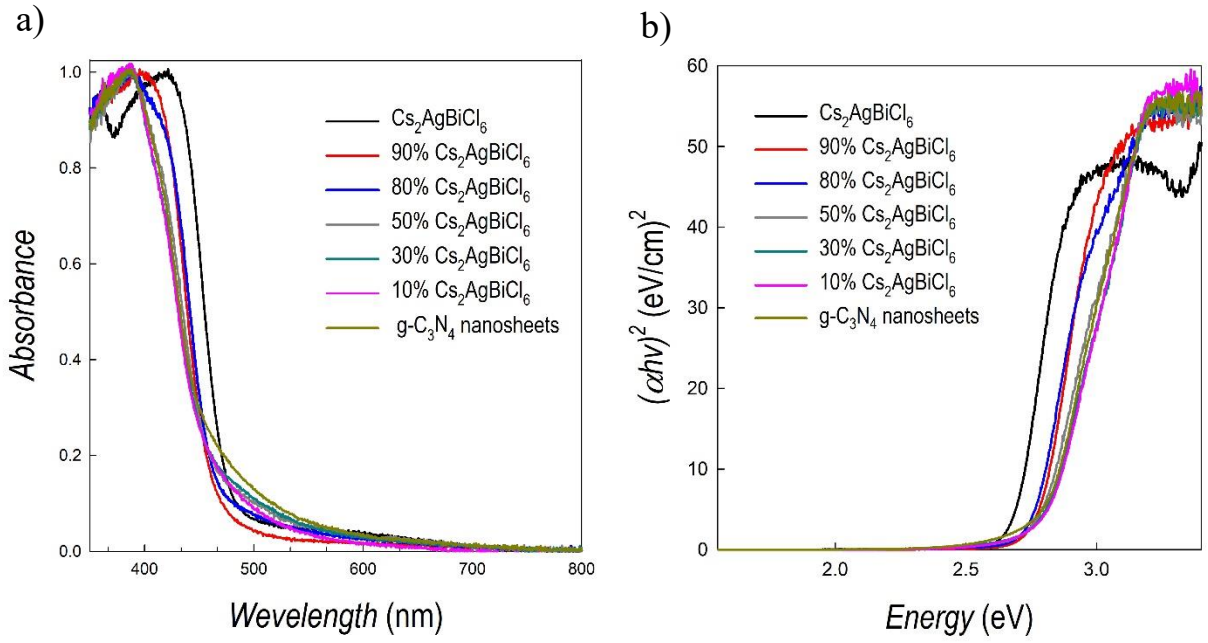

Figure S6. a) Absorption spectra and b) Tauc plots for selected samples of the $Cs_2AgBiCl_6$/g-C_3N_4 system.

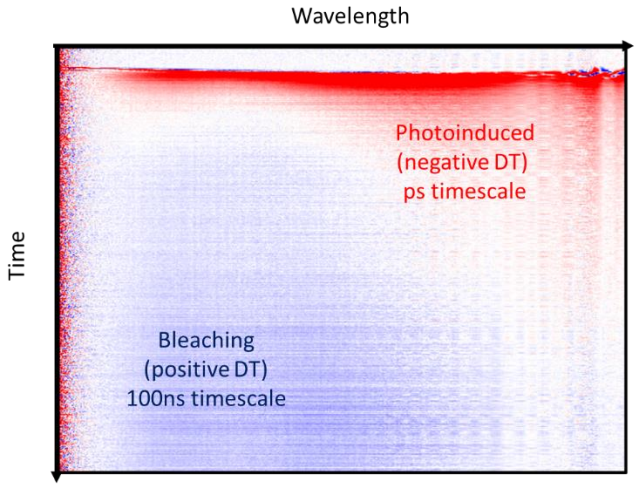

Figure S7: Sketch representing a typical spectrogram resulting from a DT measurement, with wavelength on *x* axis and time on *y* axis. The signal is generally behaving as a negative DT signal (positive DA=-DT) on the short time delay range, *i.e.* photoinduced absorption on the picosecond timescale. A positive DT signal is instead observed at longer time delay, i.e. a bleaching signal on the nanosecond timescale.

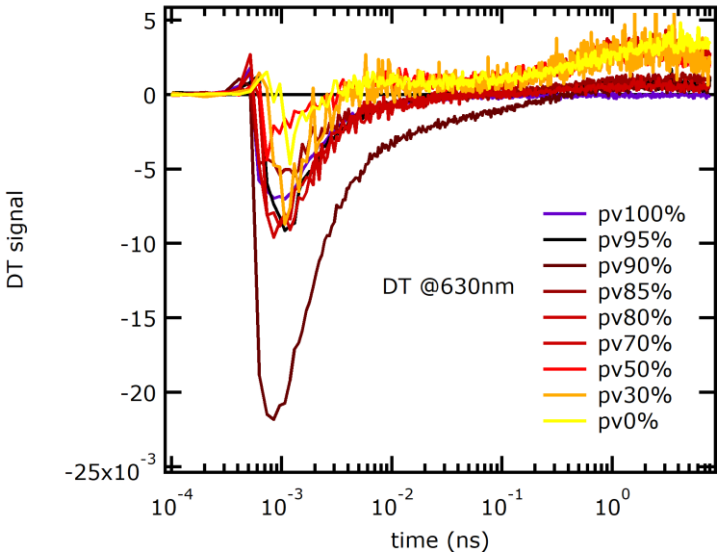

Figure S8: DT signal extracted at 630 nm for the solution with concentration used in the H_2 production (1g/L). DT amplitude is reported on time delay with log scale.

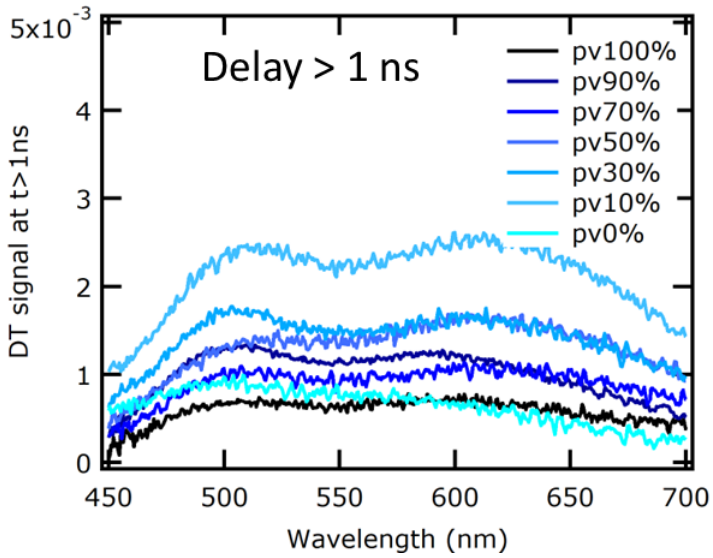

Figure S9: DT spectra extracted at delay >1ns for the solution with concentration used in NH_3 production (0.5g/L).

Table S1: Band gap of the $Cs_2AgBiCl_6$ for different functionals and fractions of exchange inside the HSE06 hybrid functional.

Method	**Band Gap (eV)**
PBE	1.83
HSE06 (α = 0.25) + SOC	2.43
HSE06 (α = 0.31) + SOC	2.78
HSE06 (α = 0.43) + SOC	3.21

Experimental	2.77

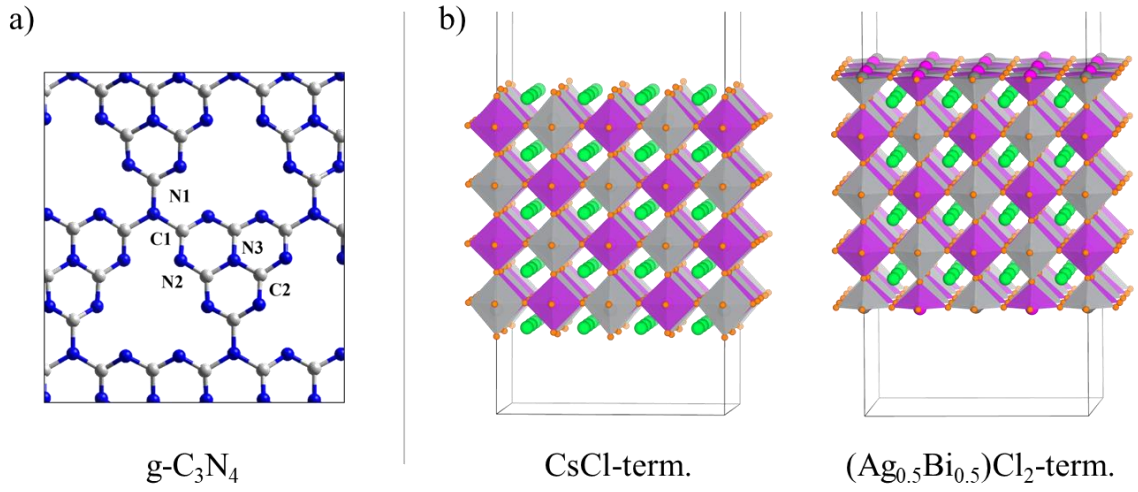

Figure S10: a) Optimized structure of pristine g-C_3N_4. b) Optimized structure of (001) $Cs_2AgBiCl_6$ surfaces with CsCl- and with $(Ag_{0.5}Bi_{0.5})Cl_2$-termination. Following colours are used: C, grey; N, blue; Bi, purple; Ag, gray; Cs, green; Cl, orange.

Table S2: Defect formation energy at E_F = 0 eV for the chloride vacancy, V_{Cl}, at the $(Ag_{0.5}Bi_{0.5})Cl_2$ terminated surface at the PBE0 level of theory.

	AgBi-terminated $Cs_2AgBiCl_6$ [Band gap = 2.81 eV]	
	DFE (eV)	**TILs (eV)**

V_{Cl}^{+}	-0.60	**(+/0)**	1.76
V_{Cl}^{0}	1.15	**(+/-)**	1.69
V_{Cl}^{-}	2.75	**(0/-)**	1.60

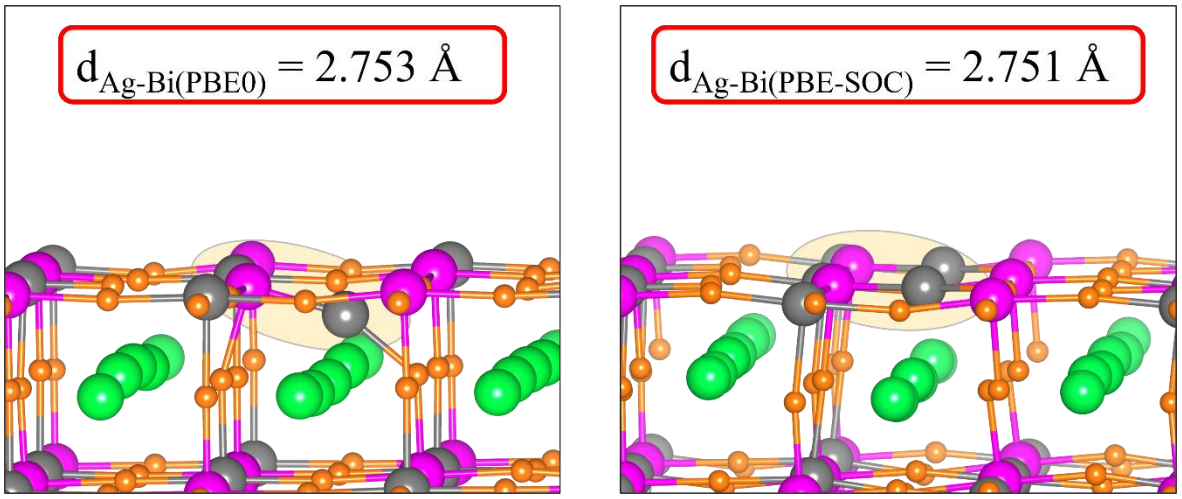

Figure S11: Optimized V_{Cl}^{-} at (left) hybrid PBE0 level of theory and (right) with PBE-SOC. The Ag-Bi dimer is highlighted and its bond length is explicitly given.

Table S3: Self-trapped exciton formation: DFT results of the absorption and emission properties, as well as singlet and triplet state relaxation energies following emission and absorption, respectively; see the Jablonski diagram in Figure S14a for the accompanying scheme.

Property	**Energy (eV)**
Absorption	2.82
Emission	1.46
Singlet relaxation	1.15
Triplet relaxation	0.21

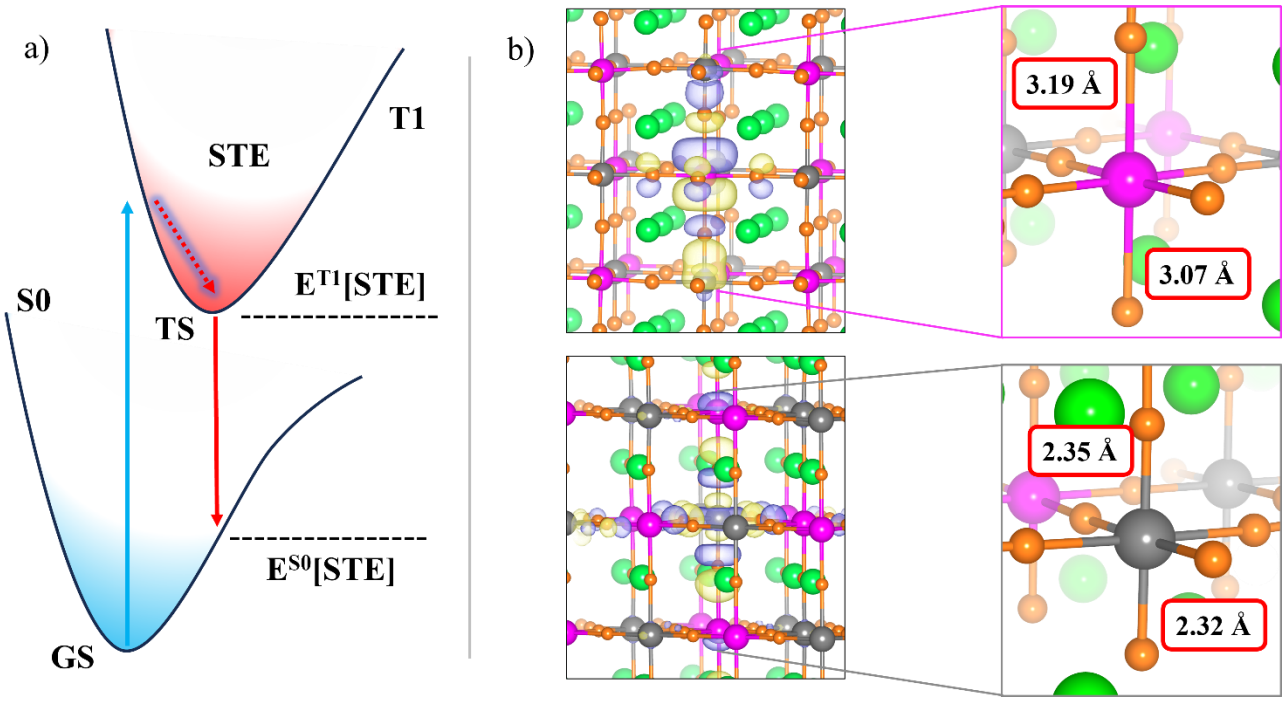

Figure S12: a) Jablonski diagram of the STE formation mechanism. b) Electron and hole Kohn-Sham orbitals of the STE in the triplet state. Distorted bond lengths upon exciton localization are explicitly visualized in panel b.

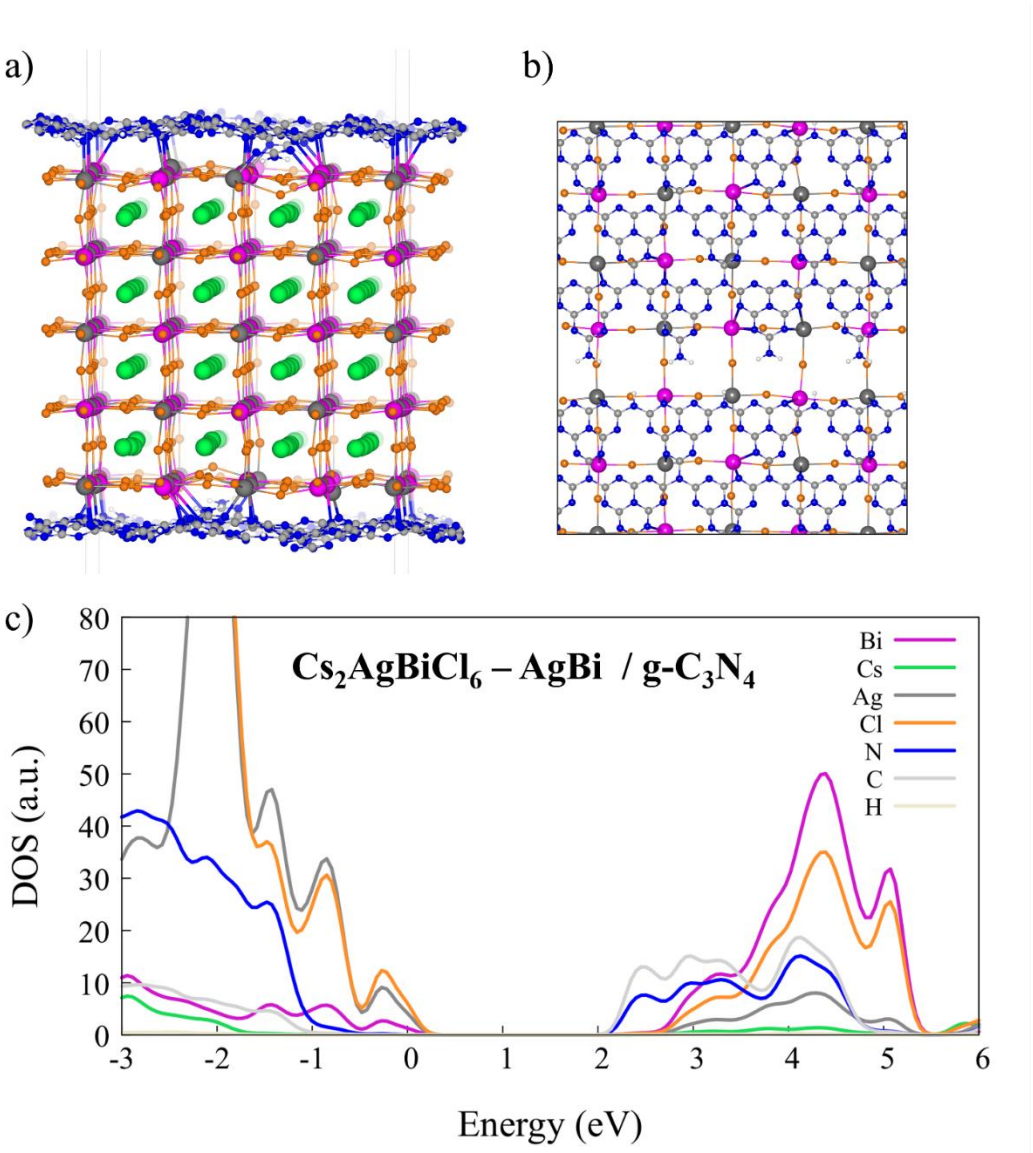

Figure S13: a) Side view of the optimized $Cs_2AgBiCl_6$-AgBi/g-C_3N_4 interface. b) Top view showing the periodicity for model system with the modified g-C_3N_4 on top of the $(Ag_{0.5}Bi_{0.5})Cl_2$-terminated surface. c) Projected density of states of the optimized interface at the PBE0 level of theory.

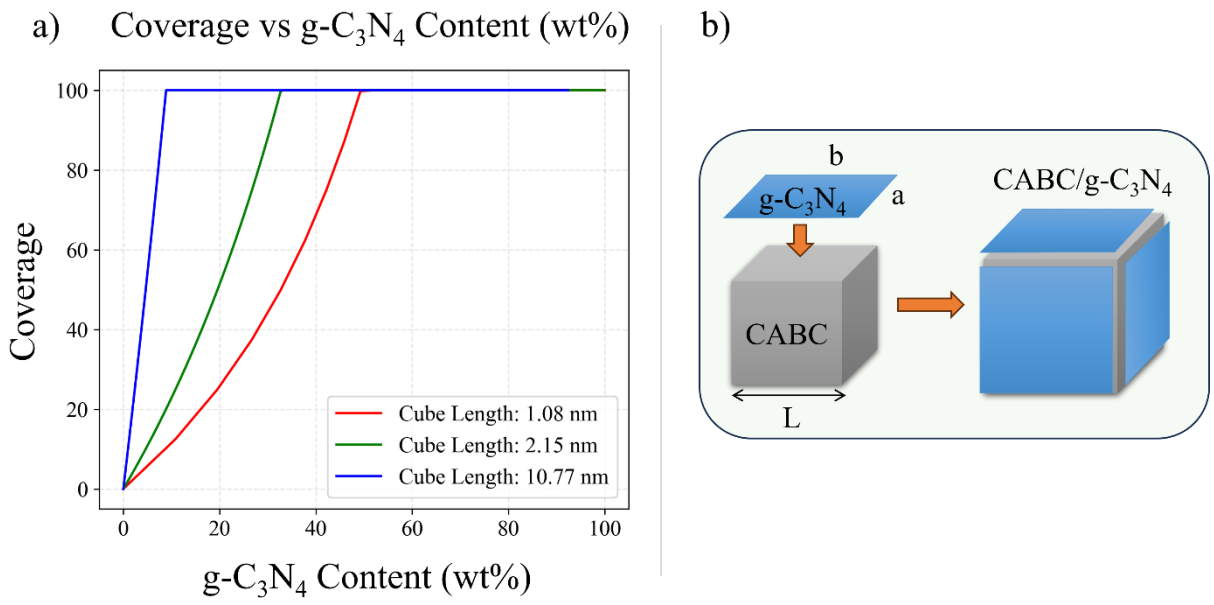

Figure S14: (a) Coverage vs g-C_3N_4 content using a different value for the length of the nanocrystal. (b) Schematic representation of the model system. CABC stays for $Cs_2AgBiCl_6$.

Table S4: Defect formation energies (DFE) at E_F = 0 eV of the different nitrogen vacancies for g-C_3N_4 at PBE0-D3 considering both doublet and quartet spin states. The energy difference between doublet and quartet states, $\Delta E_{Q\text{-}D}$, is explicitly highlighted.

V_N^0	N1	N2	N3
Doublet	4.45	3.82	3.81
Quartet	4.52	4.47	5.52
$\Delta E_{Q\text{-}D}$	0.07	0.65	1.71

Table S5: Defect formation energy (DFE) and thermodynamic ionization level (TIL) for the (0/-) transition of the nitrogen vacancies at N2 and N3 position in the monolayer and in the bulk. All values are given at HSE06+SOC level of theory.

	DFE@E_F = 0 eV [Monolayer Band Gap = 3.4 eV]		
	N2	**N3**	**TIL (0/-)**
V_N^0	3.43	3.36	2.44
V_N^{-1}	6.43	5.79	3.01
	DFE@E_F = 0 eV [Bulk Band Gap = 2.9 eV]		
	N2	**N3**	**TIL (0/-)**
V_N^0	3.89	3.51	1.56
V_N^{-1}	5.78	5.07	1.88

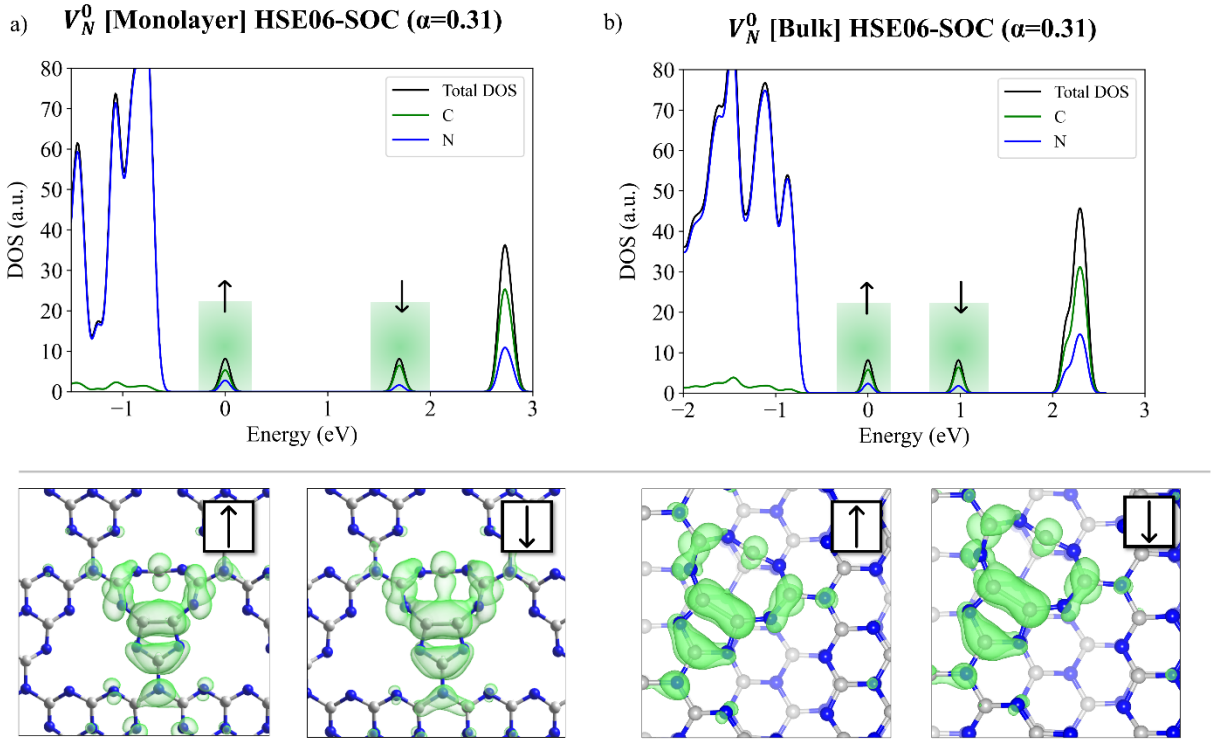

Figure S15: a) Projected density of states and isosurface plots of the most stable nitrogen vacancy, V_N^0, for the g-C_3N_4 monolayer. b) Projected density of states and isosurface plots of V_N^0 for g-C_3N_4 bulk. Both the occupied and unoccupied states, being created upon the addition of one electron, are localized on the nitrogen vacancy.

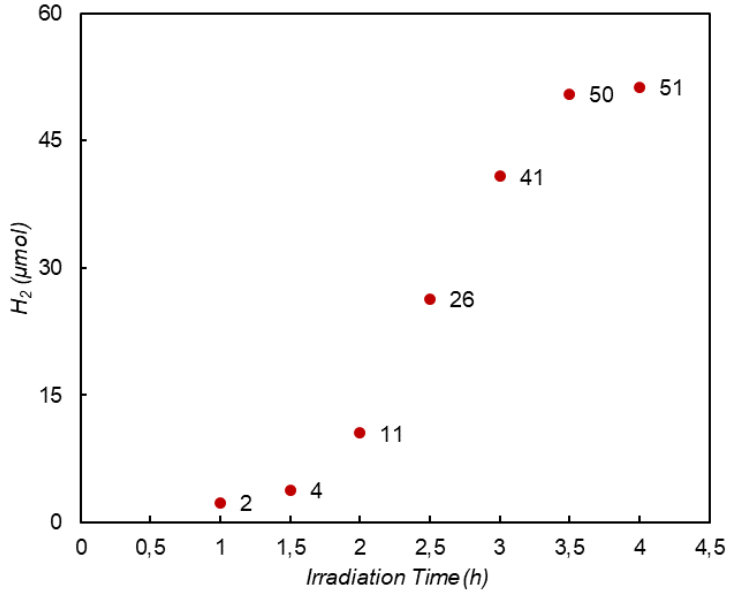

Figure S16. Hydrogen evolution profile over irradiation time for the 10 wt% g-C_3N_4 composite.

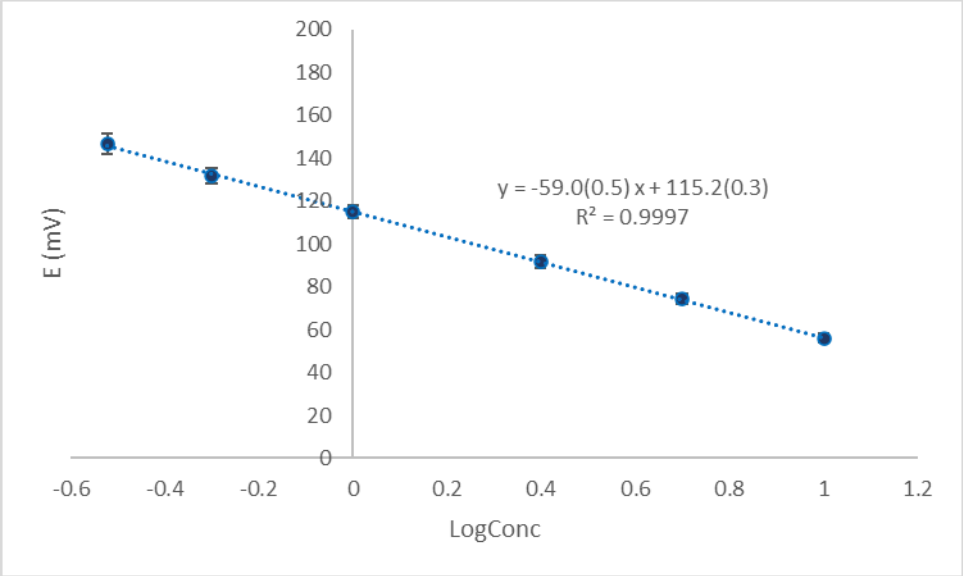

Figure S17. Mean calibration curve (*n*=8) for ammonia quantification (0.25 mg L^{-1} ÷ 10 mg L^{-1} as NH_3).

This is an open access article distributed under the terms of the Creative Commons CC BY license, which permits unrestricted use, distribution, and reproduction in any medium, provided the original work is properly cited.

© 2024 The Authors. Advanced Energy and Sustainability Research published by Wiley-VCH GmbH

CHAPTER 4

Compositional and Defect Engineering of Metal Halide Perovskite-based Heterojunctions for Efficient Nitrogen Photofixation

Costanza Tedesco,[a] Angelica Simbula,[b] Riccardo Pau,[b] Francesca Merlo,[a] Andrea Speltini,[a] Vincenza Armenise,[c] Andrea Listorti,[d] Luca Gregori,[e] Asma A. Alothman,[f] Edoardo Mosconi,[f,g] Michele Saba,[b] Antonella Profumo,[a] Lorenzo Malavasi[a,*]*

[a]Department of Chemistry and INSTM, University of Pavia, Via Taramelli 12, Pavia, 27100, Italy
[b]Department of Physics, University of Cagliari, 09042 Monserrato, Italy
[c]CNR NANOTEC - c/o Dipartimento di Chimica, Università di Bari, Via Orabona 4, 70126 Bari, Italy
[d]Department of Chemistry, University of Bari "Aldo Moro", via Orabona 4, 70126, Bari, Italy
[e]Department of Chemistry, Biology and Biotechnology, University of Perugia and INSTM, Via Elce di Sotto 8, 06123 Perugia, Italy
[f]Chemistry Department, College of Science, King Saud University, Riyadh 11451, Kingdom of Saudi Arabia
[g]Computational Laboratory for Hybrid/Organic Photovoltaics (CLHYO), Istituto CNR di Scienze e Tecnologie Chimiche "Giulio Natta" (CNR-SCITEC), Via Elce di Sotto 8, 06123 Perugia, Italy

Corresponding Authors

Edoardo Mosconi, email: edoblasco@gmail.com;
Lorenzo Malavasi, email: lorenzo.malavasi@unipv.it

TOC

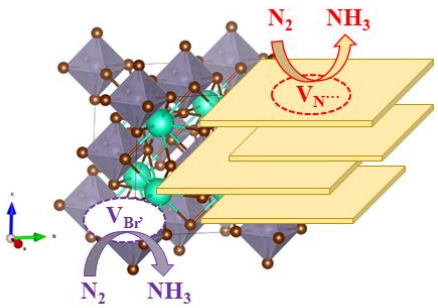

ABSTRACT

Designing innovative photocatalysts for nitrogen photofixation is becoming crucial for the development of carbon neutral ammonia production. Metal halide perovskites (MHPs) provide a rich library of materials and one of their strengths is the possibility of easily tuning the semiconductor bandgap in order to integrate them in devices with different functionalities. An under-explored path is their exploitation to run a wide range of photoredox reactions mediated by solar light. Herein, we develop a heterojunction based on the vacancy-ordered double perovskite Cs_2SnBr_6 and carbon nitride nanosheets and demonstrate its ability in running the nitrogen photofixation reaction to produce ammonia under solar light. We investigated the full Cs_2SnBr_6/g-C_3N_4 system and identified an optimal range providing an outstanding ammonia evolution rate up to 270 μmol g^{-1} h^{-1}, accurately quantified by means of ion selective electrode. Mechanistic insight into the photofixation reaction promoted by the heterojunction was obtained through a combination of advanced spectroscopy and computational modelling. Efficient ammonia production stems from an effective charge transfer from the perovskite to the nitrogen vacancies on the carbon nitride enabled by the absence of self-trapped excitons in Cs_2SnBr_6 which also provides additional reactive sites through bromide vacancies. This work paves the way to MHP-based catalyst design strategy for sustainable ammonia production.

1. INTRODUCTION

The utilization of ammonia (NH_3), obtained through nitrogen fixation, as a green alternative fuel, represents a significant promise in mitigating carbon emissions and reaching energy independence.[1–3] Ammonia stands as a cornerstone in the field of chemical compounds for commercial application owing to its multifaceted application in both industrial and academic domains.[2–4] The potential of ammonia as an energy vector lies in its ability to store and transport energy efficiently: it can be exploited to release hydrogen, to generate electricity in fuel cells, or directly as a fuel in internal combustion engines, already resulting in the development of ammonia-fueled engines for transport and power generation.[5] Currently, ammonia is primarily produced via the Haber-Bosch process, which involves the reaction of nitrogen from air with highly pure hydrogen derived mainly from natural gas. This method is energy-consuming and relies heavily on fossil fuels, contributing to CO_2 emissions, and requires high temperatures (>500°C) and extremely high pressure (200-300 bar) accounting for over 1% of total global fossil energy and for 11% of the energy consumed in chemical industries.[1,6] Photofixation of nitrogen for ammonia production represents one of the most innovative and sustainable approaches to meet the global demand of this pivotal chemical. The process leverages the energy from sunlight to convert atmospheric nitrogen (N_2) into ammonia (NH_3), mimicking the natural nitrogen fixation performed by certain bacteria and plants,[7–9] with the aid of photocatalysts to harness sunlight and drive the reduction of nitrogen to ammonia. The process involves three main steps: the first one is the absorption of light by the photocatalysts, generating excited electrons and holes. The second one is the activation of nitrogen, representing the bottleneck of the process, where the excited electrons are driven to nitrogen molecules adsorbed on the catalyst surface, breaking the strong triple bond in N_2 molecules. Although the fixation of N_2 to NH_3 is thermodynamically convenient, being the triple bond in N_2 extremely strong, the reaction cannot occur spontaneously under ambient conditions ($\Delta H_{298\,K}$ = - 92.2 kJ mol^{-1}).[3] Moreover, low solubility and slow diffusion of nitrogen in water are significant impediments for enhancing the efficiency of the process. The last step of nitrogen photofixation involves the progressive reduction of nitrogen atoms by the electrons to form ammonia, typically in the presence of a hydrogen source such as water.[4,6]

The efficiency of photofixation, as in general for photocatalytic processes, largely depends on the choice of the photocatalysts. Effective photocatalytic materials need to exhibit strong light adsorption, good charge separation, high catalytic activity, and the presence of defects

such as nitrogen, oxygen and sulfur vacancies that acts as reactive sites for N_2 adsorption.[4,6,10] Currently, the research of promising and performing materials is being conducted on three classes of photocatalytic materials: metal oxides, metals sulfides, and metal-free semiconductors.[2,3]

Metal oxides have been extensively investigated for their photocatalytic properties and most of these materials are already known for their proved performances in other photocatalytic reactions like hydrogen evolution through water splitting. Titanium dioxide (TiO_2) represents the forerunner of this material category owing its strong oxidative capability, however limited by its large band gap (3.2 eV) that causes large photoactivity in the UV range and a high rate of electron-hole recombination.[8,11,12] Barawi et al. in 2023 reached more than 105 μmol $g^{-1}L^{-1}h^{-1}$ NH_3 yield rate with 90% selectivity exploiting a Mo-doped TiO_2 nanocrystal system.[8] ZnO represents a promising material as well for nitrogen photofixation and both ZnO and TiO_2 can be easily synthesized in different nanostructures where the photofixation of N_2 can be greatly increased compared with the bulk metal oxides.[13,14] Bismuth based oxides are also emerging as promising materials for nitrogen photofixation thanks to their intense visible light activity (band gap from 2.4 to 3 eV) with BiOX (X=Cl,Br,I) materials showing significant performances in the ammonia photoproduction reaction.[15,16] For example, Wang et al. succeeded in the preparation of a bio-inspired sponge system based on BiOBr with oxygen vacancies reaching more than 2 mmol $g^{-1}h^{-1}$ of ammonia evolution rate.[9]

In the metal-free semiconductors category, graphitic carbon nitride (g-C_3N_4), already widely used in other photocatalytic reactions, has emerged as one of the most promising and widely used materials for nitrogen photofixation.[17,18] To overcome its known challenges, such as the rapid carrier recombination rate, several strategies have been developed, such as doping and co-doping. The introduction of foreign elements such as metals (e.g., Fe, Co) or non-metals (e.g., S, P) into the g-C_3N_4 matrix can enhance its electronic properties and improve charge separation.[19] Besides, the combination of g-C_3N_4 with other materials, such as metal oxides or conducting polymers, through the realization of heterojunctions, can synergistically enhance photocatalytic activity and stability promoting good ammonia production rates.[7,17,20–22] Among other approaches, the generation of nitrogen vacancies in carbon nitride, being these point defects active sites for nitrogen adsorption, shows to be a good strategy to boost the nitrogen photofixation. Dong et al. proved the importance of the role of nitrogen vacancies for the nitrogen fixation mechanism obtaining a N-vacancies rich

g-C_3N_4 that showed 2.4 times of N_2 physical adsorption ability compared with the bulk and a consequent important boost in the NH_4^+ amount detected of 2.4 mM in N_2 atmosphere.[23]

While the above-reported materials represent well-established photocatalysts, in the last years metal halide perovskites (MHPs) have demonstrated, thanks to their exceptional optoelectronic properties, to be efficient and promising materials for various photocatalytic applications. MHPs exhibit unique features that are highly advantageous for photocatalysis, such as tunable band gap, high absorption coefficient, and long charge carrier lifetime and diffusion lengths, which are crucial for reducing recombination rates and enhancing photocatalytic efficiency.[24–27] While MHPs have been extensively explored for several solar-related applications, such as photocatalytic H_2 generation, photoreduction of CO_2, and synthesis of organic molecules, their exploitation in the field of nitrogen photofixation is in its newborn era, with the first example recently published by our group, where it was proved that a heterojunction system based on g-C_3N_4 nanosheets and the $Cs_2AgBiCl_6$ double perovskite is capable, by properly tuning the heterojunction composition, to carry out both H_2 photogeneration and N_2 photofixation.[28] While this paper represents the first demonstration of a MHPs-based heterojunction for ammonia photoproduction, the obtained rates were relatively low and, based on this preliminary results, we aimed at engineering optimized perovskite-based heterojunctions for nitrogen photofixation that could provide significant production rates.

In this respect, we identified vacancy-ordered perovskite as potential good candidates. Vacancy-ordered double perovskite adopts the general formula $A_2\square BX_6$ where B is a tetravalent metal (Sn^{4+}, Ge^{4+}, or Te^{4+}) with the vacancies located at the B sites, leading to a distinctive ordered structure.[31] The introduction of vacancies significantly influences their electronic band structure for example with the creation of localized states within the band gap. These localized states can act as trap sites for charge carriers, influencing conductivity and carrier mobility.[29,30] These vacancies influence the electronic and optical behavior, enhance stability, and improve defect tolerance, making these materials highly attractive for advanced optoelectronic applications and potentially for photocatalysis.[29–31,31–33] On these bases, we report here the engineering of a novel heterojunction for nitrogen photofixation based on the vacancy-ordered Cs_2SnBr_6 perovskite and g-C_3N_4 nanosheets showing significant ammonia production rates (up to 270 μmol g^{-1} h^{-1}) which are 8 times higher than previously reported data on MHPs-based heterojunctions for nitrogen photofixation. In addition, through a combined experimental and computational work, we were able to provide

a detailed picture of the mechanism underpinning the efficient nitrogen reduction reaction to ammonia observed in this system.

2. RESULTS AND DISCUSSION

The Cs_2SnBr_6/g-C_3N_4 system has been synthesized according to the experimental procedure reported in the Supporting Information (SI). Weight ratios between Cs_2SnBr_6 and g-C_3N_4 nanosheets investigated are (wt% of perovskite) 100, 80, 65, 50, 45, 35, 20, 15, 7 and 0.

Figure 1a reports the room temperature X-ray diffraction (XRD) patterns of some selected compositions investigated. Bottom part of Figure 1a shows the pattern of Cs_2SnBr_6 vacancy-ordered double perovskite which is also reported against the calculated pattern in Figure 1b. The perovskite displays a cubic symmetry with *Fm*-3*m* space group (#225) and a lattice parameter of 10.7761(2) Å, in agreement with previous results.[34] A sketch of the cubic unit cell is reported in Figure 1c. At the top of Figure 1a, the X-ray pattern of pure g-C_3N_4 nanosheets is reported. The typical broad peaks around 13° and 28° corresponding to the (100) and (002) reflections are clearly visible. In all the patterns of the composites (cf. Figure 1a) the diffraction peaks of Cs_2SnBr_6 are clearly visible due to its high scattering power with respect to g-C_3N_4. Morphological inspection of Cs_2SnBr_6, g-C_3N_4, and selected composites has been carried out by scanning electron microscopy (SEM) and the results are reported in Figure S1. g-C_3N_4 nanosheets have also been characterized by transmission electron microscopy (TEM) and representative images showing their nanostructure are shown in Figure S2. Elemental mapping through energy-dispersive X-ray spectroscopy (EDX) has been carried out for the composite with 35 wt% of Cs_2SnBr_6, as an illustrative example, and is reported in Figure S3, confirming the formation of a composite between the two semiconductors. Electron paramagnetic resonance (EPR) measurements have been carried out on g-C_3N_4 nanosheets to confirm the presence of nitrogen vacancies which are characterized by the presence of a peculiar signal centered around g=2, as shown in Figure S4, due to the presence of unpaired electrons.[23]

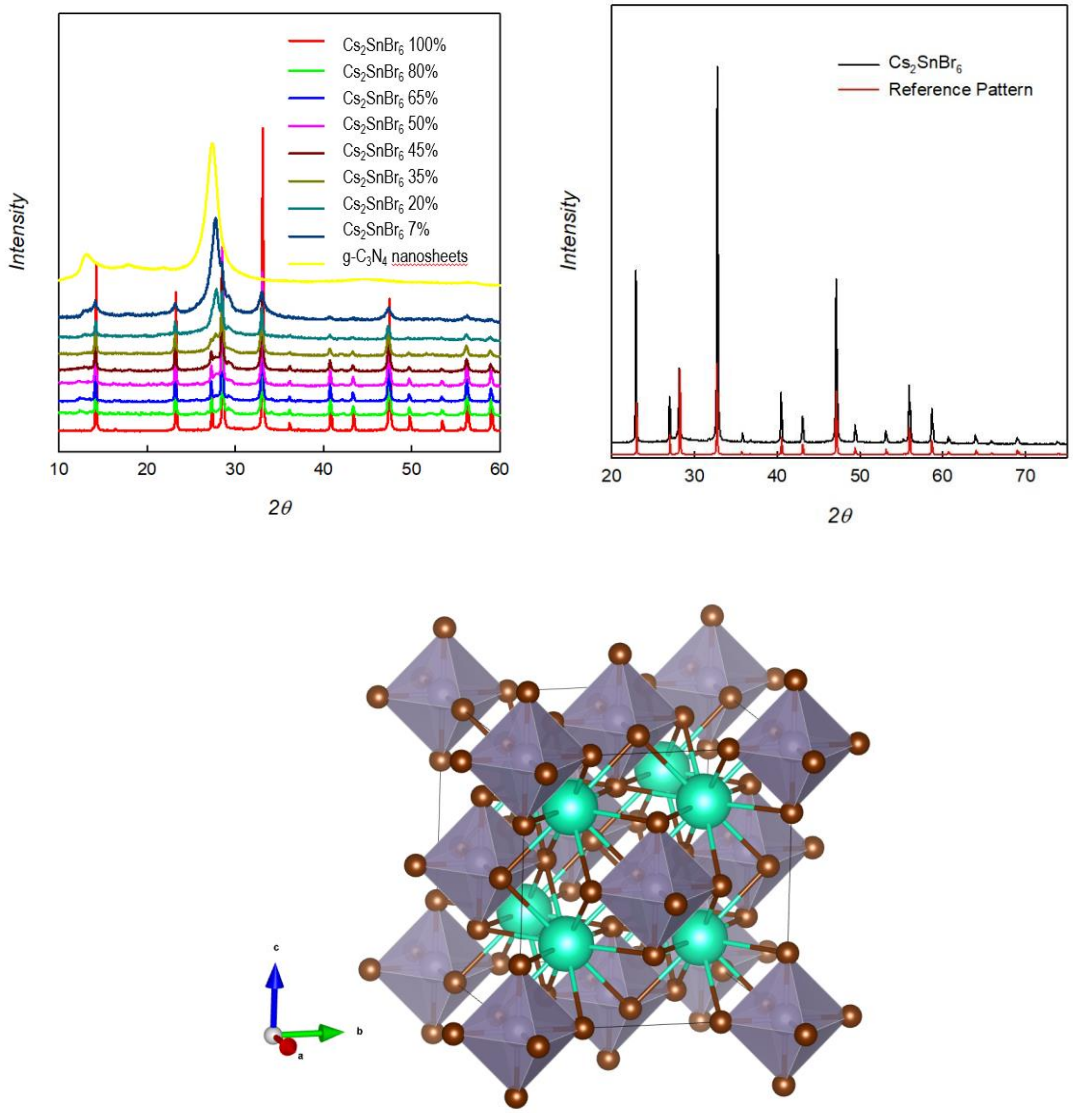

Figure 1. a) XRD pattern of Cs_2SnBr_6/g-C_3N_4 composites; b) XRD pattern of Cs_2SnBr_6 against the reference cubic structure, and c) sketch of Cs_2SnBr_6 crystal structure where Cs^+ ions are shown as green spheres and the bromide ions as grey spheres included into the octahedra.

Figure 2a reports the results in terms of ammonia evolution rates as a function of Cs_2SnBr_6 amount, expressed as μmol $g^{-1}h^{-1}$, obtained by photocatalytic experiments under simulated solar light. Experimental details are provided in the SI for both the photocatalytic experiments and the ammonia determination, technique which is based on ion selective electrode quantification instead of colorimetric methods (which tend to overestimate the actual concentrations), thus proving on a more accurate and interferent-free approach.[28]

The trend of ammonia evolution rate steeply increases from pure Cs_2SnBr_6 (about 50 μmol $g^{-1}h^{-1}$) to > 200 μmol $g^{-1}h^{-1}$ for the composites including an intermediate amount of perovskite (20-25%) and reaching the highest value of 266 μmol g^{-1} h^{-1} for the composition Cs_2SnBr_6 35 wt%/g-C_3N_4 65 wt% before decreasing for composites with a larger amount of g-C_3N_4. Note that pure g-C_3N_4, under these reaction conditions, provides an ammonia evolution rate of 2.7 μmol g^{-1} h^{-1}.

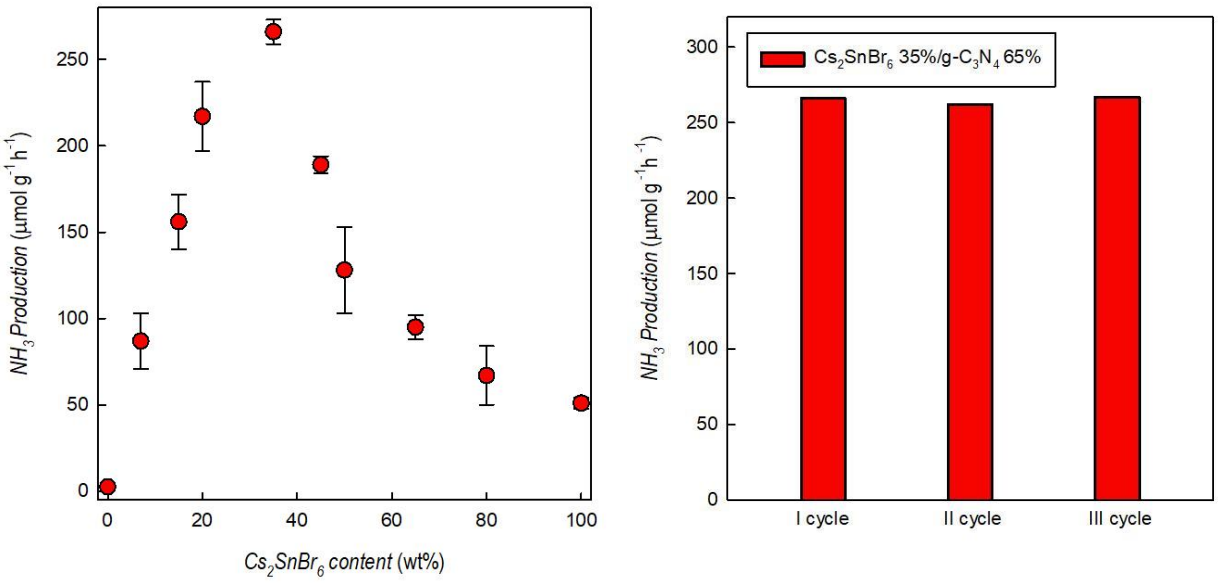

Figure 2. Ammonia photocatalytic production: a) as a function of Cs_2SnBr_6 wt% in the composites. (*n*=3, simulated solar light, 500 W m^{-2}); b) as a trend over three cycles for the best performing composite, namely Cs_2SnBr_6 35 wt%/ g-C_3N_4 65 wt%.

The data reported in Figure 2a demonstrate, first of all, that the perovskite alone is already quite active in the nitrogen reduction reaction and that such activity can be boosted through the heterojunction formation, achieving a value, for the optimal composition, which is about 4 times that of pure Cs_2SnBr_6. The absolute value of ammonia production obtained for the Cs_2SnBr_6 35 wt%/ g-C_3N_4 65 wt% composition is nearly 8 times larger than what previously reported on perovskite-based systems.[30] The good stability of the ammonia production has been tested on the top performing composite for three successive cycles as reported in Figure 2b. Post-catalysis XRD data are shown in Figure S5, indicating the stability of the system, with a slight reduction in the relative peaks intensity due to the crystallinity reduction of the perovskite phase caused by the photocatalytic reactions which however does not affect the photocatalytic performances.

UV-Vis absorption spectra and the corresponding Tauc plots for Cs_2SnBr_6/g-C_3N_4 system are reported in Figure S6. The band gap of Cs_2SnBr_6 is 2.75 eV and that of g-C_3N_4 is 2.78 eV, in agreement with previous reports.[28,34] Being the two bandgaps very close, no relevant shifts or trend are observed as a function of composition. The normalized photoluminescence spectra of the Cs_2SnBr_6/g-C_3N_4 system are reported in Figure 3. The emission is dominated by the broad and intense features of graphitic carbon nitride, even at very high perovskite loading. Such broad spectra, that completely covers the weak perovskite emission, derive from the superimposition of multiple electronic transitions.[35] In particular, three transitions have been modeled in pristine g-C_3N_4: a high energy one, centered at around 2.81 eV, which derives from the relaxation of δ* electrons to the LP state, and two low energy transitions centered at 2.70 and 2.42 eV. To access these low energy transitions a non-radiative mechanism to populate the π* state is required, thus the structure of the broadband spectrum depends on the efficiency of this process. In previous works, the interplay between the density of defects and the non-radiative population of π* state have been studied and related to the photocatalytic properties of g-C_3N_4. [35]

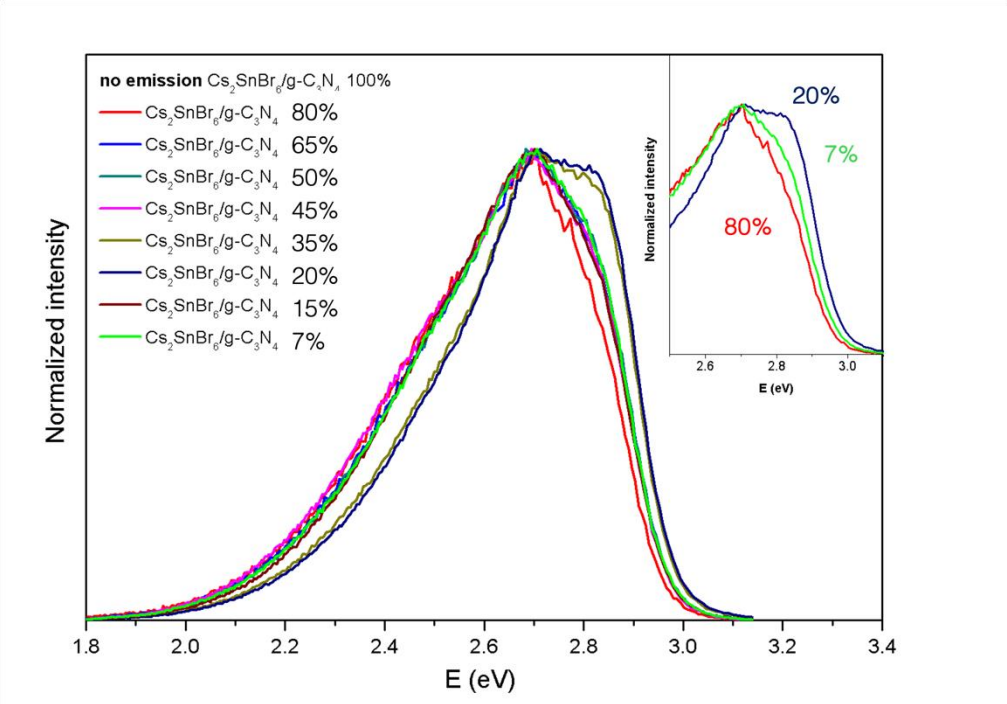

Figure 3. Emission spectra of Cs_2SnBr_6/g-C_3N_4 composites powders at different percentages of Cs_2SnBr_6 loading (wt%). λ_{ex} = 375 nm. Inset: zoom on a relevant spectral zone (see text for details).

A close inspection of the spectral region around the emission band peak (inset of Figure 3) shows that, for low perovskite loadings, there is an increase of low-lying sub-band

population, as the emission displays a reduced contribution from the high energy transition. Conversely, by increasing the perovskite content, the high energy transition (2.81 eV) became more and more pronounced, with a peak around 20% (and 35%, see main Figure 3) of perovskite content while the trend inverts after this value and, at higher perovskite loadings, one can observe again a reduced contribution to the emission band from the high energy transition. Very interestingly, the trend of the high energy transition intensity as a function of perovskite loading recalls that of the ammonia production reported in Figure 2, with the maximum values of the photocatalytic activity found in the range 20-35% of perovskite corresponding to the percentages that lead to a higher contribution to the broad band by the δ* → LP state transition. This observation points out the effect of compositional engineering in funnelling optical excitations to the sites where they can be exploited in photocatalytic processes. In a recent work on MHP/g-C_3N_4 we demonstrated that the reduction of the low-lying sub-band population allows to retain the excitation in the carbon nitride component where it can be exploited for the ammonia production.[28] Herein we further corroborate this observation and, moreover, we also underline an active role of perovskite in offering catalytic centers as it will be confirmed by the computational modelling work. Noticeably, in these composite systems, a very simple and fast checking of the steady state photoluminescent properties allows to conveniently assess composition/performances relations.

To understand the excited state dynamics as a function of Cs_2SnBr_6/g-C_3N_4 composition, Differential Transmission (DT) measurements were performed. Excitation of solutions in quartz cuvettes was provided by a femtosecond pulsed laser at 350 nm, and the transient transmission signal was collected in a pump and probe configuration with sub-ps resolution (details about experimental method in SI). A set of data extracted from the measurements are shown in Fig. 4a, where DT spectra are reported for the different compositions, from 100% g-C_3N_4 (black line) to 100% Cs_2SnBr_6 (green line). By observing the two photobleaching features centered at 500 nm and 630 nm, it is worth noticing that the intensity of transitions changes substantially with the change in composition. First of all, lower overall DT signal amplitude is obtained from the pure compounds, which are also the ones with lower ammonia evolution rates. When adding small amounts of perovskite to the g-C_3N_4 the intensity of the signal is boosted, analogously to what already observed for the ammonia production rate in Fig. 2 and, correspondingly, a broad DT peak centered around 630 nm rises. When the perovskite amount surpasses 40%, the amplitude of the DT signal decreases down to the pure perovskite case.

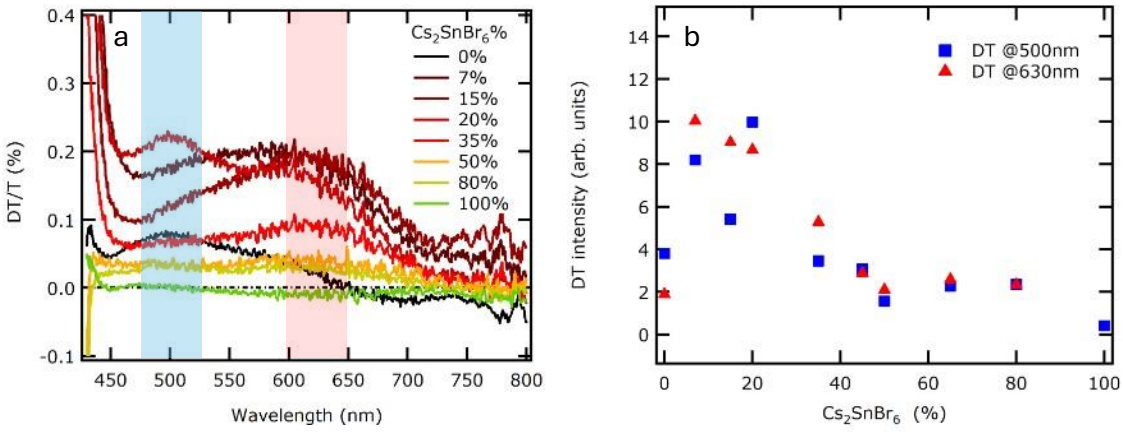

Figure 4. (a) spectra extracted from DT measurements (b) trend of DT signal extracted from different relevant wavelength regions as a function of perovskite loading.

Another interesting piece of information that can be extracted from DT measurements is the fact that DT spectra of composites with increased evolution rates (particularly from 7% to 35% perovskite content) have the same spectral features of pure g-C_3N_4, suggesting that the reaction occurs mainly at the g-C_3N_4 defect sites, with an introduction of an amount of perovskite <40% favoring the charge transfer towards g-C_3N_4 sites. The time evolution of the signal is reported in Figure S7, showing that, after a first initial decay on a picosecond scale, the signal stabilizes and follows a much slower decay. To get a complete overview of the data, in Fig. 4b are reported the integrated DT signals for different wavelength ranges and compositions. A fairly good agreement is found between the trend of the DT signals and that of the ammonia generation reported in Figure 2.

Time resolved photoluminescence emitted by the composites was also investigated and the results are reported in Figure 5: here the time decays show that compounds with low-intermediate perovskite amounts, corresponding to high ammonia production rates, have longer TRPL lifetimes. This suggests that for these compositions there is some degree of suppression of nonradiative decays for photoexcited carriers, with a lifetime longer than that of both pure Cs_2SnBr_6 and pure g-C_3N_4.

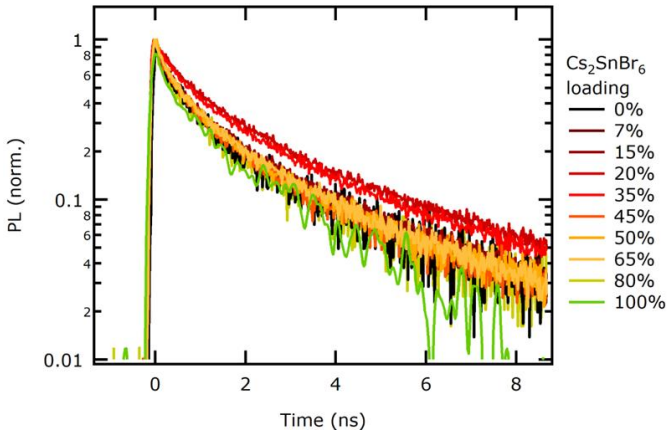

Figure 5: Normalized PL time decays obtained from spectral integration of TRPL spectrograms for different compounds.

To gain insight into the electronic properties and photocatalytic mechanism, we have performed density functional theory (DFT) calculations to understand the trends in ammonia production rates in this vacancy-ordered double perovskite system used in conjunction with g-C_3N_4. All calculations were performed to a high level of accuracy using the hybrid PBE0 functional for geometry optimization and refined by HSE06-SOC level of theory as detailed in the Computational Details section following the procedure already applied in our previous paper.[28] All alignments shown in Figure 6 were obtained from structures optimized at the PBE0 level of theory. From these structures, the absolute alignment with respect to the vacuum was corrected using the internal potential of the bulk systems calculated at the state-of-the-art level of theory.

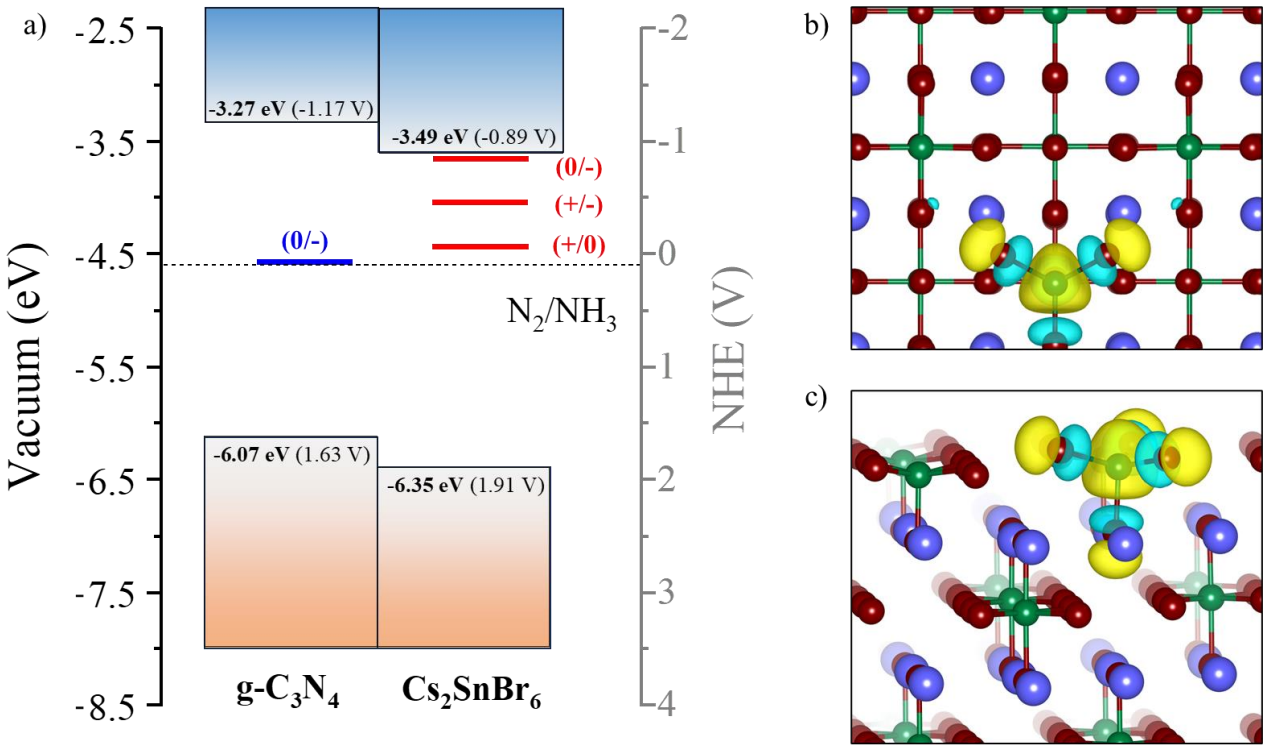

Figure 6. Band alignment of g-C_3N_4 and Cs_2SnBr_6. N_2/NH_3 redox level as well as thermodynamic transition levels for the nitrogen vacancy, V_N (blue segment) and the bromide vacancy, V_{Br} (red segment) are explicitly visualized in the respective phases. All the values are referred to the vacuum level as well as the electrode against NHE. b) Isodensity plot perpendicular to the 001 surface with $SnBr_2$ termination of the double perovskite of the localized state related to the neutral V_{Br}^0, resulting in the formation of an isolated Sn-tetrahedra superficial system. c) different orientation of the vacancy ordered double perovskite motif where the clear localization on the superficial tetrahedral Sn is also reported.

To analyze the NH_3 production mechanism, we started by investigating the pure vacancy-ordered double perovskite phase. As we can see from the experimental ammonia production rate in Figure 2a, this system, at 100% of perovskite, already generates a significant amount of ammonia. Recent studies have identified halide vacancies as critical defects affecting catalytic activity in analogues systems.[31,36] However, in our previous work, we have noticed that the $Cs_2AgBiCl_6$ perovskite alone produces a very low quantity of NH_3 while Cs_2SnBr_6 results to be ~5 time more active.[28] In contrast to $Cs_2AgBiCl_6$, Cs_2SnBr_6 does not show effective self-trapping exciton (STE) state (see SI), and in addition shows a different defect energetics. The enhanced performance could be attributed to the better alignment of the band edges, particularly with respect to the transition ionization level (+/0) associated with the bromide vacancy found to be -0.067 V (NHE) very close and slightly above to the redox

potential for N_2/NH_3 reported as dashed line in Figure 6. Due to the structure of the vacancy ordered perovskite, the electron is found to be localized in the superficial octahedra from where the bromide was removed to generate the defect. Our calculations predict this (+/0) transition level at 1.98 eV above the valence band maximum. The analysis of the charge density for this defect shows the presence of a localized electron that could in principle be transferred to the nitrogen starting the mechanism of photofixation. As we mentioned before, another important feature of Cs_2SnBr_6 is the lack of self-trapped electrons, visible both from photoluminescence spectra (Figure 3) as well as from theoretical calculations reported in the SI which shows the absence of emission from the distorted octahedral. This absence of STE removes extra non-radiative recombination channels, thus increasing the charge separation and the possible transfer to the defects active in the plausible mechanism of the ammonia generation. When we move to analyse the g-C_3N_4 material, we refer to already reported data by our group.[28] From the energy alignment reported in Figure 6 we can see that the g-C_3N_4/Cs_2SnBr_6 heterointerface provides the possibility of the electron injection upon photoexcitation from the perovskite conduction band (CB) to the nitrogen vacancy (V_N) of g-C_3N_4 promoting the electron trapping responsible of the initial N_2 reduction. At the same time, the electron can be trapped also by the bromide vacancy introducing additional reactive sites. To further verify the electronic structure of the heterointerface, we simulate the interacting g-C_3N_4/Cs_2SnBr_6 system reported in Figure S9, and we found that the interaction between perovskite and the carbon nitride takes place by the formation of N-Sn bond with a formation energy of 91 $eVnm^{-2}$ confirming a very favorable interface formation tendency. In term of the electronic properties the g-C_3N_4/Cs_2SnBr_6 interface at PBE0 (see SI), shows the same qualitative behavior of the energy level alignment reported in Figure 6 at HSE06-SOC level confirming the proposed electron transfer mechanism. The evolution of the NH_3 production with respect to the system composition results similar to that we found for $Cs_2AgBiCl_6$ but, in general, is all up-shifted in terms of absolute NH_3 production.[28] This in such way confirms that the perovskite alone already is active in producing NH_3 due to the favorable defect energy alignment, and then, when g-C_3N_4 is added, the Cs_2SnBr_6 is going to play a double role: (i) as reactive site and (ii) as light adsorber and charge generation. This aspect in conjunction with absence of STE state and the reduction of non-radiative decay lead to a higher ammonia production rate. Once the carbon nitride is coupled with Cs_2SnBr_6 the ammonia generation increase is attributed to the additional charge generation upon photoexcitation that enables a better charge transfer to the nitrogen vacancy of the carbon nitride further promoting catalytic activity. On the other hand, when the quantity of

perovskite is very low or absent, the carbon nitride itself does not generate a relevant amount of ammonia. As a matter of fact, the NH_3 production mechanism promoted by Cs_2SnBr_6/g-C_3N_4 heterojunction results similar to that of $Cs_2AgBiCl_6$/g-C_3N_4 but the strategy employed here to boost the ammonia production in this novel MHP-based heterojunction was confirmed and, from a microscopic point of view, is due, mainly, to a combination of different factors such as the absence of STE state in the perovskite that reduce charge losses, and to the active role of perovskite itself in offering efficient reactive site centered at the interfacial bromide vacancy.[28]

3. CONCLUSIONS

We reported here a novel heterojunction for efficient nitrogen photofixation based on the coupling of the vacancy ordered double perovskite Cs_2SnBr_6 and carbon nitride (g-C_3N_4). The system was investigated in the whole compositional range starting from the two end members, and a clear synergistic effect between the two semiconductors was observed, reaching a maximum ammonia production rate of 266 μmol g^{-1} h^{-1} for the Cs_2SnBr_6 35 wt%/g-C_3N_4 65 wt% composition, an outstanding value obtained with no use of additional co-catalyst as noble metals. A thorough experimental and computational modelling work allowed to highlight the microscopic mechanism underpinning nitrogen reduction reaction. Graphitic carbon nitride nanosheets, through the presence of nitrogen vacancies, represent the main reaction site for nitrogen reduction with an effective charge transfer from Cs_2SnBr_6 to such active sites thanks to the formation of a type 2 heterojunction. In addition, Cs_2SnBr_6 is a very efficient semiconductor thanks to the lack of self-trapped electrons, as demonstrated by PL spectra and computational modelling work, favoring the charge carrier separation. In addition, the presence of bromide vacancies on Cs_2SnBr_6 introduces additional reactive sites and explains the efficiency in the nitrogen photofixation reaction of the perovskite alone.

The present results demonstrate the possibility of effectively employing MHP-based heterojunctions for nitrogen photofixation in addition to other well-established photoreactions such as hydrogen generation and carbon dioxide reduction. Moreover, through a wise materials engineering approach and thanks to the tunability of MHPs it is possible to design optimized systems taking advantage of their superior optoelectronic properties. The present results are extremely encouraging for the future exploitation of perovskite-based heterojunction for ammonia photogeneration which will become a key process for the future global challenges for carbon neutrality.

Acknowledgements

A.S. acknowledges the funding PON Ricerca e Innovazione 2014-2020 REACT-EU, DM 1062 2021, project N. 04-G-14266-1. A.S., R.P., M.S acknowledge Centro Servizi Ateneo per la Ricerca (CeSAR) of University of Cagliari. R.P acknowledges PRIN 2022 CUP F53D23005090006 and PRIN 2022 F53D23001050006, funded by Italian Ministry for University and Research (MUR). M.S. acknowledges Project "Network 4 Energy Sustainable Transition—NEST", Spoke 1, Project code PE0000021, funded under the National Recovery and Resilience Plan (NRRP), Mission 4, Component 2, Investment 1.3 - MUR funded by the European Union—NextGenerationEU. M.S. acknowledges PRIN 2022 2022YM3232 – NanoPix and PRIN 2022 PNRR P2022ZYTJY - Master, funded by MUR. E.M., A.L. and L.M. acknowledge financial support under the National Recovery and Resilience Plan (NRRP), Mission 4, Component 2, Investment 1.1, Call for tender No. 104 published on 2.2.2022 by the Italian Ministry of University and Research (MUR), funded by the European Union - NextGenerationEU - Project Title 2022HRZH7P - Re-evolutionary solar fuel production envisioning water stable lead-free perovskite exploitation - REVOLUTION - CUP B53D23015350006 - Grant Assignment Decree No. 1064 adopted on 18.7.2022 by the Italian Ministry of University and Research (MUR). E.M and A.A.A wish to thank the Distinguished Scientist Fellowship Program (DSFP) of King Saud University, Riyadh, Kingdom of Saudi Arabia.

The first-author Costanza Tedesco, author of the present Ph.D. work, carried out all the experimental parts: the synthesis and the characterization of all photocatalytic materials and the revision of the experimental part of the paper.

References

[1] R. Huang, X. Li, W. Gao, X. Zhang, S. Liang, M. Luo, *RSC Adv.* 2021, *11*, 14844.

[2] M.-H. Vu, M. Sakar, T.-O. Do, *Catalysts* 2018, *8*, 621.

[3] X. Chen, N. Li, Z. Kong, W.-J. Ong, X. Zhao, *Mater. Horiz.* 2018, *5*, 9.

[4] A. Kumar, V. Krishnan, *Advanced Sustainable Systems* 2024, 2400173.

[5] D. R. MacFarlane, P. V. Cherepanov, J. Choi, B. H. R. Suryanto, R. Y. Hodgetts, J. M. Bakker, F. M. Ferrero Vallana, A. N. Simonov, *Joule* 2020, *4*, 1186.

[6] M. Cheng, C. Xiao, Y. Xie, *J. Mater. Chem. A* 2019, *7*, 19616.

[7] D. Zhang, Y. L. Pak, X. Li, S. Lv, M. Xing, Z. Yang, H. Wu, X. Gao, H. Mou, J. Song, *Journal of Alloys and Compounds* 2024, *972*, 172881.

[8] M. Barawi, M. García-Tecedor, M. Gomez-Mendoza, G. Gorni, M. Liras, V. A. De La Peña O'Shea, L. Collado, *ACS Appl. Mater. Interfaces* 2023, *15*, 53382.

[9] X. Wang, B. Wang, S. Yin, M. Xu, L. Yang, H. Sun, *Journal of Cleaner Production* 2022, *360*, 132162.

[10] G. Zhang, C. D. Sewell, P. Zhang, H. Mi, Z. Lin, *Nano Energy* 2020, *71*, 104645.

[11] M. Xia, B. Chong, X. Gong, H. Xiao, H. Li, H. Ou, B. Zhang, G. Yang, *ACS Catal.* 2023, *13*, 12350.

[12] Y. Li, R. Li, Z. Sun, L. Guo, Y. Wang, X. Ma, H. Li, T. Lei, C. Fan, J. Liu, *Journal of Colloid and Interface Science* 2024, *664*, 198.

[13] K. Pournemati, A. Habibi-Yangjeh, A. Khataee, *Journal of Colloid and Interface Science* 2023, *641*, 1000.

[14] A. R. S. C. Lazuli, V. Ramalingam, B. Neppolian, *Journal of Cleaner Production* 2024, *451*, 142095.

[15] H. Li, J. Shang, J. Shi, K. Zhao, L. Zhang, *Nanoscale* 2016, *8*, 1986.

[16] H. Li, J. Shang, Z. Ai, L. Zhang, *J. Am. Chem. Soc.* 2015, *137*, 6393.

[17] A. Alaghmandfard, K. Ghandi, *Nanomaterials* 2022, *12*, 294.

[18] H. Miao, G. Zhang, X. Hu, J. Mu, T. Han, J. Fan, C. Zhu, L. Song, J. Bai, X. Hou, *Journal of Alloys and Compounds* 2017, *690*, 669.

[19] J. Lee, S. H. W. Kok, B.-J. Ng, X. Y. Kong, L. K. Putri, S.-P. Chai, L.-L. Tan, *Journal of Environmental Chemical Engineering* 2023, *11*, 109511.

[20] E. Vesali-Kermani, A. Habibi-Yangjeh, P. Yekan Motlagh, A. Khataee, *Journal of the Taiwan Institute of Chemical Engineers* 2023, *152*, 105191.

[21] L. Lin, H. Ou, Y. Zhang, X. Wang, *ACS Catal.* 2016, *6*, 3921.

[22] R. Gupta, U. Alam, N. Verma, *Chemical Engineering Journal* 2024, *479*, 147644.
[23] G. Dong, W. Ho, C. Wang, *J. Mater. Chem. A* 2015, *3*, 23435.
[24] L. Romani, L. Malavasi, *ACS Omega* 2020, *5*, 25511.
[25] B.-M. Bresolin, Y. Park, D. W. Bahnemann, *Catalysts* 2020, *10*, 709.
[26] H. Huang, B. Pradhan, J. Hofkens, M. B. J. Roeffaers, J. A. Steele, *ACS Energy Lett.* 2020, *5*, 1107.
[27] J. Yuan, H. Liu, S. Wang, X. Li, *Nanoscale* 2021.
[28] C. Tedesco, L. Gregori, A. Simbula, F. Pitzalis, A. Speltini, F. Merlo, S. Colella, A. Listorti, E. Mosconi, A. A. Alothman, W. Kaiser, M. Saba, A. Profumo, F. De Angelis, L. Malavasi, *Adv Energy and Sustain Res* 2024, 2400040.
[29] A. E. Maughan, A. M. Ganose, D. O. Scanlon, J. R. Neilson, *Chem. Mater.* 2019, *31*, 1184.
[30] A. E. Maughan, A. M. Ganose, M. M. Bordelon, E. M. Miller, D. O. Scanlon, J. R. Neilson, *J. Am. Chem. Soc.* 2016, *138*, 8453.
[31] J. Wang, M. Zhang, Z. Chen, L. Li, G. Jiang, Z. Li, *ACS Energy Lett.* 2024, *9*, 653.
[32] P. Zhou, H. Chen, Y. Chao, Q. Zhang, W. Zhang, F. Lv, L. Gu, Q. Zhao, N. Wang, J. Wang, S. Guo, *Nat Commun* 2021, *12*, 4412.
[33] H. Ma, C. Huang, T. Tan, W. Li, W. Xu, Y. Shen, Y. Li, R. Fang, F. Dong, *Journal of Colloid and Interface Science* 2024, *671*, 486.
[34] S. Bonomi, M. Patrini, G. Bongiovanni, L. Malavasi, *RSC Adv.* 2020, *10*, 28478.
[35] A. Sharma, M. Varshney, K. H. Chae, S. O. Won, *Current Applied Physics* 2018, *18*, 1458.
[36] Z. He, Q. Tang, X. Liu, X. Yan, K. Li, D. Yue, *Energy Fuels* 2021, *35*, 15005.

SUPPORTING INFORMATION

Compositional and Defect Engineering of Metal Halide Perovskite-based Heterojunctions for Efficient Nitrogen Photofixation

Costanza Tedesco,[a] Angelica Simbula,[b] Riccardo Pau,[b] Francesca Merlo,[a] Andrea Speltini,[a] Vincenza Armenise,[c] Andrea Listorti,[d] Luca Gregori,[e] Asma A. Alothman,[f] Edoardo Mosconi,[f,g] Michele Saba,[b] Antonella Profumo,[a] Lorenzo Malavasi[a,*]*

[a]Department of Chemistry and INSTM, University of Pavia, Via Taramelli 12, Pavia, 27100, Italy

[b]Department of Physics, University of Cagliari, 09042 Monserrato, Italy

[c]CNR NANOTEC - c/o Dipartimento di Chimica, Università di Bari, Via Orabona 4, 70126 Bari, Italy

[d]Department of Chemistry, University of Bari “Aldo Moro”, via Orabona 4, 70126, Bari, Italy

[e]Department of Chemistry, Biology and Biotechnology, University of Perugia and INSTM, Via Elce di Sotto 8, 06123 Perugia, Italy

[f]Chemistry Department, College of Science, King Saud University, Riyadh 11451, Kingdom of Saudi Arabia

[g]Computational Laboratory for Hybrid/Organic Photovoltaics (CLHYO), Istituto CNR di Scienze e Tecnologie Chimiche “Giulio Natta” (CNR-SCITEC), Via Elce di Sotto 8, 06123 Perugia, Italy

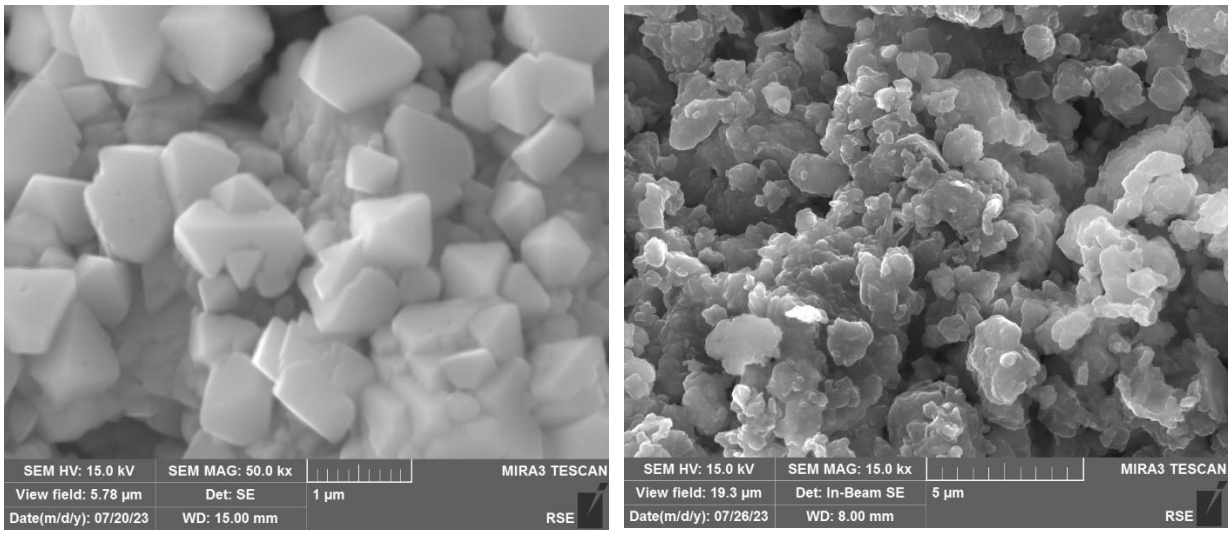

Figure S1. Representative SEM images of a) Cs_2SnBr_6 and b) Cs_2SnBr_6 35%/g-C_3N_4 65% best performing composite.

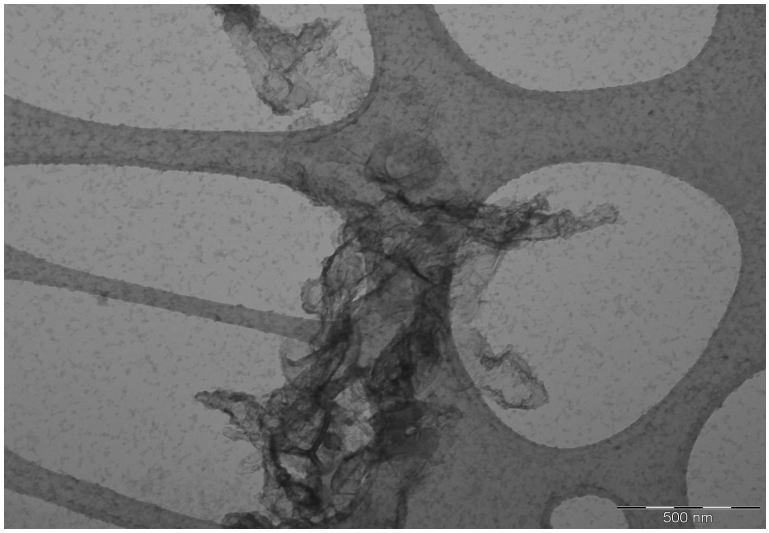

Figure S2. TEM image of g-C_3N_4 nanosheets.

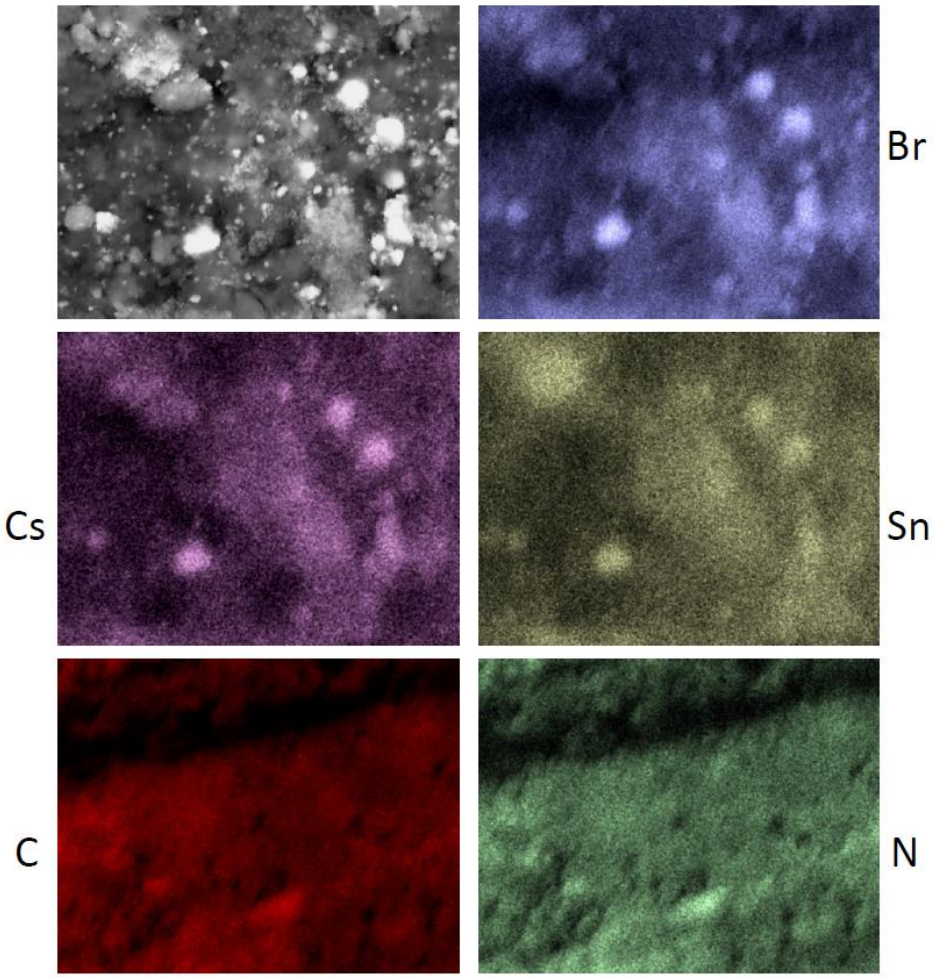

Figure S3. EDS elemental mapping for Cs_2SnBr_6 35%/g-C_3N_4 65% composite.

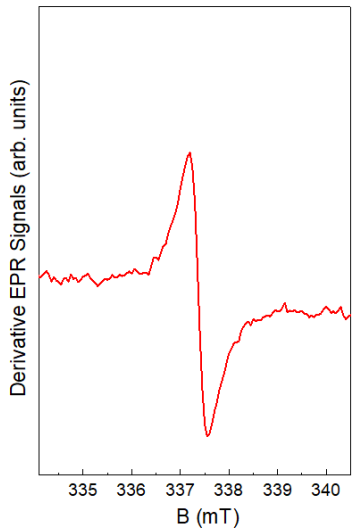

Figure S4. EPR spectrum of the g-C_3N_4 nanosheets.

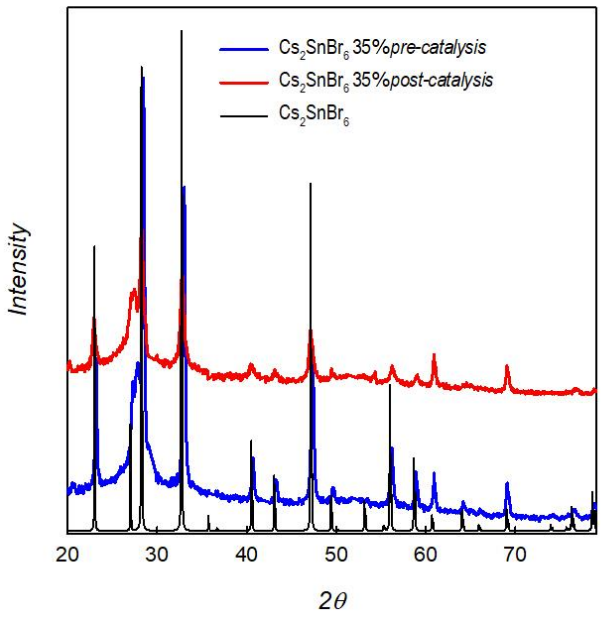

Figure S5. XRD pattern of Cs_2SnBr_6 35 wt%/g-C_3N_4 65 wt% before and after the photocatalytic run.

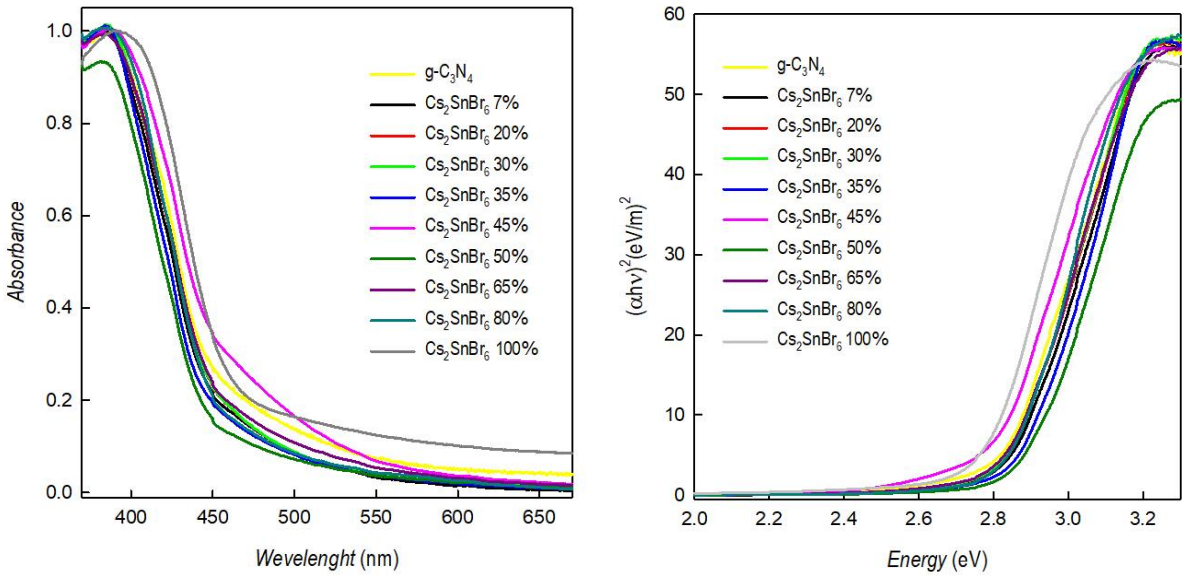

Figure S6. a) Absorption spectra and b) Tauc plots for selected samples of the Cs_2SnBr_6/g-C_3N_4 system.

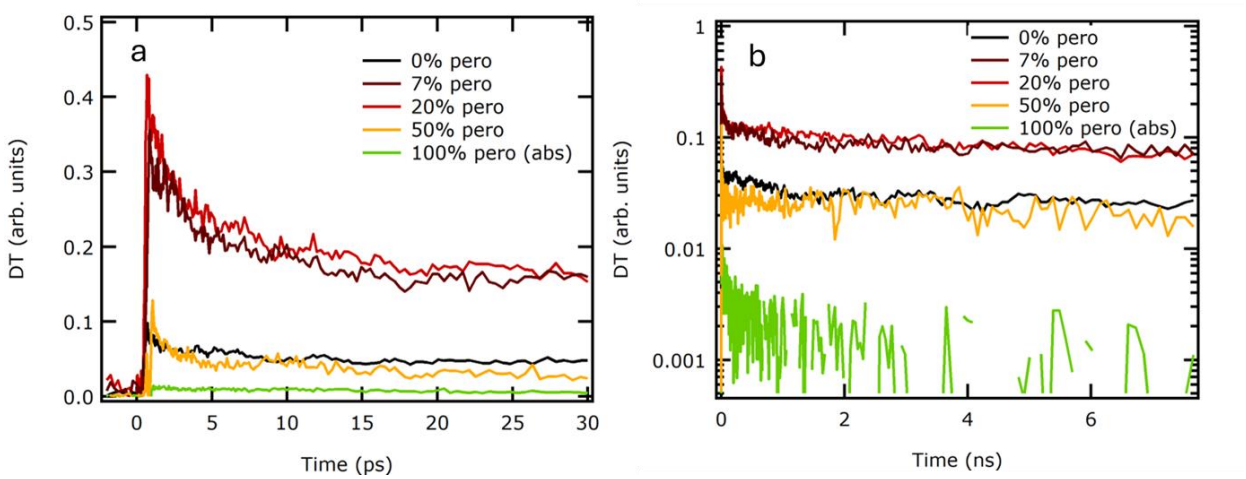

Figure S7: Time decays of integrated DT signals for a subset of measured compounds, showing a fast transient in the first 10-20 ps (a) followed by a long-living signal (b) compatible with defect states

Experimental

Sample synthesis and characterization

Nanosheets g-C_3N_4 has been synthesized from the bulk form (bulk g-C_3N_4) with a polymerization of Dicyandiamine DCD ($NH_2C(=NH)NHCN$, Aldrich, 99%) by the following thermal treatment under N_2 flux: heating (1 °C min^{-1}) to a selected temperature of 550 °C, the isothermal step for 4 hours followed by cooling to room temperature (10 °C min^{-1}). The synthesis was carried out in a partially closed alumina crucible. The thermal exfoliated catalyst (nanosheets) was prepared by heating to a selected temperature of 500 °C with an isothermal step for 2h the bulk g-C_3N_4 in air. The Cs_2SnBr_6/nanosheets g-C_3N_4 composite has been synthesized dissolving a stoichiometric ratio of the precursors salt CsBr (Aldrich 99%) and $SnBr_4$ (Aldrich 99%) in organic solvent *N,N*-dimethylformamide (DMF) and dried under vigorous stilling at 65 °C. This polar solvent can dissolve most organic and inorganic salts and may be suitable for the cations that are insoluble in HBr. The composites series have been realized changing the percentage of the perovskite (Cs_2SnBr_6) and the nanosheets g-C_3N_4 (g-C_3N_4 ns) in the composites: 100, 80, 65, 50, 45, 35, 30, 20, 7. The crystal structure of the samples has been characterized by room temperature Cu-radiation XRD acquired with Bruker D2 diffractometer. DRS spectra were acquired in the wavelength range 300-800 nm directly on the powders by using a Jasco V-750 spectrophotometer, equipped with an integrating sphere (Jasco ISV-922). Microstructural characterization of the samples was made using a high-resolution scanning electron microscope (SEM, TESCAN Mira 3) operated at 25 kV.

Nitrogen Photofixation Experiments and Ammonia Determination

N_2 photofixation experiments were conducted in tridistilled water containing 10% (v/v) methanol (Aldrich, ≥99.9%) irradiated in Pyrex glass container (250 mL capacity, 100 mL sample). The methanol plays the role of sacrificial agent. The electrons produced in photocatalyst migrate from the bulk to the surface of the material to reduce H_2O to H_2, to minimize the recombination of electron-holes a sacrificial agent is employed to be oxidated faster water to avoid the rapid recombination electron-hole and to maximize the electron extraction. After addition of the catalyst (0.5 g L^{-1}), the sample suspension was deoxygenated by N_2 bubbling (45 min) to obtain a saturated solution and then irradiated under magnetic stirring for 3 hours maintaining the temperature at 15°C. The quantification

was performed with ammonia ion selective electrode (ISE), which guarantees accurate detection over colorimetric methods (e.g. Nessler method) as previously assessed.[9] The pH of all standards was adjusted above 11 with a strong base (10N NaOH, ion strength < 1M), so that dissolved ammonia (NH_3 (aq) and NH_4^+) is converted to NH_3 (aq). A calibration curve was daily constructed (0.25-25 mg L^{-1} NH_3) plotting the mV value recorded after 2 min equilibration time against the Log Concentration, to verify the slope (varying in the range –54 ÷ -60 mV). Figure S8 reports an example of mean calibration curve (0.25 mg L^{-1} ÷ 25 mg L^{-1} as NH_3). The ammonia concentration in the sample was further confirmed by two standard additions on the sample.

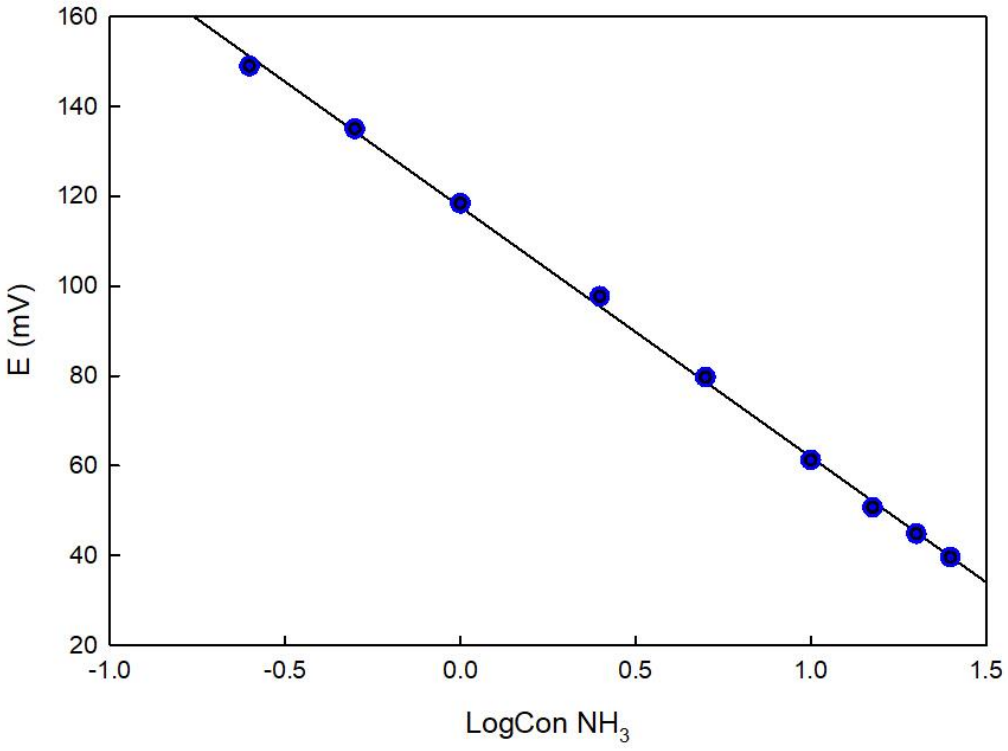

Figure S8: Mean calibration curve (n=7) for ammonia quantification (0.25 mg L-1 ÷ 25 mg L^{-1} as NH3).

Time resolved measurements

Differential transition (DT) measurements were performed directly on solutions of different composites, with the same concentration used for N_2 photofixation, i.e. 0.5g/L, keeping the solution inside a 1 mm thick quartz cuvette after sonication at 25°C for 10 minutes. The monochromatic pump at 350 nm was obtained from Titanium Sapphire femtosecond laser (Libra - Coherent), with emission at 780 nm with 1kHz repetition rate, feeding a tunable optical parametric amplifier (TOPAS- Light Conversion). The measurements were performed in a pump and probe configuration (Helios - Ultrafast Systems) where the probe was obtained by focusing the 780 nm onto a Sapphire nonlinear crystal to get supercontinuum sub-ps broadband pulses in the visible range. Probe delay was controlled with a mechanical delay line allowing for sub-ps resolution and maximum delay of 8 ns. Spectra acquisition was performed in differential mode, where transmitted and reference spectra were collected by two distinct spectrometers coupled to CMOS detectors, both in pump and no-pump condition, by means of synchronization with a chopper at 500Hz.

Time resolved photoluminescence (TRPL) measurements were performed by exciting the sample with the same pump used for DT measurements. The PL was then collected by a lens and analysed with an optical spectrometer (Acton 2300i) for spectral resolution, followed by a streak camera (Hamamatsu C10910) with 50ps time resolution for time dispersion.

Computational Details

DFT calculations have been carried out for the Cs_2SnBr_6, the interface and the defect in the supercell approach. For all the systems reported in the main text and in the SI, the ionic positions were optimized using the CP2K software package using the PBE0 exchange-correlation functional and by including DFT-D3 dispersion corrections.[1–3] For g-C_3N_4, we employ an orthorhombic $2 \times 2 \times 2$ supercell with $a = 7.08$ Å, $b = 12.27$ Å, $c = 6.97$ Å; for Cs_2SnBr_6, we use the cubic phase with $a = b = c = 10.83$ Å obtained from our XRD measurement.[4] In all cases, geometry optimization was carried out at the Γ-point of the Brillouin zone. We used the Goedecker–Teter–Hutter (GTH) norm-conserving pseudopotentials and MOLOPT double-zeta Gaussian basis sets.[5][The auxiliary density matrix method has been used to accelerate calculations with the hybrid PBE0 functional.[6] To refine the defect formation energies and thermodynamic ionization levels in order to

match the absolute level alignment against the vacuum level, single-point DFT calculations were carried out using the hybrid HSE06 functional with inclusion of spin-orbit coupling (SOC) corrections on the optimized geometries within the Quantum Espresso software package. All calculations were carried out at the Γ point of the Brillouin zone, using norm-conserving full relativistic pseudopotentials with electrons from Br 5s, 5p; Cs 5s, 5p, 6s; Sn 5s, 5p, shells explicitly included. Plane-wave basis set cutoffs for the smooth part of the wave functions and the Fock grid of 60 and 60 Ry, respectively, were chosen. Dispersion corrections were accounted for using the D3 scheme.

Defect formation energies (DFEs) and thermodynamic ionization levels (TILs) were calculated within the supercell approach following the expressions:

$$DFE[X^q] = E[X^q] - E[pristine] - \sum_i n_i\mu_i + q(\varepsilon_{VB} + \varepsilon_F) + E^q_{corr} \quad \text{Eq (1)}$$

$$\varepsilon(q/q') = \frac{DFE(E_F = 0) - DFE(E_F = 0)}{q' - q} + \frac{E^q_{corr} - E^{q'}_{corr}}{q' - q} \quad \text{Eq (2)}$$

where $E[X^q]$ is the energy of the supercell with defect X in the charge state q, E(pristine) is the energy of the pristine (non-defective) supercell. n_i and μ_i are the number and the chemical potentials of the species added or subtracted, respectively and ε_{VB} is the valence band energy of the pristine system. The middle two terms of Eq (1) represent the energy to the exchange electrons with the Fermi level of the system (ε_F). E^q_{corr} is the correction term due to the charge. Charge corrections have been applied by following the Makov-Payne scheme by using the ionic dielectric constant (7.3) of the Cs_2SnBr_6 calculated at the PBE level by following the approach of Umari et al.[7,8]

In line with our previous work, we have modelled g-C_3N_4 in order to reproduce its electronic properties, such as band gap and ionization potential, accurately relative to experimental values.[9] The defects, particularly the nitrogen vacancies, were calculated exactly as in our previous work, as these are considered to be active species in the production of ammonia. To achieve this, we optimized the geometries using PBE0 calculations. We then carried out single point calculations using the HSE06 functional with SOC correction, using an exchange fraction of 0.31. We decided to fully explore the electronic properties of the Cs_2SnBr_6 perovskite, as shown in Table S1, we screened the fraction of exchange to find

the best agreement with the experimental band gap. Table S1 demonstrates that, in contrast to g-C_3N_4, a fraction of 0.31 is insufficient to accurately reproduce the band gap. Therefore, it was necessary to increase the exchange fraction to 0.43 to achieve the desired agreement as already found for the classical $MASnI_3$.[10,11]

Table S1: Band gap of the bulk of Cs_2SnBr_6 for different functionals and fractions of exchange inside the HSE06 hybrid functional.

Method	**Band Gap (eV)**
PBE	1.14
PBE-SOC	1.06
PBE0	2.76
HSE06 (α=0.43) + SOC	2.67
HSE06 (α=0.31) + SOC	2.12
Experimental	2.75*

* This paper

Model setup

We start by optimizing a slab model of the vacancy ordered double perovskite Cs_2SnBr_6 using a 2×2 in-plane supercell, with (001) direction, and adding 15 Å of vacuum to maintain separation from periodic images. Two different surface terminations were investigated for Cs_2SnBr_6: $SnBr_2$ and CsBr, see Figure S8:

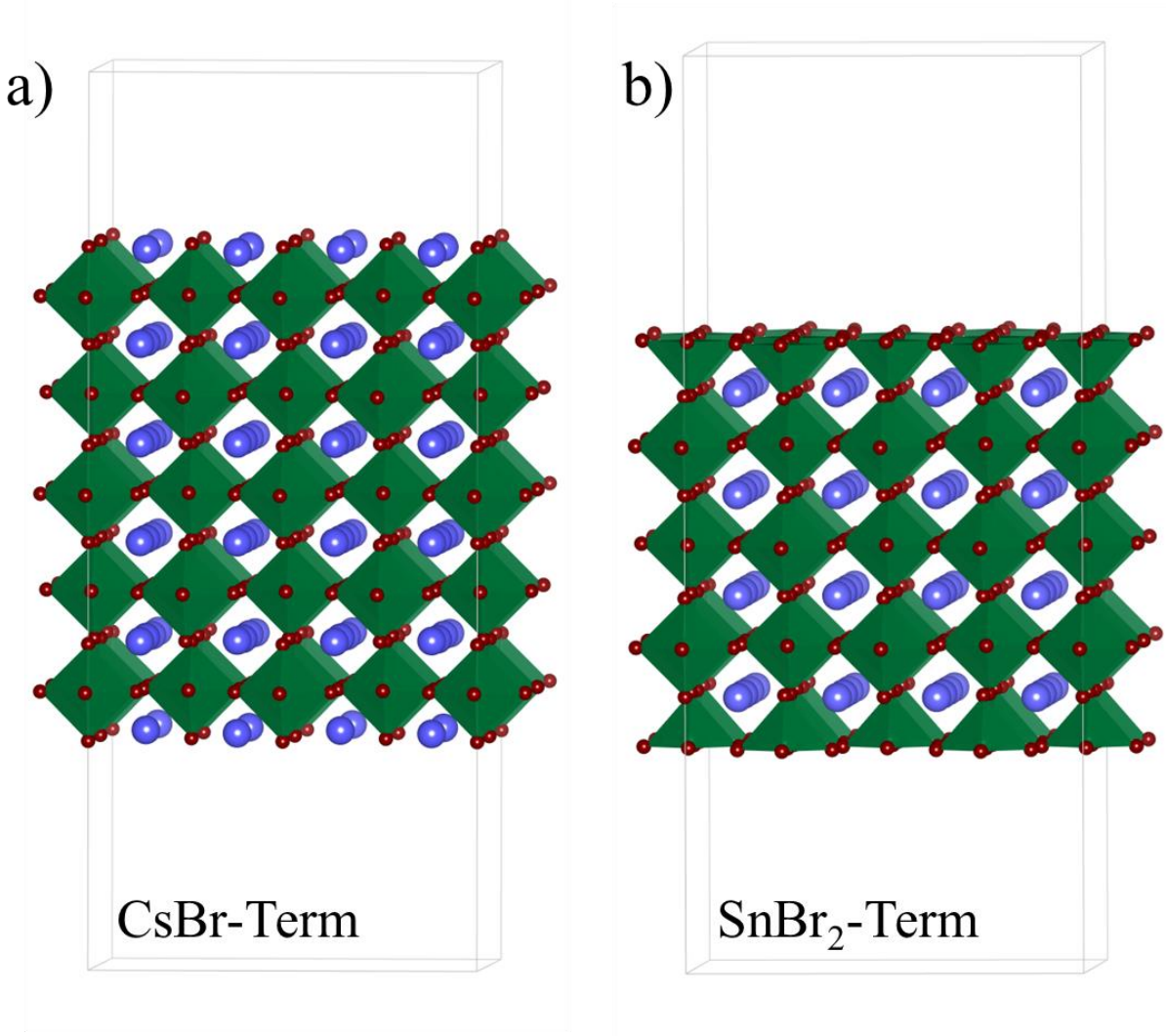

Figure S9. a) Optimized structure of (001) Cs_2SnBr_6 surfaces with CsBr and b) with $SnBr_2$-termination. Following colors are used: Sn green; Cs, cobalt; Br, red.

We study the fundamental properties of the two different terminations for the 001 surface of the Cs_2SnBr_6 perovskite.

Table S2: Band gap for the (001) surface of Cs_2SnBr_6 for both terminations at different functionals and fractions of exchange inside the HSE06 hybrid functional.

	Band Gap (eV)	
	$SnBr_2$-Terminated	CsBr-Terminated
PBE	0.89	1.16
PBE-SOC	0.78	0.96
PBE0	2.43	2.68
HSE06 (α=0.43) + SOC	2.86	2.94

Band alignment procedure

First, we carried out a calculation of the bulk Cs_2SnBr_6 to determine the alignment between the average electrostatic potential of the bulk and the edges of the bands. We carried out a simulation of the different slabs in vacuum and calculated the difference between the average electrostatic potential inside the slab, to be referred to the real bulk simulation and in vacuum. By combining the results of these two, we were able to align the band edges in particular Table S3 shows the VB before and after the alignment procedure with respect to the vacuum via the average electrostatic potential to calculate the real Ionization energy (IE). Finally, we use the same approach to calculate the correction due to the HSE06-SOC hybrid also reported in table S3. Along the main in Figure 6 we reported the SnBr-terminated slab energy alignment for which we obtain an IE of 6.35 eV in good agreement with the experimental measurements by Wang et al.[12]

Table S3: Calculated valence band maximum, Band Gap and Vacuum level at PBE with dispersion correction (Grimme-D3) level of theory to visualize the importance of alignment procedure.

Surface	**VBM (eV)**	**GAP (eV)**	**Vacuum (eV)**	**IE (ev)**	**VB (align) (eV)**	**IE (align) (eV)**	**IE (HSE06SOC) (eV)**
SnBr	-0.61	0.89	6.13	6.75	-0.47	6.61	**6.35**
CsBr	-0.78	1.16	4.39	5.17	-0.35	4.74	**4.49**

Bromide Vacancies in Cs_2SnBr_6

We thus focus on a bromide vacancy on the $SnBr_2$-terminated surface in our study of Cs_2SnBr_6. This vacancy remains stable in the positively charged (+1) state and already induces changes in the lattice structure of Cs_2SnBr_6. The thermodynamic ionization levels (TILs) for the (+/0) and (+/-) transitions are 1.98 eV and 2.38 eV above the valence band maximum, respectively, indicating a deep trap state associated with the defect (see Table S1). As pointed out in the main text of our research, this defect serves as a crucial active site for NH_3 production.

Table S4: Defect formation energy at E_F = 0 eV for the bromide vacancy, V_{Br}, at the $SnBr_2$ terminated surface at the PBE0 level of theory.

	$SnBr_2$-terminated Cs_2SnBr_6 [Band gap = 2.42 eV]		
	DFE (eV)	**TILs (eV)**	
V_{Br}^{+}	-0.53	**(+/0)**	1.98
V_{Br}^{0}	1.45	**(+/-)**	2.38
V_{Br}^{-}	4.20	**(0/-)**	2.76

Self-trapped excitons

We then move to investigate the formation of self-trapped excitons (STEs) upon illumination. Optimizing the system in the triplet state using the PBE0 functional does not result in any exciton localization, as indicated in Table S5. This absence is attributed to the specific crystal structure of the system.

Table S5: Self-trapped exciton formation: DFT results of the absorption and emission properties, as well as singlet and triplet state relaxation energies following emission and absorption, respectively.

Property	Energy (eV)
Absorption	2.01
Emission	0.28
Singlet relaxation	1.73
Triplet relaxation	1.74

Interface Model

Furthermore, to elucidate the structural and electronic changes upon interface formation, we model the interface between g-C_3N_4 and Cs_2SnBr_6. The lattice constants of g-C_3N_4 and Cs_2SnBr_6 are well aligned along the a-direction, while the b-direction shows a significant lattice mismatch of 6%. To address this, we cleave the g-C_3N_4 layer along the b direction and passivate the under coordinated nitrogen atoms with hydrogen atoms (see Figure S9). This approach ensures maximum coverage without introducing artificial strain into the g-C_3N_4. In terms of electronic properties, the modified g-C_3N_4 exhibits a band gap of 3.22 eV, which is very close to the 3.4 eV band gap of the fully periodic g-C_3N_4 monolayer. Both surfaces of the perovskite plate were passivated with the modified g-C_3N_4 layers.

An initial PBE relaxation between Cs_2SnBr_6 and g-C_3N_4, followed by a PBE0 single point calculation starting from the low energy configuration, resulted in a strongly bound heterostructure with a binding energy of -3.91 eV/nm². Detailed structural analysis confirms that each under coordinated surface metal ion is successfully passivated. The density of states (DOS) analysis in Figure S9c shows a type II band alignment similar to those reported in a previous paper, with the valence band (VB) and conduction band (CB) of g-C_3N_4 positioned above those of the perovskite layer in line with the absolute level alignment of the separated species reported in the main text.[13] We chose to report in Figure 6 the energy alignment of the separated species because in this case we have and unbalanced reproduction of the electronic band gap of the g-C_3N_4 and Cs_2SnBr_6 perovskite. In particular, as reported above, we need to use a higher fraction of exchange (0.43) for the perovskite with respect to the carbon nitride (0.31). For that reason, when we simulate the interface,

we inherently describe in an accurate way only one component depending on the exchange fraction used. However, as mentioned before, with PBE0 (that gives similar results of HSE-SOC with 0.43 of exchange, see Table S1 and S2) we found good qualitative energy level alignment with the expected overestimation of the band gap for g-C_3N_4 that move up to 3.2 eV due to the high exchange fraction adopted for Cs_2SnBr_6.

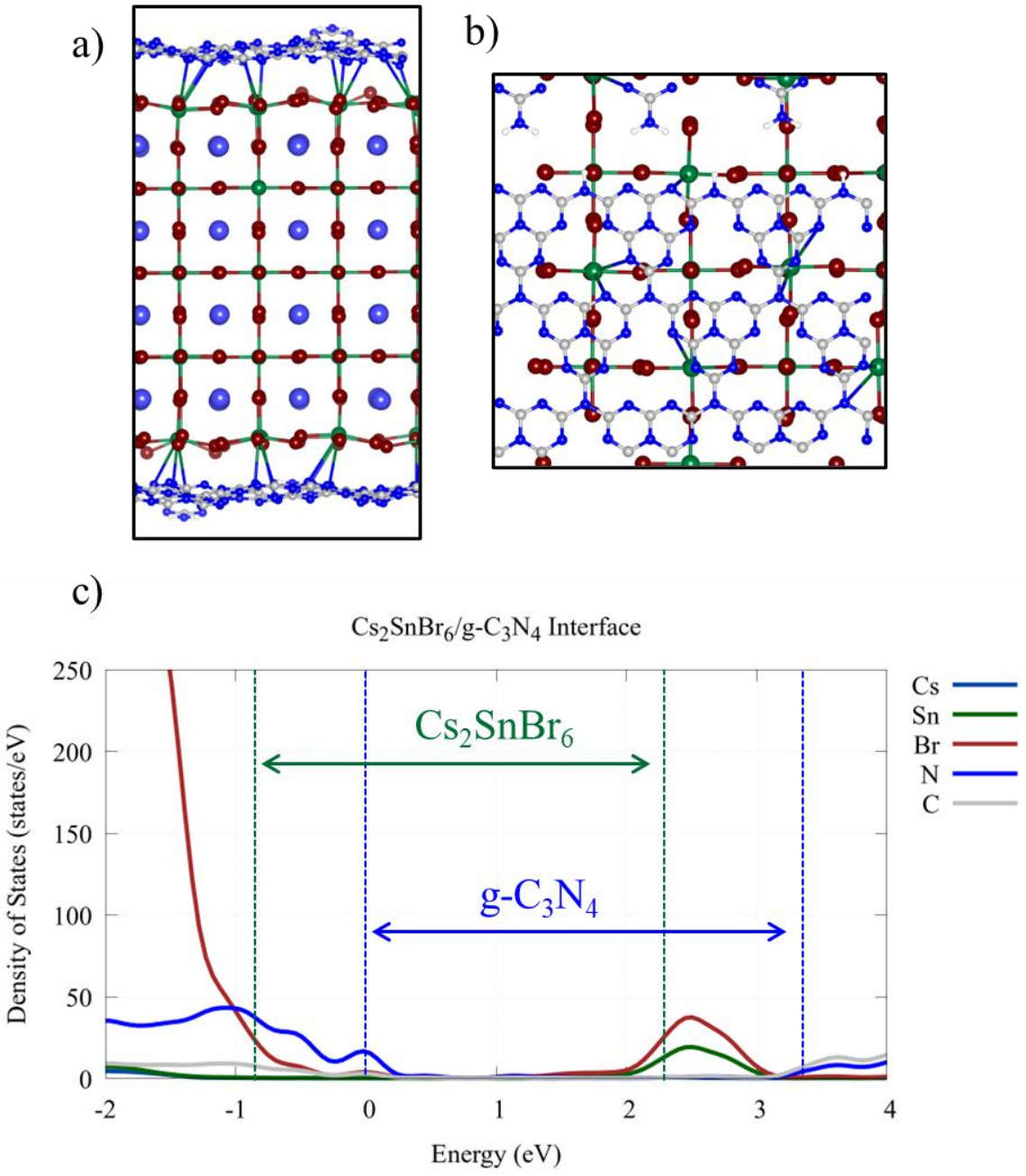

Figure S10. a) Side view of the optimized Cs_2SnBr_6-$SnBr_2$/g-C_3N_4 interface. b) Top view showing the periodicity for the model system with the modified g-C_3N_4 on top of the $SnBr_2$-terminated surface. Cs atoms are removed for better visualization c) Projected density of states of the optimized interface at the PBE0 level of theory.

References

[1] T. D. Kühne, M. Iannuzzi, M. Del Ben, V. V. Rybkin, P. Seewald, F. Stein, T. Laino, R. Z. Khaliullin, O. Schütt, F. Schiffmann, D. Golze, J. Wilhelm, S. Chulkov, M. H. Bani-Hashemian, V. Weber, U. Borštnik, M. Taillefumier, A. S. Jakobovits, A. Lazzaro, H. Pabst, T. Müller, R. Schade, M. Guidon, S. Andermatt, N. Holmberg, G. K. Schenter, A. Hehn, A. Bussy, F. Belleflamme, G. Tabacchi, A. Glöß, M. Lass, I. Bethune, C. J. Mundy, C. Plessl, M. Watkins, J. VandeVondele, M. Krack, J. Hutter, *J. Chem. Phys.* 2020, *152*, 194103.

[2] C. Adamo, M. Cossi, V. Barone, *Journal of Molecular Structure: THEOCHEM* 1999, *493*, 145.

[3] S. Grimme, J. Antony, S. Ehrlich, H. Krieg, *The Journal of Chemical Physics* 2010, *132*, 154104.

[4] L. Romani, A. Speltini, F. Ambrosio, E. Mosconi, A. Profumo, M. Marelli, S. Margadonna, A. Milella, F. Fracassi, A. Listorti, F. De Angelis, L. Malavasi, *Angewandte Chemie International Edition* 2021, *60*, 3611.

[5] S. Goedecker, M. Teter, J. Hutter, *Phys. Rev. B* 1996, *54*, 1703.

[6] M. Guidon, J. Hutter, J. VandeVondele, *J. Chem. Theory Comput.* 2010, *6*, 2348.

[7] C. Freysoldt, J. Neugebauer, C. G. Van De Walle, *Phys. Rev. Lett.* 2009, *102*, 016402.

[8] P. Umari, A. Pasquarello, *Phys. Rev. B* 2003, *68*, 085114.

[9] C. Tedesco, L. Gregori, A. Simbula, F. Pitzalis, A. Speltini, F. Merlo, S. Colella, A. Listorti, E. Mosconi, A. A. Alothman, W. Kaiser, M. Saba, A. Profumo, F. De Angelis, L. Malavasi, *Adv Energy and Sustain Res* 2024, 2400040.

[10] D. Ricciarelli, D. Meggiolaro, F. Ambrosio, F. De Angelis, *ACS Energy Lett.* 2020, *5*, 2787.

[11] D. Meggiolaro, D. Ricciarelli, A. A. Alasmari, F. A. S. Alasmary, F. De Angelis, *J. Phys. Chem. Lett.* 2020, *11*, 3546.

[12] J. Wang, M. Zhang, Z. Chen, L. Li, G. Jiang, Z. Li, *ACS Energy Lett.* 2024, *9*, 653.

[13] H. Ma, C. Huang, T. Tan, W. Li, W. Xu, Y. Shen, Y. Li, R. Fang, F. Dong, *Journal of Colloid and Interface Science* 2024, *671*, 486.

This is an open access article distributed under the terms of the Creative Commons CC BY license, which permits unrestricted use, distribution, and reproduction in any medium, provided the original work is properly cited.

© 2025 The Author(s). Solar RRL published by Wiley-VCH GmbH.

CHAPTER 5

Enhancing Visible-Light-Driven Hydrogen Production: Heterojunction Engineering of Graphitic Carbon Nitride and PBDB-T Organic Semiconductor

Costanza Tedesco [a], *Benjamin Goldman* [b], *Kevin Sivula* [b], *Lorenzo Malavasi* [a]

[a] Department of Chemistry and INSTM, University of Pavia, Via Taramelli 16, Pavia, 27100, Italy

[b] Laboratory for Molecular Engineering of Optoelectronic Nanomaterials, Institute of Chemical Sciences and Engineering, École Polytechnique Fédérale de Lausanne (EPFL), CH-1015 Lausanne, Switzerland.

ABSTRACT

Graphitic carbon nitride (g-C_3N_4), a versatile organic polymeric semiconductor, stands out as a leading visible-light active photocatalyst in metal-free green hydrogen production. Despite its potential, operational limitations such as fast charge carrier recombination, low surface area, and poor absorption coefficient have limited its extensive application particularly in photoelectrochemical (PEC) devices. This study focuses on engineering a heterojunction structure by combining g-C_3N_4 with a well-established organic semiconductor, PBDB-T, to create a bulk heterojunction (BHJ) with a favourable band alignment between the two semiconductors, anticipating an efficient PEC system. The effective formation of an efficient BHJ was also proved through photocatalytic hydrogen evolution in suspension set up. The proposed system is implemented through a scalable, low-cost, and environmentally friendly spin-coating process on fluorine-doped tin oxide (FTO) substrates. The g-C_3N_4:PBDB-T BHJ photocathode exhibits promising performance, surpassing previous g-C_3N_4-based photocathodic materials reaching, in the final configuration with Pt as cocatalyst, a current density of almost 300 μA/cm^2. This research introduces a novel approach to use g-C_3N_4 as a photocathodic material and protecting layer for photoelectrocatalytic hydrogen production. The study contributes to advancing organic semiconductor applications in photoelectrocatalysis, emphasizing the potential of g-C_3N_4 in sustainable energy systems.

1. INTRODUCTION

Graphitic carbon nitride, commonly abbreviated as g-C_3N_4, is an organic polymeric semiconductor, is considered as one of the most promising visible-light active photocatalyst in the field of metal free and green hydrogen production.[1] Hydrogen is historically well known as high potential energy vector, but even nowadays the production of low-cost and green hydrogen represents a bottleneck for the definitive replacement of fossil fuels.[2] For this reason, in the last 20 years, the search for new environmental-friendly and metal-free catalysts has become a high-priority target. g-C_3N_4 showed remarkable performances in numerous applications including CO_2 photo-reduction, N_2 photo-fixation, organic pollutant degradation as well as catalytic C-C bond formation, overall photocatalytic water splitting, and hydrogen gas evolution.[3–7] This superior potential resides in a series of interesting characteristics of g-C_3N_4 such as, among others, ease of preparation from several cheap precursors (dicyandiamide, cyanamide, melamine, urea and, thiourea), and high stability up to 600°C in air and in both acidic and basic aggressive environments.[1] The flexibility showed by this photocatalyst lies mainly in its electronic properties, with g-C_3N_4 presenting a layered-sheets structure, resembling the graphene structure, with a band gap of 2.7 eV where the conduction and valence bands have suitable energy positions to perform the above-mentioned reduction and oxidation reactions. Despite all the interesting and promising characteristics discussed, g-C_3N_4 presents important operative limitations.[1,8,9] It shows a fast recombination rate of the charge carriers, a low surface area, and a poor absorption coefficient.[10] To improve the surface area, various approaches have been proposed, such as surface acidic treatments, laser ablation, ultrasonication, the exploitation of hardeners and air and heat treatments. These methods showed a dramatic increase in terms of both surface defects and area.[1] For the other two limitations, related to optoelectronic properties, the engineering of a heterojunction structure employing g-C_3N_4 together with another (or more than one) semiconductor is one of the most effective approaches.[11] In a heterojunction structure the additional semiconductor helps in the dynamics of the charge carrier slowing the recombination rate and, at the same time, it may increase the absorption coefficient.[12,13] Therefore, the study of suitable cocatalyst materials for g-C_3N_4 that may form an opportune heterojunction is growing significantly.[8,14–16] All these efforts have led to an effective use of g-C_3N_4 as photocatalyst for green hydrogen production from aqueous media splitting.[17]

On the other hand, the research about the application of g-C_3N_4 as active material in photoelectrochemical (PEC) systems for hydrogen evolution is at an early stage. The photoelectrocatalytic performances of g-C_3N_4 as photoanode have received more attention than its use photocathode material. Main reason lies in the n-type semiconductor behaviour of g-C_3N_4 and, as previously mentioned, in an electron band position suitable for overall water splitting.[18–21] This photoanodic behaviour represents a peculiar characteristics considering the well-established role of g-C_3N_4 as photocatalytic material for hydrogen production though proton reduction.[22,23] Few studies focused on the reasons of this odd behaviour and a potential reason may lay in its anisotropic electrical conductivity.[24] Nevertheless, also for PEC materials, great interest is being addressed to the optimization of the main photoelectrocatalyst through the engineering of a heterojunction.[25–27]

On these bases, the aim of this work is an evaluation of the suitability of g-C_3N_4 as photocathodic material for photoelectrocatalytic hydrogen production. We therefore investigated the photocathodic performance of a homogeneous heterojunction between g-C_3N_4 and a well-established photoactive organic semiconductor trying to shed light on the role of g-C_3N_4 in the heterojunction both, as photoactive layer and as potential protective layer. The choice of employing an organic semiconductor (OS) in the construction of the heterojunction results from their wide use as an alternative to the classic inorganic photoactive materials for photovoltaic devices.[28–30] Indeed, in recent years, OSs have received increasing attention in the field of photoelectrocatalysis, thanks to the favourable interaction of OSs with liquid electrolytes compared to inorganic semiconductor.[31,32] Likewise, as widely demonstrated for photocatalytic H_2 evolution reaction, the most suitable architecture for photoelectrodes in PEC applications is the exploitation of electron donor/acceptor organic materials in a bulk (BHJ) or layered heterojunction (LHJ).[31–33] Based on the recent knowledge concerning the most promising polymeric OSs we selected, as photocathodic system, the g-C_3N_4:PBDB-T bulk heterojunction.[31] PBDB-T is a commercial polymeric organic semiconductor already known for its promising performances showed in organic photovoltaic applications.[34]

We report here a device based on a layered architecture including the g-C_3N_4:PBDB-T BHJ as potential photocathode material demonstrating interesting and promising performance compared to previously reported g-C_3N_4-based photocathodes. The photocathodes are realized by spin and spray coating in air, exploiting fluorine-doped tin oxide (FTO) as substrate.[31]

2. RESULTS AND DISCUSSION

The HOMO-LUMO position of PBDB-T results to be appropriate, among the known best performing OSs, to build a type II heterojunction with g-C_3N_4, whose band position have been deeply studied.[34]

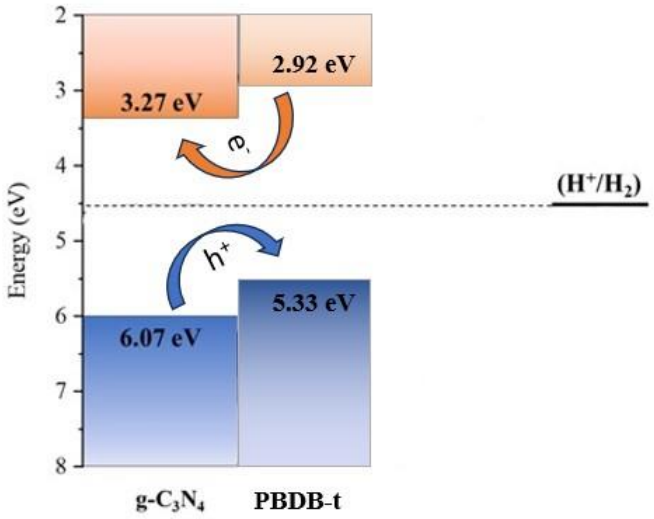

Figure 1. Hypothesized band alignment for the heterojunction system g-C_3N_4:PBDB-T. The band position for g-C_3N_4 have been established in previous work and the HOMO-LUMO position for PBDB-t have been reported from Ossila.

Based on that, g-C_3N_4 plays the electron acceptor role in the heterojunction, the hydrogen evolution reaction occurs on g-C_3N_4 active sites boosted by the photoactivity of PBDB-T. Synthesis of highly exfoliated g-C_3N_4 employed in this study was carried out as previously reported (synthetic details are included in the Supporting Information, SI). Figures 2a and 2b show scanning electron microscopy (SEM) and transmission electron microscopy (TEM) images of the prepared g-C_3N_4 confirming the expected nanosheets morphology.[13] Figure 2c shows the x-ray diffraction (XRD) pattern of g-C_3N_4 where the two main peaks around 13° and 28°, corresponding to the (100) and (002) reflections, are clearly identified. Finally, Figure 2d reports the UV-Vis absorbance spectra of nanostructured g-C_3N_4, in agreement with previous literature.[35]

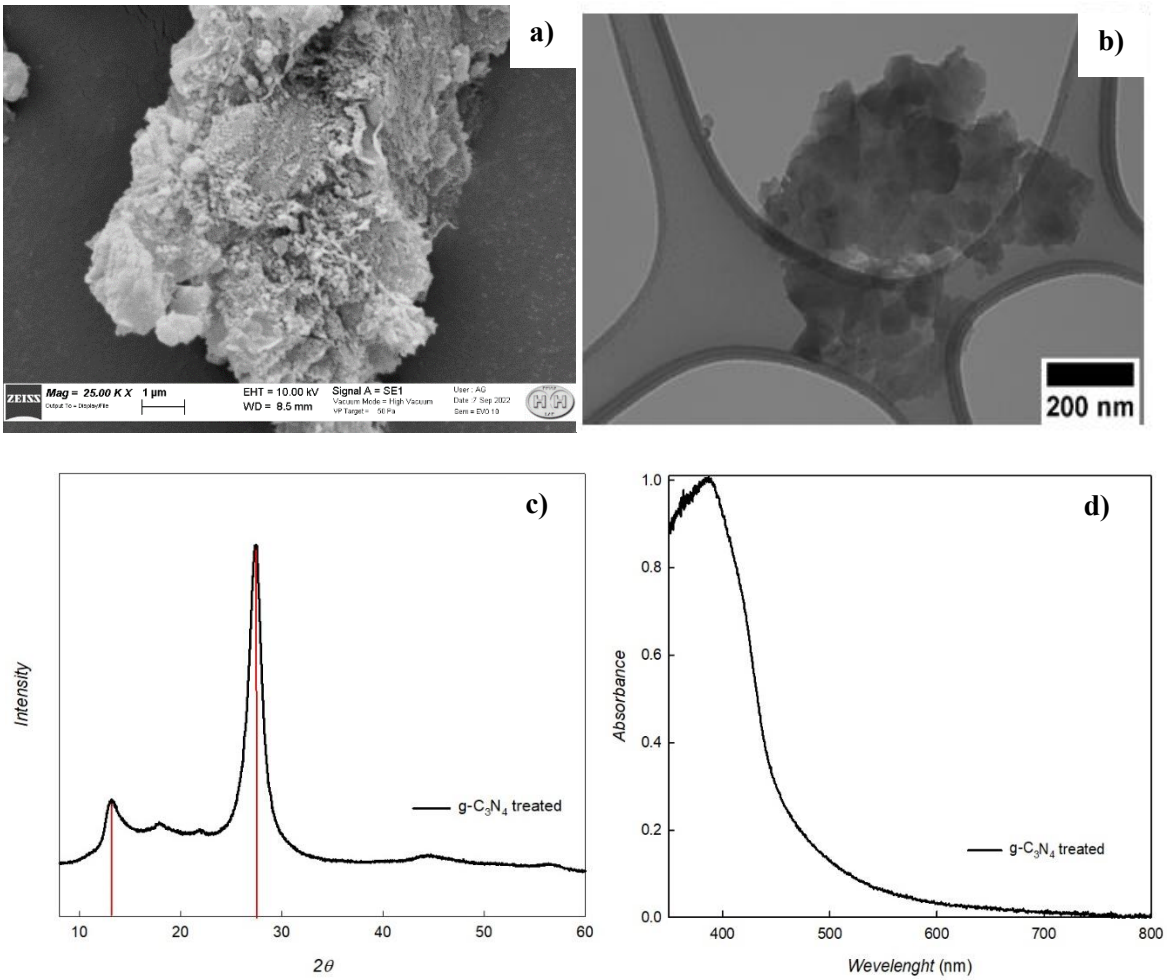

Figure 2. a-b) Representative SEM and TEM images of exfoliated g-C_3N_4 and c-d) XRD pattern and UV-Vis absorbance spectra of exfoliated g-C_3N_4.

The preliminary PBDB-/g-C_3N_4 BHJ system has been synthesized starting from the powders of the two semiconductors in weight ratios of (wt% of PBDB-T) 1,2.5,5,7.5, to study the possible interaction and the effective cohesion between the two photocatalysts. Figure 3 reports the room temperature X-ray diffraction (XRD) patterns of the compositions investigated.

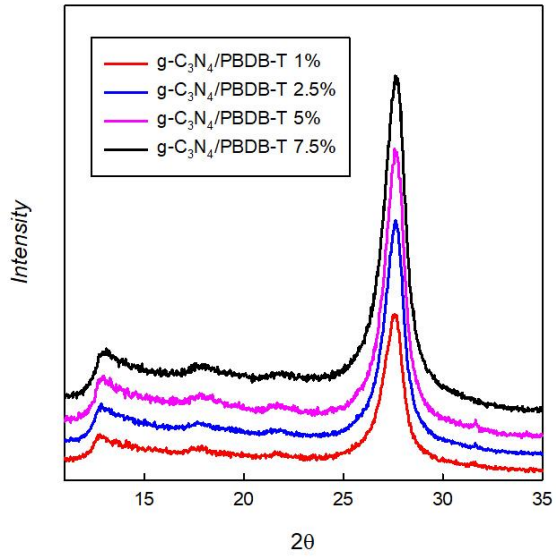

Figure 3. XRD pattern of the heterojunctions investigated, at 1, 2.5, 5, 7,5 wt% of PBDB-T.

Compared with the XRD pattern of the bare g-C_3N_4 already commented and reported in fig 2a, is possible to notice how no additional crystalline domain is detected in the heterojunction formation, being the PBDB-T manly an amorphous phase. PBDB-T-g-C_3N_4 heterojunction have also been characterized by transmission electron microscopy (TEM) and representative image showing their nanostructure are reported in figure 5. Interestingly, from TEM images is not possible to clearly distinguish the two semiconductors' phases, suggesting the formation of a thin layer of PBDB-T onto the surface of the nanosheets of g-C_3N_4.

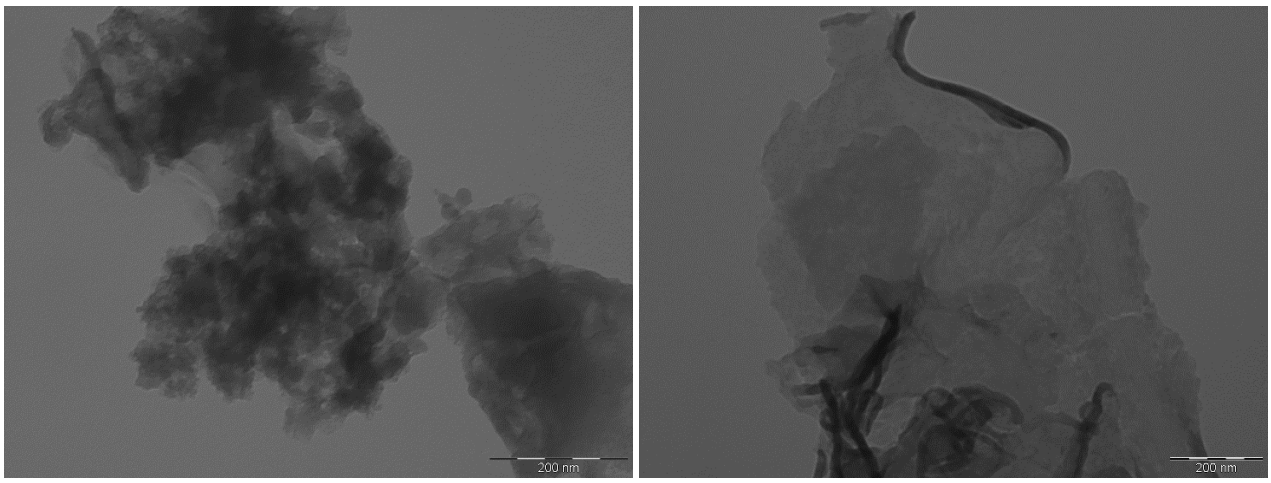

Figure 5. TEM images of PBDB-T-g-C_3N_4 2.5%

The composites series investigated have been realized changing the relative percentage of the polymer and the nanosheets g-C_3N_4. Figures 6a and b report the results in terms of hydrogen evolution rates in suspension set up of the photocatalyst in aqueous medium with and without the use of Pt as cocatalyst, expressed as μmol g^{-1} h^{-1}, obtained by photocatalytic experiments under simulated solar light (details in SI section materials and methods).

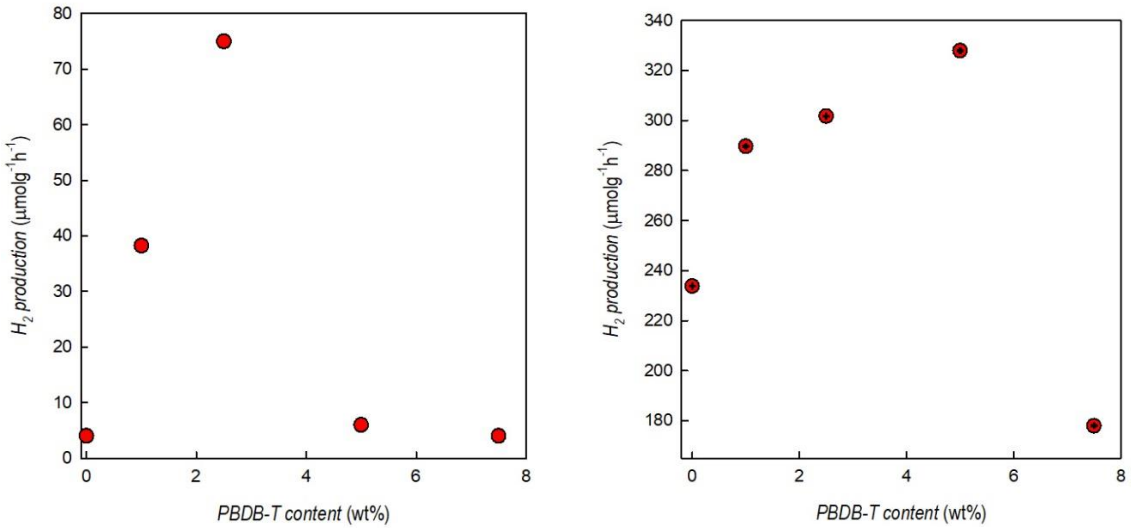

Figure 6. a) Hydrogen production as a function of PBDB-T content in wt% in the composites (n=3, simulated solar light, 500 W m^{-2}). **b)** Hydrogen production as a function of PBDB-T content in wt% in the composites (n=3, simulated solar light, 500 W m^{-2}) with Pt 1% in wt of the photocatalyst mass.

From graphs in fig 6 is possible to notice how the presence of Pt as co-catalyst deeply influences the general system performances, since for the pure composites samples no H_2 rate is detected for the pure g-C_3N_4, in accordance with previous results.[1,39] From the 6a graphs is extremely important to notice how a low amount of PBDB-T loading in the composite is sufficient increase the amount of H_2 production detecting 40 μmol g^{-1} h^{-1} for the PBDB-T-g-C_3N_4 1% and even double the result reaching more than 80 μmol g^{-1} h^{-1} for PBDB-T-g-C_3N_4 2.5%. By further increasing the loading onto the nanosheets of g-C_3N_4 the amount of H_2 dramatically decreases, suggesting some sort of disruptive cooperation between the two semiconductors. It was not possible to study a further loading of 7% of PBDB-T in the composites due to the strong hydrophobic nature of the organic semiconductor polymer (PBDB-T) because in the suspension and bubbling phases of photocatalyst powder no dispersion in the aqueous medium was possible, obtaining large a compact agglomerate of

sample. Moreover, being the PBDB-T naturally dark blue, when the concentration of polymer grows, it affects the transparency of the solution hindering the photoexcitation of sample resulting in an obstruction of the photocatalytic active sites of g-C_3N_4. On the other hand, from the results reported in figure 6b is evident how Pt plays a crucial role for the performance of the photocatalyst obtaining a boost of more than 50 times in terms of H_2 evolution rate compared to the bare composites. Here, we notice a more linear trend with a gradual increase in H_2 production rate starting from g-C_3N_4 100% and reaching the maximum with PBDB-T-g-C_3N_4 5% and consequent important drop in H_2 production rate when PBDB-T-g-C_3N_4 7% is reached. In conclusion, we can confirm that the trend of the two sets is peculiar because for the first one, without the Pt, the higher electron efficiency of the heterojunction is proved and reached a lower loading of PBDB-T, underlining how a low amount of polymer is sufficient to boost the photocatalytic performances of g-C_3N_4 on the other hand, when Pt is exploited as co-catalyst all the samples perform extremely better than the pure one, so in this secondo sets it is necessary to reach an higher loading of PBDB-T to appreciate the beneficial effect in electron transfer for the heterojunction.

Proved an increased photocatalytic efficiency of the heterojunction system the focus of the present work remains to investigate the g-C_3N_4 as potential photocatalyst material for photolectrochemical cell.

To first assess the potential use of the g-C_3N_4:PBDB-T bulk heterojunction (BHJ) as photocathodic material, pristine PBDB-T and g-C_3N_4 and a complete series of BHJs, with varying relative weight ratios between the two semiconductors (Table S1), were prepared under the same conditions (see details in SI). Linear scanning voltammetry (LSV) curves under intermittent 1 Sun illumination (Figure 7) show almost undetectable photocurrent for g-C_3N_4, a modest cathodic photocurrent for PBDB-T, and an evident increased photocurrent for the BHJ 1-1 (50wt%-50wt%), the best performing composite among the weight ratios investigated (values of the photocurrent for whole set of BHJs tested are reported in Figure S1).

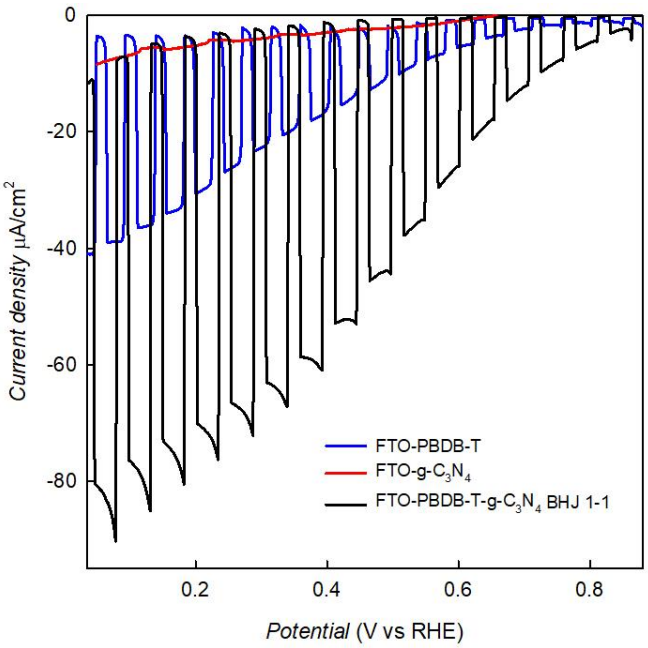

Figure 7. Linear scanning voltammetry (LSV) of pure FTO-PBDB-T, pure FTO-g-C_3N_4 and FTO-PBDB-T:g-C_3N_4 photocathode in aqueous electrolyte H_2SO_4 0.1 M pH 1.

These promising results on the photocathodic current, suggest an electronic interaction in the BHJ, as anticipated based on the relative band position of the two semiconductors shown in Figure 1, where g-C_3N_4 behaves as the electron acceptor. For the engineering of the full electrode, considering the fast charge carrier recombination rate of carbon nitride, a hole transport layer (HTL) behind the BHJ layer was added. For this purpose, three different popular HTLs, namely PEDOT-PSS, (2-(9H-carbazol-9-yl)ethyl)phosphonic acid (2PACz) and CuSCN (See SI) were initially tested. Figure 8 reports the LSV and Chronoamperometry (CA) measurements at 0 V vs RHE under continuous illumination of 1 Sun of BHJ 1-1 and CuSCN-BHJ 1-1 which resulted to be the best performing architecture in terms of current intensity and stability over 300 seconds (cfr Figure S2).[31,36,37]

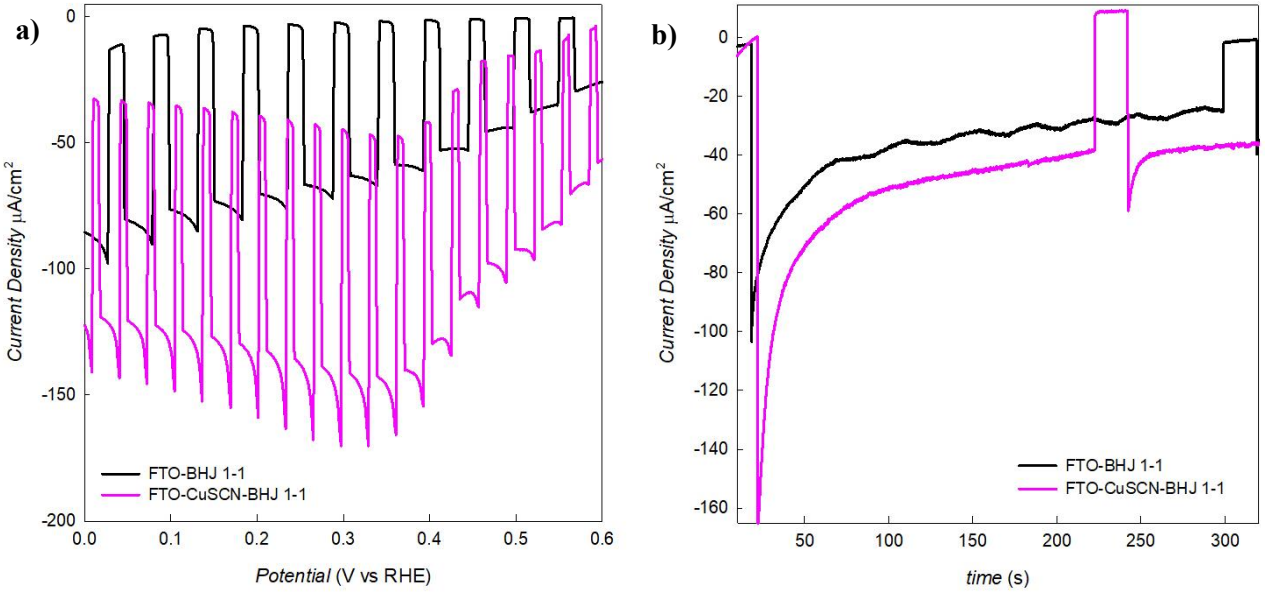

Figure 8. Photocurrent and stability of FTO-PBDB-T:g-C_3N_4 1-1 BHJ by adding a layer of CuSCN as HTL to the photocathode in aqueous electrolyte H_2SO_4 0.1 M pH 1. (a) LSV of FTO-BHJ 1-1 and FTO-CuSCN-BHJ 1-1. (b) CA of FTO-BHJ 1-1 and FTO-CuSCN-BHJ 1-1 0 V vs RHE over 300 seconds.

From the LSV is possible to notice a redox reaction that occurs in the 0.5-0.3V range that increases the dark current, probably due to the reduction of Cu^+ (CuSCN) to Cu^0, whose redox potential is $E°$=0.512 V at 25°C in acidic solution.[38] Nevertheless, the registered photocurrent of CuSCN-BHJ 1-1 is higher and more stable compared to the BHJ 1-1 electrode without the HTL. Effective deposition of a thin layer of CuSCN nanorods is confirmed by SEM images reported in Figures 9a and c, clearly showing a CuSCN layer under the BHJ 1-1 photoactive layer.[36] Figures 9b and 9d report the appearance of the CuSCN-BHJ 1-1 and BHJ 1-1 photocathodes after the photoelectrochemical measurements highlighting the increased stability achieved with the presence of CuSCN.

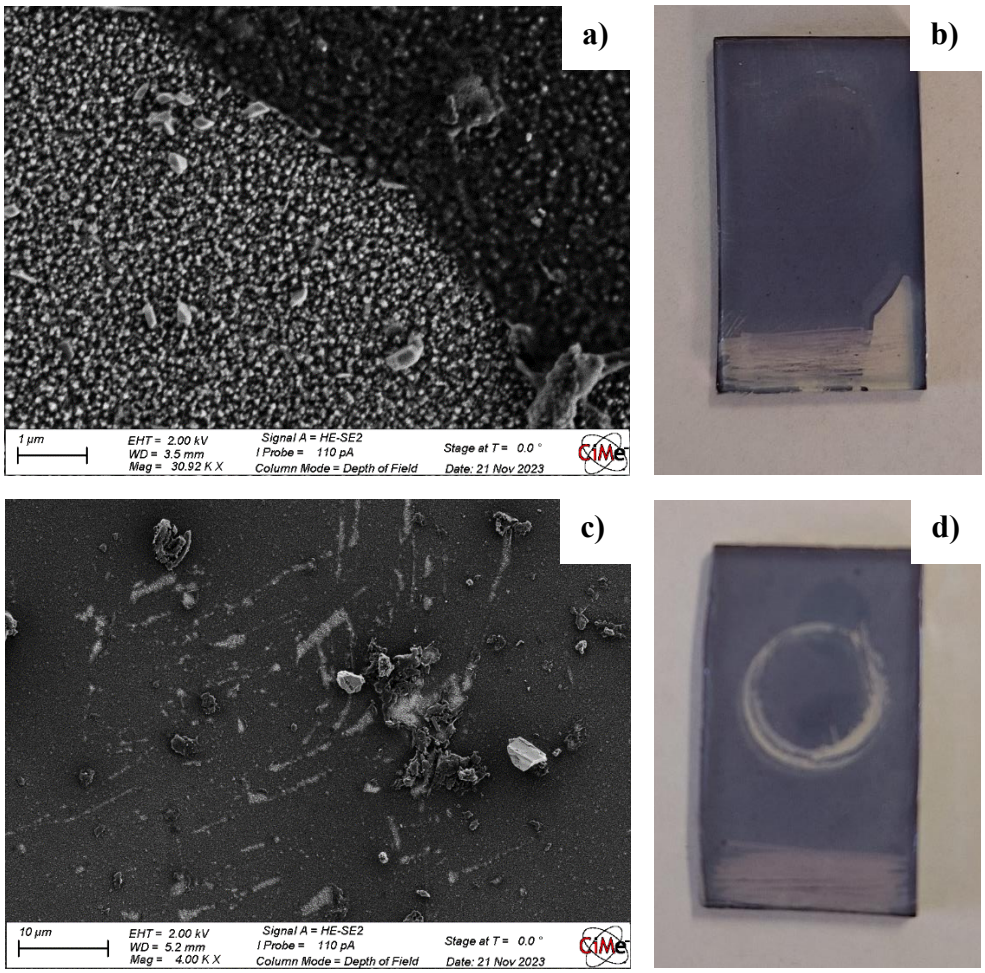

Figure 9. Photocathode characterization. (a) SEM representative image of FTO-CuSCN-BHJ 1-1 photocathode. (b) Photo of FTO-CuSCN-BHJ 1-1 of the photocathode after the photoelectrochemical measurement. (c) SEM representative image of FTO-BHJ 1-1. (d) Photo of FTO-BHJ 1-1 after the photoelectrochemical measurement.

The final element of the electrode architecture was the selection and introduction of a co-catalysts which is known to be required for an efficient photocatalytic H_2 production by g-C_3N_4.Therefore, the photocurrent response of present photocathodes was investigated after adding the co-catalyst layer.[39] We attempted diverse deposition methods for and two different cocatalysts: a photodeposition (pd) and a photoelectron deposition (ped) method for Pt, and a spray coating method for RuO_2 (see SI).[40,41] The full set of measurements for the three different photocathodes is reported in Figure S6. Based on these results, the optimal architecture identified in terms of current and stability is schematized in figure 10. As evident from LSV and CA measurements (Figure S6), both photoelectrodeposited Pt methods, galvanostatic and redox, significantly improve the performance of the photocathode but the redox method resulted to be more efficient and functional compared

to the galvanostatic method. In particular the galvanostatic method requires a higher amount of H_2PtCl_6 which makes this method less sustainable. [40]

Figure 10. Representative scheme for the photocathode architecture.

In figure 11 are reported LSV and CA measurements for the two photocathodes where it is evident the boost, in terms of photocurrent, achieved with Pt addition, almost 197 μA/cm^2 under intermittent illumination at 0 V vs RHE compared with 100 μA/cm^2 reached without the cocatalyst.

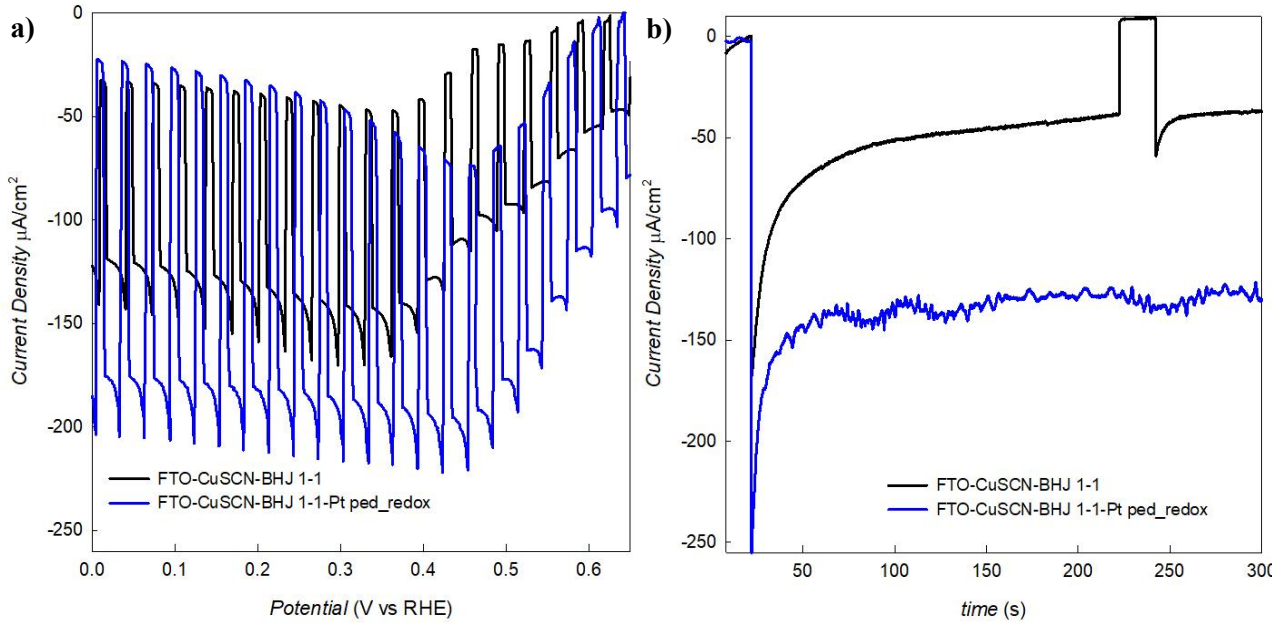

Figure 11. Photocurrent and stability of FTO-CuSCN-BHJ 1-1 by adding Pt as cocatalyst with photoelectrodeposition (ped) redox method to the photocathode in aqueous electrolyte H_2SO_4 0.1 M pH 1. (a) LSV of FTO-CuSCN-BHJ 1-1 and FTO-CuSCN-BHJ 1-1-Pt (ped) redox. (b) CA of FTO-CuSCN-BHJ 1-1 and FTO-CuSCN-BHJ 1-1-Pt (ped) redox at 0 V vs RHE over 5 minutes.

In light of that, to further confirm the effectiveness of the electronic contact between the two semiconductors in the BHJ, we performed an investigation by comparing the present BHJ 1-1 with a layered heterojunction (LHJ) where the two photoactive materials, i.e. g-C_3N_4 and PBDB-T, are deposited separately in two consequential layers. A scheme of the LHJ architecture is reported in Figure 12.

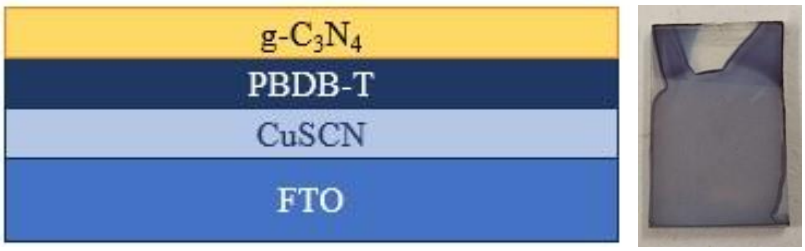

Figure 12. Representative scheme for the photocathode architecture exploiting a layered heterojunction and photo of the as realized photocathode.

Based on the previous considerations, being the g-C_3N_4 the electron acceptor in the proposed band alignment scheme (cfr Figure 1) we expect the LHJ architecture to be competitive in terms of electron transfers for the reduction reaction of water towards H_2 evolution. For this reason, diverse attempts have been performed for the g-C_3N_4 deposition onto the PBDB-T layer to maximize the g-C_3N_4 contact with the electrolyte. In figure 13, the photocurrent performances of the LHJ prepared by using different deposition methods for the g-C_3N_4 layer on PBDB-T layer, namely spray coating (sp) and drop casting (dp), are reported (full details in SI).

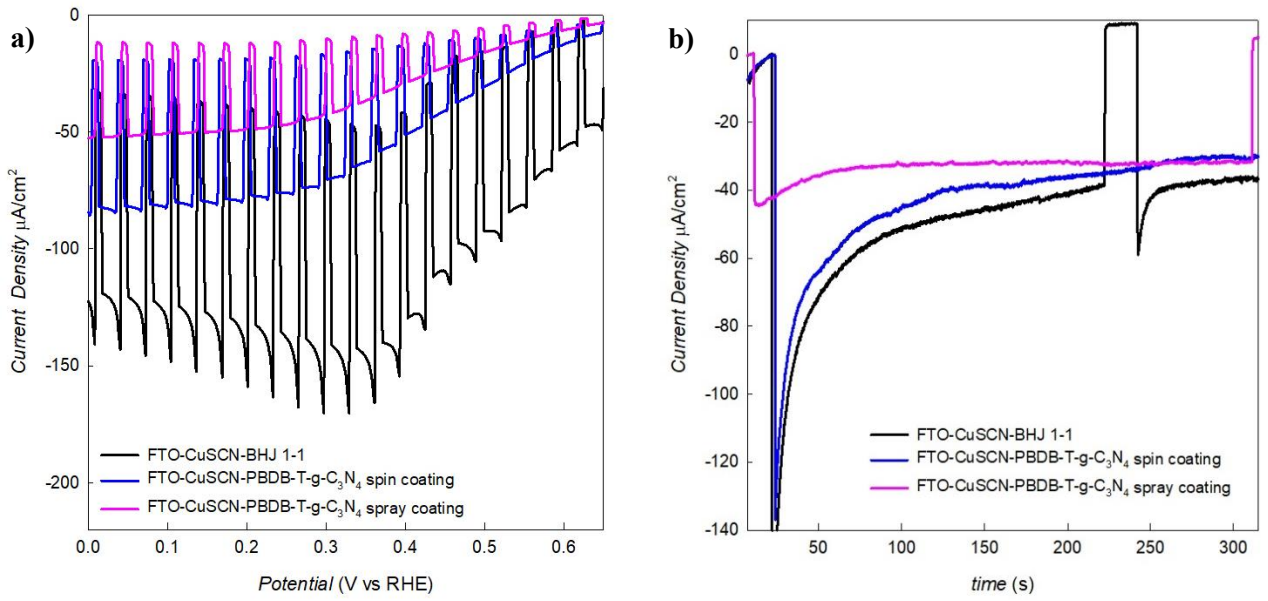

Figure 13. Photocurrent and stability of FTO-CuSCN-BHJ 1-1 compared with FTO-CuSCN-PBDB-T-g-C_3N_4 LHJ photocathode, where the FTO-CuSCN-PBDB-T-g-C_3N_4 spin coating sample the g-C_3N_4 is deposited by spin coating and in the FTO-CuSCN-PBDB-T-g-C_3N_4 spray coating sample is deposited by spray coating, in aqueous electrolyte H_2SO_4 0.1 M pH 1. (a) LSV of FTO-CuSCN-BHJ 1-1 and FTO-CuSCN-PBDB-T-g-C_3N_4 spin and spray coating. (b) CA of FTO-CuSCN-BHJ 1-1 and FTO-CuSCN-PBDB-T-g-C_3N_4 spin and spray coated at 0 V vs RHE over 300 seconds.

Although the shape of LSV for the LHJ prepared with both deposition methods for g-C_3N_4 is more typical and smoother than for BHJ 1-1, the reduction peak of Cu^+ -> Cu^0 is not observed, and the photocurrent remains higher for the BHJ 1-1 architecture. Nevertheless, it can be observed from the CA measurements that, even if the current is decreased for the FTO-CuSCN-PBDB-T-g-C_3N_4 (sc) sample, it remains more stable compared to the other samples tested over 300 seconds. The photocurrent reduction is a predictable event since, as already discussed, g-C_3N_4 is an anisotropic semiconductor, due to its graphitic structure, and the electronic conduction is favoured along the sheets surface but hindered perpendicularly to those. As a consequence, it becomes evident that g-C_3N_4 layer, while leading to a reduction of current intensity, may play a protective role against the degradation of the photoactive layer. To further test these hypotheses, we compared the photocurrent intensity and stability of the BHJ 1-1 photocathode with and without the spray coated g-C_3N_4 layer. The corresponding LSV and CA results are shown in figure 14.

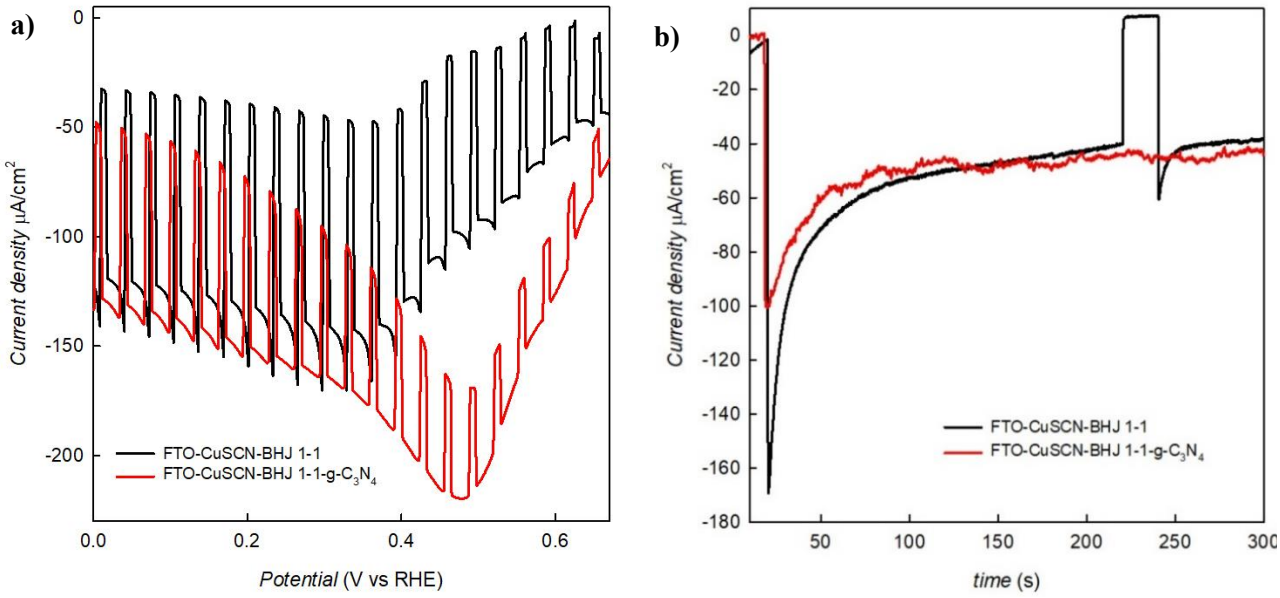

Figure 14. Photocurrent and stability of FTO-CuSCN-BHJ 1-1 compared with FTO-CuSCN-BHJ 1-1-g-C_3N_4 (sc) on top (back illuminated) photocathode, in aqueous electrolyte H_2SO_4 0.1 M pH 1. (a) LSV of FTO-CuSCN-BHJ 1-1 and FTO-CuSCN-BHJ 1-1-g-C_3N_4 (sc). (b) CA of FTO-CuSCN-BHJ 1-1 and FTO-CuSCN-BHH 1-1-g-C_3N_4 (sc) at 0 V vs RHE over 300 seconds.

We can immediately notice from LSV curve that the dark current is higher for the g-C_3N_4 coated electrode together with an intense peak around 0.5 V for the Cu^+ reduction compared to the control FTO-CuSCN-BHJ 1-1. At the same time, the photocurrent at 0 V vs RHE is just slightly decreased and as can be inferred from CA current intensity, it results to be more stable. FTO-CuSCN-BHJ 1-1-g-C_3N_4 (sc) photocathode was tested from back illumination to avoid any interference caused by the g-C_3N_4 layer and that may be the cause of the increased dark current and the more pronounced redox reduction peak of Cu^+ at 0.5 V.

To investigate the potential protective role played by the g-C_3N_4 layer two set of four photocathodes have been exposed to three types of stress for 1h. One set of photocathodes consists of FTO-CuSCN-BHJ 1-1, and the second set is FTO-CuSCN-BHJ 1-1-g-C_3N_4 (sc). The photocathodes have been exposed to electrolyte, light, and potential for 1h before the photoelectrochemical measurement and, in this way, it was possible to study the hypothetical protective role of g-C_3N_4 layer on the stability of the sample over 30 minutes of chronoamperometry. In figure 15 are showed the results.

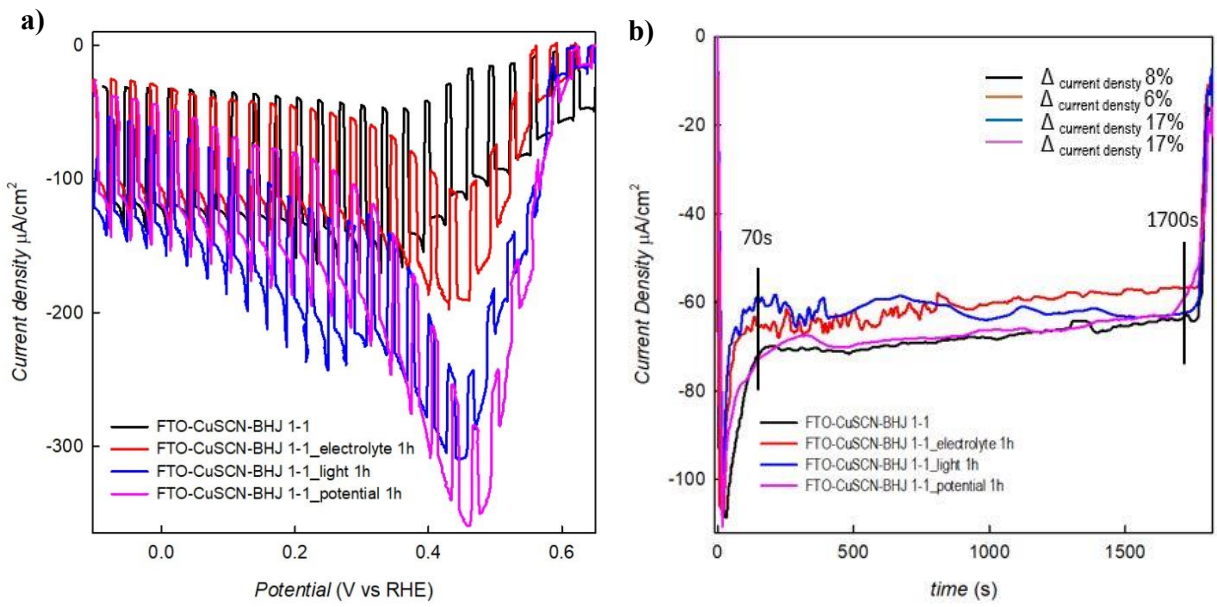

Figure 15. Photocurrent and stability of FTO-CuSCN-BHJ 1-1 subjected separately to three types of stress; electrolyte, light, potential for 1h, then tested in aqueous electrolyte H_2SO_4 0.1 M pH 1. (a) LSV of FTO-CuSCN-BHJ 1-1 control (no stress), FTO-CuSCN-BHJ 1-1 electrolyte 1h, FTO-CuSCN-BHJ 1-1 light 1h, FTO-CuSCN-BHJ 1-1 potential 1h. (b) CA of the same photocathodes in the same condition at 0 V vs RHE over 30 minutes.

Light and potential resulted to be the most detrimental stress conditions for the integrity of the electrode (significant increase in the Cu^+ redox peak) while the role of electrolyte stress has a more direct impact on the current intensity. By selecting two arbitrary points from the CA measurements, i.e. after 70 and 1700 seconds, we calculated the percentage loss in terms of current intensity of each stress condition under continuous illumination and stirring. For FTO-CuSCN-BHJ 1-1 control, not subjected to stress, the current loss after ~30 minutes is around 8%, for FTO-CuSCN-BHJ 1-1 the effect of the electrolyte for 1h, light for 1 h and potential stress for 1 h correspond to current losses of about 6, 17 and 21%, respectively.

Figure 16 reports the results for the second set of samples, namely FTO-CuSCN-BHJ 1-1-g-C_3N_4 (sc), subjected to the same stress tests of the previous samples.

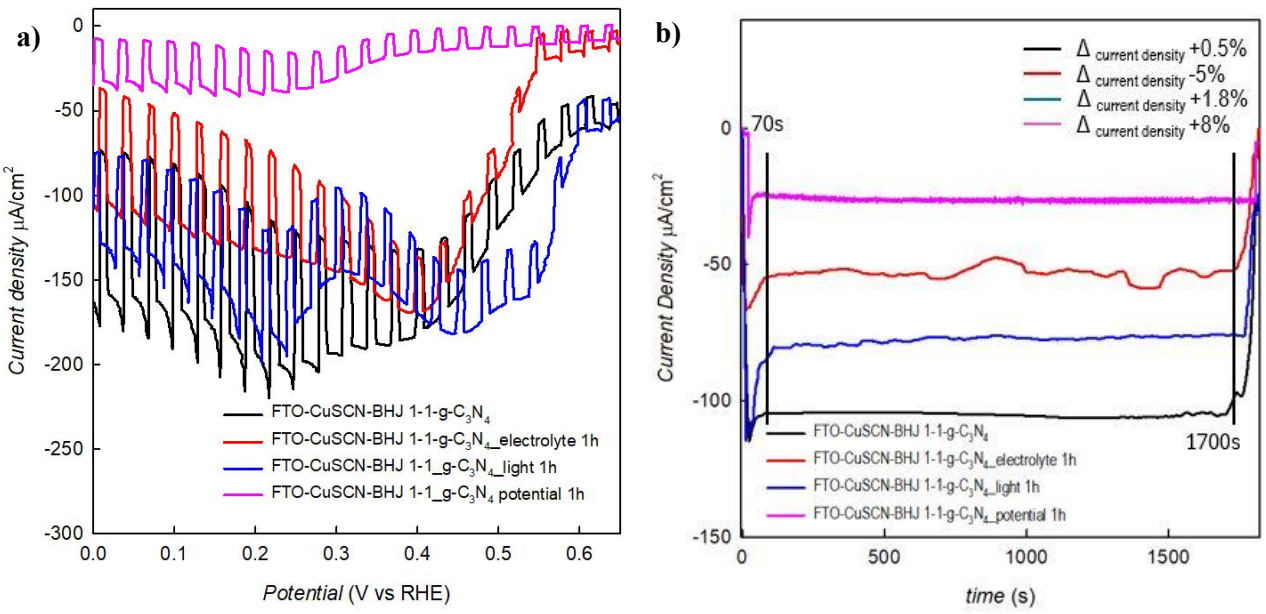

Figure 16. Photocurrent and stability of FTO-CuSCN-BHJ 1-1-g-C_3N_4 (sc) subjected separately to the same stress of the previous system; electrolyte, light, and potential for 1h, then tested in aqueous electrolyte H_2SO_4 0.1 M pH 1. (a) LSV of FTO-CuSCN-BHJ 1-1-g-C_3N_4 (sc)control (no stress), FTO-CuSCN-BHJ 1-1-g-C_3N_4 (sc) electrolyte 1h, LSV of FTO-CuSCN-BHJ 1-1-g-C_3N_4 (sc) light 1h, FTO-CuSCN-BHJ 1-1-g-C_3N_4 (sc) potential 1h. (b) CA of the same photocathodes in the same condition at 0 V vs RHE over 30 minutes.

From the LSV is evident that all the stress conditions deeply affect the photocathode performances. It is useful to remember that all the photoelectrochemical measurements conducted on the FTO-CuSCN-BHJ 1-1-g-C_3N_4 (sc)photocathode have been collected in back illumination configuration. Therefore, it is clear that, in terms of charge carrier dynamics under intermittent illumination, the g-C_3N_4 coating layer does not impart a significant efficiency improvement. However, even if the current loss intensity measured from the CA compared to the sample not subjected to stress is high for all the stress conditions, the % loss in the first 30 minutes of measurement for each photocathode is negligible and, in some cases, positive.

For FTO-CuSCN-BHJ 1-1-g-C_3N_4 (sc), not subjected to stress, the current variation after ~30 minutest is around +0.5%. ForFTO-CuSCN-BHJ 1-1-g-C_3N_4 the effect of the electrolyte for 1h, light for 1h and potential stress for 1h correspond to current variation of -5, +1.8 and +8%, respectively. This result suggests that the g-C_3N_4 layer may actually act as a protective layer during the CA measurement, especially for longer measurements. On the other hand, the loss in terms of current intensity is high, specifically for the potential stressed

photocathode and this may be correlated with the electrostatic nature of g-C_3N_4. However, the results collected so far are promising and worthy of deeper understanding and optimization, especially for the potential use of g-C_3N_4 as protective layer (SI).

After the so far reported step-by-step optimization of the photocathode architecture, an electrodeposited layer of Pt was added to FTO-CuSCN-BHJ 1-1-g-C_3N_4 (schematized in fig 8) onto the g-C_3N_4 layer following the same procedure used for the photocathodes reported in fig 7.

In figure 17 are reported LSV and CA measurements for the final configuration of the photocathode developed in the present work, namely FTO-CuSCN-BHJ 1-1-g-C_3N_4 (sc)-Pt (ped) redox.

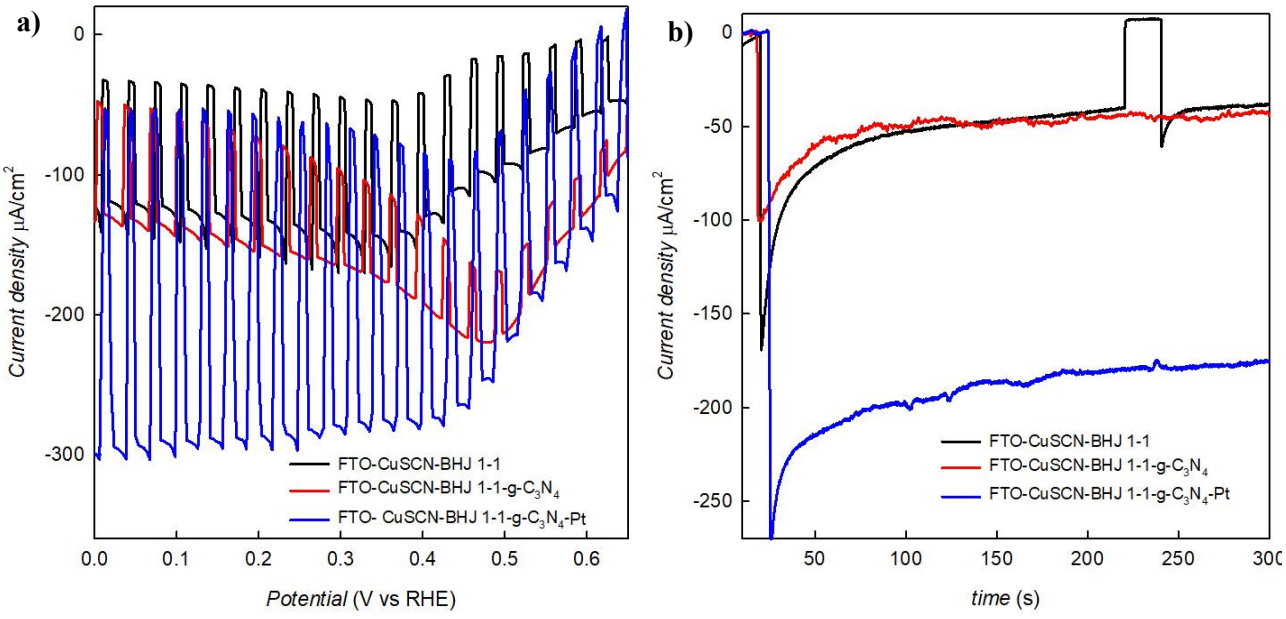

Figure 17. Photocurrent and stability of FTO-CuSCN-BHJ 1-1-g-C_3N_4 (sc)-Pt (ped) redox in aqueous electrolyte H_2SO_4 0.1 M pH 1. (a) LSV of FTO-CuSCN-BHJ 1-1-g-C_3N_4 (sc) -Pt (ped) redox. (b) CA of the same photocathode in the same condition at 0 V vs RHE over 300 seconds.

In figure 18 are reported the UV-Vis (a) and the photoluminescence spectra (b) of the investigated electrodes systems.

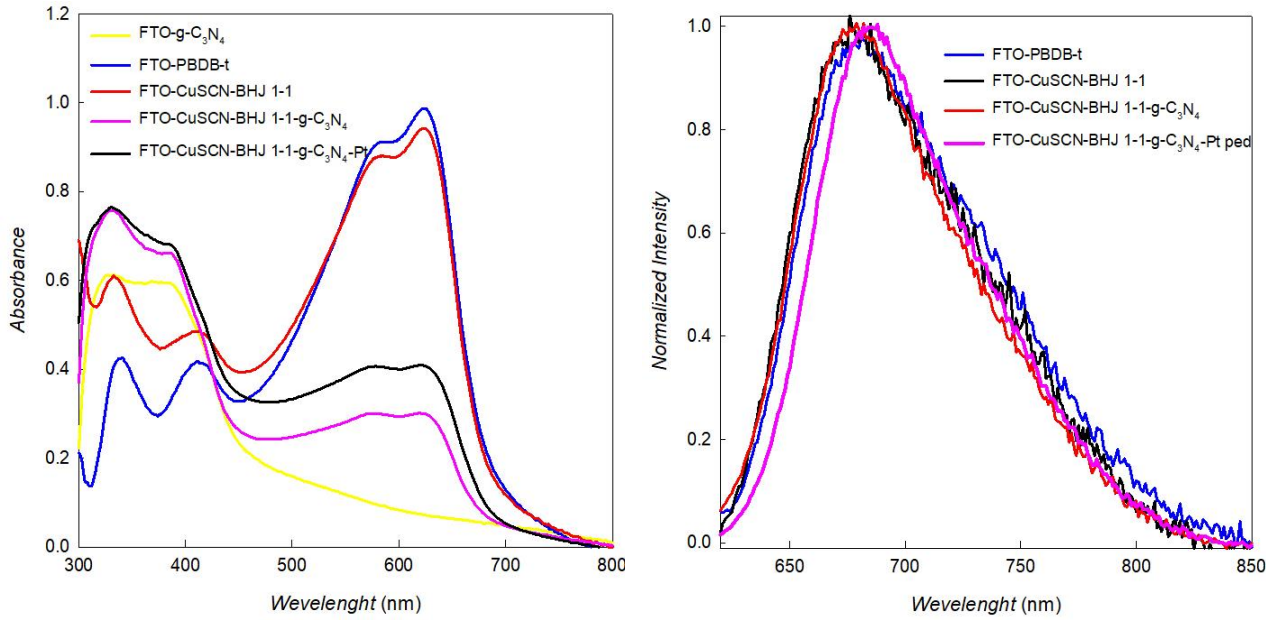

Figure 18. (a) UV-Vis absorbance spectra of the photocathodes configuration studied in the present work. (b) Photoluminescence emission spectra of the photocathode configuration studied in the present work.

In figure 18(a) is possible to observe the UV-Vis spectra of the obtained electrodes, comparing the bare g-C_3N_4 and PBDB-T onto FTO with the other electrodes presenting the complete architecture. From the g-C_3N_4 absorption spectrum (yellow line) we can appreciate the known absorbance peak at 450 nm, from the PBDB-T absorption spectrum (blue line), we can appreciate the main absorption peak at 680 nm, as already previously reported. When the HTL layer, CuSCN, and the active layer, BHJ 1-1, are present (red line) the predominant absorption peak is the PBDB-T one g-C_3N_4 is slightly detectable. On the other hand, when the additional top protecting layer of g-C_3N_4 and Pt are added to the electrode architecture, the predominant absorption peak is the g-C_3N_4 one with a dramatic decrease in the PBDB-T absorbance peak, even more evident in presence of Pt. In figure 18 (b) are reported the photoluminescence (PL) spectra of the same samples investigated with UV-Vis, except g-C_3N_4. By a first comparison between the PL spectra results is not possible to appreciate a significant difference between the photoluminescence effect of the samples, by simply engineering the architecture of the electrode. This result does not necessary implies

a not efficient separation of the charge carriers across the layers, meaning an efficient extraction and conduction of the electron to the electrode surface, also because a slight red shift is detected for the final electrode configuration presenting the complete engineered architecture, confirming an actual electron transfer in the BHJ.

3. CONCLUSIONS

In summary, we realized a novel BHJ exploiting g-C_3N_4 and PBDB-T as photocathodic materials for photoelectrochemical H_2 evolution. The obtained photocathode, in the finial configuration, delivered a photocurrent density of almost 300 μA/cm^2 and stable operation for 300 seconds while retaining more that 90% of the initial photocurrent. Optimized architecture required the presence of an HTL layer, CuSCN, to maximise the electron transport to the cathode surface where a layer of g-C3N4 is present. Moreover, Pt deposition on this final layer was found to be necessary to boost the photocatalytic performance of carbon nitride, in analogy with its behaviour as photocatalyst. The efficient electron transport in the BHJ was confirmed by photocatalytic hydrogen evolution reaction from *in suspension* set up, reporting a higher H_2 evolution rate for the BHJ at low loading of PBDB-T compared with the pure g-C_3N_4.

Overall, while some limitations have been highlighted in this work, exploiting the use of carbon nitride in a PEC, by performing a set of successive optimization strategies, encouraging results have been obtained. It is clear that the investigation of g-C3N4 as photocathodic materials in PECs still requires a significant amount of work such proper tuning of carbon nitride thickness, control of electrical conductivity anisotropy, and potential use of nanostructured g-C_3N_4. We believe that the strategy and architecture presented in this work provides new clues to design organic, low-cost, and eco-friendly photoelectrocatalysts for the production of green H_2.

The first-author Costanza Tedesco, author of the present Ph.D. work, carried out all the experimental parts: the synthesis and the characterization of all photocatalytic materials as well as the quantification of photocatalytic H_2 photoproduced and the deposition and photoelectrochemical characterization of all studied photocathodes.

The present work is in preparation for publication, in partnership with Prof Kevin Sivula and Benjiamin Goldman from LIMNO group, EPFL.

SUPPLEMENTARY INFORMATION

Enhancing Visible-Light-Driven Hydrogen Production: Heterojunction Engineering of Graphitic Carbon Nitride and PBDB-T Organic Semiconductor for Green Photoelectrocatalysis

Costanza Tedesco [a], *Benjamin Goldman* [b], *Kevin Sivula* [b], *Lorenzo Malavasi* [a]

[a] Department of Chemistry and INSTM, University of Pavia, Via Taramelli 16, Pavia, 27100, Italy

[b] Laboratory for Molecular Engineering of Optoelectronic Nanomaterials, Institute of Chemical Sciences and Engineering, École Polytechnique Fédérale de Lausanne (EPFL), CH-1015 Lausanne, Switzerland.

g-C_3N_4 %wt	PBDB-t %wt	I μA/cm^2
0	100	-43.6
10	90	-40.0
33	67	-62.1
50	**50**	**-75.2**
67	33	-65.9
90	10	10.0
100	0	1.4

Table S1. Investigated stoichiometries BHJ and relative current density recorded.

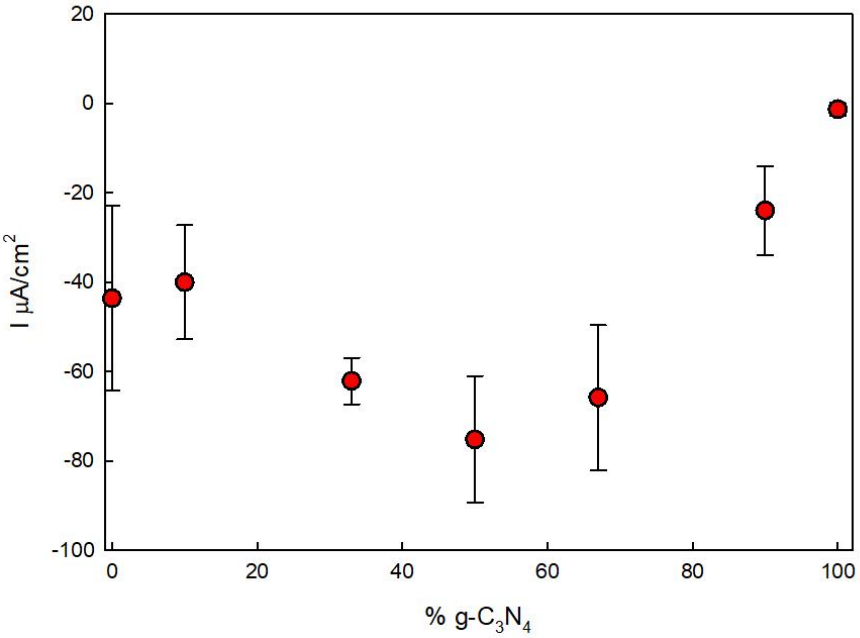

Figure S1. Current density recorded for the photocathodes set for the investigated weight ratios in the BHJ.

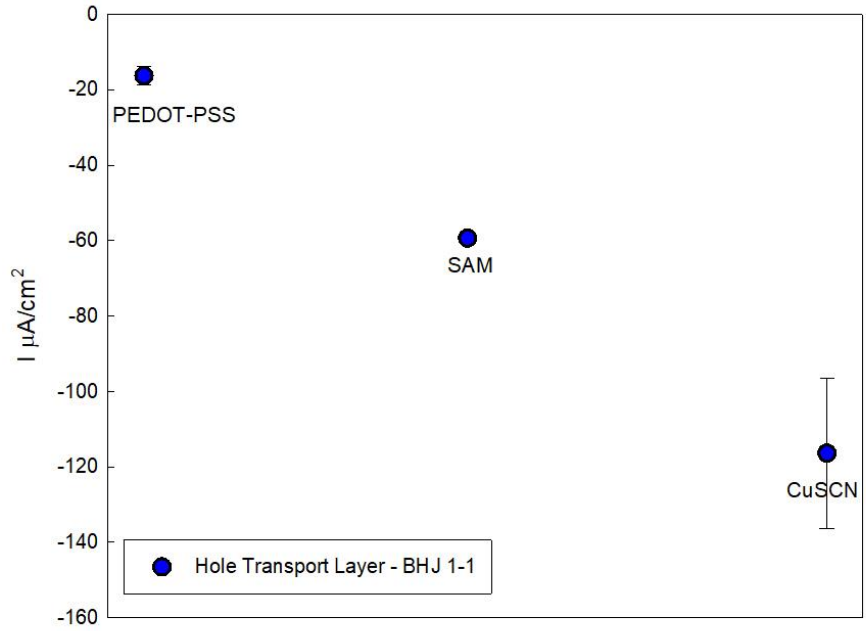

Figure S2. Current density recorded for the photocathodes set for the three hole transport layer (HTL) tested.

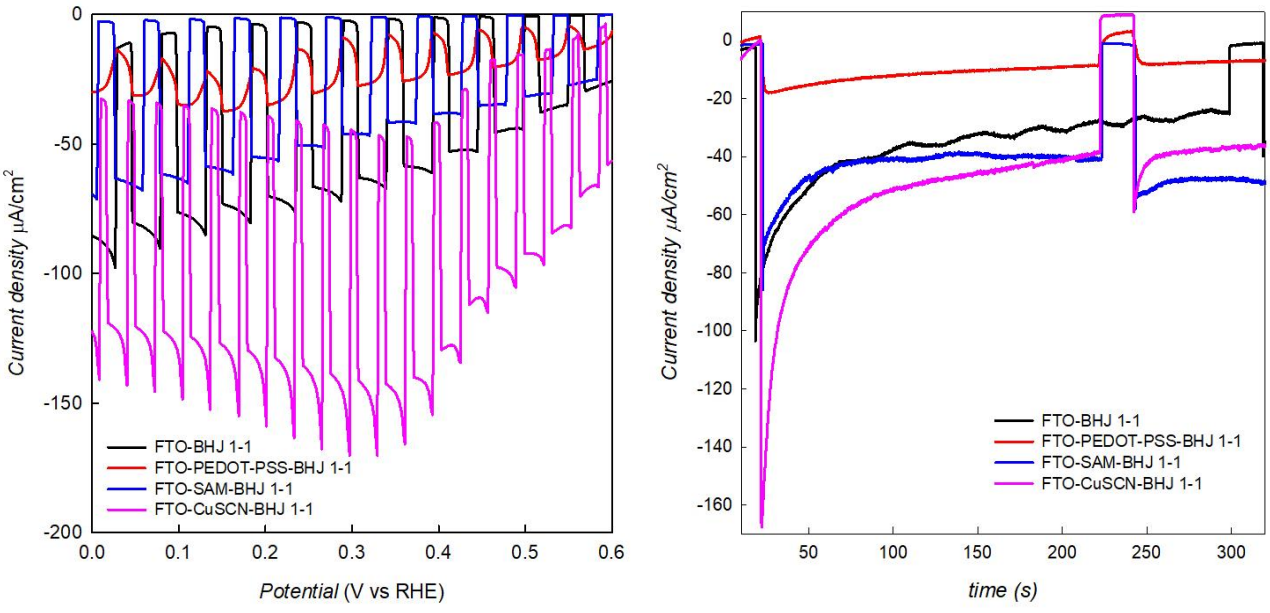

Figure S3. LSV and CA (0 V vs RHE) measurements for the FTO-BHJ 1-1 control photocathode and FTO-HTL-BHJ 1-1 photocathode exploiting the three HLT, PEDOT-PSS, SAM(2PACz), and CuSCN.

FTO-BHJ 1-1

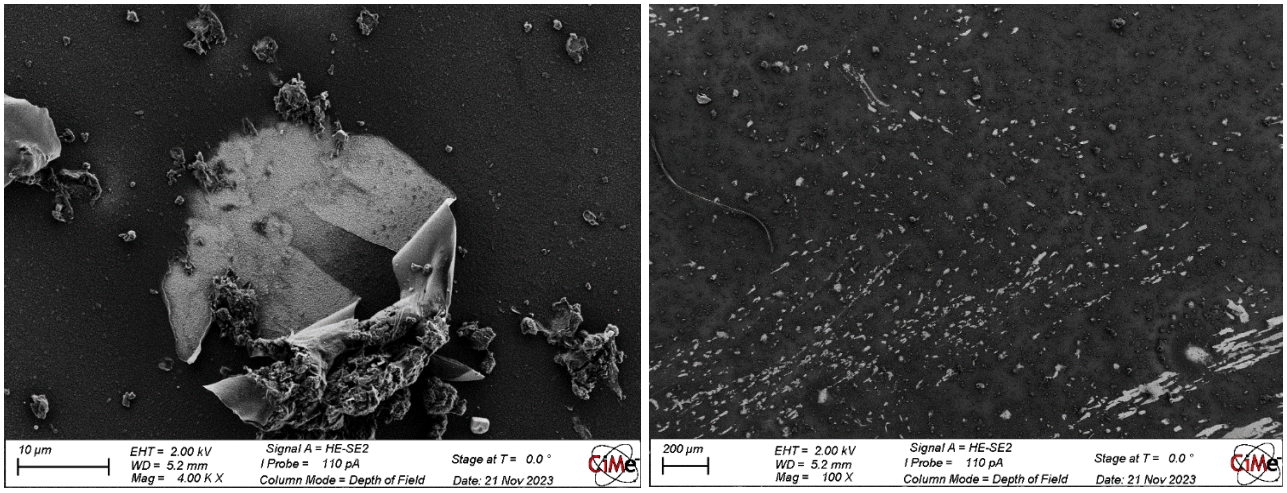

FTO-PEDOT-PSS-BHJ 1-1

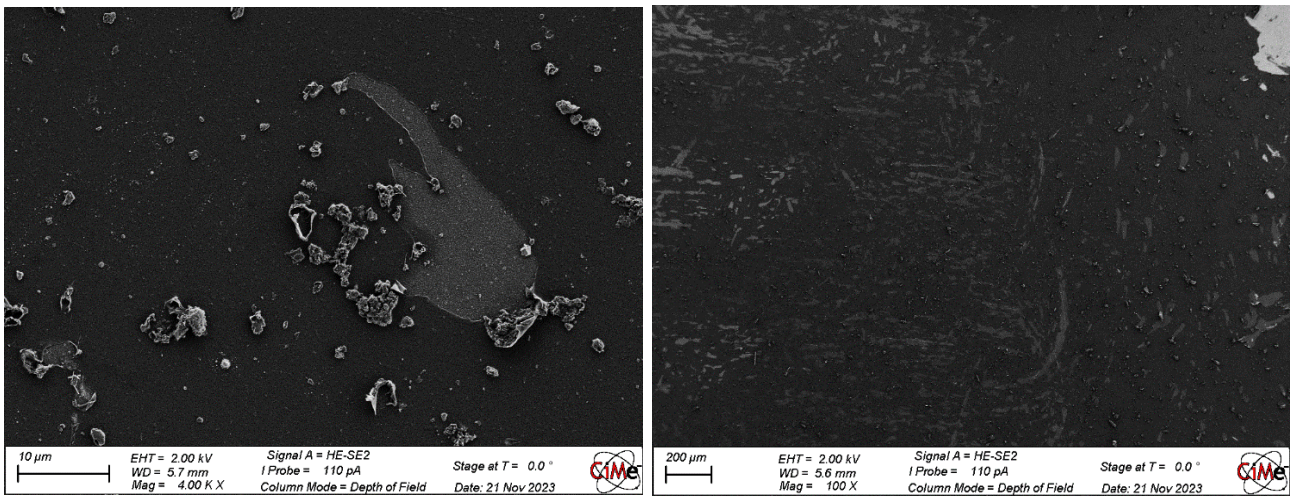

FTO-SAM(2PACz)-BHJ 1-1

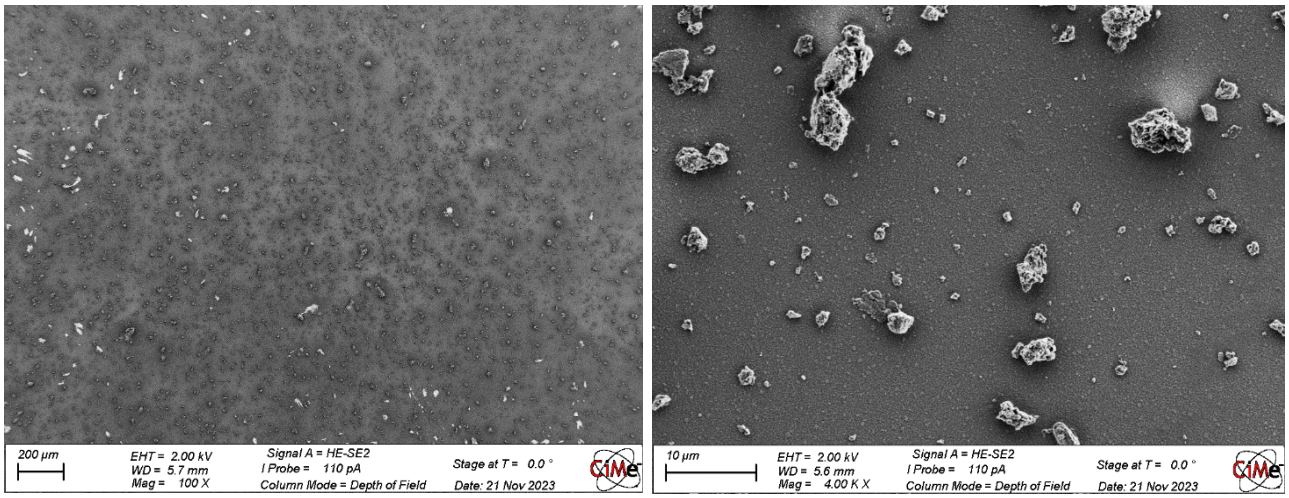

Figure S4. Representative SEM images of the photocathodes with the three different HLT.

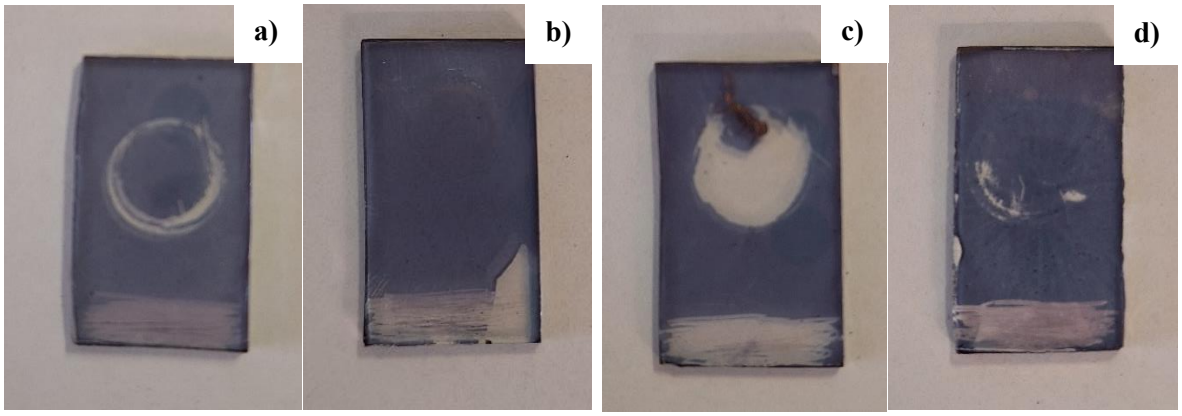

Figure S5. (a) FTO-BHJ 1-1 after photoelectrochemical measurement. (b) FTO-CuSCN-BHJ 1-1 after photoelectrochemical measurement. (c) FTO-PEDOT-PSS-BHJ 1-1 after photoelectrochemical measurement. (d) FTO-(2PACz)SAM-BHJ 1-1 after photoelectrochemical measurement.

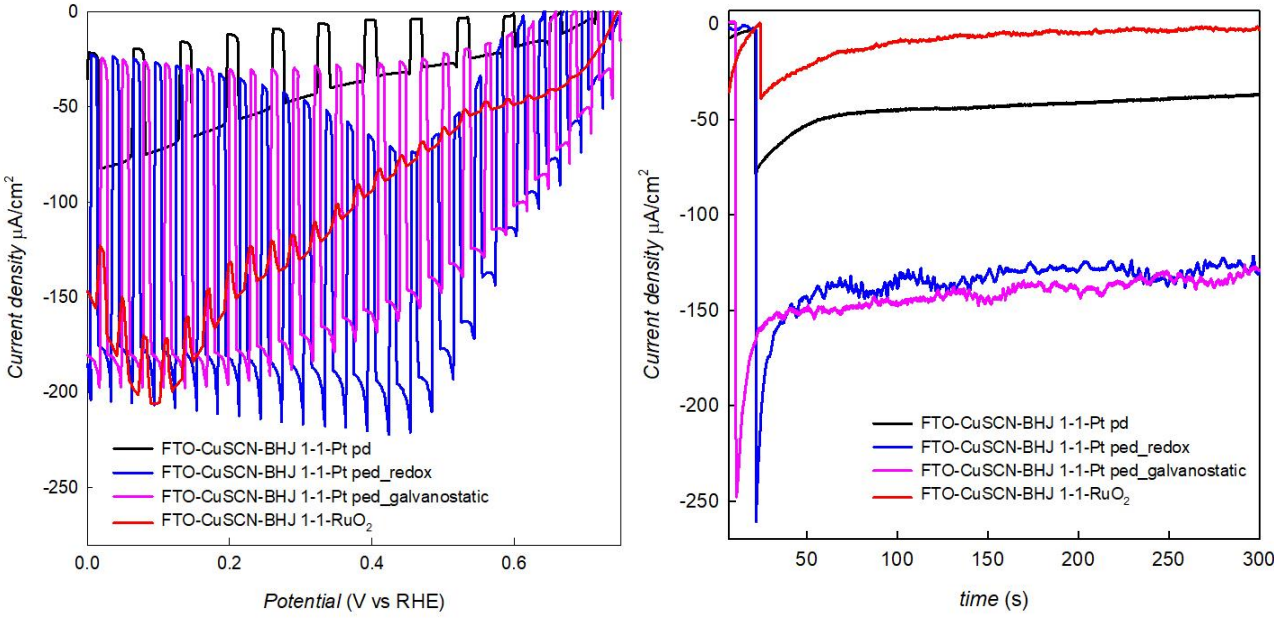

Figure S6. LSV and CA (0 V vs RHE) measurements for the FTO-CuSCN-BHJ 1-1 photocathode changing the catalyst and the deposition method. FTO-CuSCN-BHJ 1-1-Pt photodeposited (pd), FTO-CuSCN-BHJ 1-1-Pt photoelectrodeposited (ped) redox, FTO-CuSCN-BHJ 1-1-Pt photoelectrodeposited (ped) galvanostatic, FTO-CuSCN-BHJ 1-1-RuO_2.

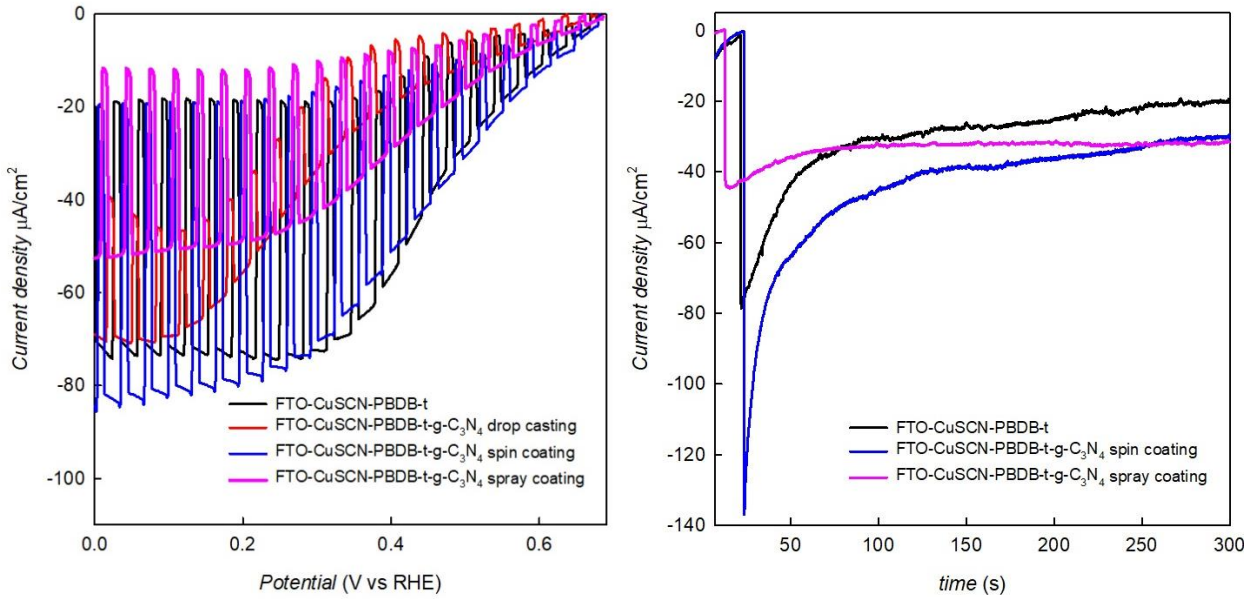

Figure S7. LSV and CA (0 V vs RHE) measurements for the layered heterojunction exploiting three different deposition methods of g-C_3N_4 layer. The tested photocathodes: FTO-CuSCN-PBDB-T, FTO-CuSCN-PBDB-T-g-C_3N_4 deposited with drop casting method, FTO-CuSCN-PBDB-T- g-C_3N_4 deposited with spin coating method, FTO-CuSCN-PBDB-T- g-C_3N_4 deposited with spray coating method.

Figure S8. Photos of the layered heterojunction structure photocathodes.

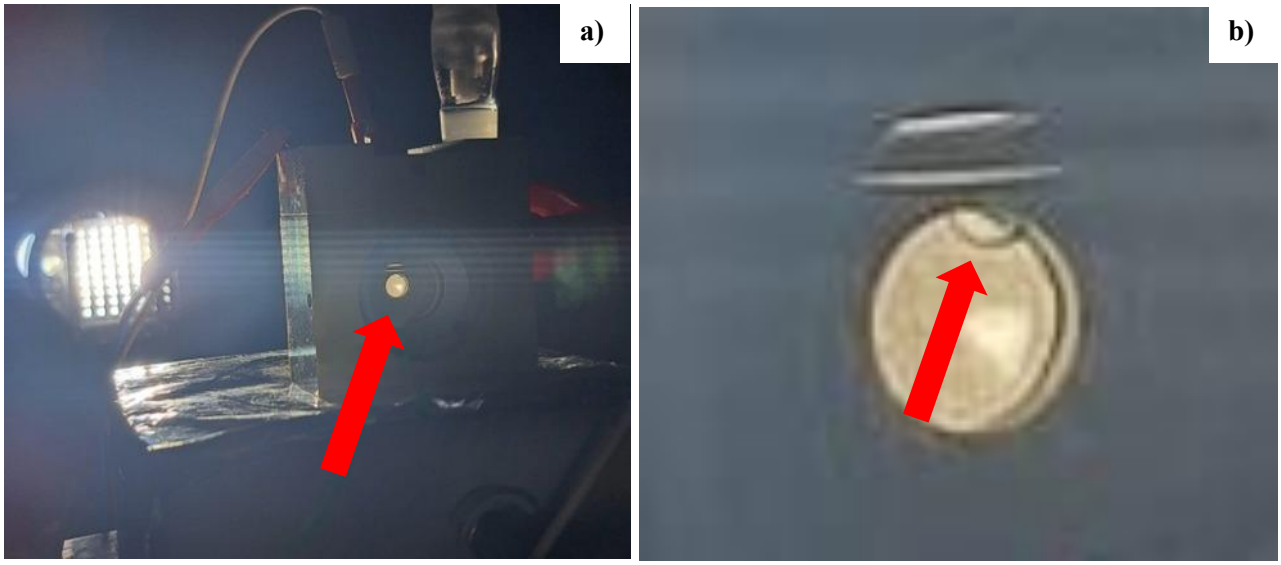

Figure S8. (a) photo of the cappuccino cell during the CA measurement, back illuminated, where is possible to observe the formation of a H_2 bubble in the electrolyte (b) insert zoomed of the cappuccino cell window to better show the bubble.

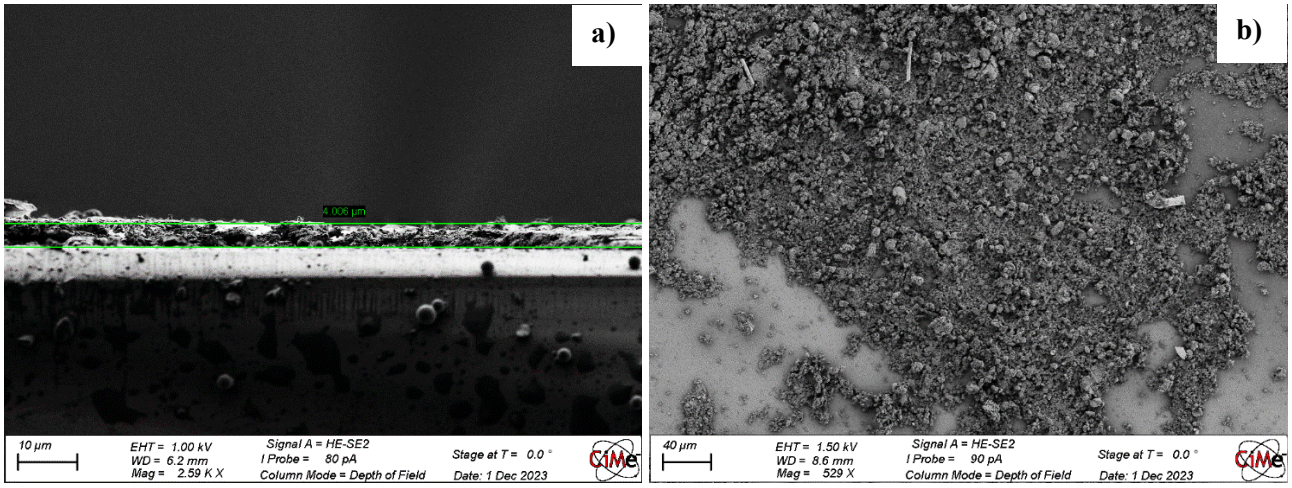

Figure S9. Representative SEM images of the final photocathode configuration FTO-CuSCN-BHJ 1-1-g-C_3N_4 (sc) on top. (a) cross-section with approximately thickness acquisition. (b) general front overview.

Materials and Methods

Materials. Bulk g-C_3N_4 was synthesized from the polymerization of dicyandiamide DCD ($NH_2C(=NH)NHCN$,Aldrich, 99%) as previously reported.[1] Nanosheets morphology g-C_3N_4 has been obtained by the following thermal treatment in air: heating 4°C/min to 500°C, isothermal step for 2 hours followed by cooling to room temperature (10°C/min). PBDB-T was purchased from Ossila. CuSCN (Sigma), PEDOT-PSS (Sigma), PACz (Dyenamo AB). Ethanol and chloroform (Acros).

Hydrogen Photocatalytic Evolution Experiments. The H_2 evolution reaction experiments have been carried out under solar simulator illumination (1500 W Xenon lamp, 300-800 nm) using a Solar Box 1500e (CO.FO.ME.GRA S.r.l., Milan, Italy) set at a power factor 500 W m^{-2}, and equipped with UV outdoor filter made of IR-treated soda lime glass. H_2 evolution experiments were conducted in 10% triethanolamine (TEOA, Aldrich) tri-distilled water solutions irradiated in Pyrex glass containers (25 mL capacity, 20 mL sample). After addition of the catalyst (1 g L^{-1}), the sample was deoxygenated by N_2 bubbling (20 min) to obtain anoxic conditions and irradiated under magnetic stirring for 4 hours. Chloroplatinic acid (H_2PtCl_6, 98% Pt basis) was added as precursor for metallic Pt (Aldrich). Since Pt is *in situ* photodeposited on the catalyst surface, after N_2 bubbling a small volume from a 42 μL^{-1} H_2PtCl_6 aqueous solution was added by a 10-100 µL micropipette to the catalyst suspension (1 g L^{-1}), corresponding to 1% w/w Pt. Each photoreactor was closed with sleeve stopper septa and irradiated, as described in the following, achieving simultaneous Pt deposition and H_2 production. The composite series has been synthesized dissolving a stoichiometric ratio of PBDB-T (Ossila) and g-C_3N_4 exfoliated powder in chlorobenzene (Aldrich) and dried under vigorous stilling at 65 °C overnight. Triplicate photoproduction experiments were done on all samples. The headspace evolved gas was quantified by gas chromatography coupled with thermal conductivity detection (GC-TCD).

Bulk heterojunction photocathode fabrication. The photocathodes were prepared according to literature.[2,3] The BHJ was realized by mixing the nanosheets powder of g-C_3N_4 to the PBDB-T powder, dispersed in chlorobenzene to obtain 10 mg/ml BHJ concentration and stirred overnight at 65°C.

Hole Transport Layer. The three hole transport layer tested in this work have been deposited as reported in literature.[2–4]

Catalyst deposition. The catalysts studied for the system of the present work are Pt and RuO_2. Two deposition method have been followed for the Pt deposition, a photodeposition and a photoelectrodeposition with two different synthetic approaches, galvanostatic and redox reported from literature.[5,6] The RuO_2 is being deposited exploiting the spray coating method as reported in literature.[2]

Layered heterojunction. The layered heterojunction photocathodes labelled 'spin coating' have been prepared according to the literature.[2] For the photocathodes labelled 'drop casting' and 'spray coating' the g-C_3N_4 layer has been deposited from a suspension of g-C_3N_4 nanosheets powder (10mg/ml) in H_2O:EtOH 8:2, ultrasonicated for 30 minutes and immediately sprayed onto the photocathode, 1 ml of suspension for sample. For the 'drop casting' sample 1 ml of the same suspension has been dropped onto the photocathode and dried at 65°C.

Photoelectrochemical measurements (PEC). PEC measurements were performed by potentiostat (SP-200 BioLogic) in a three-electrode configuration. Ag/AgCl (saturated KCl) electrode was employed as reference electrode, and a platinum wire as the conunter electrode. The working electrode has an active area of 0.25 cm^{-2} and 0.1 M H_2SO_4 solution (pH 1) was employed as electrolyte. Simulated 1-Sun illumination (AM 1.5 G, 100 mW cm^{-2}) was provided by a 450 W Muller Electronik Xenon arc lamp and calibrated with silicon photodiode. LSV data were collected at a scan rate of 10 mV^{-1} under ON 1 sec and OFF 2 sec illuminations. The potential was converted to RHE based on the equation $E_{RHE} = E_{Ag/AgCl} + 0.059 \times pH + 0.197$ as reported in literature.[3,7]

References

[1] Pisanu, A. *et al.* Enhanced hydrogen photogeneration by bulk g-C3N4 through a simple and efficient oxidation route. *Dalton Transactions* 47, 6772–6778 (2018).

[2] Mun, S. J. & Park, S. J. Graphitic carbon nitride materials for photocatalytic hydrogen production via water splitting: A short review. *Catalysts* vol. 9 Preprint at https://doi.org/10.3390/catal9100805 (2019).

[3] Corti, M. *et al.* Application of metal halide perovskites as photocatalysts in organic reactions. *Inorganics* vol. 9 Preprint at https://doi.org/10.3390/inorganics9070056 (2021).

[4] Baghdadi, Y. *et al.* Cs3Bi2Br9/g-C3N4 Direct Z-Scheme Heterojunction for Enhanced Photocatalytic Reduction of CO2 to CO. *Chemistry of Materials* 35, 8607–8620 (2023).

[5] Li, C. fan, Guo, R. tang, Zhang, Z. rui, Wu, T. & Pan, W. guo. Converting CO2 into Value-Added Products by Cu2O-Based Catalysts: From Photocatalysis, Electrocatalysis to Photoelectrocatalysis. *Small* Preprint at https://doi.org/10.1002/smll.202207875 (2023).

[6] Zhang, G., Sewell, C. D., Zhang, P., Mi, H. & Lin, Z. Nanostructured photocatalysts for nitrogen fixation. *Nano Energy* vol. 71 Preprint at https://doi.org/10.1016/j.nanoen.2020.104645 (2020).

[7] Mehtab, A., Banerjee, S., Mao, Y. & Ahmad, T. Type-II CuFe2O4/Graphitic Carbon Nitride Heterojunctions for High-Efficiency Photocatalytic and Electrocatalytic Hydrogen Generation. *ACS Appl Mater Interfaces* 14, 44317–44329 (2022).

[8] Zhao, D., Guan, X. & Shen, S. Design of polymeric carbon nitride-based heterojunctions for photocatalytic water splitting: a review. *Environmental Chemistry Letters* vol. 20 3505–3523 Preprint at https://doi.org/10.1007/s10311-022-01429-6 (2022).

[9] Liang, J. *et al.* A review on g-C3N4incorporated with organics for enhanced photocatalytic water splitting. *J Mater Chem A Mater* 9, 12898–12922 (2021).

[10] Romani, L. & Malavasi, L. Solar-Driven Hydrogen Generation by Metal Halide Perovskites: Materials, Approaches, and Mechanistic View. *ACS Omega* vol. 5 25511–25519 Preprint at https://doi.org/10.1021/acsomega.0c03829 (2020).

[11] Tedesco, C. & Malavasi, L. Bismuth-Based Halide Perovskites for Photocatalytic H2 Evolution Application. *Molecules* vol. 28 Preprint at https://doi.org/10.3390/molecules28010339 (2023).

[12] Romani, L. *et al.* PEA2SnBr4: A water-stable lead-free two-dimensional perovskite and demonstration of its use as a co-catalyst in hydrogen photogeneration and organic-dye degradation. *J Mater Chem C Mater* 8, 9189–9194 (2020).

[13] Romani, L. *et al.* Water-Stable DMASnBr3 Lead-Free Perovskite for Effective Solar-Driven Photocatalysis. *Angewandte Chemie - International Edition* 60, 3611–3618 (2021).

[14] Pandey, A., Alam, U., Gupta, A., Shim, J. J. & Verma, N. S-scheme heterojunction-mediated hydrogen production over the graphitic carbon nitride-anchored nickel stannate perovskite. *Fuel* 355, (2024).

[15] Low, J., Yu, J., Jaroniec, M., Wageh, S. & Al-Ghamdi, A. A. Heterojunction Photocatalysts. *Advanced Materials* vol. 29 Preprint at https://doi.org/10.1002/adma.201601694 (2017).

[16] Kosco, J. *et al.* Enhanced photocatalytic hydrogen evolution from organic semiconductor heterojunction nanoparticles. *Nat Mater* 19, 559–565 (2020).

[17] Zhao, D., Guan, X. & Shen, S. Design of polymeric carbon nitride-based heterojunctions for photocatalytic water splitting: a review. *Environmental Chemistry Letters* vol. 20 3505–3523 Preprint at https://doi.org/10.1007/s10311-022-01429-6 (2022).

[18] Murugan, C., Bhojanaa, K. B., Ong, W. J., Jothivenkatachalam, K. & Pandikumar, A. Improving hole mobility with the heterojunction of graphitic carbon nitride and titanium dioxide via soft template process in photoelectrocatalytic water splitting. *Int J Hydrogen Energy* 44, 30885–30898 (2019).

[19] Govindaraju, V. R. *et al.* Graphitic carbon nitride composites as electro catalysts: Applications in energy conversion/storage and sensing system. *Journal of Cleaner Production* vol. 320 Preprint at https://doi.org/10.1016/j.jclepro.2021.128693 (2021).

[20] Mary Rajaitha, P. *et al.* Graphitic carbon nitride nanoplatelets incorporated titania based type-II heterostructure and its enhanced performance in photoelectrocatalytic water splitting. *SN Appl Sci* 2, (2020).

[21] Miao, H. *et al.* A novel strategy to prepare 2D g-C3N4nanosheets and their photoelectrochemical properties. *J Alloys Compd* 690, 669–676 (2017).

[22] Han, Y. Y. *et al.* Metal-Free 2D/2D Heterojunction of Graphitic Carbon Nitride/Graphdiyne for Improving the Hole Mobility of Graphitic Carbon Nitride. *Adv Energy Mater* 8, (2018).

[23] Bao, H., Chen, X., Yuan, R., Zhang, C. & Xu, S. A dual polymer composite of poly(3-hexylthiophene) and poly(3,4-ethylenedioxythiophene) hybrid surface heterojunction with g-C3N4for enhanced photocatalytic hydrogen evolution. *RSC Adv* 11, 32671–32679 (2021).

[24] Ruan, Q., Miao, T., Wang, H. & Tang, J. Insight on Shallow Trap States-Introduced Photocathodic Performance in n-Type Polymer Photocatalysts. *J Am Chem Soc* 142, 2795–2802 (2020).

[25] Li, B. *et al.* Directional Charge Transfer Channels in a Monolithically Integrated Electrode for Photoassisted Overall Water Splitting. *ACS Nano* 17, 3465–3482 (2023).

[26] Cheng, W. H. *et al.* Monolithic Photoelectrochemical Device for Direct Water Splitting with 19% Efficiency. *ACS Energy Lett* 3, 1795–1800 (2018).

[27] Hemmerling, J. R., Mathur, A. & Linic, S. Design Principles for Efficient and Stable Water Splitting Photoelectrocatalysts. *Acc Chem Res* 54, 1992–2002 (2021).

[28] Liu, C., Xiao, C., Xie, C. & Li, W. Flexible organic solar cells: Materials, large-area fabrication techniques and potential applications. *Nano Energy* vol. 89 Preprint at https://doi.org/10.1016/j.nanoen.2021.106399 (2021).

[29] Sun, Y. *et al.* Flexible Organic Solar Cells: Progress and Challenges. *Small Science* vol. 1 Preprint at https://doi.org/10.1002/smsc.202100001 (2021).

[30] Fukuda, K., Yu, K. & Someya, T. The Future of Flexible Organic Solar Cells. *Advanced Energy Materials* vol. 10 Preprint at https://doi.org/10.1002/aenm.202000765 (2020).

[31] Zhang, D., Cho, H. H., Yum, J. H., Mensi, M. & Sivula, K. An Organic Semiconductor Photoelectrochemical Tandem Cell for Solar Water Splitting. *Adv Energy Mater* 12, (2022).

[32] Rojas, H. C. *et al.* All Solution-Processed, Hybrid Organic-Inorganic Photocathode for Hydrogen Evolution. *ACS Omega* 2, 3424–3431 (2017).

[33] Yao, L. *et al.* Establishing Stability in Organic Semiconductor Photocathodes for Solar Hydrogen Production. *J Am Chem Soc* 142, 7795–7802 (2020).

[34] Zheng, Z. *et al.* PBDB-T and its derivatives: A family of polymer donors enables over 17% efficiency in organic photovoltaics. *Materials Today* vol. 35 115–130 Preprint at https://doi.org/10.1016/j.mattod.2019.10.023 (2020).

[35] Speltini, A. *et al.* Rationalization of hydrogen production by bulk g-C3N4: an in-depth correlation between physico-chemical parameters and solar light photocatalysis. *RSC Adv* 8, 39421–39431 (2018).

[36] Caretti, M. *et al.* Transparent Porous Conductive Substrates for Gas-Phase Photoelectrochemical Hydrogen Production. *Advanced Materials* 35, (2023).

[37] Yang, Q. *et al.* Boosting Performance of Non-Fullerene Organic Solar Cells by 2D g-C3N4 Doped PEDOT:PSS. *Adv Funct Mater* 30, (2020).

[38] Liang, J. W. *et al.* Cl2-Doped CuSCN Hole Transport Layer for Organic and Perovskite Solar Cells with Improved Stability. *ACS Energy Lett* 7, 3139–3148 (2022).

[39] McCrory, C. C. L. *et al.* Benchmarking Hydrogen Evolving Reaction and Oxygen Evolving Reaction Electrocatalysts for Solar Water Splitting Devices. *J Am Chem Soc* 137, 4347–4357 (2015).

[40] Choi, J. H. *et al.* Atomic-scale platinum deposition on photocathodes by multiple redox cycles under illumination for enhanced solar-to-hydrogen energy conversion. *J Power Sources* 533, (2022).

[41] Shi, W. *et al.* PTB7:PC61BM Bulk Heterojunction-Based Photocathodes for Efficient Hydrogen Production in Aqueous Solution. *Chemistry of Materials* 31, 1928–1935 (2019).

CHAPTER 6

High Entropy Perovskite Oxides and Graphitic Carbon Nitride Hybrid Heterojunction for Solar Fuel Production

Costanza Tedesco,[a] Luca Betti,[a] Lorenzo Malavasi [a]

[a] *Department of Chemistry and INSTM Pavia, Via Taramelli 12, Pavia, 27100, Italy*

e-mail: costanza.tedesco01@universitadipavia.it

ABSTRACT

Significant efforts have been addressed to modelling novel and advanced nanocomposite materials for solar fuels production. In this respect, photoactive heterojunctions based on graphitic carbon nitride (g-C_3N_4), a versatile organic polymeric semiconductor, are promising system for the photocatalytic hydrogen. A thermal oxidation in air of the g-C_3N_4 bulk phase allows to strongly increase the surface area through an exfoliation of the graphitic sheets and a suitable cocatalyst is required for the optimization of the charge carrier dynamics. In the past years, there has been significant progress in the realization of hybrid heterojunction based on metal-oxides catalyst, thanks to their extremely high carrier density (modified-TiO_2, MoS, CdS) and photoactive organic semiconductor (i.e. g-C_3N_4). This study focuses on the preparation and characterization of heterojunctions based on g-C_3N_4 nanosheets and nanosized High Entropy Perovskite Oxides (HEPOs). This system is suitable for running photocatalytic hydrogen evolution reaction (HER) from water splitting. In this work we investigated a series of $LaFeO_3$ catalysts-based by varying elements in A-site (Ca^{2+}, Sr^{2+}) and B-site (Mn^{3+}, Fe^{3+}, Co^{3+}, Ni^{3+}). The selection of the best candidates for the target reactions has been provided by a chemometric approach, starting with the compositions that showed the highest oxygen non-stoichiometry, since these types of defects are potential active sites for redox reaction. Some of the main results suggest that O-vacancy presents in HEPOs plays a key role as well as the high carrier density influences the charge carrier dynamics of the photocatalyst system for the solar fuels evolution reactions. We found that $La_{0.6}Ca_{0.4}(MnFeCoNi)_{0.25}O_{3-\delta}$ perovskite was the most photocatalytic active phase among all those we investigated and that a small amount of perovskite in the heterojunction is sufficient to double the hydrogen evolution rate produced by g-C_3N_4, proving that 2.5% of $La_{0.6}Ca_{0.4}(MnFeCoNi)_{0.25}O_{3-\delta}$/g-$C_3N_4$ heterojunction can produce 450 μmol g^{-1} h^{-1} of hydrogen.

1. INTRODUCTION

The global demand for sustainable and renewable energy sources has drove significant research into alternative methods of hydrogen production, especially as hydrogen is a clean energy carrier that holds immense promise for reducing greenhouse gas emissions. Among the methods developed, photocatalytic water splitting, driven by solar energy, is one of the most promising approaches. Central to this technology is the development of efficient, stable, and cost-effective photocatalysts capable of driving hydrogen evolution from water media under visible light. In recent years, high entropy perovskite oxides (HEPOs) have emerged as a new class of materials that hold immense potential in photocatalysis due to their unique structural, compositional, and electronic properties.[1] High entropy perovskites (HEPs) are derived from traditional perovskite structures but are composed of multiple, typically five or more, metal cations within a single lattice. Traditional perovskites typically have a simple chemical composition with one or two cations and anions, with general formula ABX_3, where A and B are cations and X is an anion, often oxygen.[1,2] The compositional diversity of HEPs confers a high degree of configurational entropy, which stabilizes the perovskite structure and introduces various active sites for catalytic processes. Additionally, the synergy between different metal ions in HEPs allows for tunable electronic and optical properties, which is critical for optimizing light absorption and charge carrier dynamics in photocatalysis. Recent advances have demonstrated that HEPOs can be engineered to exhibit desirable band structures and defect properties, making them highly promising for photocatalytic hydrogen evolution.[1–3]

Since the discovery of high-entropy materials, research has increasingly focused on examining a wide array of compositions to identify the most efficient candidates for various applications. These materials, widely utilized in the fields of alloys, oxides, and perovskites, offer exceptional tunability through their diverse chemical compositions. The core concept behind high-entropy stabilization lies in combining multiple cations, often five or more, within a single solid solution in equimolar proportions. This approach generally leads to the formation of a stable, single-phase structure, mitigating the typical phase separation issues that arise in systems with high doping levels. Unlike traditional materials, which tend toward phase separation, high-entropy compounds allow the creation of single-phase structures in central regions of complex phase diagrams that are usually unexplored in conventional studies. Their stability is enhanced by configurational entropy, making them more resistant at higher temperatures.[4] This unique stabilization strategy has facilitated the creation of

materials with varied crystal structures, in addition to the already mentioned perovskites, rock salt, fluorite, and spinels, demonstrating the adaptability and effectiveness of the high-entropy approach in stabilizing materials with novel properties. Studies of generic high-entropy oxides (HEOs) have established that configurational entropy plays a significant role in determining the Gibbs free energy of formation. This entropy component offsets positive enthalpic contributions, underscoring the crucial role of configurational entropy in the stability of these materials. In systems with an increasing number of elements in equimolar amounts, the configurational entropy reaches a peak, enabling unique structural outcomes and fine-tuning of functional properties. This equimolar distribution of diverse elements fosters an environment in which configurational entropy and elemental composition interact, contributing to both stability and distinct material properties. Most investigations into high-entropy materials have relied on computational methods or machine learning to interpolate chemistries, predict structures, and assess performance across a broad range of compositions.[2,4] However, these methods often focus on equimolar compositions with a high number of cations, overlooking the feedback from experimental validations and missing insights into the synergies between cations. Here the identification of the most suitable candidates for the target reaction was achieved through a chemometric approach. This process began with the compositions exhibiting the highest levels of oxygen non-stoichiometry, as such defects are likely to serve as active sites for redox reactions.[2] Using this as a starting point, we focused on the study of high entropy perovskites phases obtained trought the systematic modulation of $LaFeO_3$ phase, with B sites tailored by combinations of Mn, Fe, Co, Ni and with A sites doped with bivalent cation, like Ca and Sr, to explore the impact of specific cations (beyond equimolar mixtures) on phase composition, structural geometry, and oxygen non-stoichiometry.[2,4]

The use of heterojunctions in HEPO-based photocatalytic systems has shown further potential in overcoming some of the limitations of single-component photocatalysts, such as rapid recombination of photogenerated charge carriers. By forming a heterojunction between HEPOs and other semiconductors, it is possible to create an internal electric field at the interface, promoting effective charge separation and enhancing photocatalytic efficiency.[5,6] Recently, several Z-scheme and type II heterojunction based on oxide perovskite (OPs) like $LaFeO_3$ and $SrTiO_3$ have been reported for photocatalytic hydrogen evolution reaction.[7,8] The elected semiconductor partner, in the field of green photocatalyst, is in most cases graphitic carbon nitride, g-C_3N_4. Graphitic carbon nitride is an organic semiconductor polymer that gained extreme interest due to a good absorption in the visible

range (band gap 2.7 eV), atoxicity and ecocompatibility, outstanding stability in acidic and basic media and ease synthetization from cheap precursors.[9] In OPs/g-C_3N_4 heterojunctions, usually the photogenerated electrons start from the perovskite and migrate to the g-C_3N_4, where the most density of active site for photocatalytic hydrogen evolution are present, while the hole make an opposite journey, from g-C_3N_4 to the OPs.[1,5] In this study, we investigate heterojunction system based on a series of nanosized high entropy perovskites obtained starting from $LaFeO_3$, with specific tailoring onto the B site (Co, Ni, Mn) aimed to gain redox advantage properties in addition to a controlled A-site doping (Ca and Sr) synthetized trought spray pyrolysis method, in heterostructure with nano-exfoliated graphitic carbon nitride for photocatalytic hydrogen evolution, with a focus on evaluating its structural, optical, and photocatalytic properties under visible light. The main objective of the study is to correlate the introduction of high entropy redox conditions togheter with controlled A-site doping, that is known to increase the natural oxygen-vacancies density in the perovskite phase, to the photocatalytic performances. On one hand, is established that high entropy conditions increase the redox activity of the catalyst and on the other hand, oxygen vacancies are known to be active sites for photocatalytic reactions, so in this perspective the proposed heterojunction has as its main purpose the optimization of the photocatalytic water splitting performances of bare g-C_3N_4.[2] We found that $La_{0.6}Ca_{0.4}(MnFeCoNi)_{0.25}O_{3-\delta}$ perovskite was the most photocatalytic active phase among all those we investigated and that a small amount of perovskite in the heterojunction is sufficient to double the hydrogen evolution rate produced by g-C_3N_4, proving that 2.5% of $La_{0.6}Ca_{0.4}(MnFeCoNi)_{0.25}O_{3-\delta}$/g-$C_3N_4$ heterojunction can produce 450 μmol g^{-1} h^{-1} of hydrogen. The exploitation of OPs-based heterojunction for hydrogen photogeneration is now quite well established, in the present work is presented the correlation between the enhanced redox properties and oxygen-vacancy density of doped-HEOPs, in heterojunction with g-C_3N_4, and the photocatalytic performances for green hydrogen evolution reaction.

2. RESULTS AND DISCUSSION

The $La_{1-x}M_x(MnFeCoNi)_{0.25}O_3$/g-$C_3N_4$ systems have been synthesized according to the experimental procedure in the Supplementary Information (SI). The HEPs phases elected for the investigation are $LaFeO_3$, $La(MnFeCoNi)_{0.25}O_{3-\delta}$, $La_{0.6}Ca_{0.4}FeO_{3-\delta}$, $La_{0.6}Ca_{0.4}(MnFeCoNi)_{0.25}O_{3-\delta}$, $La_{0.6}Sr_{0.4}(MnFeCoNi)_{0.25}O_{3-\delta}$ and the weight ratio investigated between $La_{1-x}M_x(MnFeCoNi)_{0.25}O_3$ and g-C_3N_4 nanosheets are 2.5, 5, 10 (wt% of perovskite).

The stoichiometry of the perovskite samples was confirmed through XRF, while the crystal structure and crystallographic characteristics were determined using Rietveld refinement. The oxygen non-stoichiometry (δ) for sample $LaFeO_{3-\delta}$ was derived from a previous chemometric study, whereas for the other samples, it was calculated to maintain electroneutrality.[2]

Figure 1a presents the diffractograms of the synthesized high entropy nanometric perovskite oxides. No impurities were detected in any of the synthesized samples, and the peak positions correspond to the Pnma space group, indicating that all the samples share the same orthorhombic crystal structure. From the peak broadening, the average size of coherent diffraction domains can be estimated using the Scherrer equation (see SI, equation 1). In this case, the average size of the coherent diffraction domains is approximately 10 nm. The size of the aggregated material particles was observed using SEM analysis (Figure 1 b).

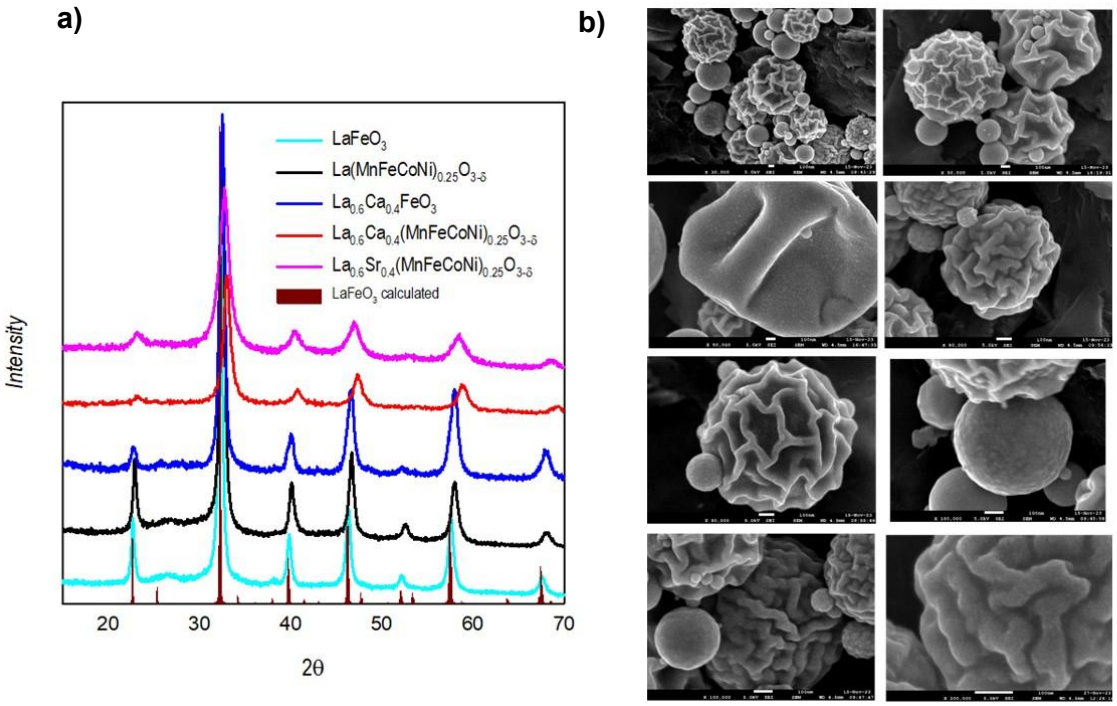

Figure 1. a) XRD pattern of selected perovskites for the heterojunction. b) SEM images of $LaFeO_{3-\delta}$.

Figure 2 reports the results in terms of hydrogen evolution rates for the three-heterojunction series realized with the perovskites phases elected. In figure 2a are reported the photocatalytic performances results for the 2.5 (wt%) of the selected perovskites/g-C_3N_4 heterojunctions, in figure 2b the results for the 5 (wt%), and in figure 2c the results for the 10 (wt%).

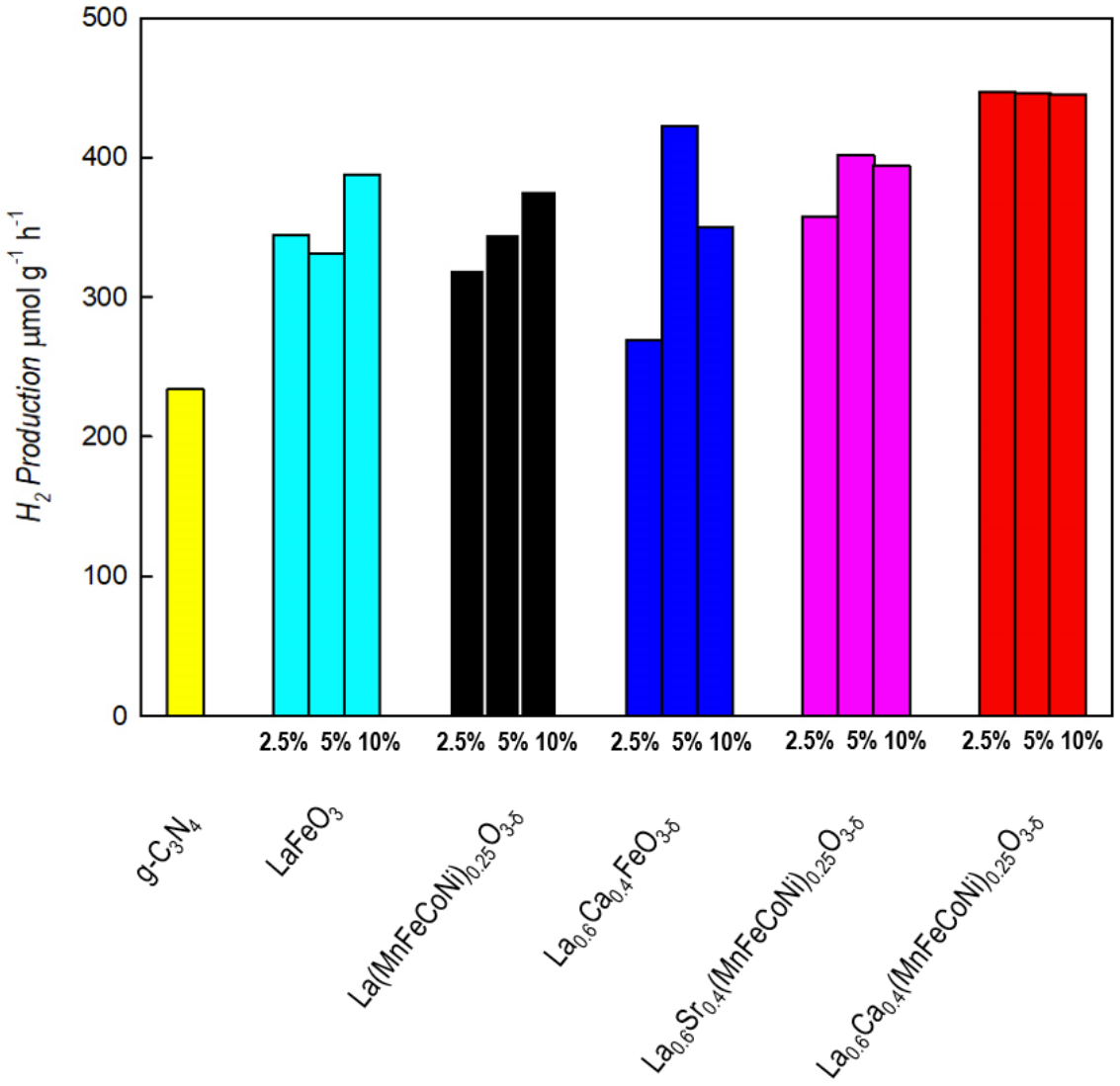

Figure 2. Hydrogen productions as a function of the perovskite phase (2.5, 5, 10 wt%) in composite with g-C_3N_4. (n=3, simulated solar light, 500 W m^{-2}).

From the results reported in figure 2 is interesting to notice how all the investigated perovskites give a boost in terms of hydrogen production rate compared to the bare g-C_3N_4 but, at the same time, the introduction of the high entropy conditions and the doping with Ca and Sr onto the La site do not give a linear response in terms of photocatalytic performances compared with the bare $LaFeO_3$. Moreover, by comparing the barchart reported in figure 2 is possible to notice how incoherent are the effects of hydrogen evolution reaction of the

photocatalyst by changing the weight ratio (wt%) of perovskite in the heterojunction. Among the investigated systems, only one heterojunction serie maintained in all the weight ratio of $La_{1-x}M_x(MnFeCoNi)_{0.25}O_3/g\text{-}C_3N_4$ an higher hydrogen production rate compared to the control $LaFeO_3/g\text{-}C_3N_4$: $La_{0.6}Ca_{0.4}(MnFeCoNi)_{0.25}O_{3-\delta}/g\text{-}C_3N_4$. This heterojunction system, on one hand, produces a sensible higher amount of hydrogen already at low loading of perovskite (2.5 wt%) reaching 450 μmol g^{-1} h^{-1}, and on the other hand because this high rate of hydrogen production does not change by increasing the perovskite loading until 10%, resulting in an important optimization of the photocatalytic performances of the $g\text{-}C_3N_4$ by exploiting a low amount of perovskite. In figure 3a and 3b are reported the $La_{0.6}Ca_{0.4}(MnFeCoNi)_{0.25}O_{3-\delta}/g\text{-}C_3N_4$ the room temperature X-ray diffraction patterns and the corresponding UV-Vis spectra of the complete heterojunction system, synthetized and investigated to study the hydrogen production rate at higher loading of 10 wt% of perovskite. Weight ratios investigated between $La_{0.6}Ca_{0.4}(MnFeCoNi)_{0.25}O_{3-\delta}$ and $g\text{-}C_3N_4$ nanosheets are (wt% of perovskite) 0, 1, 2.5, 5, 7.5, 10, 15, 25, 50, 75, and 100 and the results in terms of hydrogen evolution reaction are reported in figure 3c. From the XRD pattern are evident the main peaks of the perovskite also at very low loading of perovskite in the heterojunction, proving a high stability of the perovskite phase during the formation of the composites. Instead, from UV-Vis spectra are possible to notice how by increasing the perovskite phase in the heterojunction the absorption peaks decrease, leading to a flat shoulder for the pure perovskite that presents a narrow band gap (approximately 1.2 eV) and the main optical activity in the IR-range spectrum. From the results of hydrogen evolution reaction is possible to observe the gradual drop in amount for hydrogen production rate at higher loading of 10% of perovskite in the composite, still higher than the pure $g\text{-}C_3N_4$ until 25% of loading of perovskite. On these results, we can conclude that $La_{0.6}Ca_{0.4}(MnFeCoNi)_{0.25}O_{3-\delta}$ represents a promising and efficient co-catalyst for boost the photocatalytic performances of $g\text{-}C_3N_4$ since already a low amount of perovskite (2.5 wt%) is able to double the hydrogen evolved by bare $g\text{-}C_3N_4$.

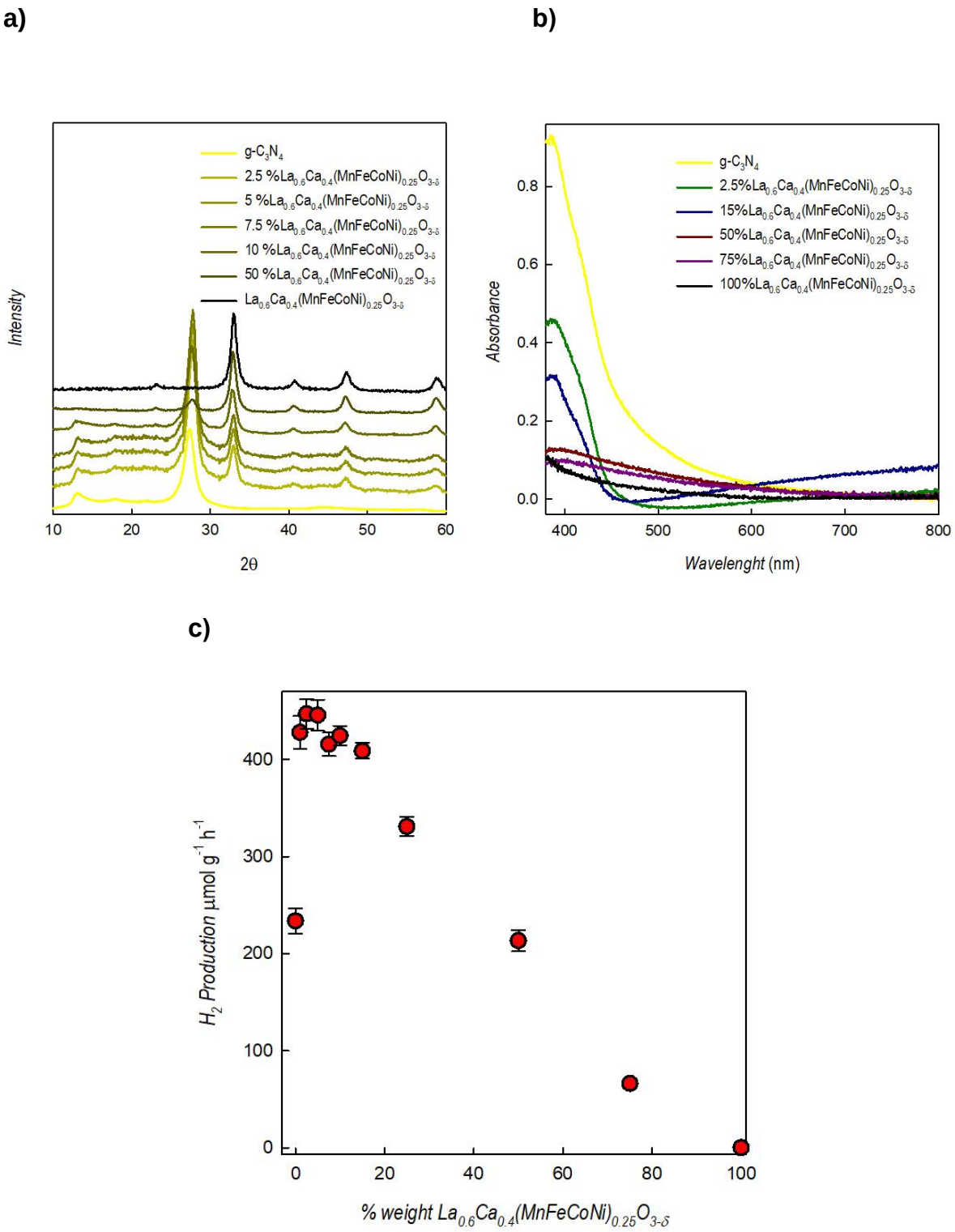

Figure 3. a) XRD pattern of selected $La_{0.6}Ca_{0.4}(MnFeCoNi)_{0.25}O_{3-\delta}$/g-$C_3N_4$ composites; b) Absorption spectra of selected $La_{0.6}Ca_{0.4}(MnFeCoNi)_{0.25}O_{3-\delta}$/g-$C_3N_4$ composites; c) hydrogen productions as a function of $La_{0.6}Ca_{0.4}(MnFeCoNi)_{0.25}O_{3-\delta}$ wt% in the composites. (n=3, simulated solar light, 500 W m^{-2}).Also, the stability of the best performing composite has been investigated and in figure 4a and b are reported the XRD pattern for the pre and post catalysis sample and the hydrogen evolution rate retention of this sample after one cycle of photocatalytic reaction.

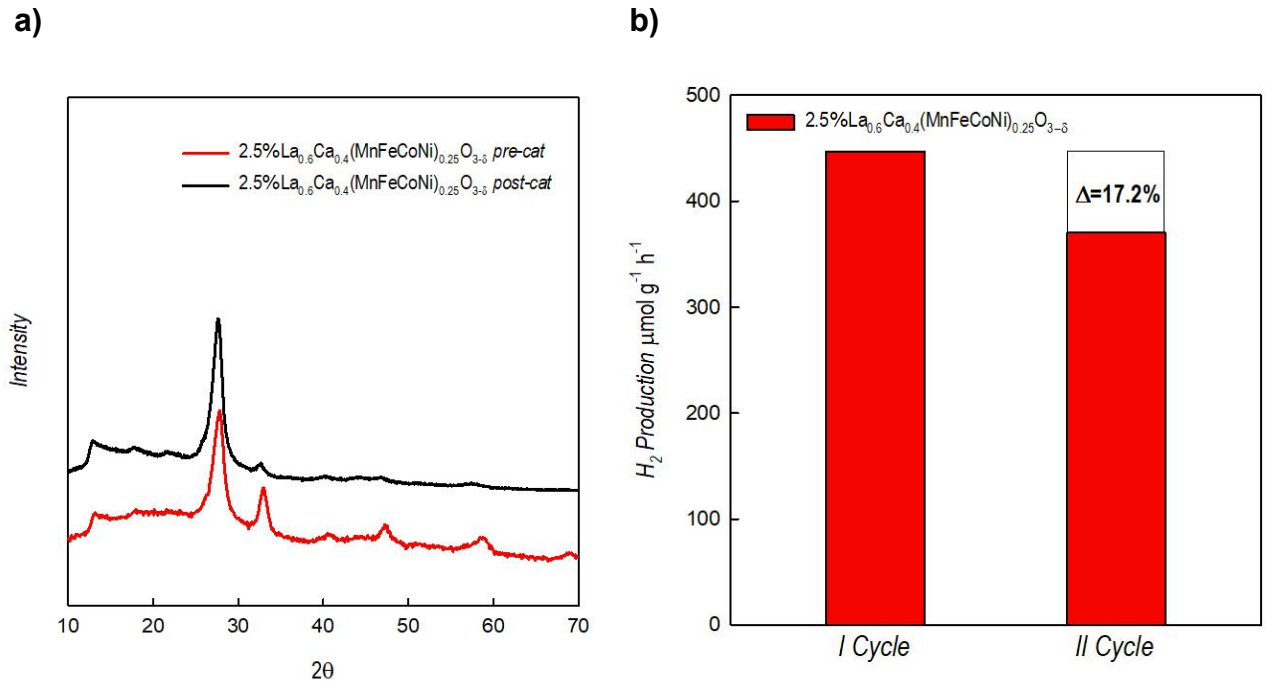

Figure 4. a) XRD pattern of the best performing sample, 2.5% $La_{0.6}Ca_{0.4}(MnFeCoNi)_{0.25}O_{3-\delta}/g\text{-}C_3N_4$ *pre* and *post* photocatalysis. b) Cyclability test of 2.5% $La_{0.6}Ca_{0.4}(MnFeCoNi)_{0.25}O_{3-\delta}/g\text{-}C_3N_4$.

From the XRD pattern reported in figure 4a is possible to confirm the stability of the elected heterojunction since in the post-catalysis pattern are still visible the main crystallographic peaks of the $La_{0.6}Ca_{0.4}(MnFeCoNi)_{0.25}O_{3-\delta}$ and from the cyclability results is possible to notice a drop-in hydrogen evolution rate after one photocatalytic cycle. This drop between the first and the second cycle can be justified by the extreme difficulties faced during the collection phase of the photocatalytic powder that needs to be optimized.

4. CONCLUSIONS

Nano-$La_{1-x}M_x(MnFeCoNi)_{0.25}O_3$/g-$C_3N_4$ heterojunctions have been investigated for hydrogen photogeneration reaction. Five perovskites phases have been synthesized with a spray-pyrolysis approach; $LaFeO_3$, $La(MnFeCoNi)_{0.25}O_{3-\delta}$, $La_{0.6}Ca_{0.4}FeO_{3-\delta}$, $La_{0.6}Ca_{0.4}(MnFeCoNi)_{0.25}O_{3-\delta}$, $La_{0.6}Sr_{0.4}(MnFeCoNi)_{0.25}O_{3-\delta}$, all combined in heterojunction with nano-sheets g-C_3N_4. Starting from the control $LaFeO_3$, was possible to study the effect of the high entropy properties reached through the introduction of Mn, Co and Ni onto the Fe-site and of the increased vacancies density reached trought the doping with divalent Ca and Sr onto the La-site for the photocatalytic hydrogen evolution performances of the obtained heterojunction. The main objective of the present study was to enhance the photocatalytic performances of g-C_3N_4, that due to its ecofriendly nature, remains the main interesting photocatalyst for green energetic purposes. From the preliminary results, where all the perovskite phases, in composite g-C_3N_4 at three different loading of perovskite (2.5,5,10 wt%), was not possible to identify a linear trend in terms of photocatalytic performance by both high entropy properties and doping, and by increasing the wt% loading of the perovskites in the heterojunction. Only one perovskites phase showed for the three weight ratio of $La_{1-x}M_x(MnFeCoNi)_{0.25}O_3$/g-$C_3N_4$ remarkable higher hydrogen evolution rate compared to the bare g-C_3N_4; the $La_{0.6}Ca_{0.4}(MnFeCoNi)_{0.25}O_{3-\delta}$. The introduction of Mn, Co and Ni onto the Fe-site lead to an hight entropy phase that from one hand makes the photocatalyst more stable and on the other hand enhances the redox activity of the perovskite leading to a more suitable photocatalyst for the target reaction. Moreover, as previously reported from Betti. L, A, *et al.* in 2024, this specific perovskite, $La_{0.6}Ca_{0.4}(MnFeCoNi)_{0.25}O_{3-\delta}$, among all those studied was proved to present the highest oxygen vacancies density and this can justify the increased photocatalytic performances, since it is well established how vacancies and defects play a central role in the photocatalytic reaction, in particular in hydrogen evolution reaction from water splitting.

SUPPLEMENTARY INFORMATION

In Figure 1a of the main text are reported the diffractograms of the nanostructured high entropy perovskites phases synthesized. From the peak width, it is possible to determine the average size of the coherent diffraction domains using the Scherrer equation (1).

1) $$\tau = \frac{K\lambda}{\beta cos\theta}$$

Where:

- τ represents the average size of coherent diffraction domains, providing an indication of grain size;
- K is a dimensionless shape factor, typically with a value of 0.9;
- λ is the wavelength of the incident radiation, in this case, Cu Kα with a value of 1.54 Å;
- β is the full width at half maximum (FWHM) of the peaks;
- cos θ is the cosine of the angle at which the reference peak appears.

Equation (1), used to calculate the average size of coherent diffraction domains (τ), is crucial for understanding the dimensions of the ordered domains within the material.

The average size of coherent diffraction domains is related to the size of small ordered regions within the crystalline material. Calculating this provides insights into the size of the crystals or ordered domains within the crystal structure. Variations in τ can indicate differences in crystal size or atomic-level ordering. This analysis is valuable for understanding how different cationic compositions influence the material's crystal structure, providing details on the coherence and size of ordered regions, which are essential for correlating the crystal structure with the material's macroscopic properties.

Structural and Optical Characterizations

The crystalline structure of the samples was analysed at room temperature using the XRD (X-Ray Diffraction) technique with Cu Kα radiation on a Bruker D2 diffractometer. The diffraction experiments were conducted in Bragg-Brentano flat-plate mode. Crystalline

structure information was obtained using the Rietveld method, performed with the FullProf software.

For microstructural characterization, a high-resolution scanning electron microscope (SEM, TESCAN Mira 3) operating at 20 kV was employed.

The stoichiometry of the samples was determined through X-ray fluorescence spectroscopy (XRF), conducted with the AXIOS spectrometer (Panalytical), equipped with an X-ray tube with a rhodium anode and a maximum power of 2.4 kW. The spectrometer's wavelength dispersion system used five crystals (LiF (200), Ge (111), PE (002), PX1, and LiF (220)), automatically selected during measurements. The characteristic X-rays induced in the sample were diffracted on one of the crystals and measured by a scintillation detector. Measurements were carried out in helium. Quantitative analysis of the spectra was performed using the PANalytical Omnian analytical program. The Omnian package is available for standardless analysis of all sample types. It includes advanced algorithms designed to address known limitations inherent to XRF spectroscopy, including spectral interferences.

Absorption spectra were acquired over a wavelength range of 300–800 nm directly from the powders using a Jasco V-750 spectrophotometer equipped with an integrating sphere (Jasco ISV-922). Since the powders appear black, with a very narrow band gap and absorption in the UV-Vis-NIR range, further characterization was performed using a Cary 5000 UV-Vis-NIR spectrophotometer.

Micro-Raman measurements were carried out at room temperature using the automated and integrated XploRA Plus confocal spectrometer (HORIBA Scientific), equipped with an Olympus BX43 microscope. Three different laser sources are available: 532 nm (100 mW), 638 nm (90 mW), and 785 nm (100 mW). Neutral density filters with varying optical densities allow the adjustment of the incident laser power. The spectrometer is equipped with a motorized XY stage for sample placement. The spectral resolution is approximately 1 cm^{-1}. A Peltier-cooled multistage air-cooled camera is used as the detector.

Synthesis of Bulk g-C_3N_4 and g-C_3N_4 Nanosheets

Bulk g-C_3N_4 was synthesized through the polymerization of DCD (dicyandiamide, $NH_2C(=NH)NHCN$, Aldrich, 99%) using the following thermal treatment under an N_2 flow: heating at a rate of 1°C/min to 550°C, maintaining an isothermal phase for 4 hours, followed by cooling to room temperature at a rate of 10°C/min.

The nanosheet form of g-C_3N_4 was obtained by thermally treating the bulk phase in air: heating at a rate of 1°C/min to 500°C, holding an isothermal phase for 2 hours, and then cooling to room temperature at a rate of 10°C/min. This thermal treatment induces exfoliation of the graphitic planes of g-C_3N_4, leading to an increase in surface area, as well as an increase in surface defects and nitrogen vacancies. These features enhance the material's performance in photocatalytic water splitting for hydrogen production.

Synthesis and Characterization of Mixed Nanoscale Perovskite Oxides

The perovskite oxides were synthesized via spray pyrolysis. This technique involves the nebulization of a solution of precursor cation nitrates, in precise concentrations and stoichiometric proportions. The aerosol is then passed through a high-temperature chamber (1000°C) where oxidation occurs, resulting in the formation of the perovskite oxide, which is finally deposited and collected on a filter.

The precursors were purchased from Sigma-Aldrich: $La(NO_3)_3 \cdot 6H_2O$ (99.999%), $Mn(NO_3)_2 \cdot 4H_2O$ (99.99%), $Fe(NO_3)_3 \cdot 9H_2O$ (99.95%), $Co(NO_3)_2 \cdot 6H_2O$ (99.999%), and $Ni(NO_3)_2 \cdot 6H_2O$ (99.999%), $SrCO_3$ (99.9%), $CaCO_3$ (99.9%).

Initially, the precursor salts were weighed into a vial and dissolved in 10 mL of distilled H_2O. The solution was placed in a nebulizer, which generated an aerosol at the entrance of a quartz tube. This tube, placed inside a furnace set at 1000°C, connected at one end to the nebulizer and at the other to a condenser. The condenser, cooled to a temperature between 5–10°C, was connected to a Büchner funnel attached to a vacuum pump that created a pressure drop within the spray pyrolysis apparatus. The powder deposited on the filter was dried in an oven at 60°C for 2 hours. The powder was then collected, with a yield of 80–90% for the entire process, the full process is outlined in fig SI 1. The reaction kinetics did not allow for crystal growth, and as will be further detailed, the resulting crystals reached nanoscale dimensions.

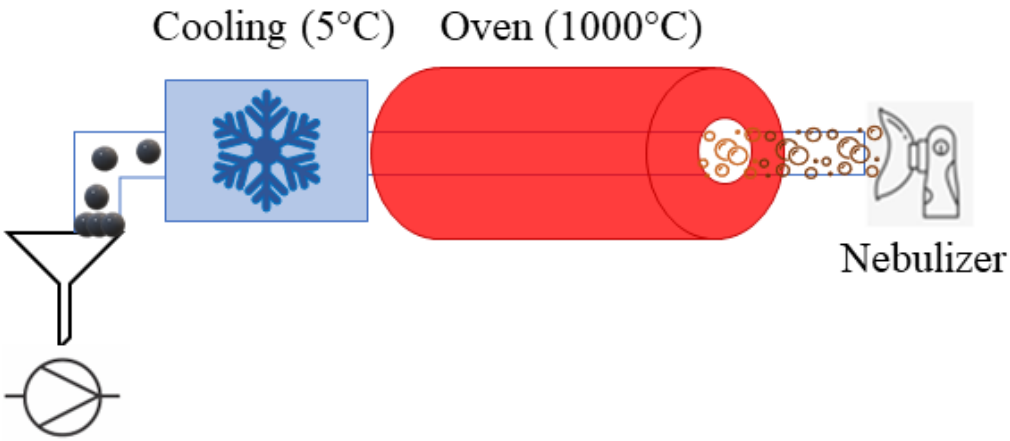

Figure SI 1. Schematic illustration of Spray-Pyrolysis synthesis.

Synthesis of heterojunctions

The $La_{1-x}M_x(MnFeCoNi)_{0.25}O_3/g\text{-}C_3N_4$ composites are prepared by suspending the appropriate stoichiometric amounts of perovskite and $g\text{-}C_3N_4$ separately in N,N-Dimethylformamide (Alfa Aesar 99.7%) solutions. The suspensions are sonicated for 4 minutes, then mixed and sonicated and placed on a heating plate (65°C) under vigorous stirring until a dry powder is obtained.

Hydrogen evolution reaction experiment *in suspension* set up

Hydrogen production experiments were conducted using Pyrex glass containers (25 mL) containing 20 mL of a 10% (v/v) aqueous solution of triethanolamine (Aldrich, 99%) and 20 mg of photocatalyst at a ratio of 1 g of catalyst per 1 mL of solution. To remove oxygen from the solution, argon was bubbled through for 20 minutes. Before sealing the glass containers, 34 µL of a 0.032 M H_2PtCl_6 solution in H_2O (chloroplatinic acid, 38% Pt, Sigma Aldrich) was added, providing a weight percentage of 1% Pt relative to the weight of the catalyst used.

During the irradiation experiment, the platinum (IV) in solution was photo-reduced onto the catalyst surface, facilitating charge separation in the semiconductor and acting as an efficient electron transport pathway to the surface, where the water reduction reaction to hydrogen occurs. The glass container was hermetically sealed with a rubber septum.

Irradiation was carried out using simulated sunlight (1500 W xenon lamp, 300–800 nm) with a Solar Box 1500e (CO.FO.ME.GRA S.r.l.) at 500 W/m^2 for 4 or 6 hours. The hydrogen production rate was expressed in micromoles per gram of catalyst per hour of irradiation (μmol g^{-1} h^{-1}). Hydrogen was measured using gas chromatography with a GC Trace 1600 ThermoFisher instrument. The gas chromatograph was operated in split mode, with a Flame Ionization Detector (FID), helium as the carrier gas, and a 30 m × 0.53 mm capillary column. Finally, the hydrogen quantity was determined through external calibration.

The first-author Costanza Tedesco, author of the present Ph.D. work, carried out the heterojunction synthesis and characterization and the quantification of photocatalytic H_2 produced.

The present work is in preparation for publication in collaboration with Luca Betti.

References

[1] J. Ma, T. Liu, W. Ye, Q. He, K. Chen, *Journal of Energy Storage* 2024, *90*, 111890.

[2] L. A. Betti, L. R. Magnaghi, A. Bosetti, R. Biesuz, L. Malavasi, *J. Mater. Chem. C* 2024, *12*, 7695.

[3] J. Ma, K. Chen, C. Li, X. Zhang, L. An, *Ceramics International* 2021, *47*, 24348.

[4] M. Fracchia, M. Coduri, P. Ghigna, U. Anselmi-Tamburini, *Journal of the European Ceramic Society* 2024, *44*, 585.

[5] K. Afroz, M. Moniruddin, N. Bakranov, S. Kudaibergenov, N. Nuraje, *J. Mater. Chem. A* 2018, *6*, 21696.

[6] S. Das, S. Kumar, S. Sarkar, D. Pradhan, C. S. Tiwary, S. Chowdhury, *J. Mater. Chem. A* 2024, *12*, 16815.

[7] A. Mishra, N. Priyadarshini, S. Mansingh, K. Parida, *Advances in Colloid and Interface Science* 2024, *333*, 103300.

[8] T. N. Q. Trang, M. Tran Van, T. B. Phan, V. T. H. Thu, *ACS Appl. Energy Mater.* 2021, *4*, 8910.

[9] S. J. Mun, S.-J. Park, *Catalysts* 2019, *9*, 805.

CHAPTER 7

CONCLUSIONS AND OUTLOOKS

In the light of the results emerged from the previous chapters, the exploration of carefully engineered heterojunction systems for photocatalytic green hydrogen and ammonia evolution has proven to be a compelling strategy for addressing the global energy and environmental challenges. This Ph.D. thesis has demonstrated, across four different heterostructured systems, the deliberated design and optimization of material interfaces, electron transfer mechanism, and morphology consistently enhance photocatalytic performance. The experimental results indicate that heterojunction engineering and morphology control not only facilitates efficient charge separation and transfer but also significantly suppresses recombination, a critical bottleneck for graphitic carbon nitride charge carrier, that is the main eco-friendly and non-critical raw material based photocatalyst investigated in the present work but also for most of the photocatalysts investigated nowadays.

Chapter 2, “Synthesis of Carbon Nitride Polymorphs by Sacrificial Template Method: Correlation between Physicochemical Properties and Photocatalytic Performance”, was dedicated to the study of the importance of morphology over the photocatalytic performances of the photocatalyst. Different carbon nitride compounds (CNCs) were synthesized using melamine (MLM) and various molar ratios of NaCl, KCl, and $CaCl_2$ as sacrificial templates, each influencing the CNCs' morphological, optical, and structural properties. It was proved how NaCl and $CaCl_2$ promoted the formation of exfoliated g-C_3N_4, while KCl led to poly(heptazine imide). Higher MClx:MLM ratios enhanced exfoliation across all samples. From optical characterization were revealed shifts in absorption thresholds, with NaCl and KCl causing slight red shifts while $CaCl_2$ induced a small blue shift. Photoluminescence decay was reduced in all cases, with EPR and FTIR analyses suggesting the formation of vacancies or cyano groups critical for improved photocatalytic H_2 production. The highest H_2 evolution rates were achieved using $CaCl_2$ (7657 μmol g^{-1} h^{-1}), attributed to enhanced porosity and surface area. This study highlighted the potential of CNCs as cost-effective, efficient photocatalysts for solar-driven H_2 production, with future work focused on scaling sustainable green hydrogen applications.

Chapter 3, "Reaction Mechanism of Hydrogen Generation and Nitrogen Fixation at Carbon Nitride/Double Perovskite Heterojunctions", investigated $Cs_2AgBiCl_6$/g-C_3N_4 complete heterojunctions series for hydrogen photogeneration (HER) and nitrogen reduction to ammonia (NRR), using advanced spectroscopy and computational modeling to elucidate reaction mechanisms. Transient absorption spectroscopy (TAS) revealed that high $Cs_2AgBiCl_6$ content optimizes HER by confining optical excitations to $Cs_2AgBiCl_6$, where the reaction occurs. On the other hand, low $Cs_2AgBiCl_6$ content enhances g-C_3N_4 activity, favouring ammonia production as active sites are confined to carbon nitride. Moreover, Density Functional Theory (DFT) calculations identified chloride vacancies (V_{Cl}) in $Cs_2AgBiCl_6$ as active sites for HER. The heterojunction enhances charge carrier lifetime and suppresses self-trapped excitons (STE) in $Cs_2AgBiCl_6$, but excessive g-C_3N_4 reduces HER efficiency by passivating V_{Cl}. For the Nitrogen Photofixation reaction, nitrogen vacancies in g-C_3N_4 were found to be the key active sites. While $Cs_2AgBiCl_6$ improves light absorption and charge transfer, excessive amounts reduce ammonia production by diverting charge carriers to perovskite sites. The study highlighted how heterostructure composition determines the balance between HER and NRR, with tailored designs promoting specific reactions, in summary the research provided a comprehensive understanding of the role of heterojunction composition in optimizing photocatalytic performance for hydrogen and ammonia production.

Chapter 4, "Compositional and Defect Engineering of Metal Halide Perovskite-based Heterojunctions for Efficient Nitrogen Photofixation Under Solar Light", introduced a novel Cs_2SnBr_6/g-C_3N_4 heterojunction for efficient nitrogen photofixation, achieving an impressive ammonia production rate of 266 μmol g^{-1} h^{-1} without the use of noble metal co-catalysts. The highest performance was observed at 35 wt% Cs_2SnBr_6 / 65 wt% g-C_3N_4, demonstrating a strong synergistic effect between the two semiconductors where the nitrogen vacancies in g-C_3N_4 nanosheets serve as primary active sites for nitrogen reduction, facilitated by effective charge transfer from Cs_2SnBr_6 through a type-II heterojunction. Furthermore, this vacancy-ordered double perovskite enhances photocatalytic efficiency through the lack of self-trapped electrons, promoting charge separation (confirmed by photoluminescence and modeling) and through bromide vacancies, which introduce additional reactive sites. The study demonstrated the versatility of metal halide perovskites (MHPs) in nitrogen photofixation, complementing their roles in hydrogen generation and CO_2 reduction. It emphasizes the tunability of MHP-based heterojunctions, enabling optimized designs for superior performance in ammonia production. Overall, the findings highlighted the promise

of perovskite-based heterojunctions in addressing future challenges in carbon neutrality and sustainable ammonia production.

In chapter 5, “Enhancing Visible-Light-Driven Hydrogen Production: Heterojunction Engineering of Graphitic Carbon Nitride and PBDB-T Organic Semiconductor”, is presented a homogeneous bulk heterojunction (BHJ) exploiting a novel organic semiconductor, PBDB-T togheter with g-C_3N_4 as photocathodic material for both photocatalytic (PC) and photoelectrochemical (PEC) hydrogen evolution. The optimized photocathode engineer achieved a photocurrent density of ~300 μA/cm² and maintained >90% stability over 300 seconds due to an additional g-C_3N_4 top layer that protected the photoactive BHJ during the photoelectrocatalytic reaction. Furthermore, the incorporation of a suitable hole transport layer (HTL), CuSCN, improved electron transport, enhancing the general performances. Also, the deposition of Pt on the g-C_3N_4 top protecting layer was essential to maximize photoelectrocatalytic efficiency, mirroring its known behaviour as a co-catalyst. The main limitations for the studied system include the need for fine-tuning g-C_3N_4 thickness of the top protecting layer, addressing electrical conductivity anisotropy, and exploring nanostructured forms of g-C_3N_4. The work underscored the potential of using carbon nitride-based PEC systems as low-cost, eco-friendly photoelectrocatalysts for sustainable hydrogen production and the presented strategy provides a foundation for developing advanced organic PEC architectures for green hydrogen generation. The research demonstrated promising results for integrating g-C_3N_4 in PEC systems while identifying avenues for further refinement and innovation.

Chapter 6, “High Entropy Perovskite Oxides and graphitic carbon nitride hybrid heterojunction for Solar Fuel Production” had as object of investigation nano-$La_{1-x}M_x(MnFeCoNi)_{0.25}O_3$/g-$C_3N_4$ heterojunctions for photocatalytic hydrogen generation focusing on enhancing the performance of eco-friendly g-C_3N_4. The main innovation presented in this work was the exploitation of a really low amounts of high entropy oxide perovskite in the composites stoichiometry. Five perovskite phases were synthesized via spray-pyrolysis, varying by composition and doping (e.g., substitution of Mn, Co, Ni at the Fe-site and Ca, Sr at the La-site). The perovskites phases were combined with g-C_3N_4 at different loadings (2.5%, 5%, 10% wt) and among all tested heterojunctions, $La_{0.6}Ca_{0.4}(MnFeCoNi)_{0.25}O_{3-\delta}$/g-$C_3N_4$ demonstrated significantly higher hydrogen evolution rates compared to bare g-C_3N_4. The incorporation of Mn, Co, and Ni created a high-entropy phase, enhancing stability and redox activity, crucial for photocatalysis. This specific

perovskite exhibited the highest oxygen vacancy density, as reported in prior studies, which plays a central role in enhancing photocatalytic activity, particularly in hydrogen evolution. The $La_{0.6}Ca_{0.4}(MnFeCoNi)_{0.25}O_{3-\delta}$/g-$C_3N_4$ heterojunction stands out due to its superior redox activity and high oxygen vacancy density, highlighting the role of structural defects in improving hydrogen generation efficiency in photocatalytic systems, proving to be a suitable and promising candidate as co-catalyst, already at low loading, for improve g-C_3N_4 photocatalytic performances.

These improvements have led to marked increases in solar fuels, both hydrogen and ammonia production rates, surpassing the capabilities of the standalone g-C_3N_4 used as benchmarks. Such enhancements underline the pivotal role of material interface tailoring in maximizing light absorption, optimizing band alignments, and improving surface reaction kinetics. From the synthesis of simple binary heterojunctions to more complex multi-component systems, the findings validate that heterojunction engineering is one of the most versatile and scalable approach to enhancing the efficiency of photocatalysts. Furthermore, as showed in the previous chapters, the adaptability of this strategy across various material systems highlights its potential for broad application in solar-driven chemical processes. In conclusion, the outcomes of this research emphasize that the careful engineering of heterojunctions represents one of the most effective pathways to improve the performance of already promising photocatalysts. This underscores the importance of continued investigation into advanced heterojunction designs, leveraging emerging materials and innovative synthesis techniques to further propel the field toward the realization of sustainable hydrogen and ammonia production technologies.

UNIONE EUROPEA
Fondo Sociale Europeo
Ministero dell'Università e della Ricerca
PON RICERCA E INNOVAZIONE 2014 - 2020
REACT EU

La borsa di dottorato è stata cofinanziata con risorse del
Programma Operativo Nazionale Ricerca e Innovazione 2014-2020, risorse FSE REACT-EU
Azione IV.4 “Dottorati e contratti di ricerca su tematiche dell’innovazione”
e Azione IV.5 “Dottorati su tematiche Green”